

DISS. ETH NO. 27951

# Functionalization of Wood Materials by Metal-organic Frameworks

A thesis submitted to attain the degree of  
DOCTOR OF SCIENCES of ETH ZURICH  
(Dr. sc. ETH Zurich)

presented by

Kunkun Tu

Master of Engineering, Chinese Academy of Forestry

born on *27.08.1990*

citizen of China

Accepted on the recommendation of

Prof. Dr. Ingo Burgert, ETH Zürich, examiner

Dr. Tobias Keplinger, ETH Zürich, co-examiner

Prof. Dr. Cordt Zollfrank, Technische Universität München, co-examiner

Prof. Dr. Tobias Kraus, Leibniz Institute for New Materials, co-examiner

2021



“A journey of a thousand miles starts with a single step.”

千里之行，始于足下。

——Laozi





# Abstract

Many materials have been explored to attain carbon neutrality and address climate change and resources scarcity. Among these, metal-organic frameworks (MOFs) are one of the most promising materials owing to their porous properties, structural diversity, and tunable pore structure. They have been widely used in various environmentally friendly applications, such as gas storage and separation, water treatment, catalysis, and energy production. However, due to their crystalline morphology, they most commonly occur as powders, and their processability and handling remain a significant challenge.

In recent years, research activities towards integrating MOFs into cellulose substrates, to produce engineered materials broaden their utilization. The resulting MOF/cellulose composites with hierarchical porosity, sophisticated multi-layered networks, and highly accessible MOF active sites have been used in many applications. In the first part of thesis, we summarize current state-of-the-art routes for the fabrication and applications of MOF/cellulose composites. We found that the most extensively utilized ways for fabricating structured MOF/cellulose composites are time and energy-consuming bottom-up methods, resulting in relatively weak mechanical properties.

Instead, wood is an ideal alternative support for MOFs as wood is a material with a natural hierarchical structure and strong mechanical performance. Hence, in the second part of this thesis, we introduced a versatile green synthesis method for the *in situ* growth of MOFs within wood substrates. Nucleation sites for MOFs were created by a sodium hydroxide treatment, which was demonstrated to be broadly applicable to different wood species. The resulting MOF/wood composites exhibited hierarchical porosity, CO<sub>2</sub> adsorption capacity, and superior mechanical properties, which surpassed those obtained for polymer/cellulose substrates.

Based on this approach, in the third part of the thesis, we were able to solve the problem of the weak polarizability of native wood by functionalizing it with a MOF (ZIF-8) and a common elastomer (PDMS). We assembled the two parts into wood triboelectric nanogenerators (W-TENGs), which are a mechanical energy-harvesting device with extremely promising applications for smart buildings. The functionalization of wood surfaces widened the spectrum of triboelectric polarities by selecting the crystal size of ZIF-8, wood species, and cutting direction. We demonstrate the applicability of our W-TENG in smart buildings by using it to power household lamps, calculators, and electrochromic windows.

In the final part of the thesis, we address the challenge of catalyst reusability and large-scale operation by structuring palladium-based catalysts on MOF functionalized wood microreactors for continuous-mode H<sub>2</sub> generation from ammonia borane. By exploiting amine-containing linkers, we demonstrate the uniform growth of distinct MOFs over the internal surfaces of different wood species. Surface functionalization of wood with MOFs is essential to stabilize well-dispersed palladium nanoparticles at high metal content. Evaluation of the structured catalysts in the continuous dehydrogenation of ammonia borane demonstrates high hydrogen production performance. In addition, the modular design of the structured catalysts is readily scalable. This part emphasized the relationship between the selected wood species and catalysis activity.

In this thesis, the developed strategies offer a stable, sustainable, and scalable platform for fabricating multifunctional MOF/wood-derived composites, showing the potential applications in environmental and energy-related fields. The research provides a deep understanding of the principle of enhancing the affinity between wood and MOFs, and wood structure-fabrication-performance relations, opening up new avenues in the utilization of wood/MOF composites.

# Zusammenfassung

Viele Materialien wurden bereits erforscht, um Kohlenstoffneutralität zu erreichen und dem Klimawandel und der Ressourcenknappheit zu begegnen. Unter diesen sind metallorganische Gerüstverbindungen (MOFs) aufgrund ihrer porösen Eigenschaften, strukturellen Vielfalt und kontrollierbaren Porenstruktur eines der vielversprechendsten Materialien, die in verschiedenen umweltfreundlichen Anwendungen wie Gasspeicherung und -trennung, Wasseraufbereitung, Katalyse und Energieerzeugung weit verbreitet sind. Aufgrund der kristallinen Beschaffenheit von MOFs liegen sie jedoch meist in Pulverform vor, und ihre Verarbeitbarkeit und Handhabung stellen nach wie vor eine grosse Herausforderung dar.

In den letzten Jahren wurden Forschungsaktivitäten zur Integration von MOFs in Zellulosesubstrate unternommen, um die Nutzung solcher Funktionsmaterialien zu erweitern. Die daraus resultierenden MOF/Zellulose-Verbundwerkstoffe mit hierarchischer Porosität, ausgeklügelten mehrschichtigen Netzwerken und gut zugänglichen aktiven MOF-Stellen wurden in vielen Anwendungen eingesetzt. Im ersten Teil der Arbeit wird der aktuelle Stand der Forschung zur Herstellung und Anwendung von MOF/Zellulose-Verbundwerkstoffen vorgestellt und zusammengefasst. Dabei sind die am häufigsten genutzten Methoden zur Herstellung von strukturierten MOF/Zellulose-Verbundwerkstoffen zeit- und energieaufwendige Bottom-up-Methoden, die zu Hybridmaterialien mit relativ eingeschränkten mechanischen Eigenschaften führen.

Im Gegensatz dazu, ist Holz eine ideales alternatives Trägermaterial für MOFs, da es mit einer natürlichen hierarchischen Struktur und sehr guten mechanischen Eigenschaften ausgestattet ist. Daher beschäftigt sich der zweite Teil dieser Arbeit mit einer vielseitigen grünen Synthesemethode für das in-situ-Wachstum von MOFs in Holzsubstraten. Die «Keimstellen» für das MOF Wachstum wurden durch eine Natriumhydroxid-Behandlung geschaffen, die auf verschiedene Holzarten anwendbar ist. Die daraus resultierenden MOF/Holz-Verbundwerkstoffe wiesen eine hierarchische Porosität, eine hohe CO<sub>2</sub>-Adsorptionskapazität und sehr gute mechanische Eigenschaften auf, welche die mit Polymer/Zellulose-Substraten erzielten Eigenschaften übertrafen.

Auf der Grundlage dieses Ansatzes gelang es im dritten Teil der Arbeit, das Problem der schwachen Polarisierbarkeit von nativem Holz zu überwinden, indem es mit einem MOF (ZIF-8) und einem gängigen Elastomer (PDMS) funktionalisiert wurde. So konnte ein triboelektrischer Holz-Nanogenerator (W-TENG) entwickelt werden, der als mechanischer Energiespeicher mit vielversprechenden Anwendungen im Bereich intelligente Gebäude

fungieren kann. Durch die Wahl der Kristallgröße von ZIF-8, der Holzart und der Schnittrichtung kann das Mass der Polarität gesteuert werden. Die Anwendbarkeit des W-TENG in intelligenten Gebäude, konnte durch die Stromversorgung von Haushaltslampen, Taschenrechnern und elektrochromen Fenstern demonstriert werden.

Im letzten Teil der Arbeit stand die Wiederverwendbarkeit von Katalysatoren im Vordergrund. Dazu wurden Katalysatoren auf Palladiumbasis auf MOF-funktionalisierten Holzmikroreaktoren für die kontinuierliche H<sub>2</sub>-Erzeugung aus Ammoniak-Boran strukturiert. Durch die Nutzung aminhaltiger Linker konnte ein gleichmäßiges Wachstum verschiedener MOFs auf den inneren Oberflächen verschiedener Holzarten erreicht werden. Die Oberflächenfunktionalisierung von Holz mit MOFs ist für die Stabilisierung von dispergierten Palladium-Nanopartikeln mit hohem Metallgehalt unerlässlich. Die Untersuchung der strukturierten Katalysatoren hinsichtlich der kontinuierlichen Dehydrierung von Ammoniak-Boran zeigt eine hohe Leistung bei der Wasserstoffproduktion. Darüber hinaus ist der modulare Aufbau der strukturierten Katalysatoren leicht skalierbar.

Die in dieser Arbeit untersuchten Strategien bieten einen nachhaltigen und skalierbaren Ansatz für die Herstellung multifunktionaler MOF/Holz-Verbundwerkstoffe und zeigen das Potenzial für Anwendungen in umwelt- und energiebezogenen Bereichen auf. Die Doktorarbeit trägt damit zu einem tieferen Verständnis der Prozesse zur Verbesserung der Affinität zwischen Holz und MOFs und der Wechselwirkungen zwischen Holzstruktur und Herstellung bei und eröffnet somit neue Wege für die Nutzung von Holz/MOF-Verbundwerkstoffen.

# Acknowledgements

First of all, I would like to express my sincere gratitude to my “Doktorvater” Prof. Ingo Burgert for the opportunity to conduct my doctoral studies in his group. He created an excellent environment for my research by providing adequate financial support, allowing me to choose my research topics, and always being patient in offering me advice, which I always appreciated. He is a kind professor who really considers his students’ future. His perseverance and integrity in scientific research set a positive model for me.

I want to thank Dr. Tobias Keplinger for his suggestions and great support both in research and life during these four years. He encouraged me to do collaborations with other groups and saving time after work to help me check my papers, making my research goes on a good track. He can always cheer me up from negative emotions and brighten my day. I would also thank Dr. Guido Panzarasa who helped to check the manuscript as well as gave many suggestions on my project. I would like to express my gratitude to Prof. Cordt Zollfrank and Prof. Tobias Kraus for co-examining my thesis.

I am very thankful to Prof. Javier Pérez-Ramírez. I felt grateful to have his professional and critical input, which are very helpful in improving the papers' quality. His enthusiasm, seriousness, and rigorous attitude toward science inspired me a lot. I also met the best collaborators, Dr. Begoña Puértolas, Dr. Sharon Mitchell, and Simon Büchele because of him. The different backgrounds lead to many fruitful discussions and expanded my horizon on catalysis and porous materials. They never feel tired of checking the manuscripts to make them perfect. Their careful and meticulous attitudes towards science let me know what a good scientist should be. I also want to thank my collaborators Dr. Laura Stricker, Dr. Zhidong Zhang, Prof. Samuel C. Zeeman, Jacqueline Traber, Roman Günther, Dr. Shivaprakash Narve Ramakrishna, Dr. Julien Allaz, Dr. Hengyu Guo, and Dr. Changsheng Wu for the help and support with constructive discussion on the idea and experiments. I am very thankful for the great support from my colleagues, who are also my important collaborators, namely Jianguo Sun, Yong Ding, Dr. Maria Adobes-Vidal, Sophie Marie Koch, Dr. Christian Goldhahn, Sandro Stucki, Thomas Schneider, and Dr. Qilian Fu. I also want to thank Dr. Karsten Kunze and Dr. Luiz Grafulha Morales in ScopeM for their training on SEM operation. Without the assistance of these specialists from different fields within and outside the ETH domain, this thesis would not have reached this level of depth and breadth.

I want to thank all my colleagues for administration and technic support, as well as interesting non-scientific discussions after work, namely Andrea Merletti, Stéphane Croptier, Huizhang

Guo, Christopher Dreimol, Eashan Saikia, Munish Chanana, Walter Sonderegger, Markus Rüggeberg, Maximilian Ritter, Paul-Antonie Spies, Samuel Olaniran, Marta Vidiella del Blanco, Falk Wittel. I also enjoy the time with Marion Frey, Philippe Grönquist, Yaru Wang, Cheng Chen, and Wenqing Yan.

I really appreciate the financial support from the China Scholarship Council (CSC) (201703270028).

All of these achievements would likely not have been possible without Prof. Xiaoqing Wang, who was the first person to introduce me to ETH Zurich and who was the one encouraging me to pursue my doctoral studies in this great university, and for which I am deeply grateful.

Without all of my friends, my PhD life would not have been the same. I want to thank my friends Chun Liu, Yingfang He, Yuliang He, Tongtong Wang, Qinlei Liu, Liqing Zheng, Tian Liu, and Qian Chen (I know I cannot name you all!) for all the fun, joys, and supports in all these years. I really enjoy the hiking, traveling, dinner, and talk we have together.

Finally, I would like to thank my parents Dekuan Tu and Cuilan Wang. They are my strong supports and powerful backing during my entire life, giving me encouragement, understanding, and love. I also want to thank my fiancé Dr. Wenjie Ge for his faithful support, careful and patient care, and valuable advice, especially during my hard and stressful moments.

# Table of Content

<b>Abstract</b> .....	<b>i</b>
<b>Zusammenfassung</b> .....	<b>iii</b>
<b>Acknowledgements</b> .....	<b>v</b>
<b>Table of Content</b> .....	<b>vii</b>
<b>1 Motivation and Objectives</b> .....	<b>1</b>
<b>2 Outline of thesis</b> .....	<b>3</b>
<b>3 Introduction</b> .....	<b>7</b>
3.1 The wood material .....	7
3.2. Metal-organic frameworks (MOFs) .....	12
3.3 Characterization methods .....	17
<b>4 Publications</b> .....	<b>21</b>
4.1 Metal-organic framework/cellulose composites: From fabrication to applications .....	23
4.2 Green Synthesis of Hierarchical Metal-Organic Framework/Wood Functional Composites with Superior Mechanical Properties .....	59
4.3 Functionalized wood with tunable tribo-polarity for efficient triboelectric nanogenerators .....	89
4.4 Structured Wood-based Catalytic Microreactors for Continuous Hydrogen Generation from Ammonia Borane .....	131
<b>5 General Discussion and Outlook</b> .....	<b>171</b>
5.1 Wood structure-fabrication-function relationships .....	171
5.2 Enhancing the affinity between wood and MOFs .....	175
5.3 Critical role of controlling MOF loading and crystal structure .....	176
5.4 Outlook .....	177
<b>Literature of Chapter 1, 3, and 5</b> .....	<b>179</b>
<b>Curriculum Vitae</b> .....	<b>187</b>
<b>Declaration</b> .....	<b>191</b>





# 1 Motivation and Objectives

Climate change, pollution, and resource shortages are among the greatest challenges of humankind. To address these issues and realize the carbon neutrality transition in the world, there are many ways, including carbon capture and storage, generation electricity from zero-emission sources, and expanding clean and renewable energy.<sup>1</sup>

Metal-organic frameworks (MOFs), a class of crystallized porous materials formed by the coordination of metal ions/clusters and organic bridging ligands,<sup>2</sup> have been fabricated and explored in various functional applications to contribute to mitigate the problems mentioned above, for example, gas storage and separation,<sup>3,4</sup> water treatment,<sup>5</sup> sensing,<sup>6</sup> catalysis,<sup>7,8</sup> and energy production.<sup>9,10</sup> Their structures can be tailored to specific functionality based on the organic linkers' geometries and the inorganic metal ions' coordination modes. The ultrahigh porosity and large surface areas of MOFs play a crucial role in these functional applications. However, MOFs are generally in powder form due to their crystalline nature, making their processability and handling a substantial issue.<sup>11</sup>

Integrating MOFs into polymer substrates to produce engineered materials is an ideal method to broaden the utilization of such functional materials.<sup>12</sup> As a result, MOFs have been integrated or grown onto a variety of polymers, yielding MOF/polymer composites with hierarchical porosity and sophisticated multi-layered networks that have been used in many applications.<sup>13</sup> However, the use of synthetic polymers derived from petrochemical products cause environmental problems. As an alternative, cellulose, as the most widely used biopolymer with biodegradability, biocompatibility, renewability, and low-cost has attracted a great deal of attention for the fabrication of MOF composites.<sup>14</sup> The most widely used methods for fabricating structured MOF/cellulose composites are bottom-up methods, such as the spinning process, casting, filtration, freeze-drying, and 3D printing.<sup>15-19</sup> Even though these techniques enable composites with sufficient porosity, they are often characterized by weak mechanical properties. Instead of applying time and energy-consuming bottom-up methods, employing wood, a material with natural hierarchical structure and strong mechanical performance, as support for MOFs is a viable approach.

Wood represents one of the oldest materials used by mankind in manifold applications such as construction or furniture, owing to its outstanding mechanical properties, environmental characteristics and aesthetic appearance.<sup>20</sup> Moreover, in recent years, due to its sophisticated hierarchical cellular structure with pronounced anisotropy and lignocellulosic composition (mainly cellulose, hemicellulose and lignin), wood has been also used in a variety of high-tech

applications, for example, water treatment, energy storage, and solar steam generators.<sup>21-24</sup> However, there is no research related to the combination of hierarchical wood materials with functional MOF crystals prior to the studies in this thesis, but there are many energy and environmental friendly applications that can be explored based on wood/MOF composites.

Hence, the goal of this work is to *in situ* grow MOFs within wood substrates to develop MOF/wood hybrid materials, and test their performance at the laboratory scale in various fields of application such as gas adsorption and separation, mechanical energy harvesting, and hydrogen generation. The characterization and functionality of these composites are shown and discussed in this thesis. The following are the main objectives of this cumulative thesis:

1. Deep understanding of the development of MOF/cellulose composites, both in terms of fabrication and function.
2. Development of a universal and green approach for the *in situ* growth of MOFs within wood substrates.
3. Tackling the challenge of weak polarizability of native wood by functionalizing wood with MOFs for building an efficient triboelectric nanogenerator.
4. Development of a controlled process for hydrogen generation in continuous mode from ammonia borane by structuring palladium-based catalysts on MOF functionalized wood microreactor.

Based on these objectives, we can have a deep understanding of the principle of enhancing the affinity between MOFs and wood, as well as wood structure-performance relations. It will open up new avenues in the utilization of wood/MOF composites.

## 2 Outline of thesis

The main part of this cumulative thesis consists of four journal articles, including one review article and three research articles. They describe the functionalization of natural wood materials and cellulose with MOFs for energy and environmental friendly applications.

Prior to the four main manuscripts in Chapter 4, a brief introduction is given regarding the background of the materials used in this thesis, which are wood materials (chapter 3.1) and MOFs (chapter 3.2). In addition, the characterization methods for wood-based functionalized materials are presented in chapter 3.3.

In chapter 4.1, the first paper “Metal–Organic Framework/Cellulose Composites: From Fabrication to Applications” is presented. In this paper, we summarize current state-of-the-art routes for the fabrication MOF/cellulose composites and highlight their utilization in various applications. In addition, the paper includes current limitations and provides possible future research directions in the field of MOF/cellulose composites for advanced functional materials.

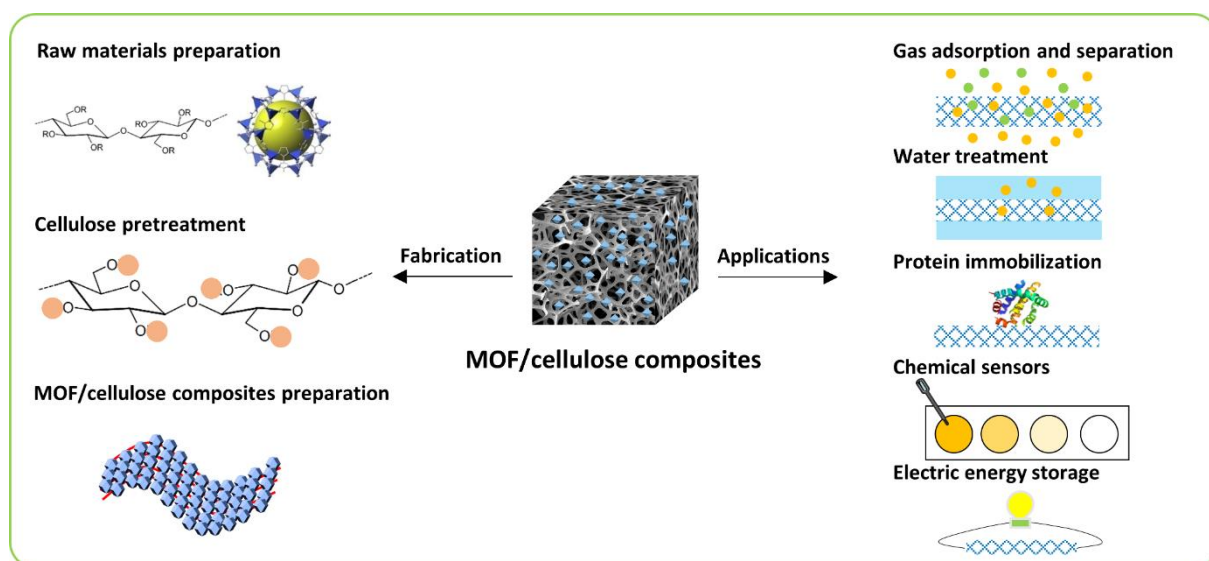


**Figure 1** Schematic of fabrication steps and applications of MOF/cellulose composites.

In chapter 4.2, the second paper “Hierarchical Metal–Organic Framework/Wood Functional Composites with Superior Mechanical Properties” presents a universal green synthesis method for the *in situ* growth of MOF nanocrystals within wood substrates. The chemical and morphological changes after each modification steps are investigated. Additionally, the porosity, mechanical properties, and CO<sub>2</sub> adsorption ability are analyzed in this paper.

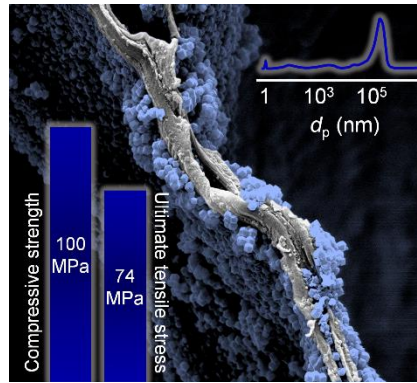


**Figure 2.** The morphology, porosity and mechanical property of the MOF/wood composites prepared by *in situ* growth method.

Chapter 4.3 consists of the third paper “Functionalized Wood with Tunable Tribo-Polarity for Efficient Triboelectric Nanogenerators”. In this paper, we functionalized wood with a metal-organic framework (ZIF-8) and a common elastomer (PDMS) to fabricate efficient triboelectric nanogenerators, in which wood is used as natural micro- and nanostructured template because of its unique structure and morphology.

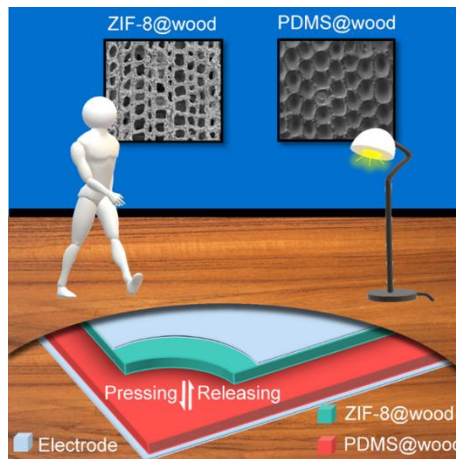


**Figure 3.** Schematic of functionalized wood with tunable tribo-polarity for triboelectric nanogenerator.

Chapter 4.4 comprises the fourth paper with the title “Structured Wood-based Catalytic Microreactors for Continuous Hydrogen Generation from Ammonia Borane”. In this paper, we developed a controllable process for hydrogen generation in continuous-mode from solid-state storage chemical (ammonia borane) by structuring palladium-based catalysts on MOF functionalized wood microreactors.

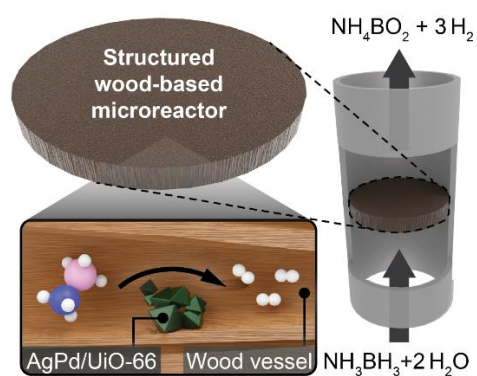


**Figure 4.** Illustration of structured wood-based catalytic microreactors for continuous hydrogen generation from ammonia borane

The final part of thesis presents a general discussion addressing the results, limitations, and provides an outlook (chapter 5).



# 3 Introduction

## 3.1 The wood material

Wood possesses good mechanical performance in view of its lightweight originating from the hierarchical structure bridging multiple length scales from the macroscale of the wood stem to macromolecules (**Figure 5 and 6**).<sup>25</sup> The rigid cell walls of wood are determined by aligned cellulose fibrils embedded in a compliant matrix of lignin and hemicelluloses. It has inspired plenty of materials science research activities to consider wood as a material to be used in high-tech applications. Before exploring new wood-based functional materials, it is crucial to have a deep understanding of the wood structure, its chemical composition, wood species, and the current state-of-the-art of such functional materials.

### 3.1.1 Hierarchical structure

Wood discussed in this work refers to the xylem (including sapwood and heartwood) of the trunk of a tree (**Figure 5a and b**). In the living tree, cell structures of the wood are mainly orientated along the longitudinal direction (**Figure 5c**). These cells not only provide mechanical support but also pathways for water transport from the roots to the leaves.

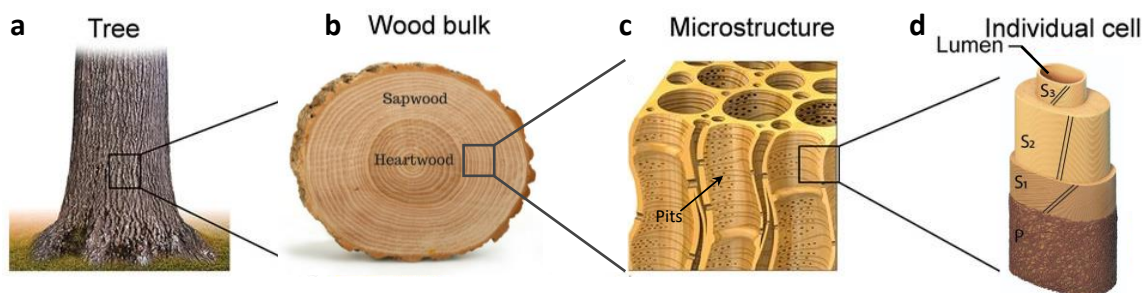


**Figure 5.** The hierarchical structure of wood. The figure (a) and (c) are adapted from Chen et al.<sup>25</sup> The individual cell in (d) is illustrated by Josh Binswanger, Bachelor thesis ZHdK, 2019

Wood species are divided into softwood and hardwood, showing different cell types, pore size and porosity, and densities. For example, as shown in **Figure 6**, softwood mainly consists of one cell type, the tracheid, which possesses different lumen size and cell wall thickness in earlywood and latewood within one growth ring. The tracheids in earlywood mainly specialized for water transport have thin cell walls and wide lumina, while tracheids in latewood specialized for mechanical support have thick cell walls and narrow lumina. By contrary, in hardwoods these two functions are covered by two cell types with different micro pore size, which are vessels and fibers, respectively. Vessels have thin cell walls and wide lumina, used for water transport. Fibers have thick cell walls and narrow lumina, used for mechanical function.



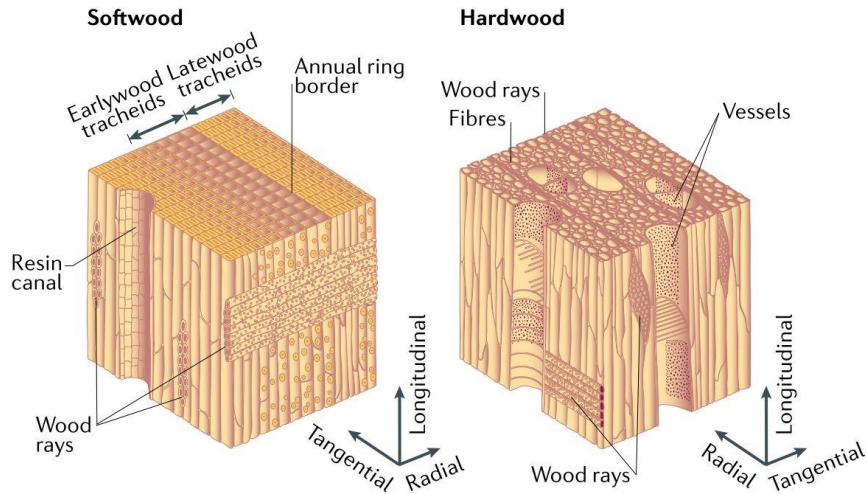


**Figure 6.** The microstructure of softwood (left) and hardwood (right).<sup>26</sup>

The diversity of cell structure results in various morphological characteristics of wood both in different species and in different parts of the tree stem. It makes wood a good candidate as a natural micro- and nanostructured template for fabricating functional materials with large directed porosity, since the diversity of wood microchannels along the longitudinal direction allows for specific selection of suitable structures for solid, gas, or liquid mass transport.

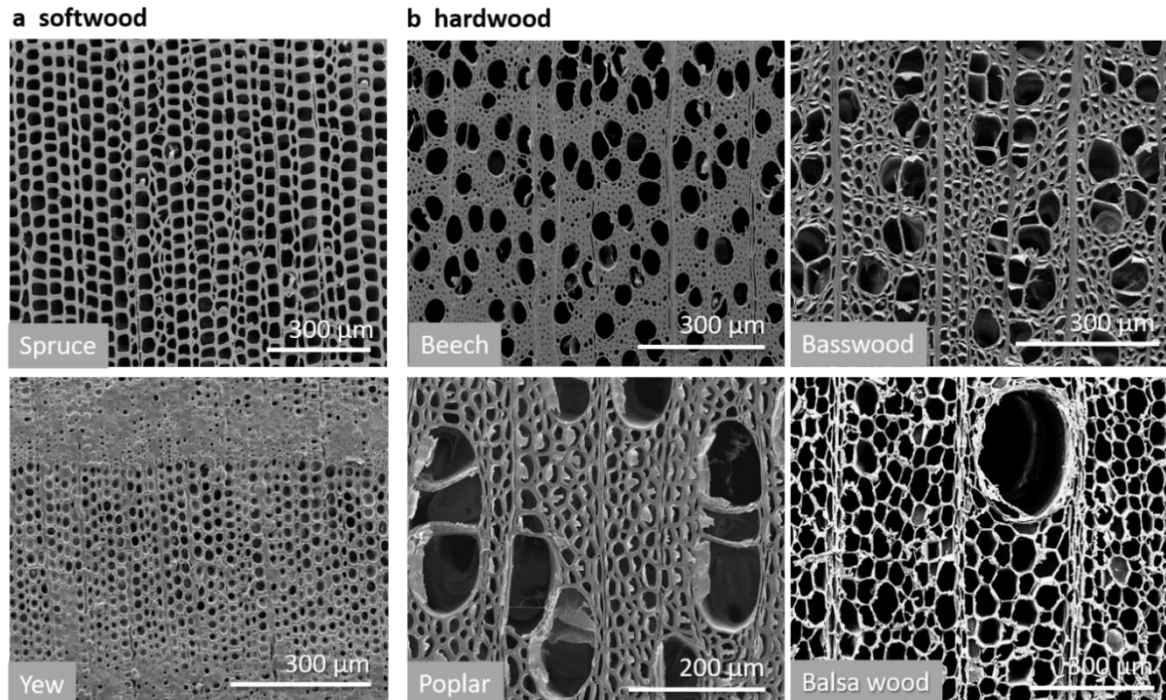


**Figure 7.** The SEM images of wood species used in this study (a) softwood and (b) hardwood.



To explore the effect of wood structure in different applications, softwood including spruce and yew (**Figure 7a**), and hardwood including beech, basswood, poplar, and balsa wood (**Figure 7b**) were selected in this study.

Each individual cell consists of a primary layer (P) and three secondary cell wall layers (S1-S3) (**Figure 5d**), with different orientations of cellulose microfibrils and chemical compositions in each layer. The middle lamella is in between neighboring cells. Pits traversing the cell walls allow water transport between individual cells (**Figure 5c**).

The chemical composition of wood is mainly cellulose, hemicelluloses, and lignin, which account for more than 90% of the wood (**Figure 8**).<sup>27,28</sup> Except for these, there is a small amount of extractives and ashes existing in wood.

The volume fraction of cellulose is approximately 40-50% of the dry substance in wood and is mainly located in the secondary cell wall. Cellulose consists of linear homopolymer chains composed of D-glucose units linked by  $\beta$ -(1,4)-glycosidic bonds.<sup>29</sup> Cellulose within wood contains both crystalline regions and amorphous regions. The cellulose chains tend to form intra- and inter molecular hydrogen bonds and aggregate together.

Hemicelluloses are polysaccharides composed of a broad variety of sugars, including the hexoses D-glucose, D-mannose, D-galactose, the pentoses D-xylose and D-arabinose and D-glucuronic acid. The contents of these sugars vary between softwoods and hardwoods. Softwoods contain higher amounts of mannose and galactose units, while hardwoods have a higher proportion of xylose units and more acetyl groups. Besides hydroxyl groups and acetyl groups mentioned above, there is a small amount of carboxyl groups in hemicellulose, around 0.01-0.02 mmol/g.<sup>30</sup>

Lignin is a three-dimensional (3D), heterogeneous polymer, which consists of various aromatic building blocks. It dominates in the compound middle lamella and cell corners but is also integral part of the matrix of the wood cell wall. The basic monolignols are p-coumaryl alcohol, coniferyl alcohol, and sinapyl alcohol. The volume fractions of monomers of lignin in softwood and hardwood are different. The softwood lignin consists mainly of guajacyl units, while hardwood consist of guajacyl and syringyl units.

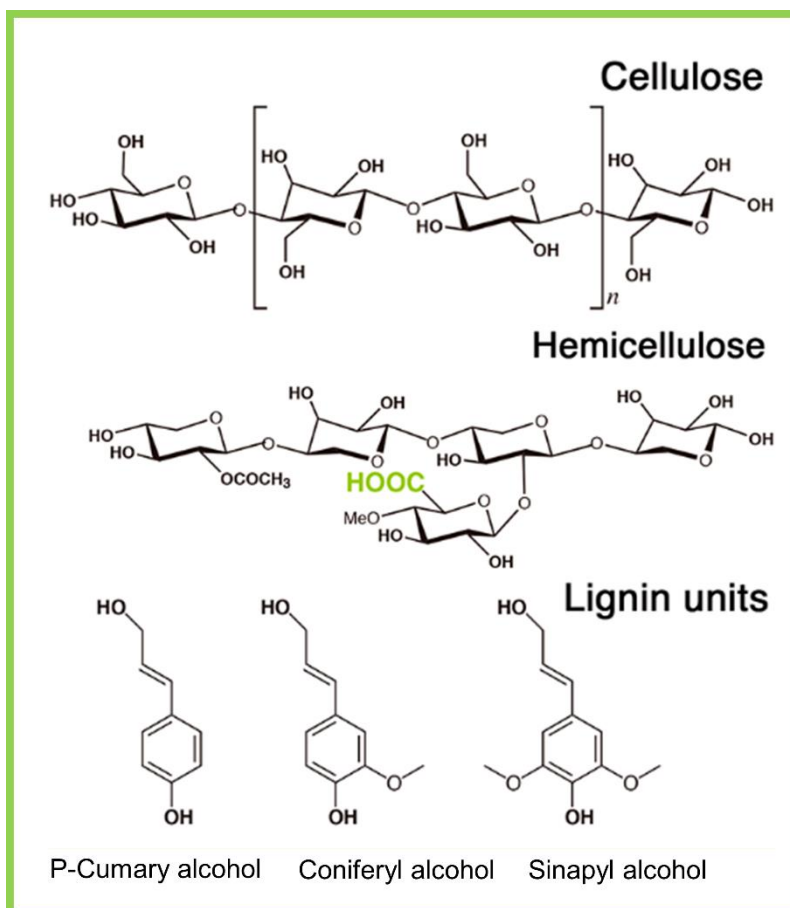


**Figure 8.** Chemical composition of wood at the molecular level.

### 3.1.2 Wood-based functional materials

Despite its sophisticated hierarchical structure based on cellulose fibrils embedded in a compliant matrix of lignin and hemicelluloses, wood was not considered as a material to be used in high tech applications in the past. Traditional wood modification approaches were mainly focused on diminishing the influence of the intrinsic drawbacks of wood (e.g. dimensional instability, fungal decay and flammability),<sup>31</sup> comprising chemical modification, surface modification, thermal modification and impregnation treatments. Among these, a few processes such as acetylation, furfurylation and thermal treatment have been commercialized and are used at large scale.<sup>32</sup>

In recent years, intensive research regarding the functionalization of wood has been performed including *in situ* polymerization<sup>9</sup>, mineralization<sup>33</sup> and metallization<sup>34</sup> in order to introduce new functionalities for new wood applications. In these functionalization approaches, additional functional groups or varieties of components are introduced into wood. These chemical modifications enable to alter the wood structure at the cell wall level and the location of the additives can be either on the surface or inside the cell walls and/or lumina (**Figure 9**). In

addition, the interface between wood and added materials plays an essential role in altering the properties and functions of chemically modified wood. Following this approach, several research studies have been conducted, such as *in situ* formations of colloidal iron oxide particles in the cell lumina for magnetic wood<sup>35</sup> or the insertion of calcium carbonate into the cell wall for flame retardancy<sup>36</sup>. In addition, a multitude of different polymerization techniques has been adapted for the modification of wood. Polymer functionalization approaches offer a versatile and modular toolbox for the modification of wood as it is possible to tune the final properties of the material by using a suitable functional monomer. In this respect, temperature and pH stimuli-responsive wood as well as conductive wood was obtained.<sup>37</sup>

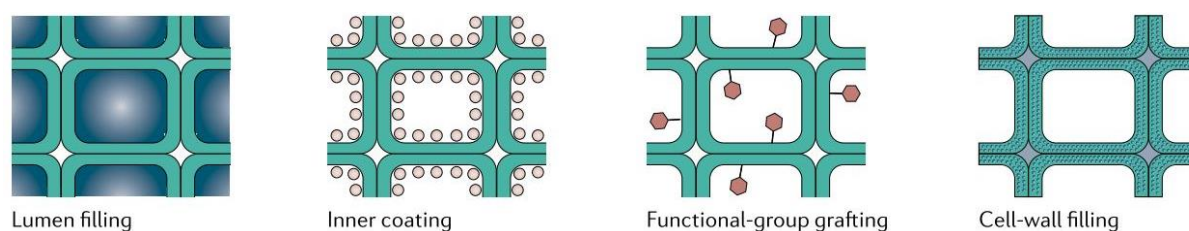


**Figure 9.** Chemical modification strategies of wood materials, including lumen filling, inner coating, functional group grafting, and cell wall filling.<sup>26</sup>

At the same time, wood has raised increasing attention in materials science due to the driving need of developing functional materials, which are derived from renewable resources. This is crucial for the transformation towards a sustainable society and to reduce the pressure of resource shortage and anthropogenic environmental deteriorations<sup>21</sup>. In particular, wood as an abundant renewable resource, equipped with a porous hierarchical structure and anisotropy, can serve as a natural template for the development of new types of functional hybrid materials, opening the path for new wood applications. In this regard exemplarily, wood for water treatment, energy storage, or solar steam generators has been developed as a potential replacement for non-renewable materials (as shown in **Figure 10**).<sup>21-24</sup> Due to the pre-fabricated hierarchical structure of wood up scaling of functionalization is eased, which is a powerful alternative to bottom-up approaches, e.g. nanocellulose.<sup>38,39</sup>

More energy and environmental-related functional wood materials can be explored, such as gas adsorption and separation, mechanical energy harvesting, and hydrogen generation. The use of inorganic materials, such as MOFs, which have been widely developed in various applications, are a promising approach to realize such emerging functional materials.

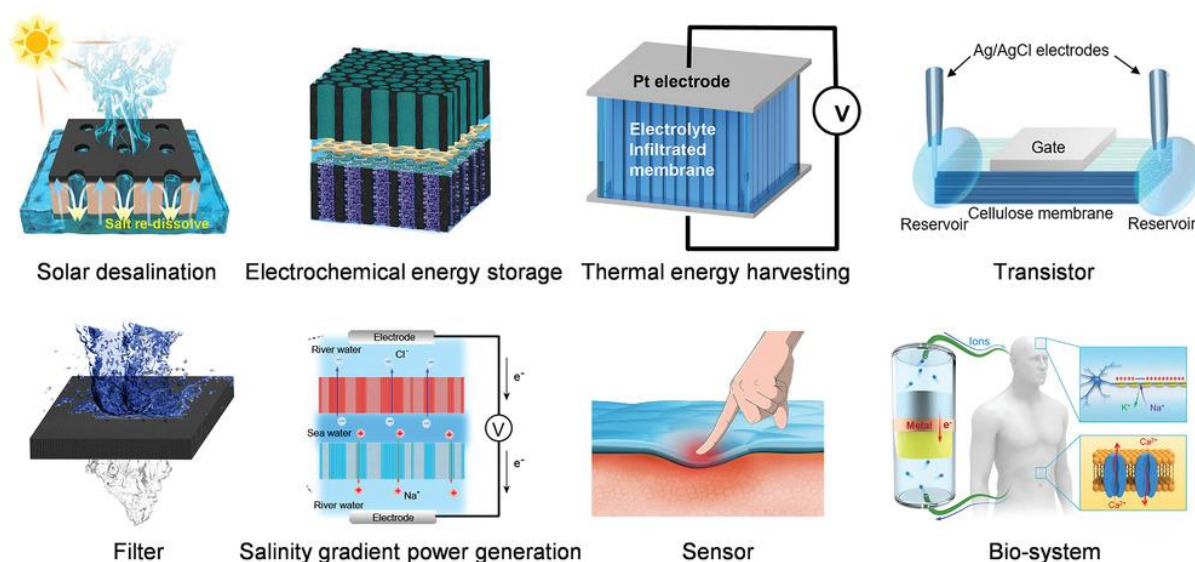


**Figure 10.** Emerging applications of wood-based functionalized materials.<sup>25</sup>

### 3.2. Metal-organic frameworks (MOFs)

Metal-organic frameworks (MOFs) also called porous coordination polymers (PCPs), are two- or three-dimensional porous crystalline materials with infinite lattices. They are synthesized from secondary building units, metal cations salts or clusters, and polydentate organic ligands.<sup>40</sup> The combination of various metal clusters and ligands arranged in a vast array of geometries has led to an expanding MOF family.<sup>41</sup> MOFs have a large surface area and ultrahigh porosity. The Brunauer-Emmett-Teller (BET) surface area of MOFs typically ranges between 1000 and 10,000 m<sup>2</sup> g<sup>-1</sup> and the porosity of MOFs is larger than 50% of the MOF crystal volume. These aspects make MOFs different from conventional porous materials such as carbon and zeolites.<sup>42</sup> Due to the benefits of well-defined pores, flexible geometry, tunable crystal sizes, and functionalities, MOFs have significantly expanded applications, such as gas storage and separation,<sup>43</sup> triboelectric nanogeneration,<sup>44</sup> catalysis,<sup>45</sup> sensing,<sup>6</sup> and energy storage.<sup>46</sup>

#### 3.2.1 MOFs' structure

To understand the structure of MOFs, we use MOF-5, one of the first MOFs to be rugged enough for practical use, as an example (**Figure 11**). It is a cubic building block formed by linking eight metallic nodes with carbon-based struts.<sup>47</sup> MOF mainly comprises three parts: 1) an organic moiety composed of a rigid organic backbone with two or more moieties capable of coordinating metallic cations; 2) an inorganic part composed of either a cation, a metal-oxo cluster or a metal-oxo chain; and 3) a well-defined pore, which has an architecture defined by the coordination between the organic and inorganic moieties.<sup>48</sup> The final structure design, functionality, and application of MOFs are contributed from various factors, such as the linker

design, linker chelation, binding affinity, number of open metal sites on the clusters, strength of the metal-organic bond, and the symmetry of the moiety.<sup>41</sup>

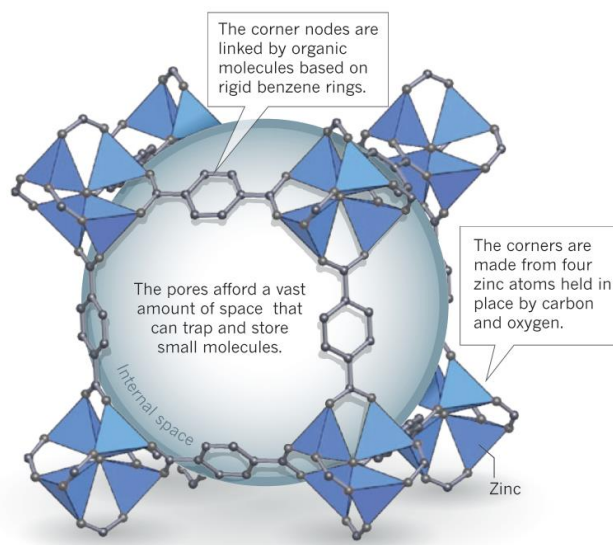


**Figure 11.** The building blocks of MOF-5 are cubes formed by linking together eight metallic nodes with carbon-based struts.<sup>47</sup>

Considering the water, thermal, chemical, and mechanical stability, the synthesis difficulty, and the price, the MOFs used for fabricating MOF-based composites mainly focus on some “star” MOFs. For example: MOF-199 (or named Cu-BTC or HKUST-1),<sup>49,50</sup> ZIF (Zeolitic imidazolate framework) family (e.g., ZIF-8, ZIF-9, ZIF-12, ZIF-67, and ZIF-90),<sup>18,51-53</sup> MIL (Materials Institute Lavoisier) series (e.g., MIL-53(Al), MIL-101(Fe), MIL-88B(Fe)),<sup>54-56</sup> and Zr-based MOFs (e.g., UiO-66 and UiO-67).<sup>57</sup> Here we introduce ZIF-8, MOF-199, and UiO-66 in detail, which are used in this study (**Figure 12**).

#### (a) ZIF-8

Zeolitic imidazole frameworks (ZIFs), a sub-family of MOFs consist of M-Im-M (where M stands for Zn, Co cation and Im stands for the imidazolate linker). Typically, the  $\text{Zn}^{2+}$  ions and the imidazolate anions form bridges with the metal-imidazole-metal angle of  $\sim 145^\circ$ .<sup>58</sup> ZIF-8 is one type of ZIFs, composed of  $\text{Zn}^{2+}$  ions and 2-methylimidazole (2-MeIm), exhibiting a sodalite-type structure illustrated in **Figure 12a**. The diameter of the micropores in the center of ZIF-8 is 11.6 Å. This pore is accessible through small apertures with a diameter of 3.4 Å.<sup>59</sup> The synthesis methods of ZIF-8 reported include solvent-based synthesis methods and solvent-free synthesis methods. When using solvothermal synthesis approaches to synthesize ZIF-8, methanol is an important organic solvent widely used. However, it is not environmentally friendly. Hence, Pan et al. realized for the first time to prepare ZIF-8 in an aqueous system at room temperature via a simple procedure.<sup>60</sup> Due to advantages of ZIF-8 in terms of ultrahigh

surface area, unimodal micropores, high crystallinities, abundant functionalities and exceptional thermal and chemical stabilities, ZIFs are widely used in various applications, such as gas adsorption and separation, water treatments, triboelectric nanogeneration, and so on.<sup>44,61</sup>

**(b) MOF-199**

MOF-199, also called Cu-BTC or HKUST-1, is an important crystalline nanoporous MOF, first reported by S.-Y. Chui et al. (1999) from Hong Kong University of Science and Technology.<sup>62</sup> MOF-199 is made of copper nodes with 1,3,5-benzenetricarboxylic acid struts between them (**Figure 12b**). It exhibits a unique turquoise-blue color because of the existence of copper. Due to its easy synthesis and the presence of open metal sites, it has been widely used in a variety of areas including gas storage and purification.<sup>63,64</sup>

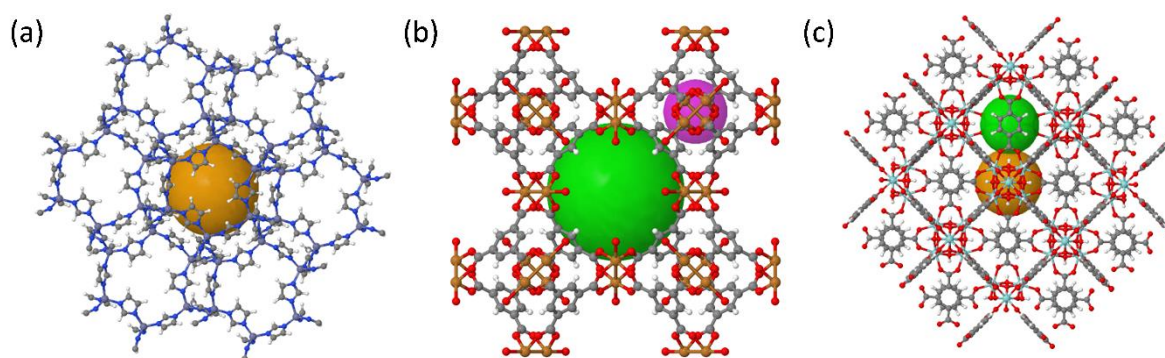


**Figure 12.** The crystalline structure of (a) ZIF-8, (b) MOF-199, and (c) UiO-66. The sphere represents the pore size within the framework. The figures are obtained via the COD (Crystallography Open Database)

**(c) UiO-66**

UiO-66 (UiO represents Norwegian Universitetet i Oslo), is mainly made of zirconium at the metal center (**Figure 12c**) and various organic linker molecules used to connect the metal nodes, in which, the most widely used is terephthalic acid. Its derivatives, such as 2-aminoterephthalic acid can also be used to build NH<sub>2</sub>-UiO-66. The additional functional group (NH<sub>2</sub>-) is not used to build the scaffold structure but for enhancing the affinity between MOF and wood via the hydrogen bonds formed between the amine groups and the hydroxyl groups of wood macromolecules. Benefiting from the strong coordination bonds between the hard-acid-hard-base interactions of the Zr(IV) atoms and carboxylate oxygens, the UiO-66 exhibits exceptional chemical and thermal stability, as well as excellent water stability.<sup>65</sup> Hence, it has been widely used for water-based applications, such as water desalination and water purification.<sup>66</sup> In addition, because of the extraordinarily high surface area, well-defined pore structure, and high porosity, UiO-66 is able to stabilize metal nanoparticles while maintaining the accessibility for



reagents.<sup>67</sup> Hence, bimetallic AgPd/UiO-66 hybrid catalysts have been explored for catalytic hydrolysis of ammonia borane,<sup>68</sup> dehydrogenation of formic acid,<sup>69</sup> propylene glycol oxidation into lactic acid.<sup>70</sup>

### **3.2.2 MOFs' applications**

The unique structure of MOFs equips them with a large surface area and high porosity. Hence, they have been used for various applications, such as gas adsorption, storage, and separation, liquid purification, catalysis, as well as drug delivery, chemical sensor.<sup>2,6,71</sup> Except these, many promising applications are explored, such as energy harvesting and hydrogen evolution.<sup>9,45</sup> A brief introduction, focusing on the application examples in the thesis, is provided in the following.

#### ***(a) Gas adsorption and separation***

Adsorptive separation with porous materials is a promising technology for reducing separation energy consumption. Compared with traditional gas adsorption materials, such as zeolites, alumina, and ceramics, MOFs are of interest owing to the following characteristics: (1) a high degree of design: To synthesize MOFs with diverse topologies, a wide range of linkers and metal ions can be used. The obtained MOFs can be further chemically modified using a post-synthetic modification technique to adjust the pore sizes and inner surface properties. (2) High porosity. When compared to the same mass loading of conventional materials, MOFs exhibit better performance due to their higher pore volume and lower density.<sup>13</sup> The sum of the adsorbate-adsorbate and adsorbate-adsorbent interaction potentials is the interaction potential energy of gas adsorption in the interior of porous materials. Adsorptive separation of gas mixtures is based on the difference in their interaction potentials with the pore surface, which are accumulative. Furthermore, until a certain threshold, only tiny and proper-shaped gas molecules may diffuse into porous materials, while all other gases are rejected, allowing for molecular sieving.<sup>72</sup> The most frequently reported MOFs for CO<sub>2</sub> selectivity over N<sub>2</sub> are Cu-BTC, IRMOF-1, IRMOF-10, ZIF-78, ZIF-8.<sup>73,74</sup>

#### ***(b) Energy harvesting***

Because of rising environmental awareness and considerable technological breakthroughs, there is a growing market for electronics based on the utilization of clean and abundant energy. Hence, solar, wind, water, and mechanical energy are exploited. The triboelectric generator (TENG) is an energy harvesting device that can convert external mechanical energy into electricity. It is constructed by stacking two thin organic/inorganic films that exhibit opposite

tribo-polarity and depositing metal films on the top and bottom of the assembled structure.<sup>75</sup> Almost all known materials exhibit the triboelectrification effect, from metal to polymer, silk, and wood, which all can be used to make TENGs. In which, native wood is close to electroneutrality. The polarity of the materials, the ability of a material to gain or lose electrons, are important to the TENGs performance.<sup>76</sup>

Khandelwal et al. (2019) were the first to report ZIF-8-based TENG for self-powered system and sensor applications.<sup>44</sup> In the following year, they developed TENGs based on the ZIF subfamily materials (ZIF-7, ZIF-9, ZIF-11, ZIF-12, and ZIF-62). However, these ZIF subfamily materials show worse electric performance than ZIF-8.<sup>9,77</sup> Except these, biodegradable MOF (MIL-88A) and humidity-resistive MOF (HKUST-1) have also been utilized to build TENGs.<sup>78,79</sup>

### ***(c) Hydrogen generation***

Green hydrogen is considered as one the most promising alternative energy carriers for meeting the growing demand for a clean and sustainable energy source. Intense studies have been conducted related to using MOFs for various hydrogen generation techniques.<sup>45</sup> In addition to the pristine form, MOFs can also be used as supporting frameworks and precursor materials for electrocatalytic, photocatalytic, and chemocatalytic hydrogen evolution reactions. Compared with energy intensive electrocatalytic process and extremely strict requirements needed for photocatalytic processes, chemocatalytic hydrogen evolution reactions might be an alternative option. Hydrogen can generate through chemocatalytic decomposition of hydrogen precursors, such as ammonia borane, hydrazine monohydrate, and sodium borohydride via suitable catalysts.<sup>45,80</sup> Ammonia borane is a hydrogen storage material with great potential since its high gravimetric capacity of hydrogen (19.6 wt.%), water-solubility, safe handling, and transportation in the dry state, nontoxicity, and chemical stability.<sup>81</sup> The catalysts can be prepared by loading active metal nanoparticles on MOFs. For example, AgPd/UiO-66, AuCo/MIL-101, and CuCo/MIL-101 are prepared for hydrolysis from ammonia borane for hydrogen generation. The catalytic activity of metal alloy can be enhanced by MOF because of the avoidance of metal aggregation.<sup>68,82,83</sup>

### **3.2.3 Limitations of MOFs**

MOFs are brittle because of their crystal and powder characteristics. Their processability and handling can be a substantial problem, limiting their applicability.<sup>84</sup> One possible option is to integrate MOFs onto or into diverse substrates using polymers<sup>85</sup>, silica<sup>86</sup> or carbon<sup>87</sup> as a support. Considering the environmental issue, cellulose, as the most abundant biopolymer on the earth,



with biodegradability, renewability, and a high number of reactive groups, represents as ideal support. A review in chapter 4.1 describes the fabrication and applications of MOF/cellulose composites in detail.

However, the most widely used methods for fabricating porous MOF-containing cellulose composites are bottom-up methods, such as the spinning process, casting, filtration, freeze-drying, and 3D printing.<sup>15-19</sup> Even though these techniques enable composites with sufficient porosity, they are often characterized by weak mechanical properties. By contrary, using wood with a hierarchical structure and good mechanical performance as MOFs supports is a promising option. However, the interface chemistry between MOFs and substrates needs to be improved and difficulties such as non-controllable spatial distribution of MOFs, poor contact between MOF crystals and substrates, and aggregation of MOF particles within the substrates should be addressed.

### **3.3 Characterization methods**

A thorough and detailed characterization of MOF/wood composites is necessary because it allows for a better understanding of the composites' structural, physical, and chemical properties, all of which are important in understanding the structure-property-function relationships of the final composites.

#### **3.3.1 Physical characterization**

##### ***(a) Structural characterization***

In general, the morphology and localization of the introduced MOFs within/on the wood are characterized using various microscopies, including optical microscopy, scanning electron microscopy (SEM), transmission electron microscopy (TEM), high-angle annular dark field-scanning transmission electron microscopy (HAADF-STEM), atomic force microscopy (AFM), and optical profilometry. They are selected according to the length scale of interest. For example, SEM is better for studying wood's surface morphology with limited to 1 nm resolution, while TEM can provide more details about surface irregularities and internal anatomy with up to 0.1 nm resolution.<sup>88</sup> STEM has an atomic resolution of 0.2 nm and under, which can be used to check the metal distribution within MOF crystals.<sup>89</sup> AFM can be effectively used to visualize cell wall layer changes and provides roughness information with a nanometric resolution. Optical profilometry is also a technique aimed at getting surface morphology, step heights, and surface roughness. It is based on the reflection of a luminous signal on a surface and allows the

topography of that same surface to be observed throughout a wide variety of measurement ranges, from a few dozens of  $\mu\text{m}^2$  to a few  $\text{mm}^2$ .

### ***(b) Porosity characterization***

For hierarchical structure analysis, investigations of porosity and surface area is also important, which can be conducted using argon (Ar) sorption and mercury intrusion porosimetry. Ar adsorption allows for the evaluation of micropores (pore width  $< 2$  nm), mesopores (pore width: 2–50 nm), and even macropores (pore width  $> 50$  nm). In addition to Ar sorption, mercury porosimetry is more relevant for larger nanopores and macropores up to 400  $\mu\text{m}$ . Hence, the combination of these two techniques allows rather comprehensive information on the pore size distribution.<sup>90</sup>

### **3.3.2 Chemical characterization**

Furthermore, changes in the chemistry and composition of the wood materials before and after functionalization are investigated using Fourier transform infrared (FTIR) spectroscopy, X-ray diffraction (XRD), X-ray photoelectron spectroscopy (XPS), inductively-coupled plasma optical emission spectroscopy (ICP-OES), energy-dispersive X-ray spectroscopy (EDX), wavelength-dispersive spectroscopy (WDS), and zeta potential.

FTIR can evaluate the functional groups' changes on wood before and after modification. XRD is a principal method for determining the crystal structure of MOFs and confirming the existence of the MOFs synthesized on wood.

The EDX and WDS attached on SEM instruments as well as the EDX system attached on TEM instruments are all used for confirming the distribution of the MOF nanoparticles within the wood in different scales, but compared with EDX, WDS is better at distinguishing the elements of silver and palladium, which have similar X-ray energy.

ICP-OES can measure the metal content within the MOF/wood composites and assuming the MOF loading according to the stoichiometric composition of MOF.

The net surface charge (zeta potential) of wood before and after modification can be assessed by streaming potential measurements using SurPASS Electrokinetic Analyzer (Anton Paar).

### **3.3.3 Characterization of functionality**

In this study, we fabricated different MOF/wood composites toward three main applications,  $\text{CO}_2$  adsorption, mechanical energy harvesting, and hydrogen generation from ammonia borane.

CO<sub>2</sub> adsorption ability is performed by recording adsorption isotherms of CO<sub>2</sub> at 0°C using a Micromeritics 3Flex Analyzer. Prior to the measurements, it needs an evacuation of the samples at 90°C for 48 h. It was used in chapter 4.2.

A sophisticated testing system was built by my colleague Jianguo Sun to analyze the electric output of the samples (**Figure 13a**).<sup>91</sup> It was used in chapter 4.3. To apply constant pressure to the samples, a linear motor (PL01-28x500/420) was used. A loading cell (50N) was also put on the stiff frame of the motor to detect the pressure applied on the samples at the same time. Finally, the electrical output of wood materials were measured by Keithley 6514 equipped with Matlab software.

The performance of wood-based catalysts for continuous hydrogen generation from ammonia borane was evaluated using the setup shown in **Figure 13b** and used in chapter 4.4. It was originally designed by my former colleague, Dr. Selin Vitas in her research on the flow-through behavior of wood-based membranes as colloidal particle filters. Then it was slightly adjusted by Dr. Christian Goldhahn, which allowed for measurements of the biocatalytic membrane reactor's efficiency.<sup>92,93</sup> The setup used in this study was further optimized with additional adaptations. The ammonia borane solution can flow through wood pellet(s) under a constant speed controlled using a calibrated peristaltic pump to generate hydrogen by the catalytic hydrolysis. The displacement of water in the gas burette was used to track the volume of the evolved gas.

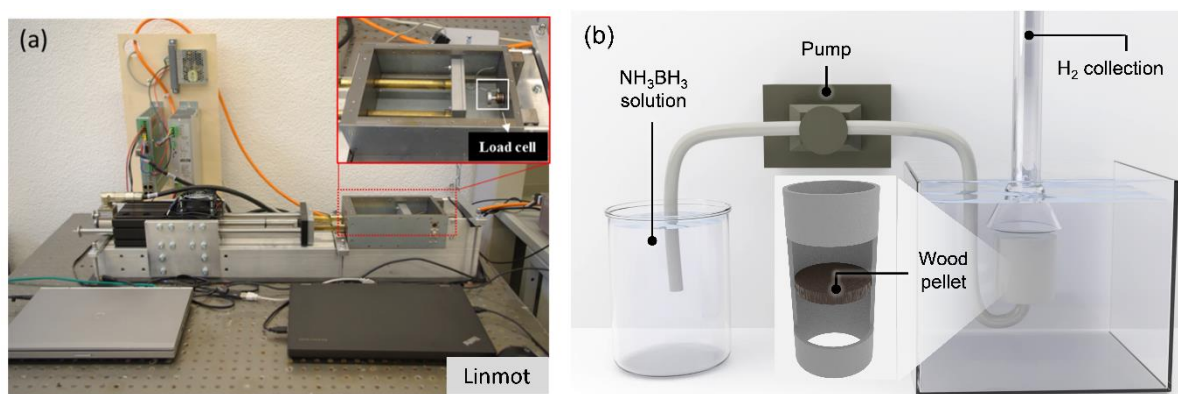


**Figure 13.** (a) Setup of electrical output measurement (Linear Motor PL01-28x500/420). A loading cell (Model 31E mid) with ranges up to 50N is shown in the inset.<sup>91</sup> (b) Schematic figure of the hydrogen generation setup for wood based catalysts in continuous flow.



## 4 Publications

This cumulative thesis mainly consists of four first (co-first)-authored journal articles, which are presented in the subchapters 4.1 to 4.4. The authors' contributions are described below.

**Subchapter 4.1: Kunkun Tu,<sup>#</sup> Yong Ding,<sup>#</sup> Tobias Keplinger.** Metal–Organic Framework/Cellulose Composites: From Fabrication to Applications. *Carbohydrate Polymers*, 2022 (Under review)

### Contributions:

<sup>#</sup>I and Y.D. contributed equally to this work. I took part in conceiving the study with T.K. I conducted literature survey and co-wrote the first version of the manuscript with Y.D.

**Subchapter 4.2: Kunkun Tu,<sup>#</sup> Begoña Puértolas,<sup>#</sup> Maria Adobes-Vidal, Yaru Wang, Jianguo Sun, Jacqueline Traber, Ingo Burgert, Javier Pérez-Ramírez, Tobias Keplinger.** Green Synthesis of Hierarchical Metal–Organic Framework/Wood Functional Composites with Superior Mechanical Properties. *Advanced Science*, 2020 (7): 1902897.

### Contributions:

<sup>#</sup>I and B.P. contributed equally to this work. I took part in conceiving the study. I designed the analysis, prepared all samples, executed experiments including SEM, FTIR, XRD, and mechanical tests, analyzed data, and co-wrote the first version of the manuscript with B.P.

**Subchapter 4.3: Jianguo Sun, <sup>#</sup> Kunkun Tu, <sup>#</sup> Simon Büchele, Sophie Marie Koch, Yong Ding, Shivaprakash Narve Ramakrishna, Sandro Stucki, Hengyu Guo, Changsheng Wu, Tobias Keplinger, Javier Pérez-Ramírez, Ingo Burgert, Guido Panzarasa.** Functionalized Wood with Tunable Tribo-Polarity for Efficient Triboelectric Nanogenerators. *Matter*, 2021 (4):3049

### Contribution:

<sup>#</sup>J.S. and I contributed equally to this work. I took part in conceiving the study, prepared all ZIF-8 modified samples, performed experiments including SEM, AFM, XRD, FTIR, optical profilometry, porosity analysis, and measurement of color changes, took part in the measurement of electrical output, mechanical tests, and video filming, analyzed data, and co-wrote the first version of the manuscript with J.S.

**Subchapter 4.4: Kunkun Tu,<sup>#</sup> Simon Büchele,<sup>#</sup> Sharon Mitchell, Laura Stricker, Chun Liu, Christian Goldhahn, Julien Allaz, Yong Ding, Roman Günther, Zhidong Zhang, Jianguo Sun, Guido Panzarasa, Samuel C. Zeeman, Ingo Burgert, Javier Pérez-Ramírez, Tobias Keplinger.** Structured Wood-based Catalytic Microreactors for Continuous Hydrogen Generation from Ammonia Borane. *ACS Applied Materials & Interfaces*. 2022 (14): 8417

**Contributions:**

<sup>#</sup>I and S.B. contributed equally to this work. I took part in conceiving the study. I designed the analysis, prepared all samples, and performed experiments including SEM, XRD, porosity analysis, all hydrogen generation tests, and video filming. I also analyzed data and co-wrote the first version of the manuscript with S.B.

## **4.1 Metal–organic framework-cellulose composites: from fabrication to applications**

Kunkun Tu<sup>1,2#</sup>, Yong Ding<sup>1,2#</sup>, Tobias Keplinger<sup>1,2\*</sup>

<sup>1</sup>Wood Materials Science, Institute for Building Materials, ETH Zürich, 8093 Zürich, Switzerland.

<sup>2</sup>WoodTec Group, Cellulose & Wood Materials, EMPA, 8600 Dübendorf, Switzerland

#These authors contributed equally to this work: Kunkun Tu and Yong Ding.

\*E-mail: tkeplinger@ethz.ch

## Abstract

Metal-organic frameworks (MOFs) are one of the most attractive functional porous materials. However, their processability and handling remains a substantial issue, because MOFs are generally in powder form due to their crystalline nature. Integrating MOFs into cellulose substrates to produce engineered materials offers an ideal solution to broaden the utilization of such functional materials. MOF/cellulose composites provide remarkable mechanical properties, tunable porosity, and accessible active sites of MOFs. In this review, we summarize current state-of-the-art fabrication routes for MOF/cellulose composites, with a specific focus on the unique potential of utilizing three-dimensional bio-based cellulosic scaffolds. We highlight their utilization as adsorbents in the gas and liquid phase, for antibacterial and protein immobilization, chemical sensors, and electrical energy storage. In addition, we include current limitations and provide potential future research directions in the field of MOF/cellulose composites for advanced functional materials.

## 1. Introduction

Metal-organic frameworks (MOFs) are a class of crystallized porous functional materials formed by the coordination of metal ions/clusters and organic bridging ligands.<sup>1,2</sup> Their structures can be specifically designed according to the targeted functionality by choosing the organic linkers' geometries and coordination modes of the inorganic metal ions.<sup>3</sup> Their key structural features are an ultrahigh porosity (up to 90% free volume) and a large internal surface area, extending even beyond a Langmuir surface area of  $10,000 \text{ m}^2 \text{ g}^{-1}$ . These properties are crucial for applications, such as gas storage and separation,<sup>4,5</sup> water treatment,<sup>6</sup> sensing,<sup>7</sup> catalysis,<sup>8,9</sup> water harvesting,<sup>10</sup> energy production,<sup>11,12</sup> and drug delivery.<sup>13,14</sup> However, there occurs one major drawback when it comes to the application of MOFs. Their powder morphology impedes processability and handling.<sup>15</sup> Hence, the integration and combination of MOFs with polymeric substrates is the method of choice to obtain durable advanced functional MOF materials.<sup>16</sup>

MOFs have been deposited or grown on/within various polymeric substrates resulting in MOF/polymer composites with hierarchical porosity and complex multi-layered networks.<sup>16</sup> These have been successfully utilized for water purification, nano-filtration, gas adsorption and separation applications.<sup>17</sup> Nevertheless, the primarily use of non-renewable synthetic polymers derived from petrochemical products drove the need for more sustainable substrate systems. Alternatives comprise, biopolymers such as cellulose, cyclodextrin, chitin, chitosan, alginate, agarose, and heparin.<sup>18,19</sup> In particular, cellulose is highly attractive as it represents one of the most abundant biopolymers on Earth, which is easily obtainable from plant cell walls.<sup>20</sup> Owing to its biodegradability, biocompatibility, renewability, and low-cost, cellulose provides a sustainable material platform for preparing functional materials, which has been widely demonstrated in materials for water treatment,<sup>21</sup> sensing,<sup>22</sup> antibacterial



applications,<sup>23</sup> and energy storage.<sup>24,25</sup> Cellulose possesses excellent mechanical properties and tunable chemistry, attracting a great deal of attention for the fabrication of MOF composites.<sup>26-29</sup>

The cellulosic materials for MOF/cellulose composites can be of different morphology and chemistry and the cellulosic materials morphology (fibrillated cellulose or cellulose scaffolds), determines the corresponding fabrication routes for the structured MOF/cellulose composites. The first approach comprises the preparation of MOF/cellulose fibers by depositing MOFs on fibrillated cellulose *via ex-situ* methods or *in-situ* methods. Then the MOF/cellulose fibers can be further processed into membranes or more advanced material structures with tunable pore size using various bottom-up fabrication strategies such as spinning, casting, filtration, freeze-drying, and three-dimensional (3D) printing. A novel approach is the direct utilization of 3D cellulose/bio-based scaffolds. Here, one profits from the hierarchical structure of biomaterials and avoids extra processing steps.

In this review, we summarize current routes for preparing MOF/cellulose composites, including raw materials preparation, cellulose pretreatments, MOF/cellulose composites preparation (**Figure 1**). We put a specific focus on recent works and potential of utilizing 3D cellulose/bio-based scaffolds as starting materials for MOF/cellulose composites. In addition, we highlight applications of MOF/cellulose composites in gas adsorption and separation, wastewater treatment, antibacterial applications, protein immobilization, chemical sensors, and electrical energy storage. At the end, we address current major limitations, challenges, and future prospects.

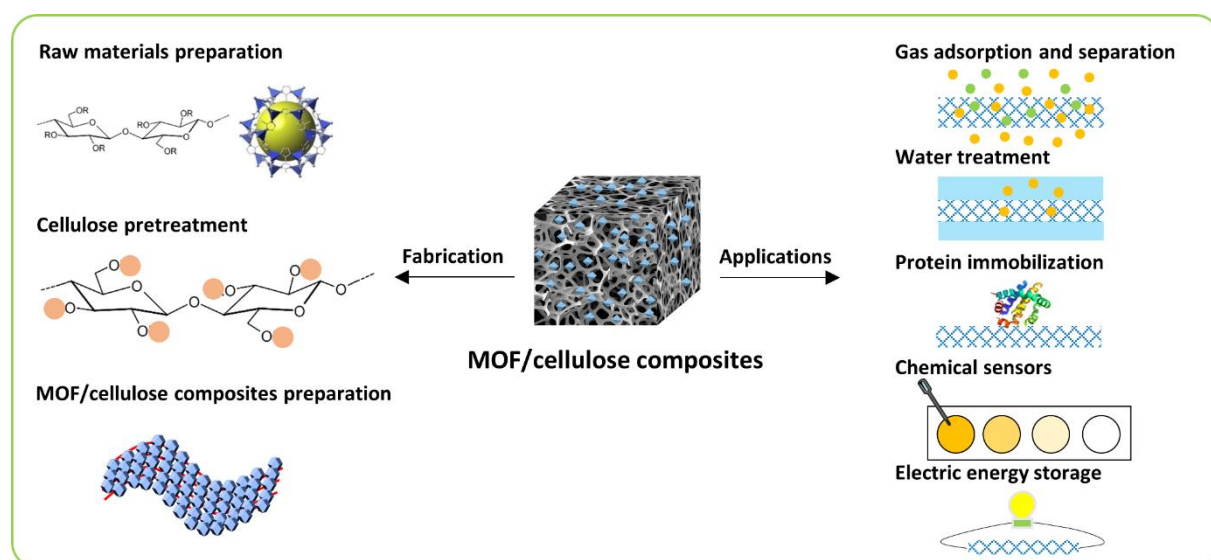


**Figure 1** Schematic of main fabrication steps and applications of cellulose/MOF composites.

## 2. Preparation of MOF/cellulose composites

The preparation of MOF/cellulose composites is a multistep process that necessitates careful tuning of each individual step. It comprises three main steps: raw materials preparation, cellulose pretreatment, and MOF/cellulose composites preparation.

### 2.1 Raw materials preparation

The chosen raw components determine the composites materials preparation process. For example, the starting cellulose materials morphology, fibrillated cellulose or cellulose scaffolds, decides whether a processing step is needed or not. For the MOF synthesis, one has the option to either directly utilize pre-synthesized MOF crystals (*ex-situ*) or to use MOF precursors for *in-situ* synthesis methods. In the following we provide a brief overview on the various sorts of raw materials that can be employed.

### 2.1.1 Cellulose

The starting cellulose material for MOF/cellulose composites can be either fibrillated cellulose or 3D cellulose scaffolds (**Figure 2**) and is derived from sources such as trees, plants, and bacteria. Fibrillated cellulosic materials include fibers, microfibrils/nanofibrils, nanocrystals, and bacterial cellulose and they primarily differ in their morphology (e.g. dimensions and shape) (**Figure 2a**).<sup>30,31</sup>

3D cellulose scaffolds can be natural 3D cellulose scaffolds obtained from natural materials characterized by a sophisticated hierarchical cellular structure, pronounced anisotropy, and good mechanical performance, such as wood, bamboo, and corncob;<sup>32-34</sup> or artificial 3D cellulose scaffolds based on fibrillated cellulose materials which are fabricated using bottom-up methods, such as aerogels, cellulose paper, and fabrics (**Figure 2b**).<sup>31,35-38</sup>

Natural cellulose scaffolds and artificial scaffolds mainly differ in terms of their specific surface area, pore structure, and mechanical properties. The avoidance of time-consuming and energy-intensive processing steps, as well as the superior mechanical performance makes natural 3D cellulose scaffolds an ideal support material for MOFs.

### 2.1.2 MOFs

Despite the substantial number of developed MOFs, applicable MOFs for MOF/ cellulose composites are restricted to several main MOF families, considering the required water, thermal, chemical, and mechanical stability, facile synthesis condition, and cost.

Possible MOFs are MOF-199 (named Cu-BTC or HKUST-1),<sup>39-41</sup> the ZIF (Zeolitic imidazolate framework) family (e.g., ZIF-8, ZIF-9, ZIF-12, ZIF-62, ZIF-67, and ZIF-90),<sup>37,42-45</sup> the MIL (Materials Institute Lavoisier) series (e.g., MIL-53(Al), MIL-101(Fe), MIL-88B(Fe)),<sup>46-48</sup> and Zr-based MOFs (e.g., UiO-66 and UiO-67).<sup>49</sup>

Pre-prepared MOF crystals can be directly used for MOF/cellulose composites via *ex-situ* synthesis methods. Especially, in the case of elevated MOF synthesis temperatures, using MOF crystals as starting materials is preferable to avoid degradation of the lignocellulosic materials (such as wood) constituents. The constituents of lignocellulosic materials have different decomposition temperatures: cellulose around 315°C, hemicellulose 220°C, and lignin 160°C.<sup>50</sup>

On the other hand, using MOF precursors (metal ions and organic ligands) as starting materials allows to prepare MOF/cellulose composites *via in-situ* synthesis methods (section 2.3.2), which can avoid MOF particle aggregation and ensures a uniform distribution of MOFs on cellulose substrates.



**Figure 2** Examples of a) fibrillated cellulose including cellulose fibers,<sup>51</sup> cellulose nanofibers (CNFs),<sup>52</sup> cellulose nanocrystals,<sup>51</sup> and bacterial cellulose<sup>53</sup> and b) cellulose scaffolds including natural materials (wood and bamboo) and processed materials (aerogel<sup>54</sup> and cellulose paper) used for preparing MOF/cellulose composites. c) Chemical structure of cellulose and its derivatives

## 2.2 Cellulose Pretreatment

A high interfacial affinity between the MOFs and cellulose is crucial to avoid the leakage of MOFs from the cellulose substrates. Hence, for a better interaction between MOFs and cellulose, and to promote compatibility between MOFs and cellulose substrates, chemical pretreatments of cellulose are required before the MOF/cellulose composites preparation. For that purpose, the cellulose is chemically modified, including adjusting cellulose charging, increasing the accessibility of the hydroxyl group, and adding functional groups, as summarized in **Table 1**.

### 2.2.1 Adjustment of cellulose charging

Changing the natural cellulose charging from neutral/slightly negative into a negative charge enables pronounced interactions between the obtained negatively charged cellulose and the positively charged metal cations of MOFs and form the nucleation site for MOFs. The MOF loading typically rises with the number of crystallization nucleation sites.<sup>55-57</sup> Common methods for adjusting the charging comprise 2,2,6,6-Tetramethylpiperidine-1-oxyl (TEMPO)-mediated oxidation, carboxymethylation, and the incorporation of anionic sulfonate moieties.

TEMPO oxidation converts the C6 hydroxymethyl group of cellulose into carboxylate groups and equips the cellulose surface with a high density of negative charges.<sup>23</sup> For example, Matsumoto et al. (2016) utilized TEMPO-oxidized CNFs (TOCNFs) to prepare cellulose/ZIF-90 film.<sup>37</sup>

Alternatively, carboxymethylation is also capable of adjusting the cellulose surface charge. The common sodium chloroacetate treatment in the presence of sodium hydroxide converts the –OH groups to negatively charged –CH<sub>2</sub>COO<sup>–</sup> group<sup>58</sup> A rather specific case arises when native wood is utilized, as in that case wood itself possesses inherent carboxyl groups, which can be converted to a carboxylate groups by a simple sodium hydroxide treatment.<sup>59,60</sup> The carboxylate groups on the cellulose surface assist the initial coordination of metal ions by ion-exchange and facilitate the growth of MOFs.<sup>61</sup> Meanwhile, the

metal center atoms in MOFs can establish coordination bonds with the carboxylate groups of the anionic cellulose and form electrostatic interactions between cellulose and MOF, which then stabilize MOF crystals on the cellulose surface.<sup>2,62</sup>

As third option, cellulose equipped with a large number of anionic sulfonate moieties, obtained using free-radical polymerization of sodium *p*-styrene sulfonate in the presence of acryloyl group-modified cellulose, can uptake and exchange metal cations, and supply adequate anchoring sites for MOF growth.<sup>63,64</sup>

Commercially available cellulose derivatives with negative charges, such as carboxymethyl cellulose,<sup>65</sup> cellulose acetate,<sup>66-68</sup> and TOCNFs,<sup>69</sup> are also widely used for the preparation of MOF/cellulose composites (**Figure 2c**).

### *2.2.2 Increasing the accessibility of the cellulose hydroxyl groups*

The accessibility of cellulose hydroxyl groups is limited due to strong inter- and intramolecular hydrogen bonds and van der Waals forces, which limits the fibers reactivity. It can be enhanced by simple dissolving cellulose in alkaline/urea solutions or by adding inorganic fillers.<sup>70,71</sup> For example, cotton linter pulps were pretreated by dissolving in NaOH/urea,<sup>43</sup> or NaOH/thiourea aqueous solutions<sup>72</sup> at low temperature before growth of MOF.<sup>43,73</sup> Yang et al. (2017) added precipitated calcium carbonate (PPC) to cellulose pulp as a filler to decrease the inter-fiber hydrogen bonds, making more hydroxyl groups available for the formation of ester functions with the MOF organic ligand.<sup>74</sup> Due to the increase of active sites, the corresponding MOF loading and surface area of the MOF/paper composites increased accordingly.

### *2.2.3 Adding functional groups*

By reacting with cellulose hydroxyl groups, functional groups such as amine groups, catechol groups, and epoxy groups can be introduced. These functional groups can form either hydrogen bonds with the metal moieties of MOFs or covalent bonds with the organic part of MOFs, facilitating the MOF nucleation, deposition and growth. For example, catechol moieties of a polydopamine (PDA) modified cellulose surface can bind strongly to a variety of metal ions, facilitating the formation of MOF crystals.<sup>42,75,76</sup> The modification of cellulose with 3-glycidyloxypropyltrimethoxysilane (GPTMS) incorporates epoxy groups that can form covalent bonds with the amino moieties of specific MOF organic linkers.<sup>38,77</sup>

**Table 1.** Summary of methods and chemicals used for cellulose pretreatment

Pretreatment Method	Cellulose Materials	Chemicals	Ref.	
Adjust charging	TEMPO-mediated oxidation	Cellulose (nano)fiber, spruce pulp, corncobs	TEMPO, NaClO and NaBr	34,78-82
	Hydrogen peroxide oxidation	Cotton	H <sub>2</sub> O <sub>2</sub> , sodium silicate and sodium hydroxide	83
	Carboxymethylation	Filter paper, cellulose fabrics, cotton fibers, lignocellulosic fibers, cellulose acetate	Sodium chloroacetate and NaOH	2,39,55,57,58
		Wood		NaOH
	Introducing anionic sulfonate	Cellulose acetate	Sodium p-styrene sulfonate and ammonium persulfate	63
Increasing the accessibility of the hydroxyl group	Dissolve cellulose	Cotton linter	NaOH/urea/H <sub>2</sub> O	43,87
	Adding filler	Cellulose pulp	Precipitated calcium carbonate (PCC)	74
Adding functional group	Catechol group	Cotton, bacterial cellulose	Dopamine hydrochloride, and tris(hydroxymethyl)aminomethane	42,88,89
	Epoxy group	Cotton fabric, and linen, CNFs	3-Glycidoxypropyltrimethoxysilane	38,77

### 2.3 Synthesis of MOF/cellulose composites

After the initial chemical modification of the cellulose material, MOF crystals can be deposited via *ex-situ* growth approaches (direct mixing and immersion coating) or *in-situ* growth approaches (one-pot synthesis, stepwise *in situ* growth, and layer-by-layer growth) which are explained in more detail in the following.

#### 2.3.1 Ex-situ growth methods

*Ex-situ* growth methods imply that MOF crystals are synthesized before the fabrication of MOF/cellulose composites and include two main approaches.

In the case of fibrillated cellulose direct mixing is the method of choice whereas for cellulose scaffolds immersion coating is typically utilized (**Figure 3**). The main advantage of *ex-situ* growth methods compared to *in-situ* growth methods is the controllable MOF loading. Except that, using pre-prepared MOF crystals avoids possible harsh MOF synthesis conditions during composites formation, for example synthesis temperatures being higher than the degradation temperature of the lignocellulosic

constituents. This approach, however, suffers from MOF particle aggregation and uneven distribution within composites.

#### a) Direct mixing

Direct mixing uses pre-prepared MOF powders- or suspensions as starting materials and mixes them with fibrillated cellulose (**Figure 3a**). It enables a high and controllable MOF loading. To avoid aggregation and precipitation of cellulose and MOFs, especially at high MOF loadings, ultrasonic and stirring processes are of significant importance during mixing. Cellulose pretreatments before the mixing stages help to increase the affinity and compatibility of cellulose and MOF powders. The obtained MOF/cellulose blends are easily processable into engineered constructs in subsequent steps. Based on this method, Zhu et al. (2016) prepared hybrid MOF/cellulose aerogels by mixing MOF nanoparticles, such as ZIF-8, UiO-66, and MIL-101(Fe) with aldehyde and hydrazide modified cellulose nanocrystals and assembled them into covalently cross-linked clusters (**Figure 3b and c**).<sup>90</sup> The prepared aerogels possessed a hierarchical porous structure with controllable MOF loadings of up to 50 wt%.

#### b) Immersion coating

Immersion coating involves submerging a cellulose scaffold in a solution containing MOF nanoparticles for a set time. (**Figure 3d**). For example, Cu-BTC MOF/cotton composites were prepared by soaking hydrogen peroxide oxidized cotton fabric in a Cu-BTC MOF solution (**Figure 3e and f**).<sup>83</sup> The Cu-BTC loading of the composites ranged from 5% to 10%, controlled by the concentration of the Cu-BTC MOF solution. Increasing the immersion coating cycles resulted in a higher MOF loading.

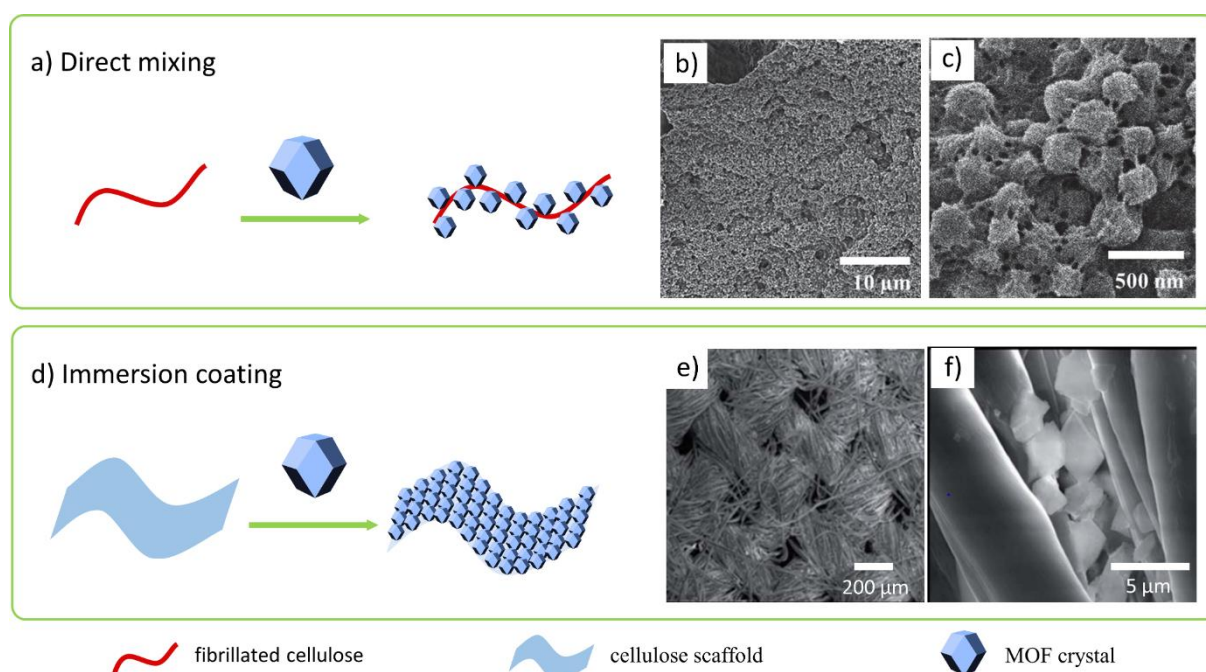


**Figure 3** *Ex situ* growth strategies for the preparation of cellulose/MOF composites. a) Direct mixing of MOF particles with fibrillated cellulose to obtain MOF/cellulose mixtures prior to processing. b-c) SEM images of UiO-66-containing cellulose aerogels prepared using direct mixing method (with 50 wt%

UiO-66).<sup>90</sup> d) Immersing cellulose scaffolds in MOF dispersion to prepare MOF/cellulose composites. e-f) SEM images of Cu-BTC@cotton prepared using immersion coating method.<sup>83</sup>

### 2.3.2 *In-situ* growth methods

*In-situ* growth methods are applicable for both fibrillated cellulose and cellulose scaffolds, and one distinguishes between one-pot synthesis, stepwise *In-situ* growth and layer-by-layer method (**Figure 4**).

#### a) One-pot synthesis.

One-pot synthesis is based on the reaction of MOF precursors and cellulose substrates in one reactor (**Figure 4a**).<sup>1</sup> Abdelhameed et al. (2017) compared Cu-BTC/fabric composites using one-pot synthesis and immersion coating method. The study revealed that the achieved MOF loadings by one-pot synthesis (102.1-110.0 mg g<sup>-1</sup>) are two times higher than with the immersion coating method.<sup>91</sup> Mirkovic et al. (2019) also used one-pot synthesis to grow MOF-5 crystals on PDA modified cotton. The MOF-5 crystals were firmly attached to the cotton fibers and exhibited a stable “necklace” morphology (**Figure 4b and c**).<sup>88</sup>

#### b) Stepwise *in-situ* growth.

Stepwise *in-situ* growth relates to the stepwise exposure of the cellulose substrate to the MOF precursors (metal ions and organic linkers), as shown in **Figure 4d**. The metal precursors are first added and form the initial coordination between metal ions and the anionic groups of the pretreated cellulose, followed by adding the organic linkers for the MOF nucleation and growth.

Pinto et al. (2012) utilized a stepwise *in-situ* growth protocol to grow MOF-199 on carboxymethylated cotton.<sup>58</sup> The initial addition of copper acetate caused an ion exchange reaction between metal ions and carboxylate groups of the anionic cellulosic substrates, resulting in a dense copper ions layer on the cellulose surface that acted as nucleation center and anchor point for the formation of MOF-199 crystals. As the ion exchange provides the nucleation site for the subsequent growth of the MOF structure, the stepwise *in-situ* growth avoids the aggregation of MOF particles. They also compared the obtained results with the one-pot synthesis method and found that stepwise *in-situ* growth exhibited a higher yield of MOF-199 on cellulose.

#### c) Layer-by-layer

For the layer-by-layer synthesis method, the cellulose substrate is immersed in a solution of the metal ions, followed by submersion in a solution of the organic ligand (or vice versa), with possible rinsing steps in between.<sup>92</sup> This method enables a homogeneous morphology and controllable coating thickness of MOFs via adjusting the number of growth cycles (**Figure 4g**). Laurila et al. (2015) reported the *in-situ* crystal growth of HKUST-1 on carboxymethylated electrospun CNFs.<sup>84</sup> The MOF loading increased from 11.8% after 8 synthesis cycles to 38.7% at 32 synthesis cycles (**Figure 4h and i**).



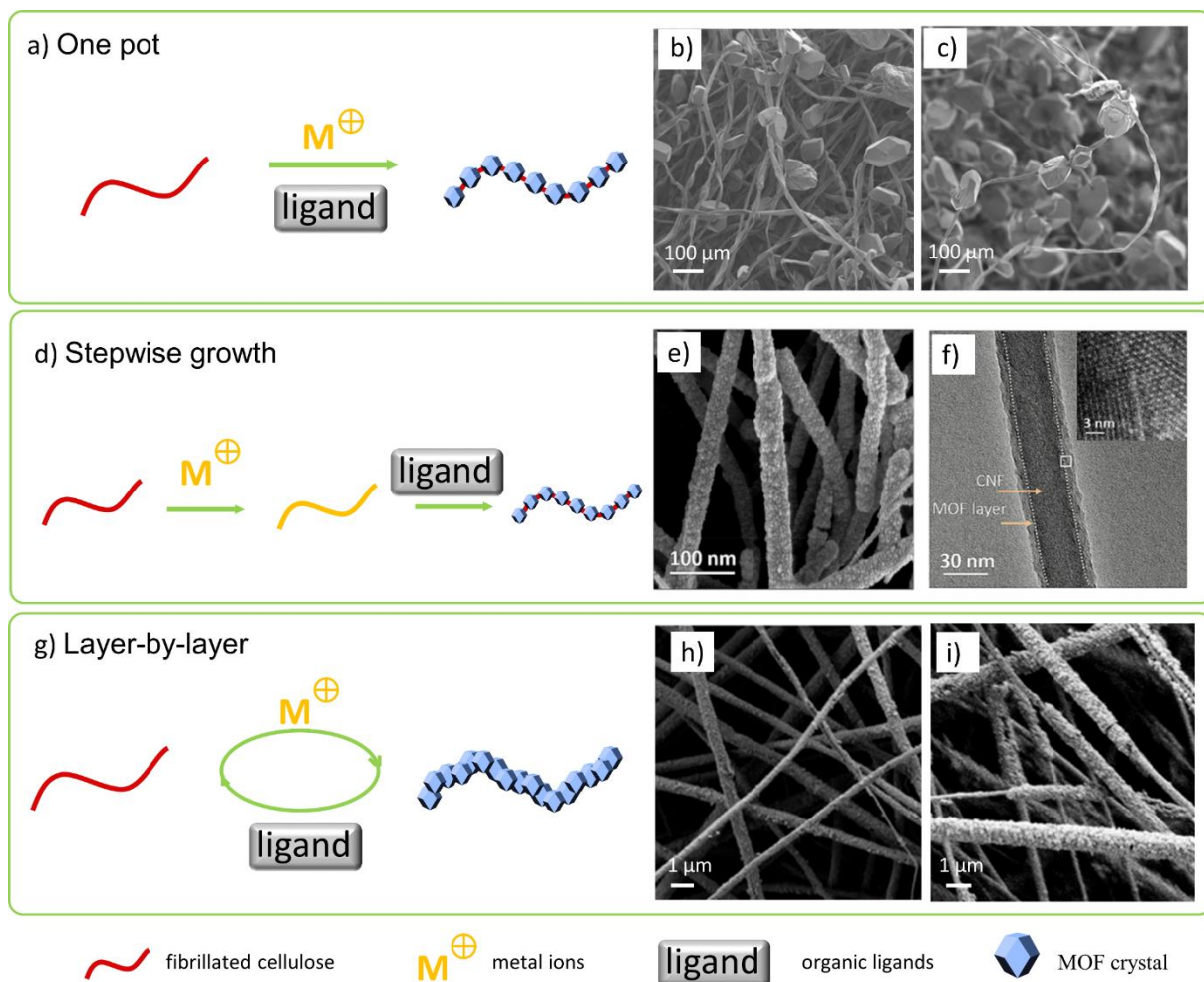


**Figure 4** *In-situ* growth strategies for the preparation of cellulose/MOF composites. a) Schematic of one-pot synthesis to prepare MOF/cellulose composites by mixing MOF precursors with fibrillated cellulose in one reactor prior to processing. b-c) SEM images of MOF-5 grown on cotton fibers using one-pot method.<sup>88</sup> d) Schematic of stepwise *in-situ* growth method to prepare MOF/cellulose composites by stepwise exposure of the cellulose substrate with the MOF precursors e) SEM image and f) TEM image of MOF/CNFs prepared using stepwise *in-situ* growth method.<sup>93</sup> g) Schematic of using layer-by-layer method to prepare MOF/cellulose composites and controlling the MOF coating thickness and loading by adjusting the number of growth cycles. h-i) SEM images of HKUST-1/CNFs prepared layer-by-layer method with 8 cycles (h) and 32 cycles (i) respectively.<sup>84</sup>

## 2.4 Processing of Cellulose/MOF Composites

For applications, MOF modified cellulose materials based on fibrillated cellulose need to be processed into 2D membranes or 3D porous structures using bottom-up approaches such as spinning, casting, filtration, freeze-drying, or 3D printing (Section 2.4.1). In contrast, the direct utilization of natural or artificial 3D cellulose scaffolds as support for MOFs avoids these additional processing steps (Section 2.4.2).

### 2.4.1 Bottom-up approaches



#### a) Spinning process

As a common technique to fabricate cellulose fibers, electrospinning has also been employed for the synthesis of MOF/cellulose composites (**Figure 5a**). First the MOF/cellulose suspension is transferred into a syringe for electrospinning, and then processed with a constant rate under a high voltage. The electrospun nanofibers are collected on a rotary drum or a grounded collector<sup>94</sup> and the fiber mats result after vaporization of the solvent.<sup>95,96</sup> The technique allows for a simple fabrication of fiber composites for a wide variety of MOF/cellulose combinations with a wide range of possible sizes and morphologies.<sup>97</sup> Moreover, the fiber diameters and the MOF loadings are tunable by varying the MOF/cellulose concentration and cellulose to MOF ratio in the initial spinning mixtures.<sup>1,96</sup>

#### b) Casting

Casting represents a straightforward way to build-up MOF/cellulose mixed matrix membranes (MMMs) (**Figure 5b**).<sup>98</sup> First, a MOF/cellulose suspension is poured onto a flat glass substrate or PTFE plate. After degassing, solvent evaporation, and drying, the MOF/cellulose membrane is peeled off from the flat substrate.<sup>99-101</sup> The cellulose fraction in the MMMs serves as the matrix and the MOFs function as filler. The composites prepared by casting show good permeability in gas separation, water purification and catalytic applications in continuous flow processes.<sup>99,101-103</sup>

#### c) Filtration

MOF/cellulose membranes fabrication by filtration has gained a lot of interest in recent years (**Figure 5c**). During filtration, the solvent of the MOF/cellulose suspension permeate the filtration membrane with the aid of a vacuum and after a drying process a MOF/cellulose membranes with symmetrical structures are obtained.<sup>104</sup> For example, Xu et al. (2018) developed hierarchical porous and conductive nanosheets composed of ZIF-67/cellulose/CNTs for flexible, foldable electronic energy storage devices based on filtration.<sup>105</sup> The suspension of cellulose, CNTs and ZIF-67 was first collected on a PVDF membrane filter and the membrane was received after drying. The thickness is adjustable by the amount of ZIF-67, cellulose, and CNTs in the initial mixture. In general, membranes obtained by filtration possess good flexibility, permeability, and hierarchical porosity.<sup>106</sup>

#### d) Freeze-drying

Freeze-drying is the most widely applied way to build up engineered porous MOF/cellulose composites (**Figure 5d**). After freezing the MOF/cellulose gel at a temperature below the freezing point of the liquid medium (usually water), the MOF/cellulose aerogel is made by sublimating the frozen small molecular solvent using liquid nitrogen freeze-drying techniques.<sup>107,108</sup> By altering the freezing speed and temperature, the pore morphology and pore distribution within the aerogel can be altered. The obtained cellulose/MOF aerogel form a 3D porous network structure, which is cross-linked by physical interactions such as van der Waals forces, hydrogen bonds, electronic associations, and chain entanglements.<sup>78</sup> The porous structure and mechanical properties of the composites depend on various key factors, such as MOF/cellulose suspension concentration, cellulose to MOF ratio, and the freezing

rate. In MOF/cellulose aerogel, MOFs particularly retain their crystallinity, porosity, and accessibility, making them suitable absorbents for water purification and other separation applications.<sup>90</sup>

#### e) 3D printing

3D Printing has gained popularity in MOF/cellulose composites processing, which includes multi-steps including MOF/cellulose ink preparing, objects structure design, and precise producing based on a computer-driven digital model in a layer by layer manner (**Figure 5e**).<sup>109</sup> It is a powerful tool for MOF/cellulose composites processing, because it offers valuable advantages, such as high reproducibility, fabrication of complex geometries, controlled pore structures, tailored directionality, low cost, time effectiveness, and up-scalability.<sup>110,111</sup> The MOF/cellulose ink used for 3D printing can be prepared using the methods mentioned in section 2.1 and 2.2, in which nanocellulose is a carrier phase for MOFs. For example, a 3D porous MOF/cellulose composite was obtained by 3D printing of a ZIF-8/TOCNF hybrid hydrogel ink, that was synthesized by in-situ growth of ZIF-8 on TOCNF using the one-pot synthesis method.<sup>112</sup> Shear thinning properties of the hybrid hydrogel inks enable the 3D printing of porous scaffolds with high shape fidelity.

#### 2.4.2 Cellulose scaffolds support

The use of 3D natural or artificial cellulose scaffolds as a support for MOF particles eliminates the need for additional processing after MOF growth on cellulose materials. The MOF/cellulose composites obtained using bottom-up methods possess relatively weak mechanical properties compared to the MOF/cellulose composite based on natural 3D cellulose scaffolds, such as wood, bamboo, and corncob.<sup>32-34,59,115-118</sup> Hence, using these robust natural cellulose scaffolds as MOFs supports is a promising method. Tu et al. (2020) prepared ZIF-8/wood composites by *in-situ* growth ZIF-8 on wood supports.<sup>59,119</sup> The obtained composites demonstrated excellent mechanical properties with 100 MPa of compressive strength and 74 MPa of ultimate tensile stress, respectively, which surpass those obtained with state-of-the-art polymer-based MOF composites. Wood aerogels prepared by delignification of wood materials are also used as substrate to support MOFs, showing an enhanced MOF loading and large surface area.<sup>82,120,121</sup> However, delignification weakens the mechanical properties of wood, whose mechanical properties is similar to the composites prepared by artificial 3D cellulose scaffolds.<sup>35,82,120,122,123</sup> Those artificial 3D cellulose scaffolds such as aerogel and paper are fabricated using bottom-up processing methods prior to the MOF deposition process, but it will lead to less homogeneous MOF particle distribution within the composites than those made by *in-situ* growth MOF on cellulose fibers and afterwards processed.<sup>87,124,125</sup>

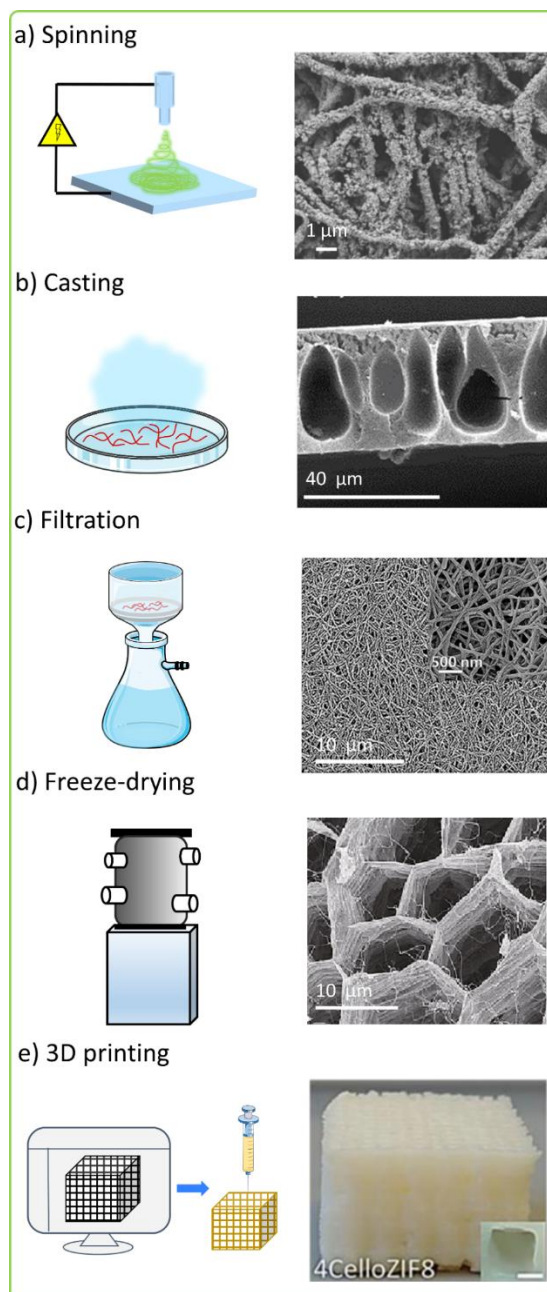


**Figure 5** Bottom-up processing strategies for preparation of cellulose/MOF composites using fibrillated cellulose as starting materials: a) spinning,<sup>84</sup> b) casting,<sup>113</sup> c) filtration,<sup>93</sup> d) freeze-drying,<sup>114</sup> and e) 3D printing.<sup>112</sup>

### 3. Applications of MOF/cellulose composites

Combining MOFs and cellulose substrates to produce engineered materials significantly expands the application potential. As described in chapter 2, one can build MOF/cellulose composites in the form of aerogels, thin membranes, etc. Because of their hierarchical porosity, high permeability, low MOF powder leakage, and easy reusability, 3D porous MOF/cellulose composites have been widely investigated as adsorbents in gas and liquid phases, which are discussed in detail in section 3.1.

In addition, due to shape flexibility, foldability, and high mechanical stability, MOF/cellulose composites can be used for other applications, such as biological applications, chemical sensing, and electric energy storage, which are discussed in detail in section 3.2.

### 3.1 Adsorbents

#### 3.1.1 Gas adsorption and separation

With rapid urbanization and industrialization, air pollution, such as accumulation of harmful gases or CO<sub>2</sub>, has a severe impact on environment, climate, and human health. Therefore, developing gas separation and adsorption systems with high absorption capability and selectivity has gained remarkable attention. In particular, membrane-based flow through devices possess great potential due to their advantages of high mass transfer efficiency, simple operation condition, low energy demand and ease of scaling (**Figure 6a**).<sup>79</sup>

The incorporated membranes, as the key element of the flow through devices, are commonly made from non-sustainable petroleum-based materials and cause secondary pollution after disposal. Therefore, developing environmental-friendly gas-separation membranes is a cutting-edge topic in both material and environmental sciences.

In this regard, cellulose-based materials have drawn considerable interest due to abundant sources, degradability, good mechanical strength and processability. In synergy with MOFs, composites with excellent absorption capacity and selectivity were developed by various techniques.<sup>59,74,79,80,86,96,126-139</sup> Overall, cellulose derivatives such as cellulose acetate, carboxymethyl cellulose and TEMPO oxidized cellulose are most common as matrixes because of their strong affinities for metal cations.<sup>37,130</sup> **Table 2** provides a detailed summary of MOF/cellulose composites gas separation systems and their related performance.

#### 3.1.2 Liquid phase sorption

Water contamination has drawn serious global concerns and is a threat to both human health and environment.<sup>140</sup> Multiple methods have been explored for the treatment of contaminated water, including oxidation-reduction,<sup>141,142</sup> precipitation,<sup>143</sup> photocatalytic degradation,<sup>144,145</sup> adsorption,<sup>146</sup> etc. Among these methods, adsorption approaches possess advantages, like low cost, high removal rate, easy accessibility, as well as low secondary pollution.<sup>147</sup> Up to now, applied adsorbents, include carbon nanomaterials,<sup>148</sup> zeolites,<sup>149</sup> clays,<sup>150,151</sup> etc. However, the practical application of these adsorbents has been limited by their weak mechanical strength, low processability and non-sustainability.

In this regard, cellulose/MOF composites show immense potential for water treatment applications. The cellulose substrates equip the composites with good mechanical performance and processability. For example, by introducing MOF into cellulose foams, respective composites could achieve the absorption of pollutants and release of clean water by a simple immersing/squeezing process (**Figure 6b**).<sup>152</sup> Moreover, MOF/cellulose composites can also be utilized in membrane-based water filtration systems

(Figure 6c).<sup>153</sup> In this application scenario, the meso-pores of MOFs enable the absorption of pollutants, while the micro-pores of the cellulose substrates allow the water flux.

Recently wood/MOF composites, were developed for liquid transport applications, profiting from the unique characteristics of natural wood, a bio-based, renewable and mechanically robust material, composed of well-connected hollow fibers.<sup>154,155</sup> MOF/wood composites can be directly utilized as freestanding filter in a continuous flow reactor. Guo et al. fabricated UiO-66/wood membranes by *in-situ* growth of mesoporous UiO-66 MOFs in the 3D low-tortuosity wood lumina.<sup>115</sup> This unique structural combination improves the mass transfer of organic pollutants and increases the contact probability of organic contaminants with UiO-66 MOFs as the water flows through the membrane, thereby improving the removal efficiency. An all-in-one filter device was designed by assembling three pieces of the UiO-66/wood membranes for large-scale organic pollutant removal. Importantly, the UiO-66/wood membrane can be readily regenerated by washing with methanol and can be scaled up by adjusting the number of membranes. (Figure 6d).

Irrespective of the cellulosic scaffold type, the adjustable pore sizes and porosities of MOFs allow the treatment of several types of adsorbates, including dyes, heavy metal ions and organic solvents. Table 3 provides a performance overview of MOF/cellulose composites in waste-water treatment.

Besides the removal of pollutants from liquids, the controlled release of molecules could also be of the interest and there are some studies focusing on the molecule releasing behavior of MOF/cellulose composites.<sup>156,157</sup> In a work by Sultan et al., ZIF-8/TOCNF composite has been synthesized as a drug molecules release system. It achieved methylene blue and curcumin release in a well-controlled manner at acidic pH (5.5) (Figure 6e).<sup>112</sup>

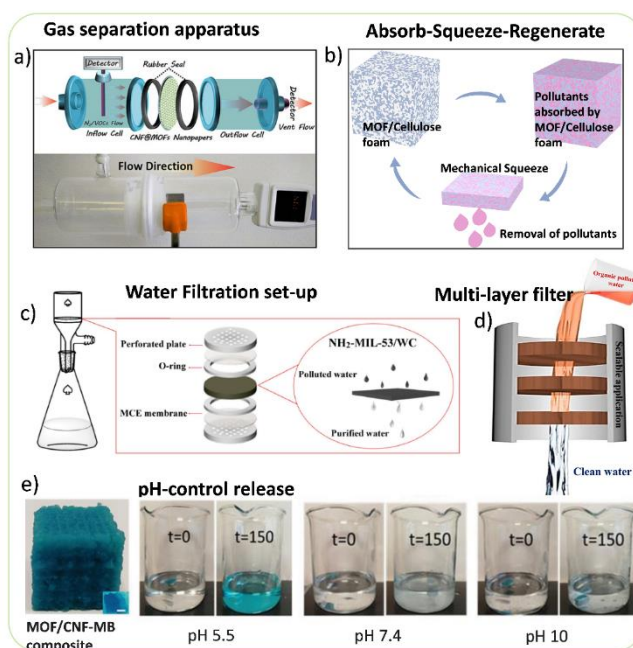


**Figure 6** Applications of MOF/cellulose composites as adsorbents a) Illustration and photograph of an apparatus for gas separation tests.<sup>79</sup> b) Illustration of the adsorption - squeeze - regeneration process of

MOF/cellulose foams for pollutant removal from water. c, d) Common waste water treatment set-up using MOF/cellulose composite membranes as filter.<sup>115,153</sup> e) Photos of MOF/cellulose-methylene blue composite showing the release of methylene blue at different pH values.<sup>112</sup>

### 3.2 Other potential applications

Beyond the above-mentioned major applications, there are also other applications gaining increasing attention, for example, anti-bacteria, protein immobilization, chemical sensors, electric energy storage, thermal insulation<sup>114</sup> and seawater desalination<sup>81,101,158</sup>. It demonstrates the high functionality and flexibility of cellulose/MOF composites to meet various needs and the following sections highlight these developments.

#### 3.2.1 Biological applications

Benefiting from their biocompatibility and biodegradability, cellulose/MOF composites possess great potential in biological fields. One of the most important application in this field is their utilization as antibacterial material.<sup>40,55,99,113,136,159-165</sup> Antibacterial effects in composites mainly origin from heavy metal nanoparticles, for example Zn, Ag, and Cu nanoparticles. The antibacterial effect of MOF/cellulose composites can be a result of the MOF metal ions and/or the loading with metal nanoparticles within the MOFs.

ZIF-8, HKUST-1, and Ag-based MOFs were commonly used to prepare antibacterial composites.<sup>33,40,55,136,161,163,165</sup> Previous works of HKUST-1/TEMPO oxidized cellulose composites reached an E. coil bacterial inactivation efficiency of up to 90%.<sup>165</sup> The disinfection mechanism is based on the Cu<sup>2+</sup> ions of HKUST-1. The interaction of Cu<sup>2+</sup> with the bacteria cell membrane via oxidation of membrane proteins and fatty acids or transmembrane potential alterations leads to rupture of membranes and cell lysis (**Figure 7 a-1**).<sup>33,55,136,163</sup>

Another intensively studied biological application is protein immobilization. The pore size and structure adjustability of MOFs makes them a perfect candidate for immobilization of various proteins, while the cellulose mostly serves as the supporting substrate for the MOFs, ensuring the processability and biocompatibility of the composites.

Fu et al reported ZIF-8/fabric composites with excellent protein adsorption ability.<sup>2</sup> The composite's porosity increased with a higher loading of ZIF-8, which favors the protein absorption. The cotton fabric provides favorable biocompatibility to maintain the bioactivity of enzyme proteins. Furthermore, results prove that carboxymethylation treatment of cellulose helps to enhance the protein immobilization ability of the cellulose/MOF composites by increasing the loading of MOF (**Figure 7 a-2**).

#### 3.2.2 Chemical sensors

Chemical sensors are of particular interest in environmental and biological systems for the sensitive and selective detection of heavy metal ions in liquids, organic toxicants and hazardous gas analyses, which

could monitor product quality, facilitate medical diagnostics and guarantee occupational safety.<sup>166-171</sup> Two kinds of chemical sensors based on photoluminescence and electrochemistry have been well developed. Both require first the adsorption of analyte molecules onto the surface of the sensors which then react to generate a signal for detection. Among the various sensing materials, MOFs, which contain electrochemically active metal sites for electrochemical sensors and photoluminescent components like inorganic clusters (especially lanthanides) or organic linkers (containing aromatic or conjugated  $\pi$  moieties) for photoluminescent sensors, are promising candidates to construct these devices.

Besides, the high porosity makes them good hosts for reversible adsorption and release of guest molecules, and the tunable pore dimensions and the functional sites, including open metal sites or Lewis basic/acidic sites with different affinities towards guest molecules, also could contribute to an enhanced sensing sensitivity. Nevertheless, the poor flexibility still hinders the application of single-phase MOFs as chemical sensors. Introducing MOFs particles to substrate materials is one of the solutions to this problem.

Cellulose serves as a very promising substrate material because of its abundant and renewable properties. Moreover, the flexibility of cellulose could adapt to different using scenarios by adjusting cellulose sources and processing techniques. Depending on the cellulose source and form of substrate, the MOF/cellulose sensors could be divided into three main categories: hydrogel of the sodium salt of carboxy methyl cellulose,<sup>168</sup> cotton textile,<sup>172</sup> and cellulose paper.<sup>171</sup> For example, Xu et al proposed an effective fluorescence sensor by dispersing methyl red@lanthanide metal-organic frameworks in water-phase sodium salt of carboxy methyl cellulose (CMC-Na). The hydrogels exhibit a color transition upon "smelling" histamine (HI) vapor. This transition and shift in the MR-based emission peak are closely related to the HI concentration. Using the HI concentration as the input signal and the two fluorescence emissions as output signals, an advanced analytical device based on a one-to-two logic gate was constructed (**Figure 7b**).<sup>168</sup>

### 3.2.3 Electric energy storage

Because of their high electrical conductivity and large surface areas, conductive metal-organic frameworks (c-MOFs) offer a lot of potential in electrochemical energy storage. However, because MOF crystals are brittle and insoluble, processing them into desirable nanomaterials with good flexibility and high areal capacitance is problematic. As a result, it is critical to develop effective solutions to these issues in order to increase the use of MOFs in electric energy storage. One intriguing answer to this problem is to embed MOFs into substrates. To date, only a few studies report the fabrication of MOF on conductive substrates (e.g., graphene oxide, MoS<sub>2</sub> nanosheet, and polycarbonate). Nonetheless, these approaches are largely dependent on the surface and structure of the substrates and not suitable for the formation of all types of MOFs.

Meanwhile, MOFs' poor processability makes the fabrication of MOF-based flexible materials more difficult. Because of its chemical and physical properties, cellulose is an excellent MOF for

electrochemical energy storage. Because of its hydrophilic properties and capacity to swell in water, cellulose can also serve as an intrinsic electrolyte reservoir. The electrolyte and diffuse ions in the electrolyte can be transferred to electrochemically active materials using the hierarchical porous structure generated by crosslinking cellulose fibers. Fabrication of hybrid materials based on MOFs and cellulose could combine the advantages of both materials and allow the construction of novel functional materials, given their diverse functions and flexibility.<sup>44,89,173,174 175 105,172 167,176</sup>

Zhou et al.<sup>173</sup> reported the fabrication of c-MOF nanolayers on CNFs. The obtained hybrid nanofibers of CNF@c-MOF can be easily constructed into freestanding nanopapers with high electrical conductivity of up to  $100 \text{ S cm}^{-1}$ , hierarchical micromesoporosity, and outstanding mechanical properties. Given these advantages, the nanopapers were tested as electrodes in a flexible and foldable supercapacitor. The electrodes' high conductivity and hierarchical porous structure allow for fast charge transfer and efficient electrolyte transport. Furthermore, after 10000 continuous charge–discharge cycles, the assembled supercapacitor demonstrates high cycle stability with capacitance retentions of >99% (Figure 7c). These promising results show that the potential of developing flexible energy storage devices based on sustainable cellulose and MOFs.

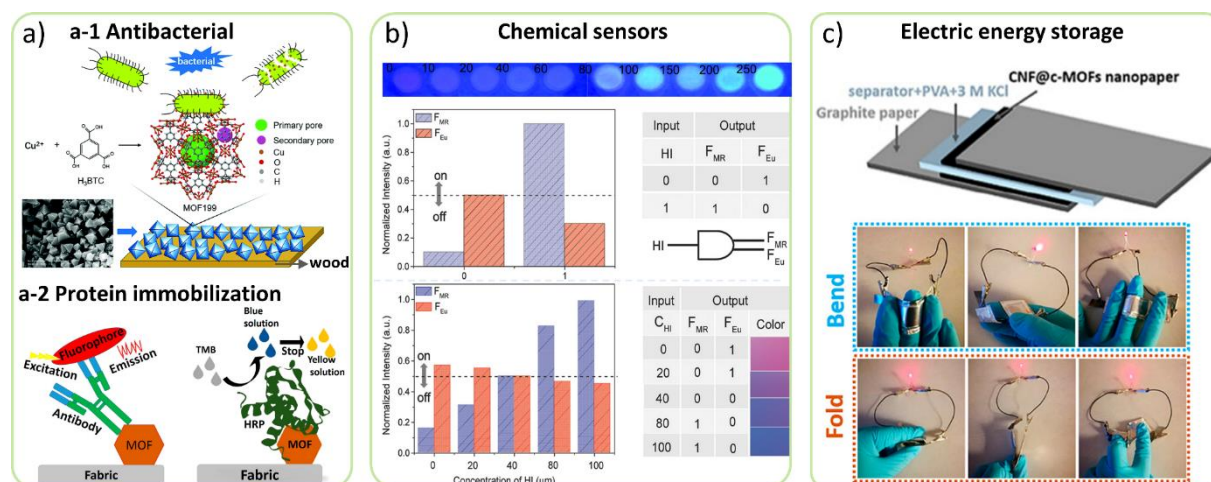


**Figure 7** a) Applications of MOF/Cellulose composite as antibacterial material and for protein immobilization. a-1) Schematics of the fabrication of MOF wood composite materials and their antibacterial mechanism.<sup>33</sup> a-2) Illustration of antibody or enzyme immobilized by MOF on fabric substrate. b) MOF/cellulose hydrogel exhibited a color transition upon sensing histamine (HI) vapor and the truth table of the logic analytical device for HI monitoring.<sup>168</sup> c) Photograph of the CNF@c-MOFs double layer supercapacitor device and the LED powered by devices in series under different deformations.<sup>93</sup>



#### 4. Conclusion and outlook

In summary, this review highlights the remarkable advances in the development of both fabrication and application of MOF/cellulose composites. However, there are still limitations and challenges that should be addressed in the future.

First, MOF/cellulose composites still face challenges in achieving sufficient mechanical properties at high porosity as well as high MOF loadings. The bottom-up processing methods used in preparing MOF/cellulose composites lead to sufficient porosity and controllable MOF loading, but limited mechanical properties, which could be an obstacle for sorbents to achieve high mass transfer under big pressure. Using mechanically robust 3D cellulose scaffolds support can partly solve this problem, still challenged by realizing high MOF loadings due to the surface area limitation of the cellulose scaffolds. Second, it is complex to maintain high MOFs loading within cellulose scaffolds along with sufficient interaction between MOFs and cellulose, to avoid significant leaching of MOFs during usage.

Enhancing the interaction between MOFs and cellulose is critical for long-term stability of the composite. Except for the methods mentioned in this review (surface modification of cellulose), the functionalization of MOFs can also be explored. Meanwhile, it may be possible to have post-modifications using cross-linkers after preparation of MOF/cellulose composites to further enhance the interaction of MOFs with cellulose substrates. Figuring out the attachment forces by simulations and molecular modeling can indicate the inner structure of a composite and provide important design guidelines for high-performance composite synthesis in the future.

Third, each of the two main components of the composites must be further developed to improve the performance and fundamental theory of MOF/cellulose composites. From the perspective of MOFs, the MOFs used are restricted to a few well-known types which limits the application scope of the MOF/cellulose composites. More efforts should be put on developing controllable, simple, cheap, low toxic, and large-scalable MOF synthesis methods as well as improving the water, thermal, chemical stability of the MOF crystals. Various promising novel synthetic routes, i.e. electrochemical, mechanochemical, microwave, spray drying, and flow chemistry synthesis can be employed for MOF/cellulose composites preparation.<sup>177</sup> In addition, biodegradation studies of the composites are still very limited and should be extended to achieve a closed-loop lifecycle of the MOF/cellulose composites. From the perspective of cellulose, we need to develop versatile processing methods to allow large-scale fabrication, and at the same time, maintain high porosity and robust mechanical properties.

In this regard Tu et al. reported a novel microreactor by MOF/wood composites which addressed the mentioned challenges.<sup>178</sup> This native wood microreactor for continuous hydrogen generation were successfully prepared using MOF-functionalized natural wood supports to stabilize metallic palladium and silver (**Figure 8**). The inherent microchannels and mechanical strength of native wood was well-preserved and served as a perfect substrate of the flow-through microreactor. The interfacial interaction between MOF and wood were improved by the amine-containing linker, which further ensured the performance and long-term stability of the MOF/wood microreactor.

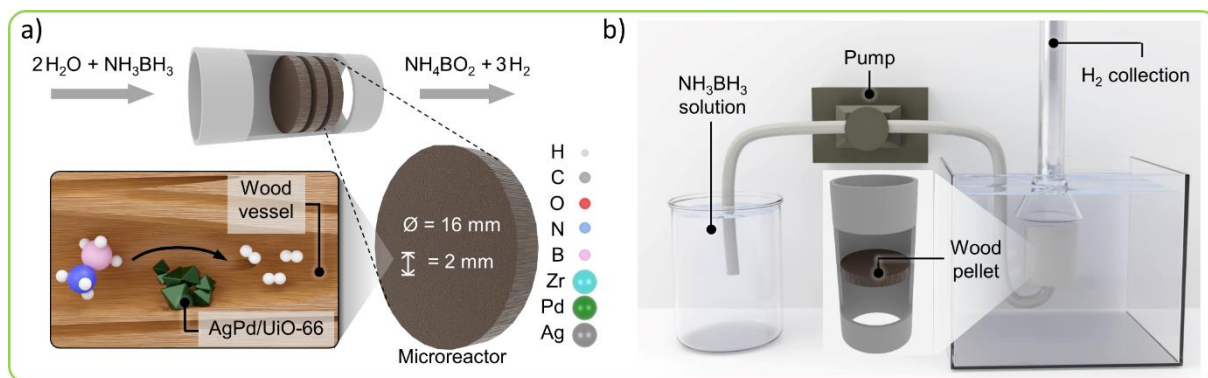


**Figure 8** a) The use of wood-based microreactors for the hydrogen generation from ammonia borane in flow and b) the hydrogen generation setup.<sup>178</sup>

Last but not least, new technologies and methods should be explored to characterize MOF/cellulose composites, Techniques like X-ray tomography might be useful as one can visualize macro pore arrangements as well as MOF crystals distribution within the cellulose substrates by 3D reconstructions with the aid of advanced image software. Detailed investigations with high resolution are possible with the help of synchrotron radiation facilities. In combination with simulation, the liquid and gas transport pathways within the composites can be predicted prior to applying it to real applications.

Overall, the development of MOF/cellulose composites is still in its infancy, but it shows huge potential and provides a springboard for further development.

**Table 2** Gas separation performance of MOF/cellulose composites

Composing materials				Permeability	Selectivity	Test conditions	Ref.
Cellulose	MOFs		Other materials				
	Types	loading					
Cellulose acetate	NH <sub>2</sub> -MIL-53(Al)	10-20 wt%	/	CO <sub>2</sub> 34.8 N <sub>2</sub> 1.2 CH <sub>4</sub> 1.1	CO <sub>2</sub> /N <sub>2</sub> 15.8 CO <sub>2</sub> /CH <sub>4</sub> 18.4	25 °C, 3 bar	129
Cellulose acetate	NH <sub>2</sub> -MIL-53(Al)	15 wt%	/	CO <sub>2</sub> 5.15 N <sub>2</sub> 0.18 CH <sub>4</sub> 0.19	CO <sub>2</sub> /N <sub>2</sub> 12.1 CO <sub>2</sub> /CH <sub>4</sub> 14.7	25 °C, 3 bar	96
Cellulose acetate	MOF-5	6%-12%	/	H <sub>2</sub> 6.08 CO <sub>2</sub> 3.19	H <sub>2</sub> /CO <sub>2</sub> 1.91	25°C, 6 bars	179
TOCNFs	ZIF-90	44.2 wt%	/	CH <sub>4</sub> 28.3 CO <sub>2</sub> 290	CO <sub>2</sub> /CH <sub>4</sub> 123	25°C, 2 bar	126
TOCNFs	UiO-66-NH <sub>2</sub>	24.4 wt%	/	CO <sub>2</sub> 139	CO <sub>2</sub> /N <sub>2</sub> 46	25°C, 2 bar	128
Carboxymethyl cellulose	ZIF-L nanosheets	30 wt%	/	H <sub>2</sub> 11.8 CO <sub>2</sub> 1.1 N <sub>2</sub> 0.55 CH <sub>4</sub> 0.062	H <sub>2</sub> /CO <sub>2</sub> 9.62 H <sub>2</sub> / N <sub>2</sub> 17.69 CO <sub>2</sub> /CH <sub>4</sub> 7.25 N <sub>2</sub> /CH <sub>4</sub> 9.62	25 °C, 1 bar	135
Pulp from Norwegian spruce	ZIF-L nanosheets	21-50 wt%	/	no	CO <sub>2</sub> /N <sub>2</sub> 10.88	25°C	80
Ethyl cellulose	ZIF-8	5-20 wt%	GO	CO <sub>2</sub> 203.3	CO <sub>2</sub> /N <sub>2</sub> 33.4,	25°C, 2 bar	132

**Table 3** Liquid-phase absorption performance of MOF/cellulose composites

Cellulose	Composing materials		Other materials	Adsorbate	Application and solution	Test conditions	Maximum adsorption capacity/ mg g <sup>-1</sup>	Ref.
	MOFs	loading						
	Types							
Cellulose aerogel (cellulose nanocrystals + carboxymethylcellulose)	UiO-66/MIL-100 (Fe)/ZIF-8	50 wt%	/	Cr(VI) (10 mg L <sup>-1</sup> potassium dichromate)/ benzotriazole (200 mg L <sup>-1</sup> )/ Rhodamine B (RhB) (0.355 mg L <sup>-1</sup> )	Dye capture, Remove ions and Organic pollutant absorb	25 °C, 24h	39.06 mg g <sup>-1</sup>	180
Nanocellulose	UiO-66	50 wt%	/	Methyl orange (MO)/ methylene blue (MB)	Dye capture	/	71.7 mg g <sup>-1</sup>	49
Cellulose nanofiber	ZIF-8/ZIF-67/HKUST-1	11 wt %–81 wt %	/	Rh B (10 mg L <sup>-1</sup> aqueous solution)	Dye capture	/	81 mg g <sup>-1</sup>	78
TEMPO oxidized corncobs	HKUST-1/ZIF-8	0.09 wt%	/	MO (50 mg L <sup>-1</sup> )	Dye capture	25 °C, pH=5	1.05 mg g <sup>-1</sup>	165
Filter paper	ZIF-8/ZIF-67	13 wt% (ZIF-8), 9 wt% (ZIF-67)	/	Organic dye ( An aqueous solution of the Organic dye (MO <sup>-</sup> , MB <sup>+</sup> , indigo carmine, rhodamine 6G, 5 mg L <sup>-1</sup> )	Dye capture	/	~99%	61
Cellulose fibers	UiO-66-NH <sub>2</sub>	~5.8 wt %	/	Cr(VI)/ MO (2.5-25 mg L <sup>-1</sup> aqueous solution)	Dye capture and Remove ions	/	78.2% for Cr(VI) and 84.5% for MO removal	181
Cellulose fibers/ cellulose foams	ZIF-8	15.8-55.2 wt%	/	RhB (667 mg L <sup>-1</sup> )/ Cr (VI) (4667 mg L <sup>-1</sup> )/ DMF (1000 mg L <sup>-1</sup> )	Dye capture, Remove ions and Organic pollutant absorb	/	24.6 mg g <sup>-1</sup> for rhodamine B, 35.6 mg g <sup>-1</sup> for Cr (VI) and 45200 mg g <sup>-1</sup> for DMF	152
Cotton	ZIF-67	40.7 wt%	/	MO 125 mg L <sup>-1</sup>	Dye capture	pH 4 to 10	617.4 mg g <sup>-1</sup>	87
Cellulose microfibril	HKUST-1	/	Fe <sub>3</sub> O <sub>4</sub>	MB (10 mg L <sup>-1</sup> )	Dye capture	/	98%	182
Regenerated cellulose	UiO-66	/	/	MB (0.0355 mg L <sup>-1</sup> )/ PEG (0.5 mg L <sup>-1</sup> )	Dye capture and Organic pollutant absorb	/	3.5 mg g <sup>-1</sup>	183
Carboxymethylcellulose	Cu-MOF	/	ibuprofen	/	Molecular release	pH 1.2-7.4	70% of release at 480 min	157

Cellulose	Composing materials		Other materials	Adsorbate	Application and solution	Test conditions	Maximum adsorption capacity/ mg g <sup>-1</sup>	Ref.
	MOFs	loading						
	Types							
Carboxymethyl cellulose	ZIF-8	17 wt%	Dexamethasone Hydroxyapatite	/	Molecular release	pH-7.4, 37 °C	75% release at day 28	156
Cotton	Cu <sub>3</sub> (NH <sub>2</sub> BTC) <sub>2</sub>	/	/	/	Molecular release	37 °C	90% Cu <sup>2+</sup> release at 24h	163
TOCNFs	ZIF-8	30.8%-70.1%	Curcumin	MB	Molecular release	pH 5.5-10	~40 mg g <sup>-1</sup> curcumin release at 30h	112
Cotton fabric	Zinc-glutamate-MOF (ZnGlu)	13.96 wt%	Nitric oxide and 5-fluorouracil	/	Molecular release	pH-7.4, 37 °C	~1% NO release at 30h, ~1% 5FU release at 75h	184
Carboxymethyl cellulose	MOF-5 (Zn-BDC)	/	/	Pb(II) (10–1000 mg L <sup>-1</sup> )	Remove ions	pH 2-6	322.58 mg g <sup>-1</sup>	185
Bacterial cellulose	ZIF-8	70 wt%	Polydopamine	I <sub>2</sub> /KI (aqueous solution 1–10.4 × 10 <sup>3</sup> mg L <sup>-1</sup> )	Remove ions	pH 7, 24h	1310 mg g <sup>-1</sup>	42
Cellulose aerogel	ZIF-8	30 wt%	/	Cr(IV) (1-100 mg L <sup>-1</sup> )	Remove ions	120 min	41.8 mg g <sup>-1</sup>	186
Bacteria cellulose	ZIF-8	5 wt%	/	Pb <sup>2+</sup> / Cd <sup>2+</sup> (100 mg L <sup>-1</sup> )	Remove ions	pH 5.5, 25°C, 50h	390 mg g <sup>-1</sup> for Pb <sup>2+</sup> 220 mg g <sup>-1</sup> for Cd <sup>2+</sup>	175
Cellulose acetate	ZIF-67	/	2-Methylimidazole	Cu(II) (78.9 mg L <sup>-1</sup> ), Cr(VI) (88.3 mg L <sup>-1</sup> ),	Remove ions	pH 6.5, 25 °C, 24h	18.9 mg g <sup>-1</sup> for Cu(II) and 14.5 mg g <sup>-1</sup> Cr(VI)	95
Bacterial cellulose	ZIF-67	46.1 wt%	Chitosan	Cu <sup>2+</sup> and Cr <sup>6+</sup> (1000 mg L <sup>-1</sup> )	Remove ions	pH 6.	200.6 mg g <sup>-1</sup> for Cu <sup>2+</sup> and 152.1 mg g <sup>-1</sup> for Cr <sup>6+</sup>	124
Cotton	UiO-66-NH <sub>2</sub>	/	/	Pb <sup>2+</sup> and Cu <sup>2+</sup> (100 mg L <sup>-1</sup> )	Remove ions	/	89.40 mg g <sup>-1</sup> for Pb <sup>2+</sup> 51.33 mg g <sup>-1</sup> for Cu <sup>2+</sup>	187
Balsa wood	NH <sub>2</sub> -MIL-53	52.2 wt%	/	Pb <sup>2+</sup> (10 mg L <sup>-1</sup> )	Remove ions	pH 6	223.405 mg g <sup>-1</sup> for Pb <sup>2+</sup>	153
Cellulose nanocrystal	Zn-BTC	/	Fe <sub>3</sub> O <sub>4</sub>	Pb <sup>2+</sup> (200 mg L <sup>-1</sup> )	Remove ions	pH 2-6, 25 °C	558.66 mg g <sup>-1</sup>	188
Cellulose acetate	Aluminum fumarate (AlFu)	2 to 10 wt%	/	Fluoride (10 to 800 mg L <sup>-1</sup> )	Organic pollutant absorb	pH 7	179 mg g <sup>-1</sup>	189

Cellulose	Composing materials		Other materials	Adsorbate	Application and solution	Test conditions	Maximum adsorption capacity/ mg g <sup>-1</sup>	Ref.
	MOFs							
	Types	loading						
Viscose fabrics	Cu-BTC	1.56 -11 wt%	/	Phenol (2500 mg L <sup>-1</sup> in noctane)	Organic pollutant absorb	30 °C	333 mg g <sup>-1</sup>	91
Basswood	UiO-66	2.22 wt%	/	Organic Pollutants (propranolol, 1-NA, BPA, and BPS in Water). Rh6G-polluted water (10 mg·L <sup>-1</sup> )	Organic pollutant absorb	/	690 mg·g <sup>-1</sup> for Rh6G (based on the content of MOFs)	115
Basswood	MIL-101(Fe)	0.79 wt%	/	Rh6G/ propranolol/ diclofenac	Organic pollutant absorb	/	~190 mg g <sup>-1</sup> for Rh6G, ~220.4 mg g <sup>-1</sup> for propranolol, and ~178.6 mg g <sup>-1</sup> for diclofenac	190
Carboxymethyl cellulose sodium cotton fabric	MOF-199 (HKUST-1)	70 wt%	/	Dipeptide EE/RR	Organic pollutant absorb	/	544.38 mg g <sup>-1</sup> for EE dipetide	191
Cotton	UiO-66-(COOH) <sub>2</sub>	15.3 wt%	/	Creatinine (200 mg·L <sup>-1</sup> in Tyrode buffer solution)	Organic pollutant absorb	37 °C	212.8 mg g <sup>-1</sup>	192
Cotton fiber	Cu-BTC	10 wt%	/	Organophosphate pesticide (100 ppm)	Organic pollutant absorb	/	182 mg g <sup>-1</sup>	83
Cotton fiber	MOF-199 (HKUST-1)	/	Polyoxometalate	pesticide ( methyl parathion 20 mg/L)	Organic pollutant absorb	25 °C	89 mg g <sup>-1</sup> based on MOF	193
Carboxymethylated cellulose fibers	MOF-199	32.53 wt%	Ag NPs	4-nitrophenol ( 4-NP) (0.1 mM) NaBH <sub>4</sub> (10 mM)	Degrade organic pollutant	/	~100% 4-NP reduction	85
Viscose fabrics	Ln (Eu <sup>3+</sup> , Tb <sup>3+</sup> ) MOF	/	/	RhB	Degrade dye	Xe-Hg lamp	~100% RhB reduction	36
Cellulose aerogel	ZIF-9/ZIF-12	30 wt%	Peroxy monosulfate	p-nitrophenol (PNP) (20 mg L <sup>-1</sup> solution)	Degrade organic pollutant	25 °C, pH 6	Remove PNP about 90% in one hour	43
Cellulose microfibril	HKUST-1	/	CuO/Fe <sub>3</sub> O <sub>4</sub>	4-NP (35.5 mg L <sup>-1</sup> 4-NP, 355 mg L <sup>-1</sup> NaBH <sub>4</sub> solution)	Degrade organic pollutant	/	~100% 4-NP reduction	194
Carboxymethyl cellulose	HKUST-1	/	Dopamine, 2-methylimi	4-NP (7.1 mg L <sup>-1</sup> 4-NP, 1420 mg L <sup>-1</sup> NaBH <sub>4</sub> aqueous solution)	Degrade organic pollutant	25 °C	~100% 4-NP reduction at 60s	195

Cellulose	Composing materials		Other materials	Adsorbate	Application and solution	Test conditions	Maximum adsorption capacity/ mg g <sup>-1</sup>	Ref.
	MOFs	loading						
	Types		dazole, and melamine					
CNFs	UiO-66-NH <sub>2</sub>	34.5 wt%	γ-Glycidoxypropyltrimethoxysilane	4-Nitrophenyl Phosphate (DMNP)	Degrade organic pollutant	25 °C	90% at 20 min	38
CNFs	NH <sub>2</sub> -MIL-88B(Fe) (NM88)	/	PAN nanofibers g-C <sub>3</sub> N <sub>4</sub>	Sulfamethoxazole (20 mg L <sup>-1</sup> )	Degrade organic pollutant	Xenon lamp	100% at 200 min	48

**Acknowledgements:** The project was conducted with the support of the SNF project “Hierarchical cellulose scaffolds for structural and functional gradient materials” (200021\_184821/1). K.T. thanks financial support from the China Scholarship Council (CSC) (201703270028).

**Declarations of interest:** The authors declare no competing interests.

## References

- 1 Li, S., and Huo, F. (2015). Metal-organic framework composites: from fundamentals to applications. *Nanoscale* 7, 7482-7501.
- 2 Fu, H., Ou, P.F., Zhu, J., Song, P.F., Yang, J.Q., and Wu, Y. (2019). Enhanced Protein Adsorption in Fibrous Substrates Treated with Zeolitic Imidazolate Framework-8 (ZIF-8) Nanoparticles. *ACS Appl Nano Mater* 2, 7626-7636.
- 3 Zhu, Q.L., and Xu, Q. (2014). Metal-organic framework composites. *Chem. Soc. Rev.* 43, 5468-5512.
- 4 Ren, J., Langmi, H.W., North, B.C., and Mathe, M. (2015). Review on processing of metal-organic framework (MOF) materials towards system integration for hydrogen storage. *International Journal of Energy Research* 39, 607-620.
- 5 Kang, Z., Fan, L., and Sun, D. (2017). Recent advances and challenges of metal-organic framework membranes for gas separation. *J. Mater. Chem. A* 5, 10073-10091.
- 6 Yao, Y., Wang, C., Na, J., Hossain, M.S.A., Yan, X., Zhang, H., Amin, M.A., Qi, J., Yamauchi, Y., and Li, J. (2021). Macroscopic MOF Architectures: Effective Strategies for Practical Application in Water Treatment. *Small*, e2104387.
- 7 Kreno, L.E., Leong, K., Farha, O.K., Allendorf, M., Van Duyne, R.P., and Hupp, J.T. (2012). Metal-organic framework materials as chemical sensors. *Chem Rev* 112, 1105-1125.
- 8 Nguyen, V.D., Nguyen, C.K., Tran, K.N., Tu, T.N., Nguyen, T.T., Dang, H.V., Truong, T., and Phan, N.T.S. (2018). Zeolite imidazolate frameworks in catalysis: Synthesis of benzimidazoles via cascade redox condensation using Co-ZIF-67 as an efficient heterogeneous catalyst. *Applied Catalysis A: General* 555, 20-26.
- 9 Chen, Y.-Z., Zhang, R., Jiao, L., and Jiang, H.-L. (2018). Metal-organic framework-derived porous materials for catalysis. *Coord. Chem. Rev.* 362, 1-23.
- 10 Kim, H., Yang, S., Rao, S.R., Narayanan, S., Kapustin, E.A., Furukawa, H., Umans, A.S., Yaghi, O.M., and Wang, E.N.J.S. (2017). Water harvesting from air with metal-organic frameworks powered by natural sunlight. *356*, 430-434.
- 11 Khandelwal, G., Maria Joseph Raj, N.P., and Kim, S.-J. (2020). ZIF-62: a mixed linker metal-organic framework for triboelectric nanogenerators. *J. Mater. Chem. A* 8, 17817-17825.
- 12 Gomes Silva, C., Luz, I., Llabres i Xamena, F.X., Corma, A., and Garcia, H. (2010). Water stable Zr-benzenedicarboxylate metal-organic frameworks as photocatalysts for hydrogen generation. *Chemistry* 16, 11133-11138.
- 13 Falcaro, P., Ricco, R., Doherty, C.M., Liang, K., Hill, A.J., and Styles, M.J. (2014). MOF positioning technology and device fabrication. *Chem. Soc. Rev.* 43, 5513-5560.
- 14 Wu, M.X., and Yang, Y.W. (2017). Metal-organic framework (MOF)-based drug/cargo delivery and cancer therapy. *Adv. Mater.* 29, 1606134.
- 15 Ashour, R.M., Abdel-Magied, A.F., Wu, Q., Olsson, R.T., and Forsberg, K. (2020). Green Synthesis of Metal-Organic Framework Bacterial Cellulose Nanocomposites for Separation Applications. *Polymers-Basel* 12, 1104.
- 16 Peterson, G.W., Lee, D.T., Barton, H.F., Epps, T.H., and Parsons, G.N. (2021). Fibre-based composites from the integration of metal-organic frameworks and polymers. *Nat. Rev. Mater.* 6, 605-621.
- 17 Zhang, Y., Feng, X., Yuan, S., Zhou, J., and Wang, B. (2016). Challenges and recent advances in MOF-polymer composite membranes for gas separation. *Inorg. Chem. Front.* 3, 896-909.
- 18 El Hankari, S., Bousmina, M., and El Kadib, A. (2019). Biopolymer@ Metal-Organic Framework Hybrid Materials: A Critical Survey. *Prog. Mater. Sci.*, 100579.



- 19 Musarurwa, H., and Tavengwa, N.T. (2022). Application of polysaccharide-based metal  
organic framework membranes in separation science. *Carbohydr. Polym.* 275, 118743.
- 20 Liu, Y., Ahmed, S., Sameen, D.E., Wang, Y., Lu, R., Dai, J., Li, S., and Qin, W. (2021). A  
review of cellulose and its derivatives in biopolymer-based for food packaging application.  
*Trends in Food Science & Technology*.
- 21 Chen, X., Zhu, X., He, S., Hu, L., and Ren, Z.J. (2020). Advanced Nanowood Materials for  
the Water–Energy Nexus. *Adv. Mater.*, 2001240.
- 22 Chen, C.J., and Hu, L.B. Nanoscale Ion Regulation in Wood-Based Structures and Their  
Device Applications. *Adv. Mater.*, 2002890.
- 23 Tavakolian, M., Jafari, S.M., and van de Ven, T.G.M. (2020). A Review on Surface-  
Functionalized Cellulosic Nanostructures as Biocompatible Antibacterial Materials. *Nano-  
Micro Letters* 12.
- 24 Wang, Z., Lee, Y.H., Kim, S.W., Seo, J.Y., Lee, S.Y., and Nyholm, L. (2021). Why cellulose-  
based electrochemical energy storage devices? *Adv. Mater.* 33, 2000892.
- 25 Zhao, D., Zhu, Y., Cheng, W., Chen, W., Wu, Y., and Yu, H. (2020). Cellulose-Based  
Flexible Functional Materials for Emerging Intelligent Electronics. *Adv. Mater.*, e2000619.
- 26 Kim, M.L., Otal, E.H., and Hinestroza, J.P. (2019). Cellulose meets reticular chemistry:  
interactions between cellulosic substrates and metal–organic frameworks. *Cellulose* 26, 123-  
137.
- 27 Abdelhamid, H.N., and Mathew, A.P. (2022). Cellulose–metal organic frameworks  
(CelloMOFs) hybrid materials and their multifaceted Applications: A review. *Coord. Chem.  
Rev.* 451, 214263.
- 28 Zhang, X.-F., Wang, Z., Ding, M., Feng, Y., and Yao, J. (2021). Advances in cellulose-metal  
organic framework composites: preparation and applications. *J. Mater. Chem. A*.
- 29 Liu, X., Xiao, Y., Zhang, Z., You, Z., Li, J., Ma, D., and Li, B. (2021). Recent Progress in  
Metal-Organic Frameworks@Cellulose Hybrids and Their Applications. *Chin. J. Chem.* 39,  
3462-3480.
- 30 Seddiqi, H., Oliaei, E., Honarkar, H., Jin, J., Geonzon, L.C., Bacabac, R.G., and Klein-Nulend,  
J. (2021). Cellulose and its derivatives: towards biomedical applications. *Cellulose*.
- 31 Huang, C., Cai, B., Zhang, L., Zhang, C., and Pan, H. (2021). Preparation of iron-based metal-  
organic framework@ cellulose aerogel by in situ growth method and its application to dye  
adsorption. *J. Solid State Chem.* 297, 122030.
- 32 Wang, Z., He, Y., Zhu, L., Zhang, L., Liu, B., Zhang, Y.K., and Duan, T. (2021). Natural  
porous wood decorated with ZIF-8 for high efficient iodine capture. *Mater. Chem. Phys.* 258,  
123964.
- 33 Su, M., Zhang, R., Li, H., Jin, X., Li, J., Yue, X., and Qin, D. (2019). In situ deposition of  
MOF199 onto hierarchical structures of bamboo and wood and their antibacterial properties.  
*Rsc Adv* 9, 40277-40285.
- 34 Duan, C., Meng, X., Liu, C., Lu, W., Liu, J., Dai, L., Wang, W., Zhao, W., Xiong, C., and Ni,  
Y. (2019). Carbohydrates-rich corncobs supported metal-organic frameworks as versatile  
biosorbents for dye removal and microbial inactivation. *Carbohydr. Polym.* 222, 115042.
- 35 Xu, L., Xiong, Y., Dang, B., Ye, Z., Jin, C., Sun, Q., and Yu, X. (2019). In-situ anchoring of  
Fe<sub>3</sub>O<sub>4</sub>/ZIF-67 dodecahedrons in highly compressible wood aerogel with excellent microwave  
absorption properties. *Materials & Design* 182.
- 36 Emam, H.E., Abdelhamid, H.N., and Abdelhameed, R.M. (2018). Self-cleaned  
photoluminescent viscose fabric incorporated lanthanide-organic framework (Ln-MOF). *Dyes  
and Pigments* 159, 491-498.
- 37 Matsumoto, M., and Kitaoka, T. (2016). Ultraselective Gas Separation by Nanoporous Metal-  
Organic Frameworks Embedded in Gas-Barrier Nanocellulose Films. *Adv. Mater.* 28, 1765-  
1769.
- 38 Shen, C.K., Mao, Z.P., Xu, H., Zhang, L.P., Zhong, Y., Wang, B.J., Feng, X.L., Tao, C.A.,  
and Sui, X.F. (2019). Catalytic MOF-loaded cellulose sponge for rapid degradation of  
chemical warfare agents simulat. *Carbohydr. Polym.* 213, 184-191.
- 39 da Silva Pinto, M., Sierra-Avila, C.A., and Hinestroza, J.P. (2012). In situ synthesis of a Cu-  
BTC metal–organic framework (MOF 199) onto cellulosic fibrous substrates: cotton.  
*Cellulose* 19, 1771-1779.

- 40 Wang, C., Qian, X., and An, X. (2015). In situ green preparation and antibacterial activity of copper-based metal–organic frameworks/cellulose fibers (HKUST-1/CF) composite. *Cellulose* 22, 3789-3797.
- 41 Ren, Y., Hersch, S.J., He, X., Zhou, R., Dong, T.G., and Lu, Q. (2022). A lightweight, mechanically strong, and shapeable copper-benzenedicarboxylate/cellulose aerogel for dye degradation and antibacterial applications. *Sep. Purif. Technol.* 283, 120229.
- 42 Au-Duong, A.-N., and Lee, C.-K. (2017). Flexible Metal–Organic Framework–Bacterial Cellulose Nanocomposite for Iodine Capture. *Crystal Growth & Design* 18, 356-363.
- 43 Ren, W., Gao, J., Lei, C., Xie, Y., Cai, Y., Ni, Q., and Yao, J. (2018). Recyclable metal-organic framework/cellulose aerogels for activating peroxymonosulfate to degrade organic pollutants. *Chem. Eng. J.* 349, 766-774.
- 44 Wang, R., Cao, J., Cai, S., Yan, X., Li, J., Yourey, W.M., Tong, W., and Tang, H. (2018). MOF@Cellulose Derived Co–N–C Nanowire Network as an Advanced Reversible Oxygen Electrocatalyst for Rechargeable Zinc–Air Batteries. *ACS Applied Energy Materials* 1, 1060-1068.
- 45 Mubashir, M., Dumée, L.F., Fong, Y.Y., Jusoh, N., Lukose, J., Chai, W.S., and Show, P.L. (2021). Cellulose acetate-based membranes by interfacial engineering and integration of ZIF-62 glass nanoparticles for CO<sub>2</sub> separation. *J. Hazard. Mater.* 415, 125639.
- 46 Mubashir, M., Fong, Y.Y., Leng, C.T., Keong, L.K., and Jusoh, N. (2020). Study on the effect of process parameters on CO<sub>2</sub>/CH<sub>4</sub> binary gas separation performance over NH<sub>2</sub>-MIL-53(Al)/cellulose acetate hollow fiber mixed. *Polym. Test.* 81, 106223.
- 47 He, S., Chen, C., Chen, G., Chen, F., Dai, J., Song, J., Jiang, F., Jia, C., Xie, H., Yao, Y., et al. (2020). A High-Performance, Scalable Wood-based Filtration Device with a Reversed-Tree Design. *Chem. Mater.*
- 48 Qiu, J.L., Fan, P., Yue, C.L., Liu, F.Q., and Li, A.M. (2019). Multi-networked nanofibrous aerogel supported by heterojunction photocatalysts with excellent dispersion and stability for photocatalysis. *J. Mater. Chem. A* 7, 7053-7064.
- 49 Wang, Z., Song, L., Wang, Y., Zhang, X.-F., Hao, D., Feng, Y., and Yao, J. (2019). Lightweight UiO-66/cellulose aerogels constructed through self-crosslinking strategy for adsorption applications. *Chem. Eng. J.* 371, 138-144.
- 50 Yang, H., Yan, R., Chen, H., Lee, D.H., and Zheng, C. (2007). Characteristics of hemicellulose, cellulose and lignin pyrolysis. *Fuel* 86, 1781-1788.
- 51 Moon, R.J., Martini, A., Nairn, J., Simonsen, J., and Youngblood, J. (2011). Cellulose nanomaterials review: structure, properties and nanocomposites. *Chem. Soc. Rev.* 40, 3941.
- 52 Chen, W., Yu, H., Liu, Y., Chen, P., Zhang, M., and Hai, Y. (2011). Individualization of cellulose nanofibers from wood using high-intensity ultrasonication combined with chemical pretreatments. *Carbohydr. Polym.* 83, 1804-1811.
- 53 Torres, F.G., Commeaux, S., and Troncoso, O.P. (2012). Biocompatibility of bacterial cellulose based biomaterials. *Journal of Functional Biomaterials* 3, 864-878.
- 54 Song, J.W., Chen, C.J., Yang, Z., Kuang, Y.D., Li, T., Li, Y.J., Huang, H., Kierzewski, I., Liu, B.Y., He, S.M., et al. (2018). Highly Compressible, Anisotropic Aerogel with Aligned Cellulose Nanofibers. *Acs Nano* 12, 140-147.
- 55 Rodríguez, H.S., Hinestroza, J.P., Ochoa-Puentes, C., Sierra, C.A., and Soto, C.Y. (2014). Antibacterial activity against *Escherichia coli* of Cu-BTC (MOF-199) metal-organic framework immobilized onto cellulosic fibers. *J. Appl. Polym. Sci.* 131, n/a-n/a.
- 56 Qian, L., Lei, D., Duan, X., Zhang, S., Song, W., Hou, C., and Tang, R. (2018). Design and preparation of metal-organic framework papers with enhanced mechanical properties and good antibacterial capacity. *Carbohydr. Polym.* 192, 44-51.
- 57 Jhinjer, H.S., Singh, A., Bhattacharya, S., Jassal, M., and Agrawal, A.K. (2021). Metal-Organic Frameworks Functional Smart Textiles for Adsorptive removal of Hazardous Aromatic Pollutants from Ambient Air. *J. Hazard. Mater.*, 125056.
- 58 Pinto, M.D., Sierra-Avila, C.A., and Hinestroza, J.P. (2012). In situ synthesis of a Cu-BTC metal-organic framework (MOF 199) onto cellulosic fibrous substrates: cotton. *Cellulose* 19, 1771-1779.

- 59 Tu, K.K., Puertolas, B., Adobes-Vidal, M., Wang, Y.R., Sun, J.G., Traber, J., Burgert, I.,  
Perez-Ramirez, J., and Keplinger, T. (2020). Green Synthesis of Hierarchical Metal-Organic  
60 Framework/Wood Functional Composites with Superior Mechanical Properties. *Adv. Sci.*  
Lu, Y., Fan, D., Shen, Z., Zhang, H., Xu, H., and Yang, X. (2022). Design and Performance  
61 Boost of a MOF-Functionalized-Wood Solar Evaporator through Tuning the Hydrogen-  
Bonding Interactions. *Nano Energy*, 107016.
- 62 Park, J., and Oh, M. (2017). Construction of flexible metal-organic framework (MOF) papers  
through MOF growth on filter paper and their selective dye capture. *Nanoscale* 9, 12850-  
12854.
- 63 Duan, C., Meng, J., Wang, X., Meng, X., Sun, X., Xu, Y., Zhao, W., and Ni, Y. (2018).  
Synthesis of novel cellulose- based antibacterial composites of Ag nanoparticles@ metal-  
organic frameworks@ carboxymethylated fibers. *Carbohydr. Polym.* 193, 82-88.
- 64 Yang, Z.H., Asoh, T.A., and Uyama, H. (2020). A cellulose monolith supported metal/organic  
framework as a hierarchical porous material for a flow reaction. *Chem. Commun.* 56, 411-414.
- 65 Ko, J., Kim, S.K., Yoon, Y., Cho, K.H., Song, W., Kim, T.-H., Myung, S., Lee, S.S., Hwang,  
Y.K., Kim, S.-W., and An, K.-S. (2018). Eco-friendly cellulose based solid electrolyte with  
high performance and enhanced low humidity performance by hybridizing with aluminum  
66 fumarate MOF. *Mater Today Energy* 9, 11-18.
- 67 Javanbakht, V., and Rafiee, Z. (2022). Fibrous polyester sponge modified with carboxymethyl  
cellulose and Zeolitic imidazolate frameworks for methylene blue dye removal in batch and  
continuous adsorption processes. *J. Mol. Struct.* 1249, 131552.
- 68 Abdelhameed, R.M., Abdel-Gawad, H., and Emam, H.E. (2021). Macroporous Cu-MOF@  
cellulose acetate membrane serviceable in selective removal of dimethoate pesticide from  
wastewater. *Journal of Environmental Chemical Engineering* 9, 105121.
- 69 Emam, H.E., El-Shahat, M., and Abdelhameed, R.M. (2021). Observable removal of  
pharmaceutical residues by highly porous photoactive cellulose acetate@ MIL-MOF film. *J.*  
*Hazard. Mater.* 414, 125509.
- 70 Chen, K., Yu, J., Huang, J., Tang, Q., Li, H., and Zou, Z. (2021). Improved mechanical, water  
vapor barrier and UV-shielding properties of cellulose acetate films with flower-like metal-  
organic framework nanoparticles. *Int. J. Biol. Macromol.* 167, 1-9.
- 71 Lin, X., Guo, L., Shaghaleh, H., Hamoud, Y.A., Xu, X., and Liu, H. (2021). A TEMPO-  
oxidized cellulose nanofibers/MOFs hydrogel with temperature and pH responsiveness for  
fertilizers slow-release. *Int. J. Biol. Macromol.* 191, 483-491.
- 72 Luo, X., and Zhang, L. (2013). New solvents and functional materials prepared from cellulose  
solutions in alkali/urea aqueous system. *Food Research International* 52, 387-400.
- 73 Bui, H.M., Lenninger, M., Manian, A.P., Abu-Rous, M., Schimper, C.B., Schuster, K.C., and  
Bechtold, T. (2008). Treatment in swelling solutions modifying cellulose fiber reactivity—Part  
2: Accessibility and reactivity. In 1. (Wiley Online Library), pp. 50-64.
- 74 Zhang, S.F., Li, H., Hou, C., Liu, L.N., Wang, Y., Zhao, M.K., and Liang, C. (2020).  
Recyclable ZIF-9@CA-Fe<sub>3</sub>O<sub>4</sub>/RGO/cellulose composite membrane as efficient catalysts for  
activating peroxydisulfate to degrade methylene blue. *Cellulose* 27, 3287-3300.
- 75 Xiong, B., Zhao, P.P., Hu, K., Zhang, L.N., and Cheng, G.Z. (2014). Dissolution of cellulose  
in aqueous NaOH/urea solution: role of urea. *Cellulose* 21, 1183-1192.
- 76 Yang, Q., Zhang, M., Song, S., and Yang, B. (2017). Surface modification of PCC filled  
cellulose paper by MOF-5 (Zn<sub>3</sub>(BDC)<sub>2</sub>) metal-organic frameworks for use as soft gas  
adsorption composite materials. *Cellulose* 24, 3051-3060.
- 77 Cui, J., Xu, X.R., Yang, L.Y., Chen, C.T., Qian, J.S., Chen, X., and Sun, D.P. (2020). Soft  
foam-like UiO-66/Polydopamine/Bacterial cellulose composite for the removal of aspirin and  
tetracycline hydrochloride. *Chem. Eng. J.* 395, 10, 125174.
- Zhou, M., Li, J., Zhang, M., Wang, H., Lan, Y., Wu, Y.-n., Li, F., and Li, G. (2015). A  
polydopamine layer as the nucleation center of MOF deposition on “inert” polymer surfaces to  
fabricate hierarchically structured porous films. *Chem. Commun.* 51, 2706-2709.
- Abdelhameed, R.M., Kamel, O., Amr, A., Rocha, J., and Silva, A.M.S. (2017). Antimosquito  
Activity of a Titanium-Organic Framework Supported on Fabrics. *ACS Appl Mater Interfaces*  
9, 22112-22120.

- 78 Zhu, L., Zong, L., Wu, X., Li, M., Wang, H., You, J., and Li, C. (2018). Shapeable Fibrous Aerogels of Metal-Organic-Frameworks Templated with Nanocellulose for Rapid and Large-Capacity Adsorption. *ACS Nano* 12, 4462-4468.
- 79 Zhou, S., Strømme, M., and Xu, C. (2019). Highly transparent, flexible, and mechanically strong nanopapers of cellulose nanofibers@ metal-organic frameworks. *Chemistry–A European Journal* 25, 3515-3520.
- 80 Valencia, L., and Abdehamid, H.N. (2019). Nanocellulose leaf-like zeolitic imidazolate framework (ZIF-L) foams for selective capture of carbon dioxide. *Carbohydr. Polym.* 213, 338-345.
- 81 Zhao, X., Ma, X., and Peng, X.S. (2019). Carbon nanofiber stringed hierarchical porous carbon polyhedrons flexible thin films for solar vapor generation. *Appl Phys a-Mater* 125.
- 82 Wang, S.N., Wang, C., and Zhou, Q. (2021). Strong Foam-like Composites from Highly Mesoporous Wood and Metal-Organic Frameworks for Efficient CO<sub>2</sub> Capture. *ACS Appl. Mater. Interfaces* 13, 29949-29959.
- 83 Abdelhameed, R.M., Abdel-Gawad, H., Elshahat, M., and Emam, H.E. (2016). Cu-BTC@cotton composite: design and removal of ethion insecticide from water. *Rsc Adv* 6, 42324-42333.
- 84 Laurila, E., Thunberg, J., Argent, S.P., Champness, N.R., Zacharias, S., Westman, G., and Öhrström, L. (2015). Enhanced Synthesis of Metal-Organic Frameworks on the Surface of Electrospun Cellulose Nanofibers. *Adv. Eng. Mater.* 17, 1282-1286.
- 85 Duan, C., Liu, C.R., Meng, X., Lu, W.L., and Ni, Y.H. (2019). Fabrication of carboxymethylated cellulose fibers supporting Ag NPs@MOF-199s nanocatalysts for catalytic reduction of 4-nitrophenol. *Appl. Organomet. Chem.* 33.
- 86 Li, Z., Hori, N., and Takemura, A. (2020). Synthesis and characterization of Cu-BTC metal-organic frameworks onto lignocellulosic fibers by layer-by-layer method in aqueous solution. *Cellulose* 27, 1733-1744.
- 87 Song, W.Q., Zhu, M., Zhu, Y.F., Zhao, Y.Z., Yang, M.X., Miao, Z.C., Ren, H.P., Ma, Q., and Qian, L.W. (2020). Zeolitic imidazolate framework-67 functionalized cellulose hybrid aerogel: an environmentally friendly candidate for dye removal. *Cellulose* 27, 2161-2172.
- 88 Mirkovic, I., Lei, L., Ljubic, D., and Zhu, S.P. (2019). Crystal Growth of Metal-Organic Framework-5 around Cellulose-Based Fibers Having a Necklace Morphology. *ACS Omega* 4, 169-175.
- 89 Zhou, J., Yuan, Y., Tang, J., and Tang, W.H. (2019). Metal-organic frameworks governed well-aligned conducting polymer/bacterial cellulose membranes with high areal capacitance. *Energy Storage Mater* 23, 594-601.
- 90 Zhu, H., Yang, X., Cranston, E.D., and Zhu, S. (2016). Flexible and Porous Nanocellulose Aerogels with High Loadings of Metal-Organic-Framework Particles for Separations Applications. *Adv. Mater.* 28, 7652-7657.
- 91 Abdelhameed, R.M., Emam, H.E., Rocha, J., and Silva, A.M.S. (2017). Cu-BTC metal-organic framework natural fabric composites for fuel purification. *Fuel Process. Technol.* 159, 306-312.
- 92 Summerfield, A., Cebula, I., Schröder, M., and Beton, P.H. (2015). Nucleation and early stages of layer-by-layer growth of metal organic frameworks on surfaces. *The Journal of Physical Chemistry C* 119, 23544-23551.
- 93 Zhou, S., Kong, X., Zheng, B., Huo, F., Stromme, M., and Xu, C. (2019). Cellulose Nanofiber @ Conductive Metal-Organic Frameworks for High-Performance Flexible Supercapacitors. *ACS Nano* 13, 9578-9586.
- 94 Zhang, W., He, Z., Han, Y., Jiang, Q., Zhan, C., Zhang, K., Li, Z., and Zhang, R. (2020). Structural design and environmental applications of electrospun nanofibers. *Composites Part A: Applied Science and Manufacturing* 137, 106009.
- 95 Hou, X., Zhou, H., Zhang, J., Cai, Y., Huang, F., and Wei, Q. (2018). High Adsorption Pearl-Necklace-Like Composite Membrane Based on Metal-Organic Framework for Heavy Metal Ion Removal. *Particle & Particle Systems Characterization* 35.
- 96 Mubashir, M., Yeong, Y.F., Chew, T.L., and Lau, K.K. (2019). Comparison of Post-Treatment Methods on the Performance of Hollow Fiber Membranes Containing Metal Organic Framework in Gases Separation. *Industrial & Engineering Chemistry Research* 58, 7120-7130.

- 97 Miranda, C.S., Silva, A.F.G., Pereira-Lima, S.M., Costa, S.P., Homem, N.C., and Felgueiras, H.P. (2022). Tunable Spun Fiber Constructs in Biomedicine: Influence of Processing Parameters in the Fibers' Architecture. *Pharmaceutics* 14, 164.
- 98 Abdelhameed, R.M., El-Shahat, M., and Emam, H.E. (2020). Employable metal (Ag & Pd)@MIL-125-NH<sub>2</sub>@cellulose acetate film for visible-light driven photocatalysis for reduction of nitro-aromatics. *Carbohydr. Polym.* 247, 116695, 116695.
- 99 Yang, S.J., Zou, Q.F., Wang, T.H., and Zhang, L.P. (2019). Effects of GO and MOF@GO on the permeation and antifouling properties of cellulose acetate ultrafiltration membrane. *J. Membr. Sci.* 569, 48-59.
- 100 Lee, S.X., Lei, Y.N., Wang, D., Li, C.X., Cheng, J.J., Wang, J.P., Meng, W.Q., and Liu, M. (2019). The Study of Zeolitic Imidazolate Framework (ZIF-8) Doped Polyvinyl Alcohol/Starch/Methyl Cellulose Blend Film. *Polymers-Basel* 11.
- 101 Wang, X.J., Ba, X.L., Cui, N., Ma, Z., Wang, L.G., Wang, Z.P., and Gao, X.L. (2019). Preparation, characterisation, and desalination performance study of cellulose acetate membranes with MIL-53(Fe) additive. *J. Membr. Sci.* 590.
- 102 Hou, J., Luan, Y., Huang, X., Gao, H., Yang, M., and Lu, Y. (2017). Facile synthesis of Cu<sub>3</sub>(BTC)<sub>2</sub>/cellulose acetate mixed matrix membranes and their catalytic applications in continuous flow process. *New J. Chem.* 41, 9123-9129.
- 103 Yang, K., Dai, Y., Zheng, W., Ruan, X., Li, H., and He, G. (2018). ZIFs-modified GO plates for enhanced CO<sub>2</sub> separation performance of ethyl cellulose based mixed matrix membranes. *Sep. Purif. Technol.*
- 104 Zhu, W., Han, M., Kim, D., Zhang, Y., Kwon, G., You, J., Jia, C., and Kim, J. (2022). Facile preparation of nanocellulose/Zn-MOF-based catalytic filter for water purification by oxidation process. *Environ. Res.* 205, 112417.
- 105 Xu, C., Kong, X.Y., Zhou, S.Y., Zheng, B., Huo, F.W., and Stromme, M. (2018). Interweaving metal-organic framework-templated Co-Ni layered double hydroxide nanocages with nanocellulose and carbon nanotubes to make flexible and foldable electrodes for energy storage devices. *J. Mater. Chem. A* 6, 24050-24057.
- 106 Voisin, H., Bergström, L., Liu, P., and Mathew, A.P. (2017). Nanocellulose-based materials for water purification. *Nanomaterials* 7, 57.
- 107 Sharma, A., Thakur, M., Bhattacharya, M., Mandal, T., and Goswami, S. (2019). Commercial application of cellulose nano-composites – A review. *Biotechnology Reports* 21, e00316.
- 108 Long, L.-Y., Weng, Y.-X., and Wang, Y.-Z. (2018). Cellulose aerogels: Synthesis, applications, and prospects. *Polymers-Basel* 10, 623.
- 109 Hu, X., Yang, Z., Kang, S., Jiang, M., Zhou, Z., Gou, J., Hui, D., and He, J. (2020). Cellulose hydrogel skeleton by extrusion 3D printing of solution. *Nanotechnology Reviews* 9, 345-353.
- 110 Wang, Q., Sun, J., Yao, Q., Ji, C., Liu, J., and Zhu, Q. (2018). 3D printing with cellulose materials. *Cellulose* 25, 4275-4301.
- 111 Rossi, S., Puglisi, A., and Benaglia, M. (2018). Additive manufacturing technologies: 3D printing in organic synthesis. *ChemCatChem* 10, 1512-1525.
- 112 Sultan, S., Abdelhamid, H.N., Zou, X.D., and Mathew, A.P. (2019). CelloMOF: Nanocellulose Enabled 3D Printing of Metal-Organic Frameworks. *Adv. Funct. Mater.* 29.
- 113 Kim, T., Choi, M.K., Ahn, H.S., Rho, J., Jeong, H.M., and Kim, K. (2019). Fabrication and characterization of zeolitic imidazolate framework-embedded cellulose acetate membranes for osmotically driven membrane process. *Sci. Rep* 9.
- 114 Zhou, S.Y., Apostolopoulou-Kalkavoura, V., da Costa, M.V.T., Bergstrom, L., Stromme, M., and Xu, C. (2020). Elastic Aerogels of Cellulose Nanofibers@Metal-Organic Frameworks for Thermal Insulation and Fire Retardancy. *Nano-Micro Lett* 12.
- 115 Guo, R., Cai, X., Liu, H., Yang, Z., Meng, Y., Chen, F., Li, Y., and Wang, B. (2019). In Situ Growth of Metal-Organic Frameworks in Three-Dimensional Aligned Lumen Arrays of Wood for Rapid and Highly Efficient Organic Pollutant Removal. *Environ. Sci. Technol.* 53, 2705-2712.
- 116 Zhang, X.-F., Wang, Z., Song, L., and Yao, J. (2021). In situ growth of ZIF-8 within wood channels for water pollutants removal. *Sep. Purif. Technol.* 266, 118527.
- 117 Zhu, X., Li, M., Song, L., Zhang, X.-F., and Yao, J. (2021). Metal organic framework enabled wood evaporator for solar-driven water purification. *Sep. Purif. Technol.*, 119912.

- 118 Huang, G., Huang, C., Tao, Y., and Li, H. (2021). Localized heating driven selective growth of metal-organic frameworks (MOFs) in wood: A novel synthetic strategy for significantly enhancing MOF loadings in wood. *Appl. Surf. Sci.* 564.
- 119 Sun, J., Tu, K., Büchele, S., Koch, S.M., Ding, Y., Ramakrishna, S.N., Stucki, S., Guo, H., Wu, C., and Keplinger, T. (2021). Functionalized wood with tunable tribopolarity for efficient triboelectric nanogenerators. *Matter* 4, 3049-3066.
- 120 Wu, M.-B., Zhang, C., Xie, Y., Huang, S., Liu, C., Wu, J., and Xu, Z.-K. (2021). Janus Metal–Organic Frameworks/Wood Aerogel Composites for Boosting Catalytic Performance by Le Châtelier’s Principle. *ACS Appl. Mater. Interfaces*.
- 121 Chen, G., He, S., Shi, G., Ma, Y., Ruan, C., Jin, X., Chen, Q., Liu, X., Dai, H., Chen, X., and Huang, D. (2021). In-situ immobilization of ZIF-67 on wood aerogel for effective removal of tetracycline from water. *Chem. Eng. J.* 423.
- 122 Chen, Y., Zhang, L., Yang, Y., Pang, B., Xu, W., Duan, G., Jiang, S., and Zhang, K. (2021). Recent Progress on Nanocellulose Aerogels: Preparation, Modification, Composite Fabrication, Applications. *Adv. Mater.*, 2005569.
- 123 Wang, Q., Yao, Q., Liu, J., Sun, J., Zhu, Q., and Chen, H. (2019). Processing nanocellulose to bulk materials: A review. *Cellulose* 26, 7585-7617.
- 124 Li, D.W., Tian, X.J., Wang, Z.Q., Guan, Z., Li, X.Q., Qiao, H., Ke, H.Z., Luo, L., and Wei, Q.F. (2020). Multifunctional adsorbent based on metal-organic framework modified bacterial cellulose/chitosan composite aerogel for high efficient removal of heavy metal ion and organic pollutant. *Chem. Eng. J.* 383.
- 125 Thunberg, J., Zacharias, S.C., Hasani, M., Oyetunji, O., Noa, F.M.A., Westman, G., and Öhrström, L. (2021). Hybrid Metal-Organic Framework-Cellulose Materials Retaining High Porosity: ZIF-8@ Cellulose Nanofibrils. *Inorganics* 9, 84.
- 126 Matsumoto, M., and Kitaoka, T. (2016). Ultraselective Gas Separation by Nanoporous Metal-Organic Frameworks Embedded in Gas-Barrier Nanocellulose Films. *Adv. Mater.* 28, 1765-1769.
- 127 Chen, G., Koros, W.J., and Jones, C.W. (2016). Hybrid Polymer/UiO-66(Zr) and Polymer/NaY Fiber Sorbents for Mercaptan Removal from Natural Gas. *ACS Appl. Mater. Interfaces* 8, 9700-9709.
- 128 Zhang, X.F., Feng, Y., Wang, Z.G., Jia, M.M., and Yao, J.F. (2018). Fabrication of cellulose nanofibrils/UiO-66-NH<sub>2</sub> composite membrane for CO<sub>2</sub>/N<sub>2</sub> separation. *J. Membr. Sci.* 568, 10-16.
- 129 Mubashir, M., Yeong, Y.F., Lau, K.K., Chew, T.L., and Norwahyu, J. (2018). Efficient CO<sub>2</sub>/N<sub>2</sub> and CO<sub>2</sub>/CH<sub>4</sub> separation using NH<sub>2</sub>-MIL-53(Al)/cellulose acetate (CA) mixed matrix membranes. *Sep. Purif. Technol.* 199, 140-151.
- 130 Zhuang, J.L., Ar, D., Yu, X.J., Liu, J.X., and Terfort, A. (2013). Patterned Deposition of Metal-Organic Frameworks onto Plastic, Paper, and Textile Substrates by Inkjet Printing of a Precursor Solution. *Adv. Mater.* 25, 4631-4635.
- 131 Dhainaut, J., Bonneau, M., Ueoka, R., Kanamori, K., and Furukawa, S. (2020). Formulation of Metal-Organic Framework Inks for the 3D Printing of Robust Microporous Solids toward High-Pressure Gas Storage and Separation. *ACS Appl. Mater. Interfaces* 12, 10983-10992.
- 132 Yang, K., Dai, Y., Zheng, W., Ruan, X., Li, H., and He, G. (2018). ZIFs-modified GO plates for enhanced CO<sub>2</sub> separation performance of ethyl cellulose based mixed matrix membranes. *Sep. Purif. Technol.*
- 133 Pimentel, B.R., Fultz, A.W., Presnell, K.V., and Lively, R.P. (2017). Synthesis of Water-Sensitive Metal–Organic Frameworks within Fiber Sorbent Modules. *Industrial & Engineering Chemistry Research* 56, 5070-5077.
- 134 Arjmandi, M., Pakizeh, M., Saghi, M., and Arjmandi, A. (2018). Study of Separation Behavior of Activated and Non-Activated MOF-5 as Filler on MOF-based Mixed-Matrix Membranes in H<sub>2</sub>/CO<sub>2</sub> Separation. *Petrol Chem+* 58, 317-329.
- 135 Zhang, F., Dou, J., and Zhang, H. (2018). Mixed Membranes Comprising Carboxymethyl Cellulose (as Capping Agent and Gas Barrier Matrix) and Nanoporous ZIF-L Nanosheets for Gas Separation Applications. *Polymers-Basel* 10.

- 136 Ma, S.S., Zhang, M.Y., Nie, J.Y., Tan, J.J., Yang, B., and Song, S.X. (2019). Design of double-component metal-organic framework air filters with PM<sub>2.5</sub> capture, gas adsorption and antibacterial capacities. *Carbohydr. Polym.* *203*, 415-422.
- 137 Su, Z.P., Zhang, M.Y., Lu, Z.Q., Song, S.X., Zhao, Y.S., and Hao, Y. (2018). Functionalization of cellulose fiber by in situ growth of zeolitic imidazolate framework-8 (ZIF-8) nanocrystals for preparing a cellulose-based air filter with gas adsorption ability. *Cellulose* *25*, 1997-2008.
- 138 Ma, S., Zhang, M., Nie, J., Yang, B., Song, S., and Lu, P. (2018). Multifunctional cellulose-based air filters with high loadings of metal-organic frameworks prepared by in situ growth method for gas adsorption and antibacterial applications. *Cellulose* *25*, 5999-6010.
- 139 Ho, N.A.D., and Leo, C. (2021). A review on the emerging applications of cellulose, cellulose derivatives and nanocellulose in carbon capture. *Environ. Res.* *197*, 111100.
- 140 Schwarzenbach, R.P., Egli, T., Hofstetter, T.B., Von Gunten, U., and Wehrli, B. (2010). Global water pollution and human health. *Annual review of environment and resources* *35*, 109-136.
- 141 Marinho, B.A., Cristóvão, R.O., Boaventura, R.A., and Vilar, V.J. (2019). As (III) and Cr (VI) oxyanion removal from water by advanced oxidation/reduction processes—a review. *Environmental Science and Pollution Research* *26*, 2203-2227.
- 142 Vilar, V.J., Dos Santos, E.V., and Martínez-Huitle, C.A. (2021). Advanced oxidation/reduction technologies: a perspective from Iberoamerican countries. Springer.
- 143 Sharma, S., and Bhattacharya, A. (2017). Drinking water contamination and treatment techniques. *Applied water science* *7*, 1043-1067.
- 144 Som, I., Roy, M., and Saha, R. (2020). Advances in Nanomaterial-based Water Treatment Approaches for Photocatalytic Degradation of Water Pollutants. *ChemCatChem* *12*, 3409-3433.
- 145 Velepini, T., Prabakaran, E., and Pillay, K. (2021). Recent developments in the use of metal oxides for photocatalytic degradation of pharmaceutical pollutants in water—a review. *Materials Today Chemistry* *19*, 100380.
- 146 Cheng, N., Wang, B., Wu, P., Lee, X., Xing, Y., Chen, M., and Gao, B. (2021). Adsorption of emerging contaminants from water and wastewater by modified biochar: A review. *Environ. Pollut.* *273*, 116448.
- 147 Ali, I., and Gupta, V. (2006). Advances in water treatment by adsorption technology. *Nature protocols* *1*, 2661-2667.
- 148 Thines, R., Mubarak, N., Nizamuddin, S., Sahu, J., Abdullah, E., and Ganesan, P. (2017). Application potential of carbon nanomaterials in water and wastewater treatment: a review. *Journal of the Taiwan Institute of Chemical Engineers* *72*, 116-133.
- 149 Wang, S., and Peng, Y. (2010). Natural zeolites as effective adsorbents in water and wastewater treatment. *Chem. Eng. J.* *156*, 11-24.
- 150 Srinivasan, R. (2011). Advances in application of natural clay and its composites in removal of biological, organic, and inorganic contaminants from drinking water. *Advances in Materials Science and Engineering* *2011*.
- 151 Han, H., Rafiq, M.K., Zhou, T., Xu, R., Mašek, O., and Li, X. (2019). A critical review of clay-based composites with enhanced adsorption performance for metal and organic pollutants. *J. Hazard. Mater.* *369*, 780-796.
- 152 Ma, S., Zhang, M., Nie, J., Tan, J., Song, S., and Luo, Y. (2019). Lightweight and porous cellulose-based foams with high loadings of zeolitic imidazolate frameworks-8 for adsorption applications. *Carbohydr. Polym.* *208*, 328-335.
- 153 Gu, Y., Wang, Y., Li, H., Qin, W., Zhang, H., Wang, G., Zhang, Y., and Zhao, H. (2020). Fabrication of hierarchically porous NH<sub>2</sub>-MIL-53/wood-carbon hybrid membrane for highly effective and selective sequestration of Pb<sup>2+</sup>. *Chem. Eng. J.* *387*.
- 154 Berglund, L.A., and Burgert, I. (2018). Bioinspired Wood Nanotechnology for Functional Materials. *Adv. Mater.* *30*, 1704285.
- 155 Chen, C., Kuang, Y., Zhu, S., Burgert, I., Keplinger, T., Gong, A., Li, T., Berglund, L., Eichhorn, S.J., and Hu, L.J.N.R.M. (2020). Structure-property-function relationships of natural and engineered wood. 1-25.

- 156 Sarkar, C., Chowdhuri, A.R., Garai, S., Chakraborty, J., and Sahu, S.K. (2019). Three-dimensional cellulose-hydroxyapatite nanocomposite enriched with dexamethasone loaded metal-organic framework: a local drug delivery system for bone tissue engineering. *Cellulose* 26, 7253-7269.
- 157 Javanbakht, S., Pooresmaeil, M., Hashemi, H., and Namazi, H. (2018). Carboxymethylcellulose capsulated Cu-based metal-organic framework-drug nanohybrid as a pH-sensitive nanocomposite for ibuprofen oral delivery. *Int. J. Biol. Macromol.* 119, 588-596.
- 158 Mansor, E.S., Jamil, T.S., Abdallah, H., and Shaban, A.M. (2018). Highly thin film nanocomposite membrane based metal organic complexes for brackish water desalination. *J. Environ. Chem. Eng.* 6, 5459-5469.
- 159 Lu, L., Hu, C.C., Zhu, Y.J., Zhang, H.H., Li, R., and Xing, Y.J. (2018). Multi-functional finishing of cotton fabrics by water-based layer-by-layer assembly of metal-organic framework. *Cellulose* 25, 4223-4238.
- 160 Qian, L.W., Lei, D., Duan, X., Zhang, S.F., Song, W.Q., Hou, C., and Tang, R.H. (2018). Design and preparation of metal-organic framework papers with enhanced mechanical properties and good antibacterial capacity. *Carbohydr. Polym.* 192, 44-51.
- 161 Rickhoff, T.A., Sullivan, E., Werth, L.K., Kissel, D.S., and Keleher, J.J. (2019). A biomimetic cellulose-based composite material that incorporates the antimicrobial metal-organic framework HKUST-1. *J. Appl. Polym. Sci.* 136.
- 162 Duan, C., Meng, J.R., Wang, X.Q., Meng, X., Sun, X.L., Xu, Y.J., Zhao, W., and Ni, Y.H. (2018). Synthesis of novel cellulose-based antibacterial composites of Ag nanoparticles@ metal-organic frameworks@ carboxymethylated fibers. *Carbohydr. Polym.* 193, 82-88.
- 163 Rubin, H.N., Neufeld, B.H., and Reynolds, M.M. (2018). Surface-Anchored Metal-Organic Framework-Cotton Material for Tunable Antibacterial Copper Delivery. *ACS Appl. Mater. Interfaces* 10, 15189-15199.
- 164 Su, M.L., Zhang, R., Li, H.R., Jin, X.B., Li, J.P., Yue, X.F., and Qin, D.C. (2019). In situ deposition of MOF199 onto hierarchical structures of bamboo and wood and their antibacterial properties. *Rsc Adv* 9, 40277-40285.
- 165 Duan, C., Meng, X., Liu, C.R., Lu, W.L., Liu, J., Dai, L., Wang, W.L., Zhao, W., Xiong, C.Y., and Ni, Y.H. (2019). Carbohydrates-rich corncobs supported metal-organic frameworks as versatile biosorbents for dye removal and microbial inactivation. *Carbohydr. Polym.* 222.
- 166 Roales, J., Moscoso, F.G., Gamez, F., Lopes-Costa, T., Sousaraei, A., Casado, S., Castro-Smirnov, J.R., Cabanillas-Gonzalez, J., Almeida, J., Queiros, C., et al. (2017). Preparation of Luminescent Metal-Organic Framework Films by Soft-Imprinting for 2,4-Dinitrotoluene Sensing. *Materials* 10.
- 167 Giannakoudakis, D.A., Hu, Y., Florent, M., and Bandosz, T.J. (2017). Smart textiles of MOF/g-C<sub>3</sub>N<sub>4</sub> nanospheres for the rapid detection/detoxification of chemical warfare agents. *Nanoscale Horizons* 2, 356-364.
- 168 Xu, X.Y., Lian, X., Hao, J.N., Zhang, C., and Yan, B. (2017). A Double-Stimuli-Responsive Fluorescent Center for Monitoring of Food Spoilage based on Dye Covalently Modified EuMOFs: From Sensory Hydrogels to Logic Devices. *Adv. Mater.* 29.
- 169 Li, X., Li, D.W., Zhang, Y.N., Lv, P.F., Feng, Q., and Wei, Q.F. (2020). Encapsulation of enzyme by metal-organic framework for single-enzymatic biofuel cell-based self-powered biosensor. *Nano Energy* 68.
- 170 Wang, H.P., Pei, Y.J., Qian, X.R., and An, X.H. (2020). Eu-metal organic framework@TEMPO-oxidized cellulose nanofibrils photoluminescence film for detecting copper ions. *Carbohydr. Polym.* 236.
- 171 Li, L., Zhang, Y., Zhang, L.N., Ge, S.G., Yan, M., and Yu, J.H. (2017). Steric paper based ratio-type electrochemical biosensor with hollow-channel for sensitive detection of Zn<sup>2+</sup>. *Sci Bull* 62, 1114-1121.
- 172 Xu, X.Y., and Yan, B. (2018). A fluorescent wearable platform for sweat Cl<sup>-</sup> analysis and logic smart-device fabrication based on color adjustable lanthanide MOFs. *Journal of Materials Chemistry C* 6, 1863-1869.
- 173 Zhou, S.Y., Kong, X.Y., Zheng, B., Huo, F.W., Stromme, M., and Xu, C. (2019). Cellulose Nanofiber @ Conductive Metal-Organic Frameworks for High-Performance Flexible Supercapacitors. *ACS Nano* 13, 9578-9586.



- 174 Zhang, X.J., Gao, X.Y., Wu, Z.Y., Zhu, M.H., Jiang, Q.H., Zhou, S.B., Hong, K., and Rao, Z.H. (2019). Effects of binders on electrochemical sodium storage performance with porous CoFe<sub>2</sub>O<sub>4</sub> nanocubes derived from metal-organic frameworks. *Chem. Phys.* *523*, 124-129.
- 175 Ma, X.T., Lou, Y., Chen, X.B., Shi, Z., and Xu, Y. (2019). Multifunctional flexible composite aerogels constructed through in-situ growth of metal-organic framework nanoparticles on bacterial cellulose. *Chem. Eng. J.* *356*, 227-235.
- 176 Ozer, R.R., and Hinestroza, J.P. (2015). One-step growth of isoreticular luminescent metal-organic frameworks on cotton fibers. *Rsc Adv* *5*, 15198-15204.
- 177 Rubio-Martinez, M., Avci-Camur, C., Thornton, A.W., Imaz, I., MasPOCH, D., and Hill, M.R. (2017). New synthetic routes towards MOF production at scale. *Chem. Soc. Rev.* *46*, 3453-3480.
- 178 Tu, K., Büchele, S., Mitchell, S., Stricker, L., Liu, C., Goldhahn, C., Allaz, J., Ding, Y., Günther, R., and Zhang, Z. (2022). Natural Wood-Based Catalytic Membrane Microreactors for Continuous Hydrogen Generation. *ACS Appl. Mater. Interfaces.*
- 179 (!!! INVALID CITATION !!! 134).
- 180 Zhu, H., Yang, X., Cranston, E.D., and Zhu, S.P. (2016). Flexible and Porous Nanocellulose Aerogels with High Loadings of Metal-Organic-Framework Particles for Separations Applications. *Adv. Mater.* *28*, 7652-+.
- 181 Hashem, T., Ibrahim, A.H., Woll, C., and Alkordi, M.H. (2019). Grafting Zirconium-Based Metal-Organic Framework UiO-66-NH<sub>2</sub> Nanoparticles on Cellulose Fibers for the Removal of Cr(VI) Ions and Methyl Orange from Water. *Acs Appl Nano Mater* *2*, 5804-5808.
- 182 Lu, H.L., Zhang, L.L., Wang, B.B., Long, Y.D., Zhang, M., Ma, J.X., Khan, A., Chowdhury, S.P., Zhou, X.F., and Ni, Y.H. (2019). Cellulose-supported magnetic Fe<sub>3</sub>O<sub>4</sub>-MOF composites for enhanced dye removal application. *Cellulose* *26*, 4909-4920.
- 183 Trinh, D.X., Tran, T.P.N., and Taniike, T. (2017). Fabrication of new composite membrane filled with UiO-66 nanoparticles and its application to nanofiltration. *Sep. Purif. Technol.* *177*, 249-256.
- 184 Noorian, S.A., Hemmatinejad, N., and Navarro, J.A. (2019). BioMOF@ cellulose fabric composites for bioactive molecule delivery. *J. Inorg. Biochem.* *201*, 110818.
- 185 Jin, H.X., Xu, H.P., Wang, N., Yang, L.Y., Wang, Y.G., Yu, D., and Ouyang, X.K. (2019). Fabrication of Carboxymethylcellulose/Metal-Organic Framework Beads for Removal of Pb(II) from Aqueous Solution. *Materials* *12*.
- 186 Bo, S., Ren, W., Lei, C., Xie, Y., Cai, Y., Wang, S., Gao, J., Ni, Q., and Yao, J. (2018). Flexible and porous cellulose aerogels/zeolitic imidazolate framework (ZIF-8) hybrids for adsorption removal of Cr(IV) from water. *J. Solid State Chem.* *262*, 135-141.
- 187 Lei, C., Gao, J.K., Ren, W.J., Xie, Y.B., Abdalkarim, S.Y.H., Wang, S.L., Ni, Q.Q., and Yao, J.M. (2019). Fabrication of metal-organic frameworks@cellulose aerogels composite materials for removal of heavy metal ions in water. *Carbohydr. Polym.* *205*, 35-41.
- 188 Wang, N., Ouyang, X.-K., Yang, L.-Y., and Omer, A.M. (2017). Fabrication of a Magnetic Cellulose Nanocrystal/Metal-Organic Framework Composite for Removal of Pb(II) from Water. *ACS Sustainable Chemistry & Engineering* *5*, 10447-10458.
- 189 Karmakar, S., Bhattacharjee, S., and De, S. (2017). Experimental and modeling of fluoride removal using aluminum fumarate (AlFu) metal organic framework incorporated cellulose acetate phthalate mixed matrix membrane. *J. Environ. Chem. Eng.* *5*, 6087-6097.
- 190 He, S., Chen, C., Chen, G., Chen, F., Dai, J., Song, J., Jiang, F., Jia, C., Xie, H., and Yao, Y. (2020). High-Performance, Scalable Wood-Based Filtration Device with a Reversed-Tree Design. *Chem. Mater.* *32*, 1887-1895.
- 191 Cui, X.F., Sun, X.D., Liu, L., Huang, Q.H., Yang, H.C., Chen, C.H., Nie, S.X., Zhao, Z.X., and Zhao, Z.X. (2019). In-situ fabrication of cellulose foam HKUST-1 and surface modification with polysaccharides for enhanced selective adsorption of toluene and acidic dipeptides. *Chem. Eng. J.* *369*, 898-907.
- 192 Abdelhameed, R.M., Rehan, M., and Emam, H.E. (2018). Figuration of Zr-based MOF@cotton fabric composite for potential kidney application. *Carbohydr. Polym.* *195*, 460-467.

- 193 Lange, L.E., and Obendorf, S.K. (2015). Functionalization of cotton fiber by partial etherification and self-assembly of polyoxometalate encapsulated in Cu<sub>3</sub>(BTC)<sub>2</sub> metal-organic framework. *ACS Appl. Mater. Interfaces* 7, 3974-3980.
- 194 Lu, H.L., Zhang, L.L., Ma, J.X., Alam, N., Zhou, X.F., and Ni, Y.H. (2019). Nano-Cellulose/MOF Derived Carbon Doped CuO/Fe<sub>3</sub>O<sub>4</sub> Nanocomposite as High Efficient Catalyst for Organic Pollutant Remedy. *Nanomaterials-Basel* 9.
- 195 Sun, X.D., He, P., Gao, Z., Liao, Y.X., Weng, S.X., Zhao, Z.X., Song, H., and Zhao, Z.X. (2019). Multi-crystalline N-doped Cu/Cu<sub>x</sub>O/C foam catalyst derived from alkaline N-coordinated HKUST-1/CMC for enhanced 4-nitrophenol reduction. *J. Colloid Interface Sci.* 553, 1-13.

## 4.2 Green Synthesis of Hierarchical Metal-Organic Framework/Wood Functional Composites with Superior Mechanical Properties

*Kunkun Tu<sup>1,2,5</sup>, Begoña Puértolas<sup>3,5</sup>, Maria Adobes-Vidal<sup>1,2</sup>, Yaru Wang<sup>1,2</sup>, Jianguo Sun<sup>1,2</sup>, Jacqueline Traber<sup>4</sup>, Ingo Burgert<sup>1,2</sup>, Javier Pérez-Ramírez<sup>3\*</sup>, Tobias Keplinger<sup>1,2\*</sup>*

1. Wood Materials Science, Institute for Building Materials, ETH Zürich, 8093 Zürich, Switzerland
2. WoodTec Group, Cellulose & Wood Materials, EMPA, 8600 Dübendorf, Switzerland
3. Institute for Chemical and Bioengineering, Department of Chemistry and Applied Biosciences, ETH Zurich, 8093 Zurich, Switzerland
4. Eawag, Swiss Federal Institute of Aquatic Science and Technology, 8600 Dübendorf, Switzerland
5. These authors contributed equally

\*Correspondence: [jpr@chem.ethz.ch](mailto:jpr@chem.ethz.ch); [tkeplinger@ethz.ch](mailto:tkeplinger@ethz.ch)

## Abstract

The applicability of advanced composite materials with hierarchical structure that conjugate metal-organic frameworks (MOFs) with macroporous materials is commonly limited by their inferior mechanical properties. Here, a universal green synthesis method for the *in situ* growth of MOF nanocrystals within wood substrates is introduced. Nucleation sites for different types of MOFs are readily created by a sodium hydroxide treatment, which is demonstrated to be broadly applicable to different wood species. The resulting MOF/wood composite exhibits hierarchical porosity with 130 times larger specific surface area compared to native wood. Assessment of the CO<sub>2</sub> adsorption capacity demonstrates the efficient utilization of the MOF loading along with similar adsorption ability to that of pure MOF. Compression and tensile tests reveal superior mechanical properties, which surpass those obtained for polymer substrates. The functionalization strategy offers a stable, sustainable and scalable platform for the fabrication of multifunctional MOF/wood-derived composites with potential applications in environmental and energy-related fields.

## Keywords:

green synthesis, metal-organic frameworks, wood-based composites, hierarchical porosity, mechanical properties

## 1 Introduction

Metal-organic frameworks (MOFs) are crystalline coordination polymers with tunable porosity that are composed of three-dimensional (3D) networks of metal ions (or clusters) and organic linkers. Their unique micro/mesopore architecture results in high specific surface area, large porosity, low density and structural diversity,<sup>1</sup> which makes them highly attractive candidates for numerous applications, including gas storage and separation,<sup>2-4</sup> catalysis,<sup>5</sup> drug delivery,<sup>6</sup> sensing<sup>7</sup> and energy storage.<sup>8</sup> However, due to the crystalline nature of MOFs, they are most commonly found as powders, thus, their processability and handling remain a significant challenge.<sup>9</sup> Integrating MOFs onto or into various substrates to produce shapeable and cost-efficient materials constitutes one way to expand the potential applications of these functional materials. In this regard, MOFs have been deposited or grown on various polymer substrates<sup>10-17</sup> by means of direct mixing,<sup>18</sup> *in situ* growth,<sup>19</sup> layer-by-layer<sup>20</sup> and continuous flow synthesis<sup>21</sup> resulting in composite materials that exhibit a complex multilevel network of macropores, mesopores and micropores, in which the macro- and mesoporous structures enhance the diffusion kinetics and accessibility to the active sites located in the micropores of MOFs.<sup>22</sup>

A common way to fabricate porous MOF-containing composites are bottom-up methods such as freeze-casting,<sup>23</sup> freeze-drying,<sup>24</sup> solvent-casting,<sup>25</sup> or electrospinning<sup>18</sup>. While these methods lead to composites with sufficient porosity, they are often characterized by relatively weak mechanical properties,<sup>26</sup> due to the well-known trade-off between high porosity and satisfying mechanical properties, which substantially limits their applicability in pressure-driven gas or liquid adsorption and separation processes.<sup>27,28</sup> Even though various methods have been proposed to improve the mechanical properties, *i.e.*, increasing the polymer-volume fraction within the composites,<sup>29</sup> cross-linking of the polymer<sup>30,31</sup> as well as the incorporation of additional reinforcing fibers,<sup>32</sup> the resulting composites can still be limited by MOF aggregation, weak interaction between the substrate and MOFs, or low permeability. Furthermore, the flexibility and swelling of the polymer membrane may result in the segregation of the MOF layer from the membrane surface.<sup>33,34</sup>

Hence, finding an alternative substrate that provides both sufficient porosity and excellent mechanical properties is a prerequisite.<sup>35</sup> A range of biological materials that fulfill these requirements are available in nature, among which wood outstands as a promising example. Wood is a hierarchically-structured material across several length scales composed of well-connected hollow fibrous structures.<sup>36</sup> This unique hierarchical and open porous structure with superior mechanical properties along with its light weight offers an ideal scaffold to manufacture high-performance composite materials, such as transparent wood,<sup>37</sup> oil/water separation membranes,<sup>38,39</sup> solar steam generation devices,<sup>40</sup> mechanically tunable wood<sup>41</sup> and stimuli responsive wood.<sup>42</sup> Additionally, wood exhibits abundant hydroxyl groups that can act as active sites for chemical modifications facilitating the *in situ* functionalization with polymers or inorganic materials leading to advanced functionality.<sup>43-45</sup> However, studies that exploit all these beneficial aspects to develop MOF/wood composites are scarce.<sup>46</sup>

Here, we report a versatile and simple strategy for the sustainable synthesis of composites with unique hierarchical structure and superior mechanical properties, based on the *in situ* growth of different types of MOFs within diverse wood substrates (**Figure 1**). While MOF provides the micro- and mesoporous network, macroporous wood serves as mechanical support, opening up the avenue for a new type of composite materials.

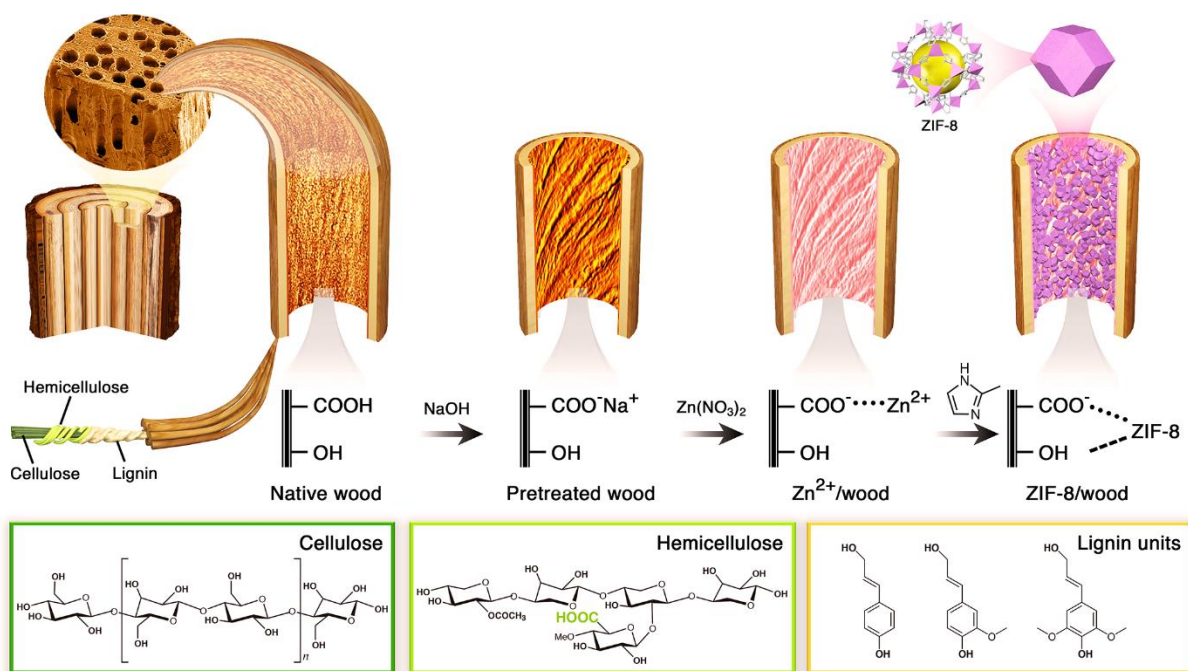


**Figure 1.** Schematic representation of the fabrication process to obtain ZIF-8/wood composites.

## 2 Results and discussion

Beech, a widely used diffuse-porous hardwood species, mainly composed of tubular cells, *i.e.*, vessels and fibers along the longitudinal direction, whose cell walls consist of cellulose fibrils embedded in a matrix of hemicelluloses and lignin (Figure 2a,b), was selected to prepare the initial composite material. First, we performed a simple and effective sodium hydroxide (NaOH) solution pretreatment of the wood samples. This step fulfills simultaneously two main functions: (i) it ensures the ion exchange of the proton in the wood inherent carboxyl groups by sodium cations, providing the nucleation sites for the subsequent growing of the MOF structure, and (ii) it provides a rough fibrillar structure that boosts the anchoring of the MOFs to the wooden substrate. Fourier-transform infrared (ATR-FTIR) spectra confirmed the successful chemical transformations that occurred during this NaOH pretreatment process (Figure 2m). The decrease in the intensity of the carbonyl group ( $\text{-C=O}$ ) at  $1735\text{ cm}^{-1}$  and the increase of carboxylate groups ( $\text{-COO}^-$ ) at  $1593\text{ cm}^{-1}$  for the pretreated beech indicate partial removal of hemicelluloses and the successful transformation from  $\text{-COOH}$  to  $\text{-COONa}$  after the alkaline treatment. Hence, the negative surface charge of bulk beech samples measured by zeta potential analysis increased by the pretreatment from  $-12.05 \pm 1.87\text{ mV}$  to  $-38.44 \pm 1.99\text{ mV}$ , leading to strong affinity to metal cations (Table S1). Atomic Force Microscopy (AFM) revealed that the NaOH pretreatment also removed the innermost surface layer of the cell walls facing to the empty lumen of the cells (Figure 2c) and exposed the underlying cellulose microfibril structure

(Figure 2f). This surface layer is composed of hemicelluloses (mannan and xylan) and lignin-like polyphenols.<sup>47,48</sup> The decrease of the IR-peaks at  $1396\text{ cm}^{-1}$  attributed to C–H deformation in hemicellulose and  $1234\text{ cm}^{-1}$  corresponding to C–O stretch in lignin demonstrated the partial removal of hemicellulose and lignin. Note that the X-ray diffraction (XRD) pattern confirmed that the NaOH pretreatment does not alter cellulose as its initial crystal structure remains intact (Figure 2n). After pretreatment, the beech samples were thoroughly washed with water until the pH value of the washing water equaled 9. In order to retain the porous structure, the samples were kept in wet state after washing, as conventional vacuum drying of pretreated beech leads to pronounced cell wall shrinkage accompanied by the blockage of the lumina (Figure S1), which would hamper the subsequent growth of the MOF. To fix the original pretreated beech structure in the dry state for SEM and AFM analysis, the samples were subjected to a freeze-drying process to avoid shrinkage (Figure S2).

The next step consists of the *in situ* formation of the MOF, *i.e.*, zeolitic imidazolate framework-8 (ZIF-8) in this case, crystal nuclei within pretreated beech. For that purpose, primary addition of  $\text{Zn}(\text{NO}_3)_2$  solution promoted the ion-exchange between  $\text{Na}^+$  ions in the carboxyl groups of pretreated beech by  $\text{Zn}^{2+}$  ions. After the addition of 2-Methylimidazole (2-MeIm), ZIF-8 nanoparticles of *ca.* 420 nm were uniformly and firmly deposited on the lumen surface *via* H-bonding and electrostatic interactions resulting in the ZIF-8/beech composite (Figure 2g-k, Figure S3a). The formation of the composite rarely occurs without the pretreatment as exemplified in Figure S3b. Elemental mapping images of the ZIF-8/beech composite revealed the homogeneous distribution of ZIF-8 nanoparticles on the lumen surface of vessels, fibers and rays as indicated by the uniform detection of zinc (green) across the entire bulk wood structure (Figure 2l). Conventional vacuum impregnation or filtration of pre-synthesized ZIF-8 favors the agglomeration of the ZIF-8 particles at the outer surface of wood, which blocks the pathway into the inner part of the wood and limits the inner functionalization of the bulk sample (Figure S4), thus emphasizing the impact and importance of the *in situ* growth treatment on the distribution of MOF crystals (Figure 2g-l). The FTIR spectra of the ZIF-8/beech composite displayed the bands at  $1146$ ,  $420\text{ cm}^{-1}$  and  $758\text{ cm}^{-1}$  associated with C–N, Zn–N and out-of-plane bending of the 2-MeIm ring of ZIF-8, respectively (Figure 2m).<sup>49</sup> The asymmetric peak of  $\text{COO}^-$  shifted from  $1593\text{ cm}^{-1}$  in the case of pretreated beech to  $1581\text{ cm}^{-1}$  for the ZIF-8/beech composite, owing to the changes in the metal–carboxylate interaction from  $\text{COO}^- \text{-Na}^+$  to  $\text{COO}^- \text{-Zn}^{2+}$ . In addition, the XRD pattern of the ZIF-8/beech composite revealed two broad diffraction peaks centered around  $2\theta=16.1^\circ$  and  $22.3^\circ$  associated with cellulose, along with the characteristic diffraction peaks at  $2\theta=7.3^\circ$ ,  $10.4^\circ$ ,  $12.8^\circ$ ,  $14.7^\circ$  and  $18.1^\circ$  corresponding to the



(110), (200), (211), (220) and (222) crystal faces of ZIF-8, thus confirming the successful formation of ZIF-8 crystals (Figure 2n).

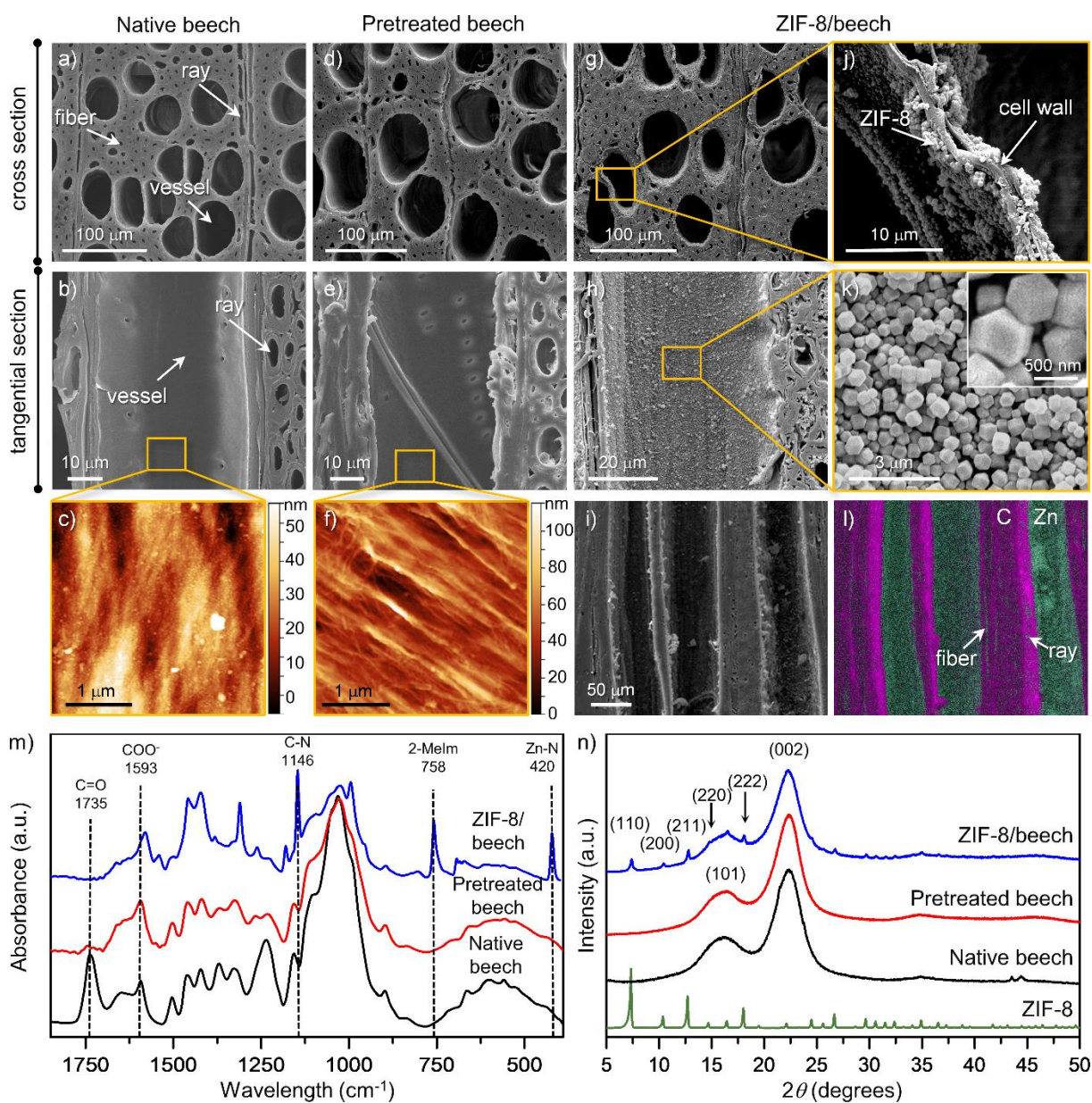


**Figure 2.** Cross-sectional (first line) and tangential-sectional (second line) SEM images of a,b) native beech, d,e) pretreated beech and g-k) ZIF-8/beech composite. The inset in k) correspond to the magnified SEM image of ZIF-8 nanocrystals in ZIF-8/beech composite. AFM images of the cell wall layer facing to the cell lumen of c) native beech and f) pretreated beech. i) SEM image and l) corresponding elemental maps of zinc (green) and carbon (pink) for the ZIF-8/beech composite. m) FTIR spectra of native beech, pretreated beech and ZIF-8/beech composite. n) XRD patterns of native beech, pretreated beech, ZIF-8/beech composite and pure ZIF-8.



The presented protocol mainly differs from state-of-the-art preparation methods in the pretreatment step. In the case of polymer-derived composites, the pretreatment generally involves TEMPO oxidation, esterification, cysteamine or carboxymethylation reactions, which are performed in the presence of toxic chemicals such as sodium hypochlorite (NaClO), cyanuric chloride ( $C_3Cl_3N_3$ ) and sodium chloroacetate ( $ClCH_2COONa$ ).<sup>50</sup> In contrast, the treatment with NaOH offers a simple and renewable solution for the targeted wood functionalization. To compare both processes, a conventional carboxymethylation process was also applied (sample code: ZIF-8/CM beech). The results showed that both methods led to similar MOF distribution (Figure S5).

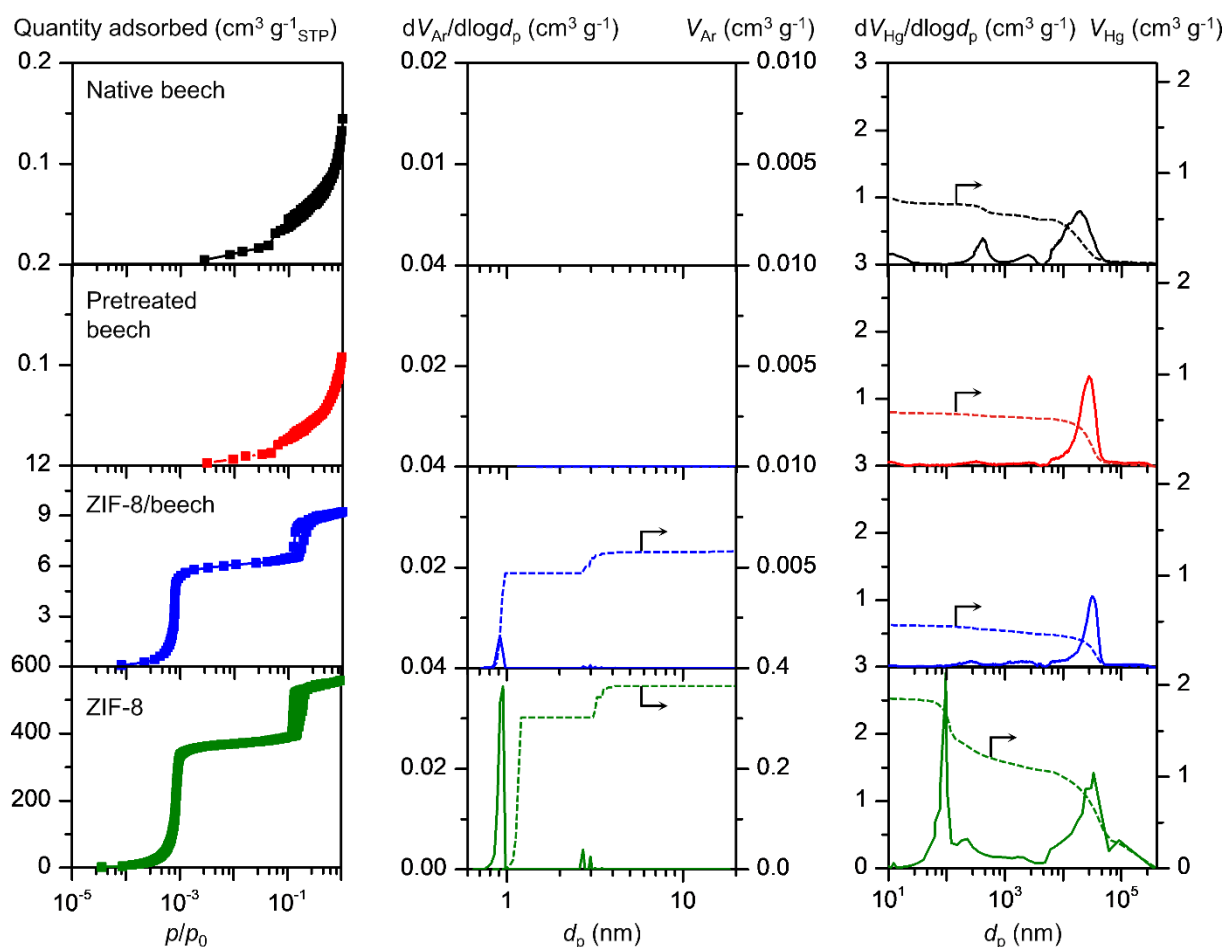


**Figure 3.** Adsorption isotherms (left), pore size and cumulative pore volumes from argon sorption (middle) and mercury porosimetry (right) of native beech, pretreated beech, ZIF-8/beech composite and pure ZIF-8.

Following the synthesis of the ZIF-8/beech composite, a sorbent activation procedure was conducted. It involves two steps: washing with methanol followed by heating under vacuum to fully remove the excess precursors that could otherwise block the microporous structure of ZIF-8 (Figure S6).<sup>51</sup> As exemplified in Figure S7, traces of the precursor were still evidenced in the

composite when water was used as a solvent due to the lower solubility of 2-MeIm in water compared to methanol, which suggests that the selected solvent has a key impact on the final porosity and morphological properties of the composite.

**Table 1.** Porous properties of native beech, pretreated beech, ZIF-8/beech composite and pure ZIF-8.

Sample	$S_{\text{BET}}$ [m <sup>2</sup> g <sup>-1</sup> ] <sup>a)</sup>	$S_{\text{meso}}$ [m <sup>2</sup> g <sup>-1</sup> ] <sup>b)</sup>	$V_{\text{micro}}$ [cm <sup>3</sup> g <sup>-1</sup> ] <sup>c)</sup>	$V_{\text{pore}}$ [cm <sup>3</sup> g <sup>-1</sup> ] <sup>c)</sup>
Native beech	0.2	0.2	0	0
Pretreated beech	0.1	0.1	0	0
ZIF-8/beech	26	4	0.006	0.011
ZIF-8	1562	222	0.39	0.68

<sup>a)</sup> BET method; <sup>b)</sup> *t*-plot method; <sup>c)</sup> Volume adsorbed at  $p/p_0=0.99$ .

In order to determine the complete distribution of macropores, mesopores and micropores of the ZIF-8/beech composite, argon sorption and mercury porosimetry analyses were conducted (**Figure 3**). The argon adsorption isotherms of both native and pretreated beech revealed negligible porosity whereas the resulting ZIF-8/beech composite clearly exhibited the characteristic features of the ZIF-8 bulk material, *i.e.*, the presence of microporosity along with the hysteresis loop, which is associated with capillary condensation taking place in mesopores. The porous properties derived from the adsorption isotherms are summarized in **Table 1**. The ZIF-8/beech composite exhibited a surface area of 26 m<sup>2</sup> g<sup>-1</sup>, which is 130 times higher than that obtained for native beech, and a micropore volume of 0.006 cm<sup>3</sup> g<sup>-1</sup>. The substantial increase of the surface area compared to native beech proves the existence of ZIF-8 within wood, in line with previous analyses (Figure 2g-n). Indeed, the comparison of the porous properties of native beech and the composite revealed a ZIF-8 loading of *ca.* 1.8 wt.% in the composite. The MOF loading could be further increased by longer MOF synthesis times, by layer-by-layer buildup of MOF multilayers or simply by using wood species with higher porosity. Increasing the synthesis time up to 48 h resulted in a surface area of 39 m<sup>2</sup> g<sup>-1</sup> and by using the two cycles layer-by-layer method during the ZIF-8 synthesis, the surface area of the composite reached values up to 84 m<sup>2</sup> g<sup>-1</sup>, which is 419.5 times higher than that obtained for native beech (Table S2). The application of the nonlocal density functional theory (NLDFT) to the argon sorption isotherms enabled to determine the pore size distribution (PSD) in the micro and mesopore ranges (Figure 3, middle panel). Similarly, the PSD in the macropore range was calculated from the mercury intrusion data (Figure 3, right panel). The results revealed the

absence of micro- and mesoporosity for the native and pretreated beech and the presence of micropores of *ca.* 0.8 nm and mesopores of *ca.* 3 nm in both the composite and pure ZIF-8, which confirms the successful incorporation of ZIF-8 into the wood matrix. The PSD obtained from the mercury porosimetry data of native wood evidenced the presence of pores of 10 nm, 400 nm, 0.3  $\mu\text{m}$  and 20  $\mu\text{m}$ , from which the first three diminished during the pretreatment step, as conventional vacuum drying after the pretreatment leads to the shrinkage of the cell walls. Therefore, the pores diminish within the cell walls and pits, as well as the lumen of the fibers and vessels. Bigger pores are preserved upon incorporation of ZIF-8, thus suggesting the trimodal porosity of the final ZIF-8/beech composite. The macropores (100 nm and 100  $\mu\text{m}$ ) detected in pure ZIF-8 originate from the intraparticle porosity between the nanocrystals, and therefore, were not detected in the case of the composite owing to the uniform monolayer distribution of ZIF-8 on wood. Accordingly, the final material evidenced a multimodal porous structure consisting of interconnected pores with different lengths ranging from micro- and meso- to macropores and can be accurately tuned by modifications in the synthesis protocol and/or in the selected MOFs and wood species.

This type of hierarchically-organized porous materials are of high relevance for applications dealing with large molecules and nanomaterials. The microporous network of the composite provides the shape selectivity function for guest molecules such as  $\text{CO}_2$  and  $\text{N}_2$  while the meso- and macroporous networks can improve the accessibility to the active sites and the diffusion kinetics. To exemplify the functionality of the composite, we have evaluated the adsorption capacity of  $\text{CO}_2$  and compared it with that of pure ZIF-8 (Figure S8b). The amount of  $\text{CO}_2$  adsorbed per gram of ZIF-8 in the case of the composite (*ca.*  $48 \text{ cm}^3 \text{ g}^{-1}_{\text{ZIF-8}}$  at  $p/p_0=1$ ) is comparable to that of pure ZIF-8 (*ca.*  $44 \text{ cm}^3 \text{ g}^{-1}_{\text{ZIF-8}}$  at  $p/p_0=1$ ) in line with the similar crystal sizes, *i.e.*,  $420 \pm 113 \text{ nm}$  and  $460 \pm 57 \text{ nm}$  for ZIF-8 within the composite and pure ZIF-8, respectively. This indicates i) the efficient utilization of ZIF-8 in the composite and ii) that the embedding process did not alter the adsorption capacity of the MOF. The adsorption capacity of  $\text{N}_2$  was also evaluated under equivalent experimental conditions. The composite did not adsorb  $\text{N}_2$ , thus demonstrating the superior selectivity towards  $\text{CO}_2$  adsorption.

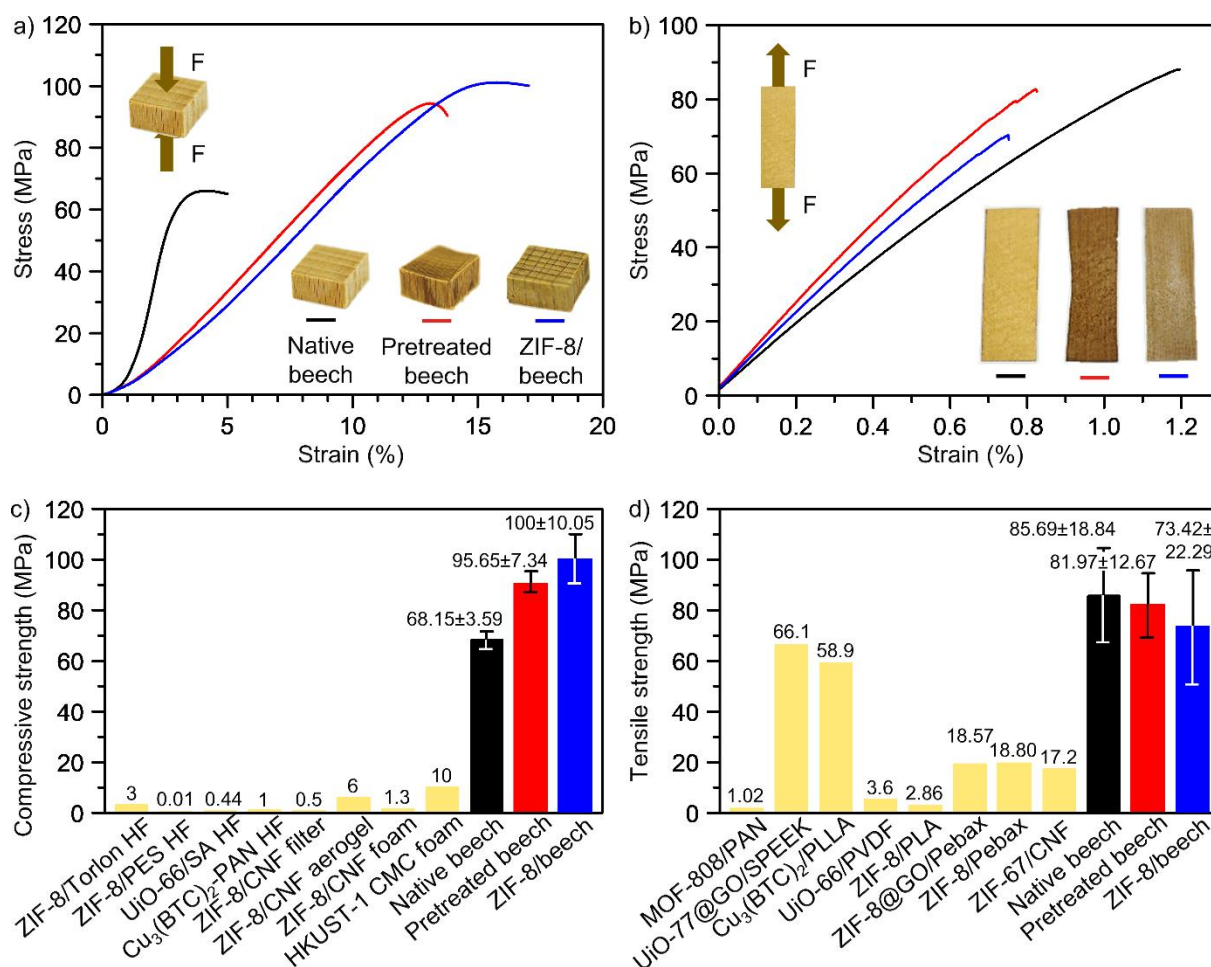


**Figure 4.** Mechanical performance of native beech, pretreated beech and ZIF-8/beech composite. a) Compressive and b) tensile stress–strain curves of native beech, pretreated beech and ZIF-8/beech composite. The insets in a) and b) show the schematic representation of the respective mechanical tests and the images of native beech, pretreated beech and ZIF-8/beech composite samples used in the tests. Comparison of c) compressive strength and d) ultimate tensile stress of the materials used in this work with other polymer substrates/templates-supported MOFs composites (additional details are provided in Table S3,4).

In addition to the functionality, mechanical properties are key for further processing and application of the final composite. Upon pressure-driven applications in gas adsorption and separation processes, the MOF/wood composites need to be strong enough to retain the hierarchical porosity under the applied pressure conditions. Therefore, we have conducted a comprehensive mechanical characterization by compression and tensile tests (Figure 4a and b, Figure S9). Compression tests in the longitudinal direction of wood showed that pretreated beech exhibited higher strength (96 MPa) than native beech (68 MPa), but experienced pronounced reduction of the elastic modulus in compression and showed a 3-fold higher strain-

to-failure value. Wood became slightly more flexible after the pretreatment step owing to the partial removal of the cell wall matrix components, lignin and hemicellulose (Figure 4a, Figure S9a). The compressive strength of the ZIF-8/beechn composite was 100 MPa and showed similar mechanical performance as the pretreated beech, thus demonstrating that the presence of ZIF-8 crystals within wood did not significantly affect the mechanical properties. In tensile tests in the longitudinal wood direction, native beech, pretreated beech and the ZIF-8/beechn composites exhibited similar ultimate tensile stress levels, *i.e.*, 87 MPa, 81 MPa and 73 MPa, respectively (Figure 4b, Figure S9b). The stress-strain curves show that the pretreatment did not affect the tensile modulus, which indicates that the stress transfer between fibers was not altered. Notably, wood offers a robust scaffold, which supplies excellent mechanical properties to the final composite. Indeed, both compressive strengths and ultimate tensile stress of the ZIF-8/beechn composite reported in this study are substantially higher than those obtained for the widely-synthesized polymer-based MOF composites previously reported (Figure 4c,d and Table S3,4).

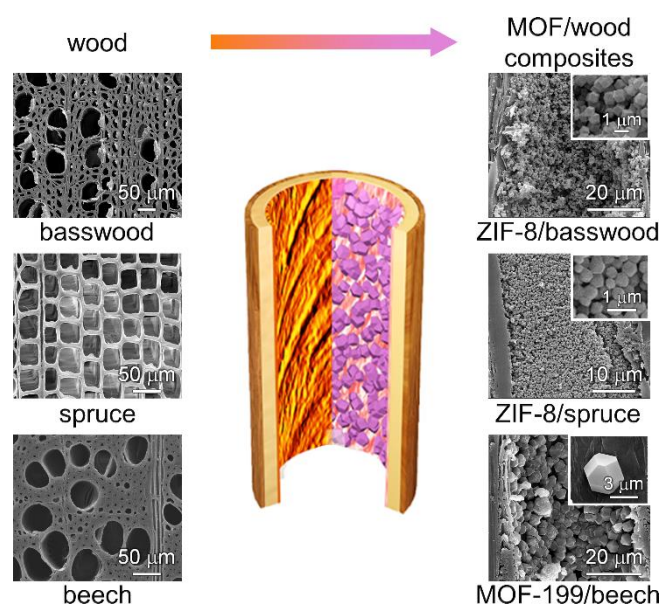


**Figure 5.** Schematic representation of the versatility of the synthetic approach to other wood species and MOFs. Cross-sectional SEM images (left) of native wood (basswood, spruce and beech) and tangential-sectional SEM images (right) of MOF/wood composites (ZIF-8/basswood, ZIF-8/spruce and MOF-199/beechn). The inset corresponds to the magnified SEM images of MOF nanocrystals in MOF/wood composites.

Finally, as a proof of concept, we demonstrate the feasibility of the synthesis protocol to be extended to other wood species, metal organic frameworks as well as different sample geometries depending on the final application. The developed synthesis approach was applied

to MOF-199 and other wood types, *e.i.*, basswood and spruce. Both SEM (**Figure 5**) and XRD (Figure S10) analyses confirmed the successful formation of MOF/wood composites in all cases. The size of the ZIF-8 particles in beech, basswood and spruce was 420 nm, 1  $\mu\text{m}$  and 450 nm, respectively owing to the different water adsorption and transport abilities of the wood species. Additionally, MOF/wood composite can be built in different shapes. Indeed, ZIF-8 nanocrystals were successfully synthesized within both wood veneer and cubic, and their morphology and surface area were similar (Figure S11). These results clearly reveal the high potential of wood-derived composites towards the practical implementation of MOFs.

### 3 Conclusion

In this work, we have developed a universal strategy for the green synthesis of a ZIF-8/beech composite by the *in situ* growth of ZIF-8 nanocrystals within beech. The effective growth of ZIF-8 was facilitated by the pretreatment of beech with a sodium hydroxide solution. The as-synthesized hierarchical ZIF-8/beech composite exhibits a complex network of macropores, mesopores and micropores resulting in a 130-times higher surface area compared to native beech. Assessment of the  $\text{CO}_2$  adsorption capacity revealed the efficient utilization of the ZIF-8 loading along with the preservation of the adsorption ability upon embedding of ZIF-8 into the composite. Most importantly, this composite demonstrates excellent mechanical properties. Evaluation of the compressive strength and ultimate tensile stress resulted in values of 100 MPa and 74 MPa, respectively, which surpass those obtained with state-of-the-art polymer-derived composites. In addition, the versatility of this synthetic approach was further proved with other MOFs, *i.e.*, MOF-199, and wood types, *i.e.*, basswood and spruce, thus evidencing the wide potential for tuning the properties of the final material for a targeted application. The reported functionalization strategy offers a low-cost, sustainable and scalable platform with great potential in the fabrication of functional materials.

### 4 Experimental section

*Materials:* European beech (*Fagus sylvatica*), American basswood (*Tilia americana*) and Norway spruce (*Picea abies*) wood samples were cut into cuboids with the dimensions  $10 \times 10 \times 5 \text{ mm}^3$  (radial  $\times$  tangential  $\times$  longitudinal, R  $\times$  T  $\times$  L). Tangential cut beech veneers with a thickness of 6 mm, a length of 6 cm and a width of 2 cm were used. Zinc nitrate hexahydrate ( $\text{Zn}(\text{NO}_3)_2 \cdot 6\text{H}_2\text{O}$ , 98%), copper(II) acetate ( $\text{Cu}(\text{OAc})_2$ , 98%), triethylamine ( $\text{C}_3\text{H}_9\text{N}$ ,  $\geq 99\%$ ) and sodium chloroacetate ( $\text{ClCH}_2\text{COONa}$ , 98%) were purchased from Sigma-Aldrich. 2-Methylimidazole (2-MeIm,  $\text{C}_6\text{H}_6\text{N}_2$ , 97%) and sodium hydroxide (NaOH) were supplied by Thermo Fisher GmbH. 1,3,5-benzenetricarboxylic acid was obtained from EMD Millipore

Corporation. Methanol ( $\geq 99.9\%$ ), ethanol ( $\geq 99.8\%$ ) and *N,N*-dimethylformamide (DMF,  $\geq 99.8\%$ , Sigma-Aldrich) were used as solvents. All chemicals were used as received.

*Wood Pretreatment:* Native beech wood samples were pretreated by immersion in a 15% w/v NaOH aqueous solution for 1 h. The resulting wood samples denoted as pretreated beech, were washed under stirring with water for 24 h until the pH value of the washing solution reached 9.

*Preparation of ZIF-8/beech composite:* The pretreated beech wood samples were vacuumed for 1 h prior to the vacuum impregnation with a  $\text{Zn}(\text{NO}_3)_2$  solution, which was prepared by dissolving  $\text{Zn}(\text{NO}_3)_2 \cdot 6\text{H}_2\text{O}$  (2.4 g, 0.002 mol) in methanol (20 g) and deionized water (3 g). The impregnation time was 2 h to ensure a sufficient ion-exchange between Zn and Na ions.

A 2-MeIm solution, containing 13.2 g (0.04 mol) of MeIm in methanol (20 g) and deionized water (3 g) was subsequently added to the above solution. Stirring at room temperature for 24 h led to the ZIF-8/beech composite. The composite was then rinsed three times with 50 ml of methanol for 5 min to remove the unreacted precursors, followed by drying in the vacuum-oven at  $103^\circ\text{C}$  for 48 h. The same synthesis procedure was used for the other wood species. For the preparation of the two cycles layer-by-layer sample, the above-described synthesis procedure was repeated twice.

*Preparation of MOF-199/beech composite:* The synthesis route of MOF-199 was adapted from a method reported by Tranchemontagne *et al.*<sup>52</sup> Similarly to the procedure used in the preparation of the ZIF-8/beech composite, a vacuum impregnation protocol was applied. After the pretreated beech was vacuumed for 1 h, a  $\text{Cu}(\text{OAc})_2$  solution prepared by dissolving  $\text{Cu}(\text{OAc})_2$  (860 mg) in a DMF:ethanol:water (12 ml, 1:1:1, v/v/v) solution was added. The resulting mixture was stirred for 24 h in order to ensure a sufficient ion-exchange between Cu and Na ions. 500 mg of 1,3,5-benzenetricarboxylic acid previously dissolved in 12 ml of the same solvent mixture were subsequently added dropwise followed by the addition of 0.5 ml of trimethylamine. The resulting mixture was stirred at room temperature and the final MOF-199/beech composite was obtained after 24 h. The composite was rinsed three times with 25 ml DMF for 5 min to remove the unreacted precursors and then immersed in ethanol for 30 min before drying under vacuum at  $103^\circ\text{C}$  for 48 h.

*Materials Characterization:* Scanning electron microscopy (SEM) was performed on a FEI Quanta 200F instrument. Prior to the analysis, a 10 nm thick Pt/Pd layer was sputtered onto all the sample surfaces to improve conductivity using a Safematic CCU-010 Metal Sputter Coater. Energy dispersive X-ray (EDX) spectroscopy was conducted using an Ametek-EDAX Octane Super detector in secondary electrons mode at 20 kV and a working distance of *ca.* 10 mm.

Atomic force microscopy (AFM) images were acquired in air using a NanoWizard 4 microscope (JPK Instruments AG - Bruker Nano GmbH). Specific measurement parameters are reported in the Supporting Information. Fourier-transform infrared (ATR-FTIR) spectra were measured on a Bruker Tensor 27 spectrometer equipped with an ATR module. Wood samples used for testing were 0.1 g fibers cut from cuboids with a length of 5 mm and a width of 0.2 mm. Measurements were carried out in the spectral range from 650-4000  $\text{cm}^{-1}$ . Each measured spectrum was an average of 64 scans and the displayed spectrum is an average of 10 spectra. Baseline correction of the obtained average spectra was conducted in the software OPUS (Bruker). Zeta potential analysis was conducted using a SurPASS Electrokinetic Analyzer (Anton Paar). Specific measurement parameters and procedures are reported in the Supporting Information. Powder X-ray diffraction (XRD) was measured using a PANalytical X'Pert PRO MPD diffractometer with a Ni-filtered  $\text{CuK}\alpha$  radiation ( $\lambda = 0.15418 \text{ nm}$ ). For the measurements, small cut beech veneers with a thickness of 6 mm, a length of 2 cm and a width of 1 cm and MOF (ZIF-8 and MOF-199) powders were used. The diffraction data was recorded in the  $2\theta=5-60^\circ$  range with an angular step size of  $0.03^\circ$  and a counting time of 1 s per step.

Ar sorption at  $-196^\circ\text{C}$  was undertaken in a Micromeritics 3Flex instrument. Prior to the measurement, the samples were evacuated at  $90^\circ\text{C}$  for 48 h. Mercury intrusion porosimetry was conducted with a Micromeritics Autopore IV 9510 following *in situ* sample evacuation and using a contact angle of  $140^\circ$ . Adsorption isotherms of  $\text{N}_2$  and  $\text{CO}_2$  at  $0^\circ\text{C}$  were recorded using a Micromeritics 3Flex Analyzer. Prior to the measurement, the samples were evacuated at  $90^\circ\text{C}$  for 48 h.

Compression tests and tensile tests were performed using a universal testing machine (Zwick Roell) equipped with a 10 kN load cell. Prior to the compression tests, 10 specimens with the dimensions of  $10\times 10\times 5 \text{ mm}^3$  (R $\times$ T $\times$ L) were dried in an oven at  $65^\circ\text{C}$  until constant mass. The testing speed was  $0.5 \text{ mm min}^{-1}$  and a preloading of 100 N was used. For the tensile tests, 10 previously dried specimens with the dimensions  $0.6\times 20\times 60 \text{ mm}^3$  (R $\times$ T $\times$ L) were used with 40 mm initial length between two grips. Due to the sample geometry, we use the term “ultimate tensile stress” instead of “tensile strength”. The preload was set to 10 N and the displacement was measured with a travel sensor at a speed of  $0.35 \text{ mm min}^{-1}$ . Both the compression and tensile tests were conducted at  $20^\circ\text{C}$  and 65% relative humidity.

## Acknowledgements



The project was conducted in the framework of the SNF project “Hierarchical cellulose scaffolds for structural and functional gradient materials” (200021\_184821/1). We thank Thomas Schnider for the wood sample preparation and the technical support. Evgeniya Vorobyeva is acknowledged for mercury porosimetry analyses. K.T. acknowledges financial support from the China Scholarship Council (CSC) (201703270028).

### Author Contributions

#Kunkun Tu and Begoña Puértolas contributed equally to this work. K.T., B.P., J.P.R. and T.K. conceived the study. K.T., B.P., M.V-A., Y.W., J.S. and J.T. performed experiments and analyzed data. K.T., B.P., I.B., J.P.R. and T.K. co-wrote the manuscript. All authors discussed the results and commented on the manuscript.

### Declaration of Interests

The authors declare no competing financial interests.

### References

- 1 Shekhah, O., Liu, J., Fischer, R.A., and Woll, C. (2011). MOF thin films: existing and future applications. *Chem. Soc. Rev.* *40*, 1081-1106.
- 2 Wang, H., Lustig, W.P., and Li, J. (2018). Sensing and capture of toxic and hazardous gases and vapors by metal-organic frameworks. *Chem. Soc. Rev.* *47*, 4729-4756.
- 3 Millward, A.R., and Yaghi, O.M. (2005). Metal-organic frameworks with exceptionally high capacity for storage of carbon dioxide at room temperature. *Journal of the American Chemical Society* *127*, 17998-17999.
- 4 Liu, J., Thallapally, P.K., McGrail, B.P., Brown, D.R., and Liu, J. (2012). Progress in adsorption-based CO<sub>2</sub> capture by metal-organic frameworks. *Chem. Soc. Rev.* *41*, 2308-2322.
- 5 Lee, J., Farha, O.K., Roberts, J., Scheidt, K.A., Nguyen, S.T., and Hupp, J. (2009). Metal-organic framework materials as catalysts. *Chem. Soc. Rev.* *38*, 1450-1459.
- 6 Horcajada, P., Gref, R., Baati, T., Allan, P.K., Maurin, G., Couvreur, P., Ferey, G., Morris, R.E., and Serre, C. (2012). Metal-organic frameworks in biomedicine. *Chem Rev* *112*, 1232-1268.
- 7 Kreno, L.E., Leong, K., Farha, O.K., Allendorf, M., Van Duyne, R.P., and Hupp, J.T. (2012). Metal-organic framework materials as chemical sensors. *Chem Rev* *112*, 1105-1125.
- 8 Han, Y., Qi, P., Feng, X., Li, S., Fu, X., Li, H., Chen, Y., Zhou, J., Li, X., and Wang, B. (2015). In situ growth of MOFs on the surface of Si nanoparticles for highly efficient lithium storage: Si@MOF nanocomposites as anode materials for lithium-ion batteries. *ACS Appl. Mater. Interfaces* *7*, 2178-2182.
- 9 Denny Jr, M.S., Moreton, J.C., Benz, L., and Cohen, S.M. (2016). Metal-organic frameworks for membrane-based separations. *Nat. Rev. Mater.* *1*, 16078.
- 10 Chen, Y., Zhang, S., Cao, S., Li, S., Chen, F., Yuan, S., Xu, C., Zhou, J., Feng, X., Ma, X., and Wang, B. (2017). Roll-to-Roll Production of Metal-Organic Framework Coatings for Particulate Matter Removal. *Adv. Mater.* *29*, 1606221.

- 11 Yang, Q., Zhang, M., Song, S., and Yang, B. (2017). Surface modification of PCC filled cellulose paper by MOF-5 ( $Zn_3(BDC)_2$ ) metal–organic frameworks for use as soft gas adsorption composite materials. *Cellulose* *24*, 3051-3060.
- 12 Rubin, H.N., Neufeld, B.H., and Reynolds, M.M. (2018). Surface-Anchored Metal-Organic Framework-Cotton Material for Tunable Antibacterial Copper Delivery. *ACS Appl. Mater. Interfaces* *10*, 15189-15199.
- 13 Abdelhameed, R.M., Abdel-Gawad, H., Elshahat, M., and Emam, H.E. (2016). Cu–BTC@cotton composite: design and removal of ethion insecticide from water. *RSC Adv.* *6*, 42324-42333.
- 14 da Silva Pinto, M., Sierra-Avila, C.A., and Hinestroza, J.P. (2012). In situ synthesis of a Cu-BTC metal–organic framework (MOF 199) onto cellulosic fibrous substrates: cotton. *Cellulose* *19*, 1771-1779.
- 15 Küsgens, P., Siegle, S., and Kaskel, S. (2009). Crystal Growth of the Metal-Organic Framework  $Cu_3(BTC)_2$  on the Surface of Pulp Fibers. *Adv. Eng. Mater.* *11*, 93-95.
- 16 Duan, C., Meng, J., Wang, X., Meng, X., Sun, X., Xu, Y., Zhao, W., and Ni, Y. (2018). Synthesis of novel cellulose- based antibacterial composites of Ag nanoparticles@ metal-organic frameworks@ carboxymethylated fibers. *Carbohydr. Polym.* *193*, 82-88.
- 17 Ma, K., Islamoglu, T., Chen, Z., Li, P., Wasson, M.C., Chen, Y., Wang, Y., Peterson, G.W., Xin, J.H., and Farha, O.K. (2019). Scalable and Template-Free Aqueous Synthesis of Zirconium-Based Metal-Organic Framework Coating on Textile Fiber. *Journal of the American Chemical Society* *141*, 15626-15633.
- 18 Zhang, Y., Yuan, S., Feng, X., Li, H., Zhou, J., and Wang, B. (2016). Preparation of Nanofibrous Metal-Organic Framework Filters for Efficient Air Pollution Control. *Journal of the American Chemical Society* *138*, 5785-5788.
- 19 Centrone, A., Yang, Y., Speakman, S., Bromberg, L., Rutledge, G.C., and Hatton, T.A. (2010). Growth of metal– organic frameworks on polymer surfaces. *Journal of the American Chemical Society* *132*, 15687-15691.
- 20 Lu, L., Hu, C., Zhu, Y., Zhang, H., Li, R., and Xing, Y. (2018). Multi-functional finishing of cotton fabrics by water-based layer-by-layer assembly of metal–organic framework. *Cellulose* *25*, 4223.
- 21 Marti, A.M., Wickramanayake, W., Dahe, G., Sekizkardes, A., Bank, T.L., Hopkinson, D.P., and Venna, S.R. (2017). Continuous Flow Processing of ZIF-8 Membranes on Polymeric Porous Hollow Fiber Supports for CO<sub>2</sub> Capture. *ACS Appl. Mater. Interfaces* *9*, 5678-5682.
- 22 Mitchell, S., Michels, N.L., and Pérez-Ramírez, J. (2013). From powder to technical body: the undervalued science of catalyst scale up. *Chem. Soc. Rev.* *42*, 6094-6112.
- 23 Ma, S., Zhang, M., Nie, J., Tan, J., Song, S., and Luo, Y. (2019). Lightweight and porous cellulose-based foams with high loadings of zeolitic imidazolate frameworks-8 for adsorption applications. *Carbohydr. Polym.* *208*, 328-335.
- 24 Zhu, L., Zong, L., Wu, X., Li, M., Wang, H., You, J., and Li, C. (2018). Shapeable Fibrous Aerogels of Metal-Organic-Frameworks Templated with Nanocellulose for Rapid and Large-Capacity Adsorption. *ACS Nano* *12*, 4462-4468.
- 25 Sabetghadam, A., Seoane, B., Keskin, D., Duim, N., Rodenas, T., Shahid, S., Sorribas, S., Le Guillouzer, C., Clet, G., Tellez, C., et al. (2016). Metal Organic Framework Crystals in Mixed-Matrix Membranes: Impact of the Filler Morphology on the Gas Separation Performance. *Adv. Funct. Mater.* *26*, 3154-3163.

- 26 Su, P., Li, W., Zhang, C., Meng, Q., Shen, C., and Zhang, G. (2015). Metal based gels as versatile precursors to synthesize stiff and integrated MOF/polymer composite membranes. *J. Mater. Chem. A* *3*, 20345-20351.
- 27 Ojuva, A., Järveläinen, M., Bauer, M., Keskinen, L., Valkonen, M., Akhtar, F., Levänen, E., and Bergström, L. (2015). Mechanical performance and CO<sub>2</sub> uptake of ion-exchanged zeolite A structured by freeze-casting. *J. Eur. Ceram. Soc.* *35*, 2607-2618.
- 28 Moosavi, S.M., Boyd, P.G., Sarkisov, L., and Smit, B. (2018). Improving the Mechanical Stability of Metal-Organic Frameworks Using Chemical Caryatids. *ACS Cent. Sci.* *4*, 832-839.
- 29 Ma, S., Zhang, M., Nie, J., Tan, J., Yang, B., and Song, S. (2019). Design of double-component metal-organic framework air filters with PM<sub>2.5</sub> capture, gas adsorption and antibacterial capacities. *Carbohydr. Polym.* *203*, 415-422.
- 30 Li, W., Meng, Q., Zhang, C., and Zhang, G.J.C.A.E.J. (2015). Metal-organic framework/PVDF composite membranes with high H<sub>2</sub> permselectivity synthesized by ammoniation. *Chem.: Eur. J.* *21*, 7224-7230.
- 31 Zhu, H., Yang, X., Cranston, E.D., and Zhu, S. (2016). Flexible and Porous Nanocellulose Aerogels with High Loadings of Metal-Organic-Framework Particles for Separations Applications. *Adv. Mater.* *28*, 7652-7657.
- 32 Qian, L., Lei, D., Duan, X., Zhang, S., Song, W., Hou, C., and Tang, R. (2018). Design and preparation of metal-organic framework papers with enhanced mechanical properties and good antibacterial capacity. *Carbohydr. Polym.* *192*, 44-51.
- 33 Li, W., Yang, Z., Zhang, G., Fan, Z., Meng, Q., Shen, C., and Gao, C. (2014). Stiff metal-organic framework-polyacrylonitrile hollow fiber composite membranes with high gas permeability. *J. Mater. Chem. A* *2*, 2110-2118.
- 34 Zhang, Y., Feng, X., Yuan, S., Zhou, J., and Wang, B. (2016). Challenges and recent advances in MOF-polymer composite membranes for gas separation. *Inorg. Chem. Front.* *3*, 896-909.
- 35 Loh, Q.L., and Choong, C. (2013). Three-dimensional scaffolds for tissue engineering applications: role of porosity and pore size. *Tissue Eng. Part B Rev.* *19*, 485-502.
- 36 Berglund, L.A., and Burgert, I. (2018). Bioinspired Wood Nanotechnology for Functional Materials. *Adv. Mater.* *30*, 1704285.
- 37 Li, Y., Vasileva, E., Sychugov, I., Popov, S., and Berglund, L. (2018). Optically Transparent Wood: Recent Progress, Opportunities, and Challenges. *Adv. Opt. Mater.* *6*, 1800059.
- 38 Guan, H., Cheng, Z., and Wang, X. (2018). Highly Compressible Wood Sponges with a Spring-like Lamellar Structure as Effective and Reusable Oil Absorbents. *ACS Nano* *12*, 10365-10373.
- 39 Fu, Q., Ansari, F., Zhou, Q., and Berglund, L.A. (2018). Wood Nanotechnology for Strong, Mesoporous, and Hydrophobic Biocomposites for Selective Separation of Oil/Water Mixtures. *ACS Nano* *12*, 2222-2230.
- 40 Zhu, M., Li, Y., Chen, F., Zhu, X., Dai, J., Li, Y., Yang, Z., Yan, X., Song, J., Wang, Y., et al. (2018). Plasmonic Wood for High-Efficiency Solar Steam Generation. *Adv. Energy Mater.* *8*, 1701028.
- 41 Frey, M., Biffi, G., Adobes-Vidal, M., Zirkelbach, M., Wang, Y., Tu, K., Hirt, A.M., Masania, K., Burgert, I., and Keplinger, T. (2019). Tunable Wood by Reversible Interlocking and Bioinspired Mechanical Gradients. *Adv. Sci.* *6*, 1802190.

- 42 Keplinger, T., Cabane, E., Berg, J.K., Segmehl, J.S., Bock, P., and Burgert, I. (2016). Smart Hierarchical Bio-Based Materials by Formation of Stimuli-Responsive Hydrogels inside the Microporous Structure of Wood. *Adv. Mater. Interfaces* 3, 1600233.
- 43 Merk, V., Chanana, M., Gierlinger, N., Hirt, A.M., and Burgert, I. (2014). Hybrid wood materials with magnetic anisotropy dictated by the hierarchical cell structure. *ACS Appl. Mater. Interfaces* 6, 9760-9767.
- 44 Wan, J., Song, J., Yang, Z., Kirsch, D., Jia, C., Xu, R., Dai, J., Zhu, M., Xu, L., Chen, C., et al. (2017). Highly Anisotropic Conductors. *Adv. Mater.* 29.
- 45 Lv, S., Fu, F., Wang, S., Huang, J., and Hu, L. (2015). Novel wood-based all-solid-state flexible supercapacitors fabricated with a natural porous wood slice and polypyrrole. *RSC Adv.* 5, 2813-2818.
- 46 Guo, R., Cai, X., Liu, H., Yang, Z., Meng, Y., Chen, F., Li, Y., and Wang, B. (2019). In Situ Growth of Metal-Organic Frameworks in Three-Dimensional Aligned Lumen Arrays of Wood for Rapid and Highly Efficient Organic Pollutant Removal. *Environ. Sci. Technol.* 53, 2705-2712.
- 47 Kim, J.S., Awano, T., Yoshinaga, A., and Takabe, K. (2012). Ultrastructure of the innermost surface of differentiating normal and compression wood tracheids as revealed by field emission scanning electron microscopy. *Planta* 235, 1209-1219.
- 48 Ding, S., Liu, Y., Zeng, Y., Himmel, M.E., Baker, J.O., and Bayer, E.A.J.S. (2012). How does plant cell wall nanoscale architecture correlate with enzymatic digestibility? *Science* 338, 1055-1060.
- 49 Nadar, S.S., and Rathod, V.K. (2017). Facile synthesis of glucoamylase embedded metal-organic frameworks (glucoamylase-MOF) with enhanced stability. *Int. J. Biol. Macromol.* 95, 511-519.
- 50 Kim, M.L., Otal, E.H., and Hinstroza, J.P. (2019). Cellulose meets reticular chemistry: interactions between cellulosic substrates and metal-organic frameworks. *Cellulose* 26, 123-137.
- 51 Samokhvalov, A. (2017). Adsorption on Mesoporous Metal-Organic Frameworks in Solution for Clean Energy, Environment and Healthcare (CRC Press).
- 52 Tranchemontagne, D.J., Hunt, J.R., and Yaghi, O.M. (2008). Room temperature synthesis of metal-organic frameworks: MOF-5, MOF-74, MOF-177, MOF-199, and IRMOF-0. *Tetrahedron* 64, 8553-8557.

## **Supplementary Information**

### **1. Experimental section**

#### **Preparation of carboxymethylated wood (CM wood)**

Native beech was immersed in a 1 M sodium chloroacetate and 15% w/v NaOH solution for 1 h. The resulting CM beech was thoroughly washed with deionized water for 24 h in order to remove the residual reactants.

#### **Preparation of ZIF-8/CM beech composite**

The CM beech samples were vacuumed for 1 h prior to the vacuum impregnation with a  $\text{Zn}(\text{NO}_3)_2$  solution, which was prepared by dissolving  $\text{Zn}(\text{NO}_3)_2 \cdot 6\text{H}_2\text{O}$  (2.4 g, 0.002 mol) in methanol (20 g) and deionized water (3 g). The impregnation time was 2 h to ensure a sufficient ion-exchange between Zn and Na ions at the surface of the lumen. A 2-MeIm solution, containing 13.2 g (0.04 mol) of MeIm in methanol (20 g) and deionized water (3 g) was subsequently added to the above solution. Stirring at room temperature for 24 h led to the ZIF-8/CM beech composite. The resulting material was then rinsed three times with 50 ml of methanol for 5 min to remove the unreacted precursors, followed by drying in the vacuum-oven at 103°C for 48 h.

#### **Synthesis of ZIF-8**

For the synthesis of ZIF-8, a solution of 2.4 g of  $\text{Zn}(\text{NO}_3)_2 \cdot 6\text{H}_2\text{O}$  in 20 g of methanol and 3 g of deionized water and a second a solution containing 13.2 g of 2-MeIm in the same solvent mixture were prepared. Both solutions were mixed and then stirred at room temperature for 24 h. The obtained solid was collected by centrifugation and thoroughly washed with methanol (3 times). The product was subsequently dried under vacuum overnight at 103°C. By adding 0.5 g of ZIF-8 powders into 50 ml of methanol, a 1% w/v ZIF-8 solution was formed.

#### **Synthesis of MOF-199**

860 mg of  $\text{Cu}(\text{OAc})_2$  were dissolved in a 12 ml solvent solution of DMF:ethanol:water (1:1:1). 500 mg of 1,3,5-benzenetricarboxylic acid were subsequently dissolved in 12 ml of the same solvent mixture. Both solutions were mixed and then stirred vigorously at room temperature for 24 h. The obtained solid was collected by centrifugation and thoroughly washed (3 times) with 30 ml of DMF, followed by drying under vacuum overnight at  $103^\circ\text{C}$ .

### **Preparation of ZIF-8/beechn by vacuum impregnation method**

Pretreated beech wood samples were vacuumed for 1 h before adding the 1% w/v ZIF-8 solution. The vacuum impregnation was sustained 24 h, after which the resulting ZIF-8/beechn composite was dried in the vacuum-oven at  $103^\circ\text{C}$  for 48 h.

### **Preparation of ZIF-8/beechn by filtration method**

The filtration method is adapted from a protocol reported by Sun *et al.*<sup>1</sup> In short, a beech wood cube was placed with its cross section facing up into a suction filter. 10 ml of 1% w/v ZIF-8 solution were then slowly poured into the filter and soaked through by vacuum. The procedure was repeated 3 times followed by drying of the sample in the vacuum-oven at  $103^\circ\text{C}$  for 48 h.

### **Materials characterization**

Zeta potential analysis was conducted using a SurPASS Electrokinetic Analyzer (Anton Paar). Tangential beech samples were cut into dimensions of  $2 \times 10 \times 20 \text{ mm}^3$  (R×T×L) and attached to an adjustable gap cell (gap height was adjusted to  $100 \mu\text{m} \pm 20 \mu\text{m}$ ) by double-sided adhesive tape. Prior to the measurements, native wood was conditioned by immersion in deionized water, and pretreated wood as well as CM wood were conditioned by immersion into a NaOH solution (pH 9) overnight to avoid swelling of the wood during the measurement. Measurements were carried out at 400 mbar in a 0.001 M KCl electrolyte solution at pH  $5.7 \pm 0.1$  (native wood) and pH 9 (pretreated wood and CM wood). The mean value and standard deviation of the  $\zeta$  potential for the native wood, pretreated wood and CM wood were obtained from eight independent ramps measured for two samples each.

Atomic force microscopy (AFM) images of native and pretreated beech wood were acquired in air and in solution using a NanoWizard 4 microscope (JPK Instruments AG - Bruker Nano GmbH). The beech cubes were glued to AFM sample mounting disks using cementit universal adhesive (Merz+Benteli ag) with the tangential section oriented parallel to the disk surface. The cube surface was then polished with a microtome equipped with a steel knife (RM2255, Leica) under wet conditions. Measurements in air were performed under controlled climatic conditions (65% R.H., 20°C) in alternating contact mode (AC mode), using rectangular-shaped silicon cantilevers (NCHR, Nano World) with a resonant frequency of 320 kHz and 42 N m<sup>-1</sup> nominal spring constant. The images were obtained at a line scan rate of 0.4 Hz and a resolution of 512×512 pixels. Topographical investigations in solution were performed on cubes submerged in 5 ml of deionized water in contact mode (CM mode) using rectangular-shaped silicon cantilevers (CONT, Nano World) with a resonant frequency of 13 kHz and 0.2 N m<sup>-1</sup> nominal spring constant. The images were obtained at line scan rates of 0.1-0.4 Hz, a setpoint of 0.5-2.5 nN and a resolution of 512×512 pixels. All images were first analyzed with the JPK image processing software (JPK Instruments AG), where a first order polynomial fit correction was applied to each scan line to correct large background height changes, and then plotted using Gwyddion 2.44.

## 2. Results section

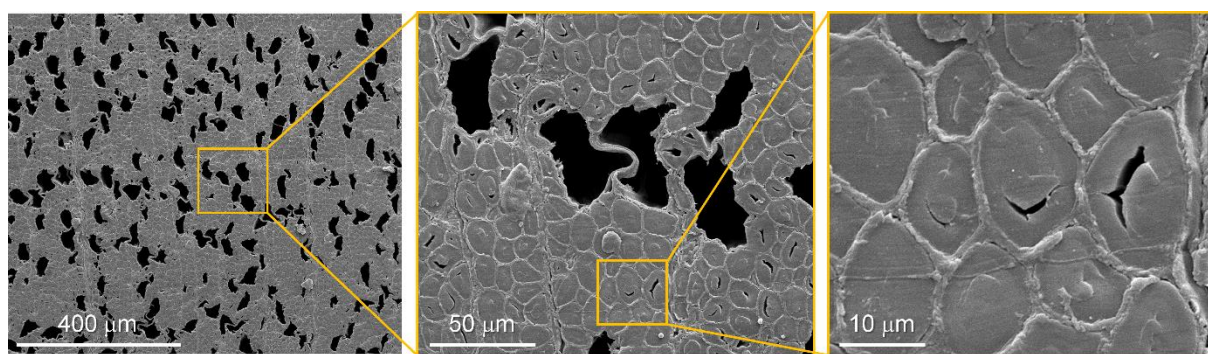


**Figure S1.** Cross-sectional SEM images at different magnification of beech after the NaOH pretreatment followed by a drying process at 103°C under vacuum.

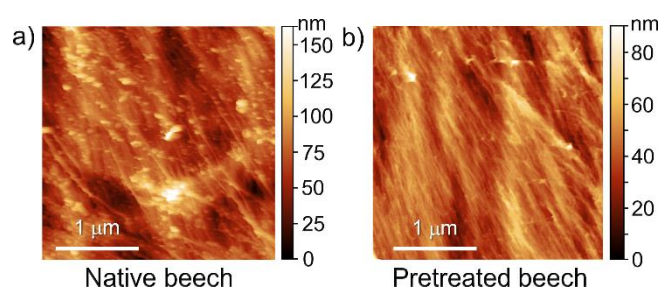


**Figure S2.** AFM images of a) native beech and b) pretreated beech tested under *in situ* contact mode in wet state.



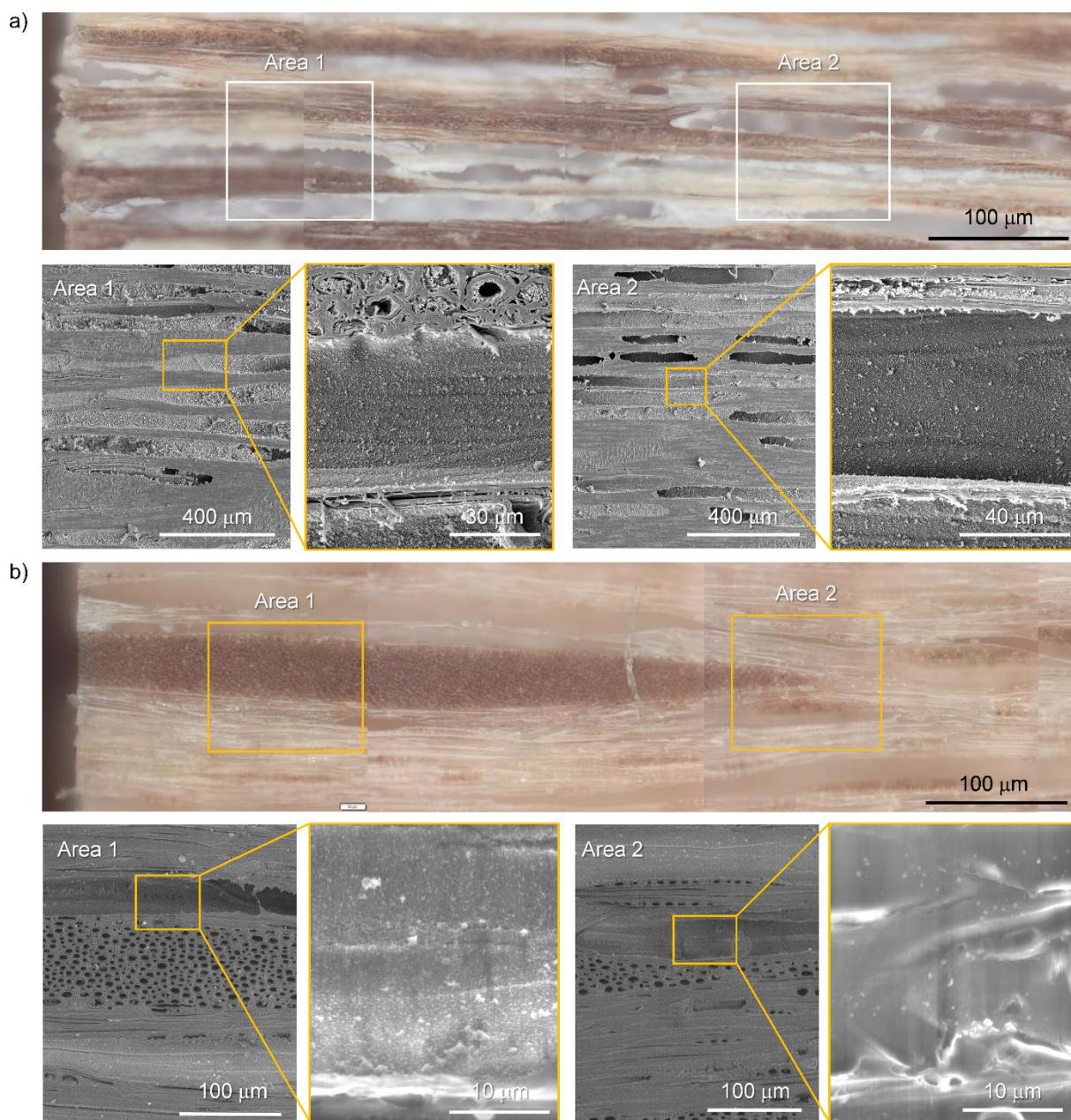


**Figure S3.** Light microscope and SEM images of ZIF-8/beechn composites a) with and b) without NaOH pretreatment.



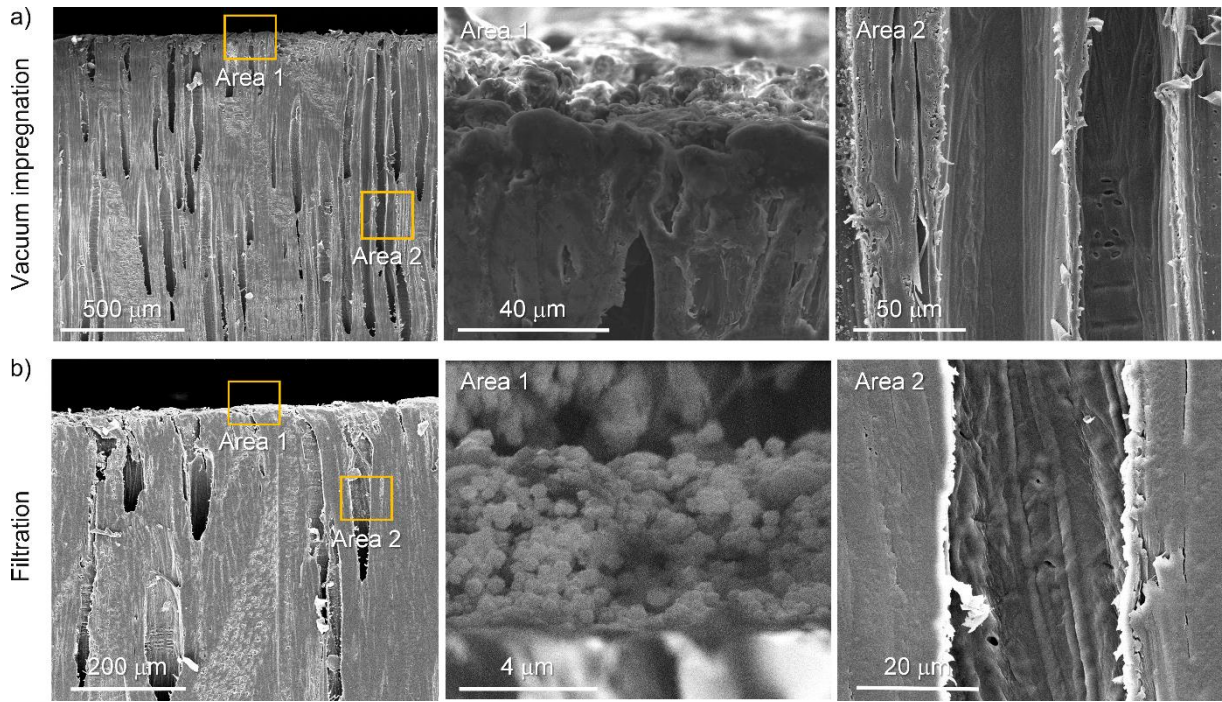


**Figure S4.** SEM images of the ZIF-8/beechn composites fabricated by a) vacuum impregnation and b) filtration methods.

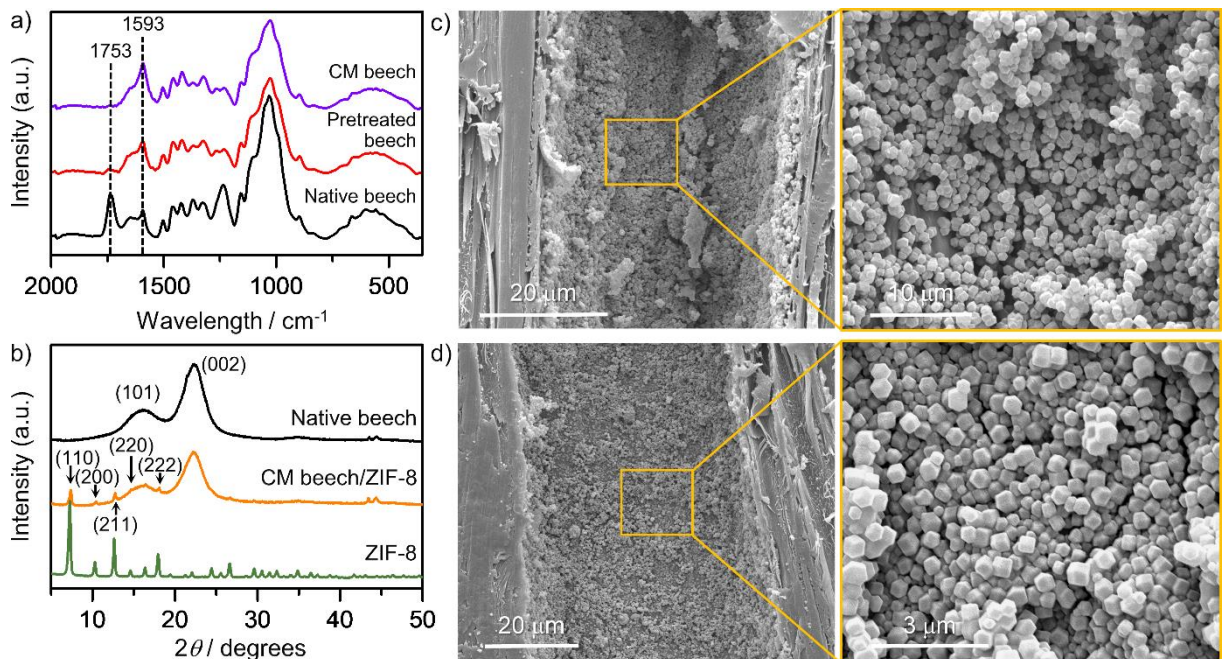


**Figure S5.** a) FTIR spectra of CM beech, pretreated beech and native beech. b) XRD patterns of native beech, ZIF-8/CM beech and pure ZIF-8. c) SEM images of ZIF-8/CM beech composite. d) SEM images of ZIF-8/beechn composite.

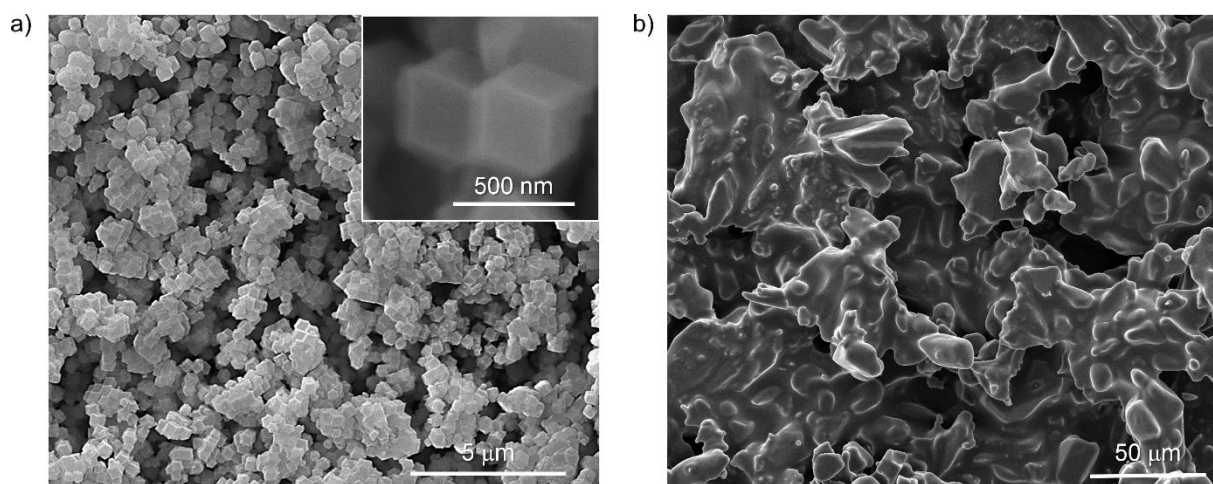


**Figure S6.** SEM images of pure ZIF-8 a) with and b) without washing with methanol after the synthesis process.

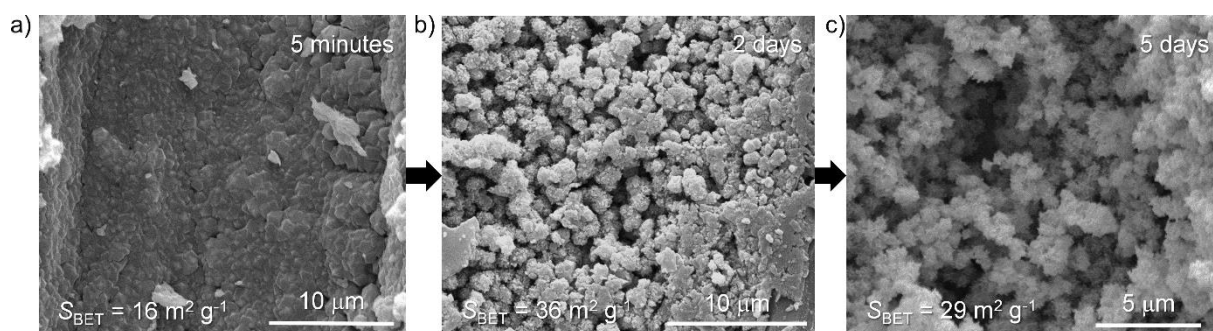


**Figure S7.** SEM images and surface areas of the ZIF-8/beech composites washed with water during a) 5 minutes, b) 2 days and c) 5 days.

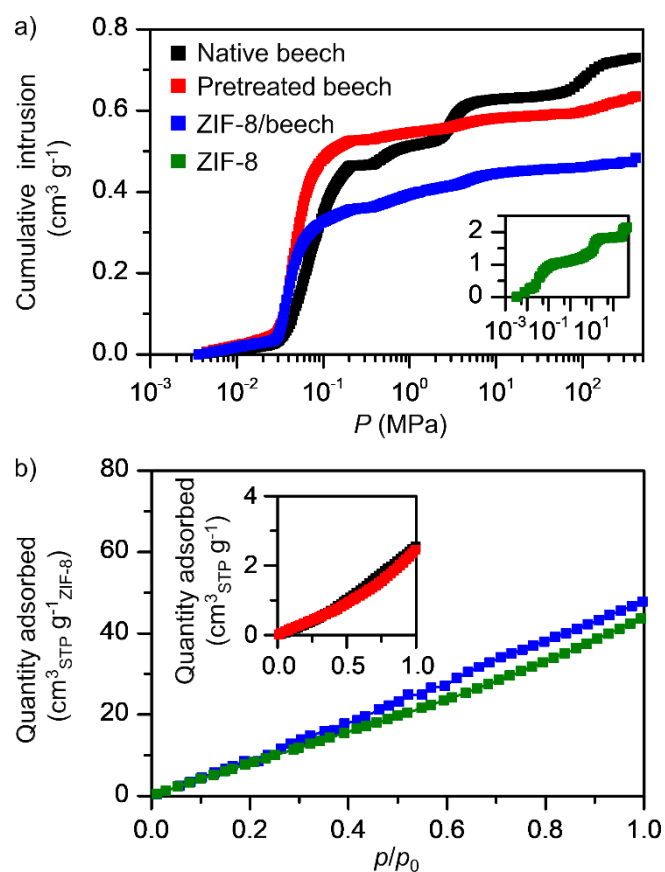


**Figure S8** a) Mercury intrusion of native beech, pretreated beech and ZIF-8/beech composite. The inset represents the mercury intrusion of pure ZIF-8. b) CO<sub>2</sub> adsorption isotherms of ZIF-8/beech composite and pure ZIF-8 expressed per gram of ZIF-8. The inset corresponds to the adsorption isotherms of native beech and pretreated beech expressed per gram of sample.

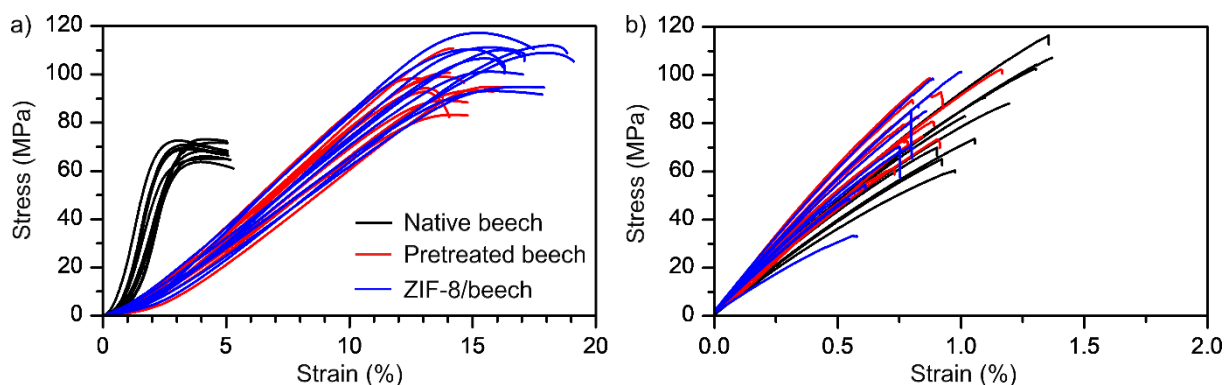


**Figure S9.** a) Compressive and b) tensile stress-strain curves of native beech, pretreated beech and ZIF-8/beech composite.



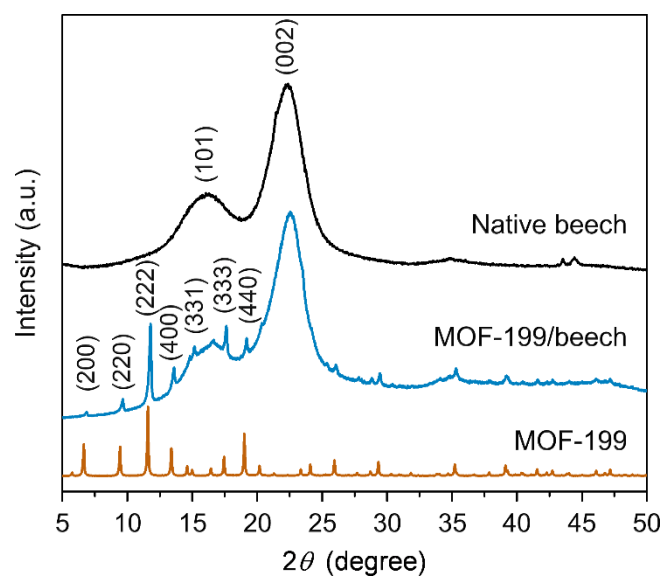


**Figure S10.** XRD patterns of native beech, MOF-199/beech composite and pure MOF-199.

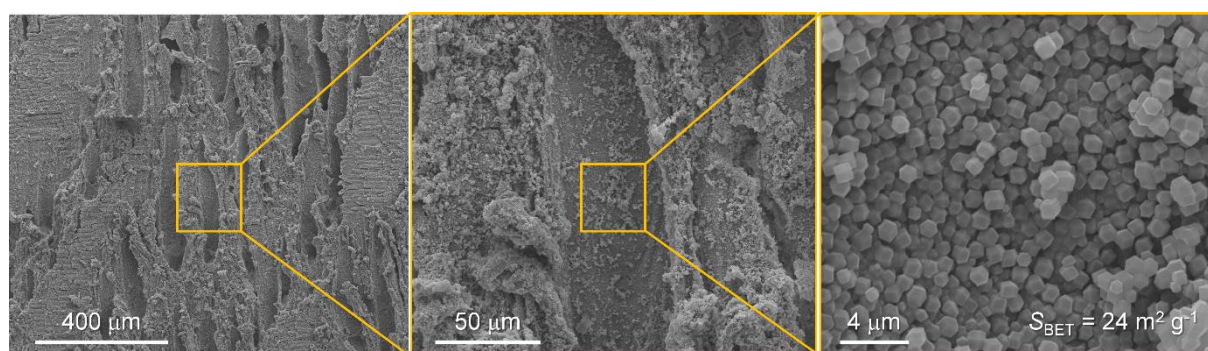


**Figure S11.** SEM images of ZIF-8/beech (tangential cut sample) at different magnification.

**Table S1.** Zeta potential of native beech, pretreated beech and CM beech.

Sample	Zeta potential [mV]
Native beech	-12.05±1.87
Pretreated beech	-38.44±1.99
CM beech	-64.24±1.29

**Table S2.** Porous properties of ZIF-8/beechn composites prepared with different time and synthesis method.

Sample	$S_{\text{BET}}$ [m <sup>2</sup> g <sup>-1</sup> ] <sup>a)</sup>	$S_{\text{meso}}$ [m <sup>2</sup> g <sup>-1</sup> ] <sup>b)</sup>	$V_{\text{micro}}$ [cm <sup>3</sup> g <sup>-1</sup> ] <sup>c)</sup>	$V_{\text{pore}}$ [cm <sup>3</sup> g <sup>-1</sup> ] <sup>c)</sup>
ZIF-8/beechn (1 h synthesis)	16	3	0.006	0.01
ZIF-8/beechn (24 h synthesis)	26	4	0.006	0.011
ZIF-8/beechn (48 h synthesis)	39	5.6	0.01	0.016
ZIF-8/beechn (layer-by-layer)	84	14.6	0.02	0.037

<sup>a)</sup> BET method; <sup>b)</sup> *t*-plot method; <sup>c)</sup> Volume adsorbed at  $p/p_0=0.99$ .

**Table S3.** Comparison of the compressive strength of the ZIF-8/beechn composite with other polymer substrates/templates-supported MOFs composites.

Material	Compressive strength [MPa]	Ref.
ZIF-8/Torlon HF	3	2
ZIF-8/PES HF	0.01	3
UiO-66/SA HF	0.44	4
Cu <sub>3</sub> (BTC) <sub>2</sub> -PAN HF	1	5
ZIF-8/CNF filter	0.5	6
ZIF-8 cellulose aerogel	6	7
ZIF-8 cellulose foam	1.3	8
HKUST-1 CMC foam	10	9
Native beech	68.15±3.59	This work
Pretreated beech	95.65±7.34	This work
ZIF-8/beechn	100±10.05	This work

**Table S4.** Comparison of the ultimate tensile stress of the ZIF-8/beechn composite with other polymer substrates/templates-supported MOFs composites.

Material	Tensile strength [MPa]	Ref.
MOF-808/PAN	1.02	10
UiO-66@GO/SPEEK	66.1	11
Cu <sub>3</sub> (BTC) <sub>2</sub> /PLLA	58.9	12
UiO-66/PVDF	3.6	13
ZIF-8/PLA	2.86	14
ZIF-8@GO/Pebax	18.57	15
ZIF-8/Pebax	18.8	15
ZIF-67/CNF	17.2	16
Native beech	85.691±18.84	This work
Pretreated beech	81.97±12.67	This work
ZIF-8/beechn	73.42±22.29	This work

## References

- 1 Sun, J., Yang, T., Wang, C., and Chen, L. (2018). A flexible transparent one-structure tribo-piezo-pyroelectric hybrid energy generator based on bio-inspired silver nanowires network for biomechanical energy harvesting and physiological monitoring. *Nano Energy* 48, 383-390.
- 2 Marti, A.M., Wickramanayake, W., Dahe, G., Sekizkardes, A., Bank, T.L., Hopkinson, D.P., and Venna, S.R. (2017). Continuous Flow Processing of ZIF-8 Membranes on Polymeric Porous Hollow Fiber Supports for CO<sub>2</sub> Capture. *ACS Appl. Mater. Interfaces* 9, 5678-5682.
- 3 Su, P., Li, W., Zhang, C., Meng, Q., Shen, C., and Zhang, G. (2015). Metal based gels as versatile precursors to synthesize stiff and integrated MOF/polymer composite membranes. *J. Mater. Chem. A* 3, 20345-20351.
- 4 Chen, Y., Chen, F., Zhang, S., Cai, Y., Cao, S., Li, S., ... & Wang, B. (2017). Facile fabrication of multifunctional metal-organic framework hollow tubes to trap pollutants. *J. Am. Chem. Soc.* 139, 16482-16485.
- 5 Li, W., Yang, Z., Zhang, G., Fan, Z., Meng, Q., Shen, C., and Gao, C. (2014). Stiff metal-organic framework-polyacrylonitrile hollow fiber composite membranes with high gas permeability. *J. Mater. Chem. A* 2, 2110-2118.
- 6 Ma, S., Zhang, M., Nie, J., Tan, J., Yang, B., and Song, S.J.C.p. (2019). Design of double-component metal-organic framework air filters with PM<sub>2.5</sub> capture, gas adsorption and antibacterial capacities. 203, 415-422.
- 7 Zhu, L., Zong, L., Wu, X., Li, M., Wang, H., You, J., and Li, C. (2018). Shapeable Fibrous Aerogels of Metal-Organic-Frameworks Templated with Nanocellulose for Rapid and Large-Capacity Adsorption. *ACS Nano* 12, 4462-4468.

- 8 Ma, S., Zhang, M., Nie, J., Tan, J., Song, S., and Luo, Y. (2019). Lightweight and porous cellulose-based foams with high loadings of zeolitic imidazolate frameworks-8 for adsorption applications. *Carbohydr. Polym.* *208*, 328-335.
- 9 Chen, Y., Huang, X., Zhang, S., Li, S., Cao, S., Pei, X., Zhou, J., Feng, X., and Wang, B. (2016). Shaping of Metal-Organic Frameworks: From Fluid to Shaped Bodies and Robust Foams. *Journal of the American Chemical Society* *138*, 10810-10813.
- 10 Efome, J.E. (2018). Development and Characterization of Novel Nanofibrous Metal–Organic Framework Adsorption Membranes for Water Treatment. Doctor Thesis (University of Ottawa).
- 11 Sun, H., Tang, B., and Wu, P. (2017). Rational Design of S-UiO-66@GO Hybrid Nanosheets for Proton Exchange Membranes with Significantly Enhanced Transport Performance. *ACS Appl. Mater. Interfaces* *9*, 26077-26087.
- 12 Kathuria, A., Abiad, M.G., and Auras, R. (2013). Toughening of poly(l-lactic acid) with Cu<sub>3</sub>BTC<sub>2</sub> metal organic framework crystals. *Polymer* *54*, 6979-6986.
- 13 Semino, R., Moreton, J. C., Ramsahye, N. A., Cohen, S. M., & Maurin, G. (2018). Understanding the origins of metal–organic framework/polymer compatibility. *Chem. Sci.* *9*, 315-324.
- 14 Dai, X., Li, X., and Wang, X. (2018). Morphology controlled porous poly(lactic acid)/zeolitic imidazolate framework-8 fibrous membranes with superior PM<sub>2.5</sub> capture capacity. *Chem. Eng. J.* *338*, 82-91.
- 15 Dong, L., Chen, M., Li, J., Shi, D., Dong, W., Li, X., and Bai, Y. (2016). Metal-organic framework-graphene oxide composites: A facile method to highly improve the CO<sub>2</sub> separation performance of mixed matrix membranes. *J. Membrane. Sci.* *520*, 801-811.
- 16 Qian, L., Lei, D., Duan, X., Zhang, S., Song, W., Hou, C., and Tang, R. (2018). Design and preparation of metal-organic framework papers with enhanced mechanical properties and good antibacterial capacity. *Carbohydr. Polym.* *192*, 44-51.



### **4.3 Functionalized wood with tunable tribo-polarity for efficient triboelectric nanogenerators**

*Jianguo Sun<sup>1,2,7</sup>, Kunkun Tu<sup>1,2,7</sup>, Simon Büchele<sup>3</sup>, Sophie Marie Koch<sup>1,2</sup>, Yong Ding<sup>1,2</sup>, Shivaprakash Narve Ramakrishna<sup>4</sup>, Sandro Stucki<sup>1,2</sup>, Hengyu Guo<sup>5</sup>, Changsheng Wu<sup>6</sup>, Tobias Keplinger<sup>1,2</sup>, Javier Pérez-Ramírez<sup>3</sup>, Ingo Burgert<sup>1,2</sup>, Guido Panzarasa<sup>1,2\*</sup>*

<sup>1</sup>Wood Materials Science, Institute for Building Materials, ETH Zürich, 8093 Zürich, Switzerland.

<sup>2</sup>WoodTec Group, Cellulose & Wood Materials, Empa, 8600 Dübendorf, Switzerland.

<sup>3</sup>Institute for Chemical and Bioengineering, Department of Chemistry and Applied Biosciences, ETH Zürich, 8093 Zürich, Switzerland

<sup>4</sup>Surface Science and Technology, Department of Materials, ETH Zürich, 8093 Zürich, Switzerland.

<sup>5</sup>School of physics, Chongqing University, 400054 Chongqing, China

<sup>6</sup>Department of Materials Science and Engineering, Northwestern University, 60208 Illinois, USA

<sup>7</sup>These authors contributed equally

\*Correspondence: [guido.panzarasa@ifb.baug.ethz.ch](mailto:guido.panzarasa@ifb.baug.ethz.ch)

## Abstract

Wood is a state-of-art, renewable and sustainable building material with excellent mechanical properties but negligible triboelectric polarizability. Strategies to improve and rationally tune the triboelectric properties of wood are needed to further its application for mechanical energy harvesting in smart buildings. We found that wood becomes more triboelectrically positive when modified by *in situ* grown zeolitic imidazolate framework-8 (ZIF-8), a metal-organic framework (MOF), and more triboelectrically negative when coated with poly(dimethylsiloxane) (PDMS). A TENG made with two radial-cut wood samples ( $L \times R \times T$ :  $35 \times 20 \times 1 \text{ mm}^3$ ), respectively functionalized with ZIF-8 and PDMS, can generate an open-circuit voltage ( $V_{oc}$ ) of 24.3 V and a short-circuit current ( $I_{sc}$ ) of  $0.32 \mu\text{A}$  upon 50 N, 80 times higher compared to that of native wood. We demonstrate the applicability of our functionalized wood-TENG (FW-TENG) in smart buildings by using it to power household lamps, calculators, and electrochromic windows.

## Keywords:

wood, ZIF-8, PDMS, triboelectric nanogenerator, energy-efficient building materials

## 1 Introduction

The concept of “smart building” has witnessed ever-increasing attention in recent decades. Conventional approaches heavily rely on power supplies with limited lifetime (batteries),<sup>1-3</sup> so that increasing environmental and technological concerns motivated the emergence of triboelectric nanogenerators (TENGs) for the direct conversion of mechanical energy (*e.g.* inhabitants' movements) into useful electricity.<sup>4-7</sup> However, typical TENGs are often made from non-sustainable highly fluorinated polymers, such as poly(tetrafluoroethylene) (PTFE), obtained from non-renewable sources and difficult to recycle, thus inappropriate for large-scale applications in smart homes.<sup>6,8-11</sup>

Wood, one of the most abundant natural biomaterials on Earth, is convenient, renewable, biocompatible, biodegradable, and is used as an excellent construction material since thousands of years.<sup>12</sup> For these reasons, wood would be an ideal material to be implemented in TENGs for large-scale applications in smart homes. Nevertheless, native wood has a negligible triboelectric effect due to its weak polarizability, limiting its ability to generate surface charges. In the triboelectric series, which orders materials from the most electron-donating (tribopositive) to the most electron-attracting (tribonegative), native wood nearly sits in the middle *i.e.* close to

electro-neutrality. This may account for the absence of significant progress in the development of wood-based TENGs so far.<sup>6,13</sup> Pairing materials with opposite tribo-polarities, and increasing surface roughness to facilitate contact, are effective strategies to improve the electrical performance of TENGs.<sup>14-16</sup> In recently proposed examples of wood-based TENGs, the triboelectric output was generated by simply coupling native wood with highly polarizable materials (such as PTFE). In such approach, however, wood itself does not play a role improving the output performance of TENG.<sup>6,17</sup> To promote the use of wood in TENGs, it is thus necessary to develop approaches to increase, and tune, the triboelectric polarizability of wood.

Metal-organic frameworks (MOFs) are porous materials composed of metal ions coordinated by organic ligands. MOFs have been identified as highly promising triboelectric materials thanks to their flexibility regarding composition, size, and functionality.<sup>18-20</sup> In particular, the zeolitic imidazolate framework-8 (ZIF-8), a subclass of MOFs with sodalite topology, has been shown to display positive triboelectric behavior.<sup>18</sup> In addition to its tribopositive behavior, the unique particle geometry and the possibility to tune their size, thus adjusting the nano-roughness of ZIF-8-functionalized triboelectric surfaces, make it a promising candidate for the development of TENGs. However, the challenging processability of its powder form limited the application of ZIF-8 use in TENGs.<sup>21</sup> On the other hand, poly(dimethylsiloxane) (PDMS) is an industrial polymer with excellent electron-accepting properties and good flexibility, making it an almost ideal tribonegative layer. However, there is still a long way for using pure PDMS to satisfy smart building applications, especially because this requires to increase its surface roughness by means of complicated and energy-consuming processes.<sup>22-24</sup>

Surface modification of native wood with ZIF-8 and PDMS allowed to changing its triboelectrical properties, making it more tribopositive (ZIF-8@wood) and more tribonegative (PDMS@wood), thus enhancing the electrical output. However, changes in the surface chemical composition alone cannot be considered the sole responsible for the observed behavior. As a scaffold, wood provides not only increased mechanical strength and toughness, also its natural micro-and nanoscale roughness can influence the triboelectric properties of the composite. The specific roughness manifests differently due to wood's hierarchical structure, and depends both on the chosen wood species and the cutting direction. For this reason, we investigated the effects of different wood species and cutting directions, as well as of different ZIF-8 sizes, on the triboelectric output of the wood composites. The resulting optimized FW-TENG displayed a triboelectric output over 80 times higher than that of a native wood TENG, and could be used to power household devices (from lamps to calculators) as well as to actuate

a miniature electrochromic window, useful to modulate indoor lighting.<sup>25-27</sup> Our study will inform the design of next-generation energy-efficient building materials.

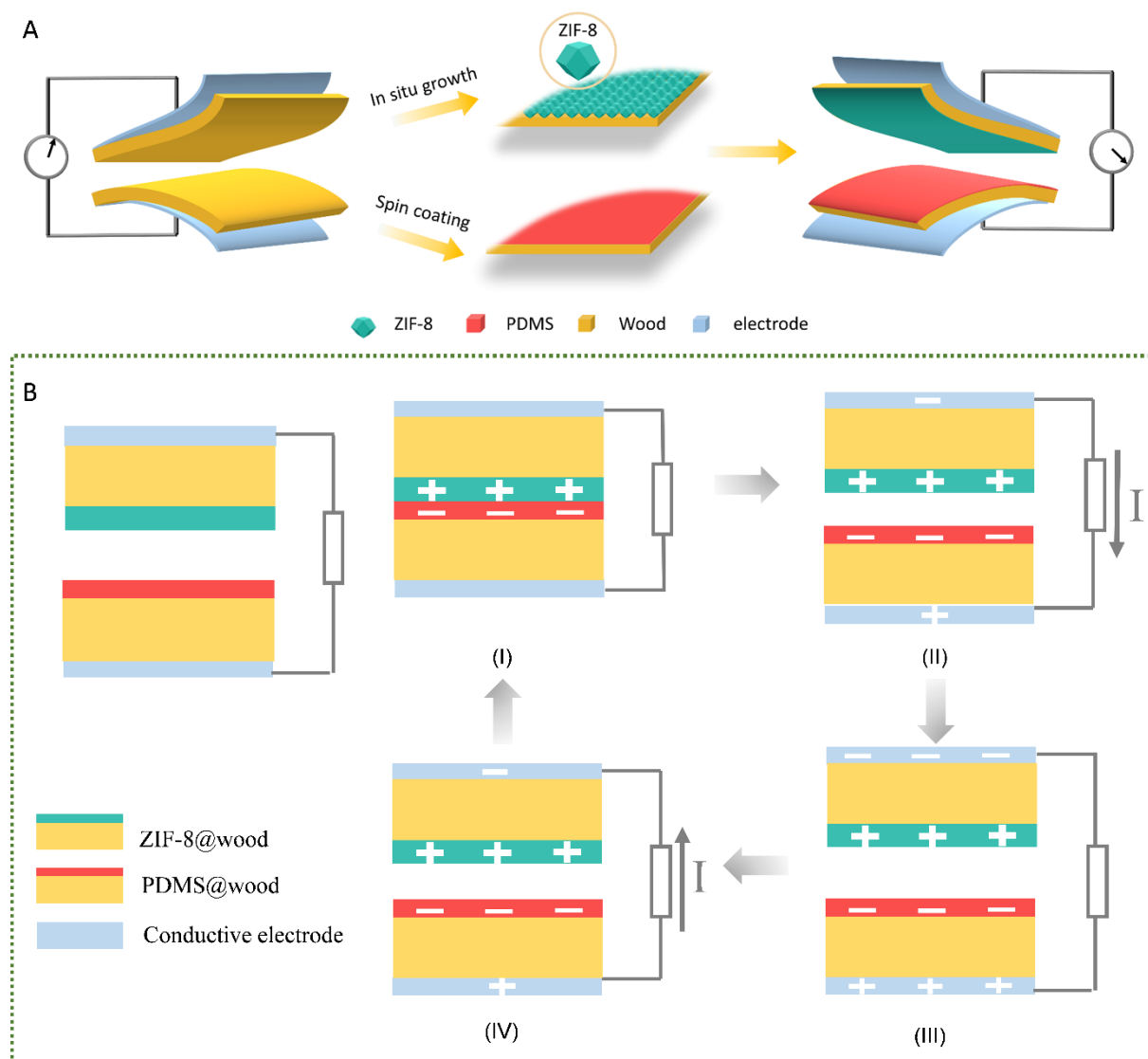


**Figure 1.** Schematic representation of the fabrication and working mechanism of our functionalized wood triboelectric nanogenerator (FW-TENG) (A) Schematic representation of the FW-TENG made with ZIF-8@wood and PDMS@wood. (B) Schematic representation of the triboelectrification process in our FW-TENG.

## 2 Results and Discussion

Our approach for the fabrication of a functionalized wood triboelectric nanogenerator (FW-TENG) is represented schematically in Figure 1A. Two pieces of wood veneer are modified, respectively, with ZIF-8 particles (by *in situ* growth) and with PDMS (by spin-coating and curing). The resulting surface chemical and morphological changes increase the ability of wood to donate (ZIF-8@wood) or acquire (PDMS@wood) electrons during periodic contact-

separation cycles and, consequently, the amount of electricity produced. Metal electrodes are then attached on the backside of each functionalized veneer to collect and transfer the electrostatically induced charges through an external circuit.

The working principle of our FW-TENG is illustrated in Figure 1B, with the coupled effects of contact electrification and electrostatic induction.<sup>2</sup> When the more tribopositive ZIF-8@wood is put in contact with the more tribonegative PDMS@wood, static charges of opposite sign are generated by contact electrification. Electrons transfer from the surface of ZIF-8@wood to the surface of PDMS@wood, resulting in fully balanced, electrostatically paired charges. There is no electron flow in the external circuit at this stage (stage I).<sup>10,28</sup> Once, the two layers are separated, the negative charges on the surface of PDMS@wood cannot be compensated by the ones on the surface of ZIF-8@wood, inducing a potential difference across the top and bottom electrodes. Simultaneously, opposite charges are induced on the electrodes under the action of electrostatic induction. In order to screen this potential difference, the electrostatically induced free charges will be driven to flow between the two conductive electrodes through the external load (stage II). Both the current and voltage outputs are generated during this process until the potentials of the two electrodes reach equilibrium again (stage III). Once the ZIF-8@wood is reverted to approach the PDMS@wood, the potential difference will begin to decrease, driving the charges to flow back in the opposite direction until the original state is attained, resulting in a reversed electrical output (stage IV).<sup>29</sup>

It has already been demonstrated<sup>30 31</sup> that the internal circuit in a TENG is determined by the displacement current (first introduced by Maxwell in 1861, it is not an electric current of moving free charges<sup>32</sup>), while the observed current in the external circuit is the capacitive conduction current. As shown in Figure S1, the internal circuit and external circuit meet at the two electrodes to form a loop. Therefore, the displacement current is the intrinsic physical core of current generation while the capacitive conduction current is the external manifestation of displacement current.<sup>31</sup>

To investigate the effect of wood microstructure on the electrical output performance, three wood species (balsa, spruce, and yew), widely different in terms of cell structure, porosity (from 64% to 16%, Figure S2 and Table S1), and density (from 83 kg m<sup>-3</sup> to 814 kg m<sup>-3</sup>), were tested in the present study. Figure 2A-B and Figure S3 display the scanning electron microscopy (SEM) images of cross-cuts (C) of balsa, spruce, and yew. Balsa wood is a light-weight diffuse-porous hardwood species, mainly composed of vessels, parenchyma cells, and fibers aligned along the longitudinal direction. It is different from spruce and yew, which are both softwoods and have

relatively similar anatomical features. However, on average, yew tracheids have a lower lumen diameter and a higher cell wall thickness than spruce, which is reflected in a much higher density.<sup>33</sup> Different wood species thus have different surface morphologies, which in turn display different microstructures. We also investigated the influence of morphologies originated from different cutting directions. Spruce wood was cut into three planes: cross (C), radial (R), and tangential (T). As shown in Figure 2B-D, these three cuts have different morphologies and microstructures due to the intrinsic anisotropy of wood, resulting in different surface roughness.

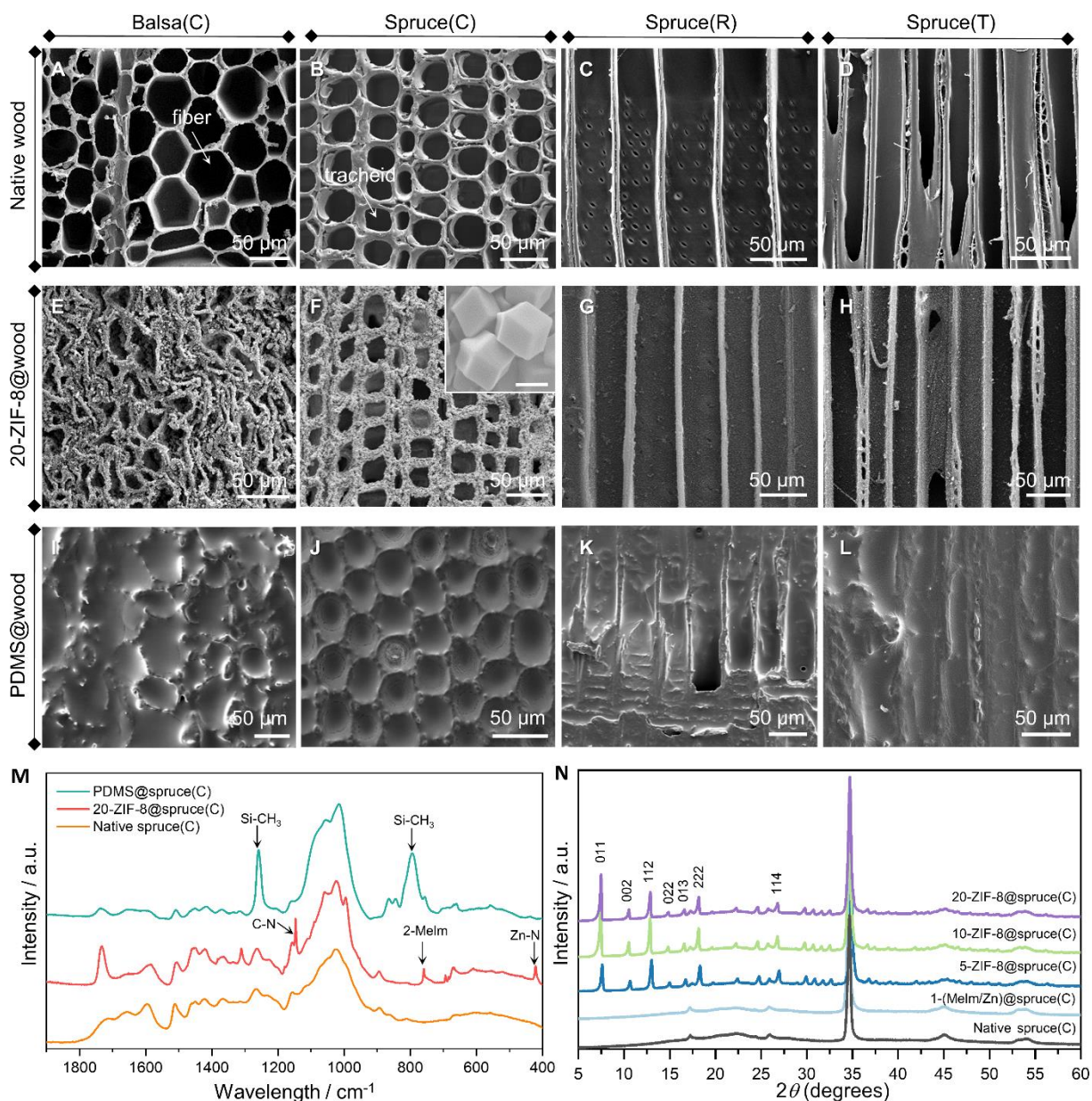


**Figure 2.** Morphological and physico-chemical characterization of native wood, ZIF-8@wood, and PDMS@wood samples (A-F) SEM images of cross-cut balsa (first column) and spruce wood (second column), radial-cut spruce (third column), and tangential-cut spruce (fourth column) (A-D) without functionalization, (E-H) after functionalization with *in situ* grown ZIF-

8 (2-MeIm/Zn<sup>2+</sup> = 20), and (I-L) after functionalization with PDMS. Inset in (F) shows the morphology of ZIF-8 grown on wood (scale bar of e: 500 nm). (M) FT-IR spectra of native spruce(C), 20-ZIF-8@spruce(C), and PDMS@spruce(C), respectively. (N) XRD results for native spruce (C) and ZIF-8@spruce(C) with an increased 2-MeIm/Zn<sup>2+</sup> ratio from 5 to 10, and 20, as well as 1-(MeIm/Zn)@spruce(C), respectively. The spruce samples used here are cross-cut by laser, resulting in an unusual cellulose peak intensity distribution. For more details, Figure S11 shows the XRD spectra of different sections (tangential, radial, and cross-section) of native spruce veneer prepared with different methods (saw cutting, laser cutting).

Nanocrystals of ZIF-8 were then grown on wood using a two-step synthesis process. First, wood was pretreated with an alkaline solution to generate nucleation sites, which promoted a stable attachment of the nanocrystals. Then, ZIF-8 nanocrystals were grown by the stepwise addition of zinc nitrate Zn(NO<sub>3</sub>)<sub>2</sub> and 2-methylimidazole (2-MeIm) solutions. The size of ZIF-8 nanocrystals can be tuned by controlling the ratio between ligand (2-MeIm) and metal ions (zinc cations, Zn<sup>2+</sup>). When the 2-MeIm/Zn<sup>2+</sup> molar ratio was increased from 5 to 20, the average ZIF-8 particle size increased from ~616 nm to ~1008 nm, and the associated particle size distribution broadened. (Figure S4 and Figure S5). The typical morphology of a ZIF-8@wood sample, prepared with a 2-MeIm/Zn<sup>2+</sup> molar ratio of 20 (20-ZIF-8@wood), is shown in Figure 2E-H and Figure S6. As can be seen in Figure 2E, the structure of the analogue 20-ZIF-8@balsa(C) is dramatically affected by the alkaline pretreatment, which partially removes lignin and hemicelluloses, causing the cell walls to wrinkle and resulting in extensive shrinkage after drying (Figure S7).<sup>19</sup> The SEM images of wood samples coated with PDMS are shown in Figure 2I-L and Figure S8. Compared to that of native wood, the surface of PDMS@wood is smoother. In particular, cross-cut wood samples are no longer macroporous, since the PDMS is entirely covering the whole surface as well as the lumina, forming a concave surface. The thickness of the PDMS film coated on different wood species is within 10 μm, much smaller than the thickness of wood (1 mm), as shown in Figure S9. These results show that the modification of wood, both with ZIF-8 and PDMS, introduces relevant morphological changes.

By functionalizing wood with PDMS and ZIF-8, the wood surface's chemical composition was changed as well (Figure 2M,N and Figure S10). The Fourier-transform infrared (FT-IR) spectra of PDMS@spruce(C), 20-ZIF-@spruce(C), and native spruce(C) samples are displayed in Figure 2M. The strongest absorption bands for PDMS@spruce(C) are at 796 cm<sup>-1</sup> (Si-C stretching in Si-CH<sub>3</sub>) and 1258 cm<sup>-1</sup> (deformation of -CH<sub>3</sub> in Si-CH<sub>3</sub>), confirming the presence of PDMS on the surface.<sup>34</sup> On the other hand, the 20-ZIF-8@spruce(C) sample shows bands at



1147  $\text{cm}^{-1}$ , 422  $\text{cm}^{-1}$ , and 759  $\text{cm}^{-1}$ , associated with the stretching of C-N and Zn-N bonds, and the out-of-plane bending of the 2-MeIm ring, which confirms the successful modification of wood with ZIF-8. Both the 5-ZIF-8@spruce(C) and 10-ZIF-8@spruce(C) samples have FT-IR spectra similar to that of the 20-ZIF-8@spruce(C), the only notable exception being 1-ZIF-8@spruce(C) (Figure S10). This difference can be explained by taking into account the associated powder X-ray diffraction (XRD) patterns (Figure 2N). The strong peaks at  $2\theta = 7.48$ ,  $10.54$ ,  $12.88$ ,  $14.80$ ,  $16.58$  and  $18.16^\circ$ , which correspond respectively to planes (011), (002), (112), (022), (013), and (222), indicate the high crystallinity of the 5-, 10- and 20-ZIF-8 samples. However, 1-ZIF-8@spruce(C) shows only an XRD pattern similar to that of native spruce (C), without the typical peaks from ZIF-8 crystals, suggesting that a 2-MeIm/ $\text{Zn}^{2+}$  ratio of 1 does not result in ZIF-8 formation (Figure 2N and Figure S11). The amount of Zn incorporated by each kind of sample was measured by inductively coupled plasma-optical emission spectrometry (ICP-OES) and used to calculate the percentage of MOF loading. Results (Table S2) showed that the 5-, 10- and 20-ZIF-8@spruce(C) composites had similar ZIF-8 contents, respectively 11.0 wt.%, 9.3 wt.%, and 8.8 wt.%, while a zinc-based material of unknown structure was generated with a 2-MeIm/ $\text{Zn}^{2+}$  ratio of 1 (sample 1-(MeIm/Zn)@spruce(C)).

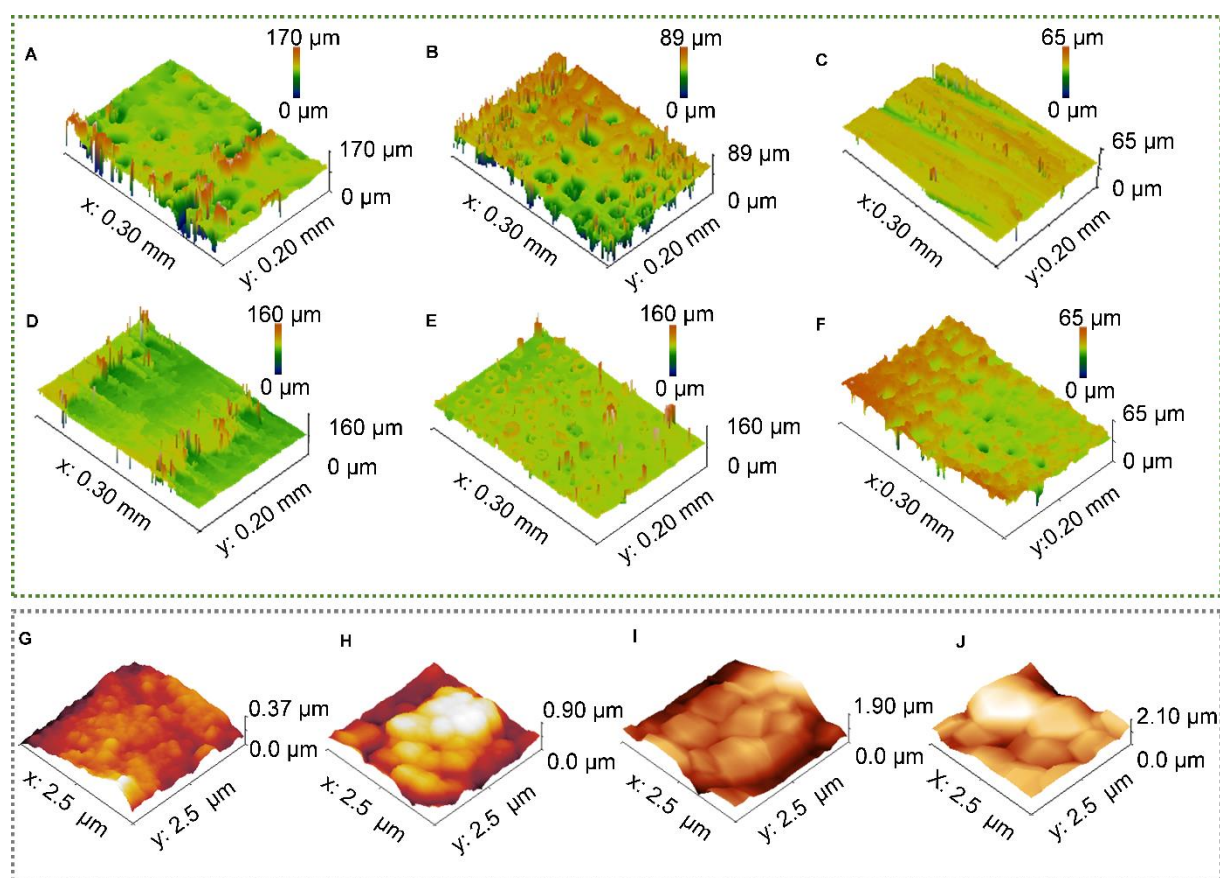


**Figure 3.** Surface roughness of native wood and functionalized wood samples. (A-F) 3D surface profiles obtained by optical profilometry for (A) cross-cut native balsa, (B) cross-cut



native spruce, (C) tangential-cut native spruce veneer, (D) radial-cut native spruce, (E) PDMS@spruce(C), (F) 20-ZIF-8@spruce(C). (G-J) AFM results for 1-(MeIm/Zn)@spruce(C) and ZIF-8@spruce(C) samples. The 2-MeIm/Zn<sup>2+</sup> ratio is increased from 1 to 5, 10, 20, respectively.

Higher surface roughness usually results in an increased effective surface area, thus improving the electrical performance of a TENG.<sup>10,35</sup> However, an excessively rough surface can produce tip-to-tip contacts between the triboelectric materials, causing incomplete contact and consequently decreasing the electrical output.<sup>36</sup> Hence, control of surface roughness is vital for TENGs. Although the real contact area may be proportional to surface roughness, its quantitative analysis remains an open challenge due to the many factors that need to be taken into account (such as applied mechanical load, number of microcontacts, and conductance between the surfaces).<sup>37-38</sup> Therefore, a more empirical approach is conventionally adopted, in which differences in the electrical output are directly related to changes in surface morphology and roughness. Surface roughness can be increased by surface micro/nano-structuration techniques, including photolithography templates, nanoimprint, and physical/chemical etching.<sup>39-41</sup> However, these methods require complex processes and dedicated instrumentation. Here we take advantage of the variety of wood's microstructures to generate unique micro/nano roughness through its functionalization with ZIF-8 nanocrystals and PDMS.

Figure 3A,B, and Figure S12 show 3D surface profiling images of cross-cut native balsa, spruce, and yew, respectively. As shown in Table S3, different wood species, cut with the same directions, lead to different surface roughness. Native balsa(C) has the highest average roughness (Ra) value of 11.9  $\mu\text{m}$ , while native yew(C) the lowest (6.5  $\mu\text{m}$ ). Figure 3C,D show 3D surface profiling images of tangential- and radial-cut native spruce, respectively. Compared to the Ra value of native spruce(C) (11.4  $\mu\text{m}$ ), native spruce(R) and native spruce(T) have much lower Ra values, respectively of 6.3 and 7.6  $\mu\text{m}$  (Table S3). The higher Ra value of cross-cut wood samples may result from their highly porous structure. These different Ra parameters are representative of the inherent roughness of the wood surface, which originates from the specific arrangement of microscale cells. As shown in Figure 3E, Figure S13 and Table S3, the wood surface roughness after coated with PDMS is significantly reduced at the microscale, consistent with SEM results. Modifying the wood scaffold with ZIF-8 reduced by a certain extent the overall microscale roughness (Figure 3F, Figure S14 and Table S3), but at the same time increased the nanoscale surface roughness. This change of nanoscale roughness was investigated by atomic force microscopy (AFM), imaging on the earlywood's cell wall of cross-

cut spruce with a scan size of  $2.5 \mu\text{m} \times 2.5 \mu\text{m}$ . As shown in Figure 3G-J and Table S4, when the 2-Melm/ $\text{Zn}^{2+}$  ratio increased from 5 to 20, the Ra of ZIF-8@wood increased gradually from 169.1 nm to 286.5 nm. When the 2-Melm/ $\text{Zn}^{2+}$  ratio is 1, the Ra of 1-(MeIm/Zn)@spruce(C) has a lowest value of 37.1 nm. Modification with *in situ* grown ZIF-8 can be a valid method to adjust the surface nano-roughness of triboelectric materials. In the following, we show that the modification of wood both with ZIF-8 and with PDMS plays an essential role in enhancing the electrical output of our FW-TENG by improving the surface roughness.

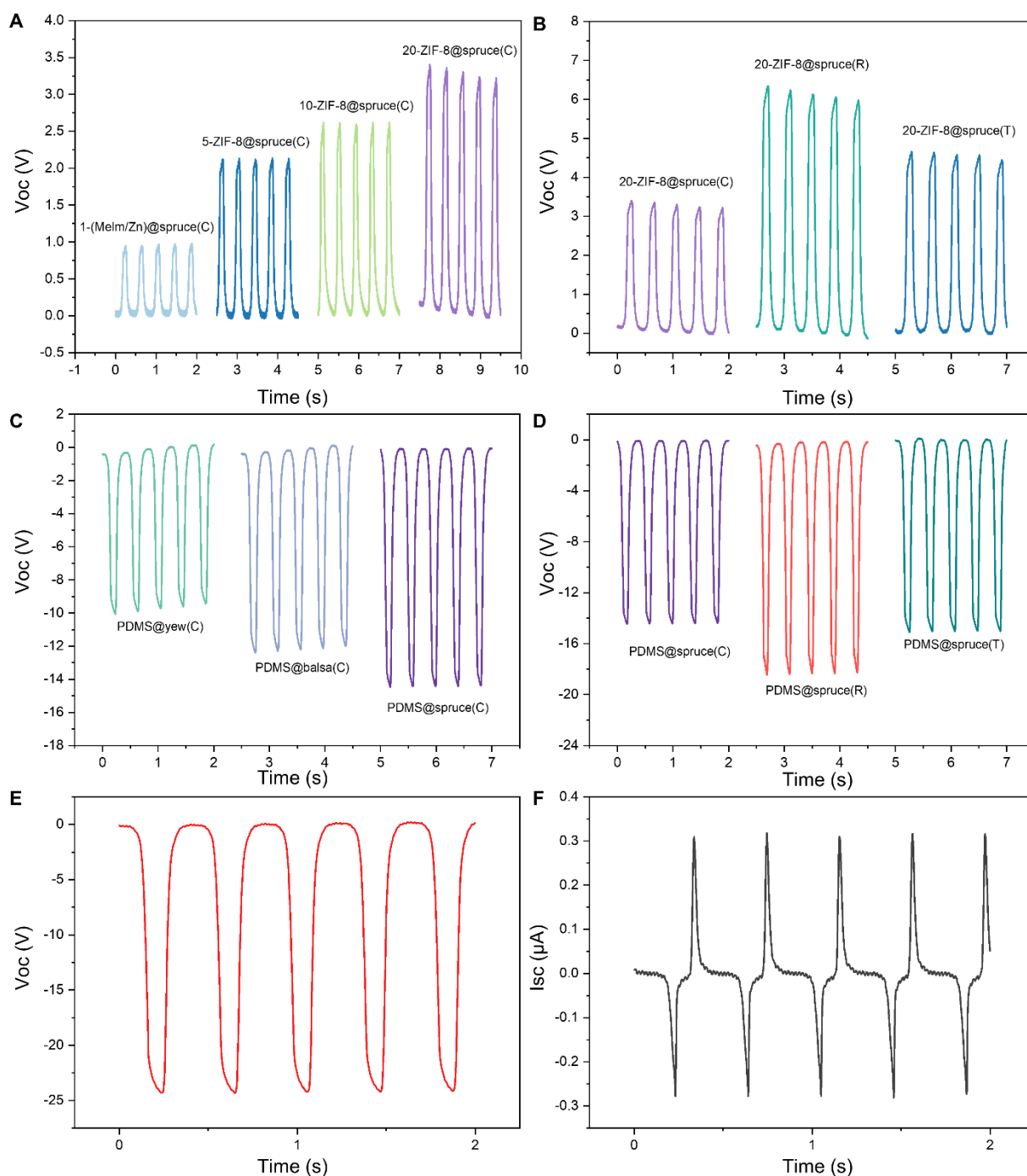


**Figure 4.** Effect of different parameters on the triboelectric performance of FW-TENG. (A-D) Effect of different parameters on the open-circuit voltage of functionalized wood TENGs. All

samples are tested against radial-cut native wood (reference material). (A) ZIF-8@spruce(C) samples: effect of the 2-MeIm/Zn<sup>2+</sup> ratio. In addition, the 1-(MeIm/Zn)@spruce(C), which does not form ZIF-8 shows lowest Voc. (B) ZIF-8@spruce: effect of cutting direction. A constant 2-MeIm/Zn<sup>2+</sup> ratio of 20 is used. (C) PDMS@wood samples: effect of the wood species. (D) PDMS@wood samples: effect of cutting direction. (E) Open-circuit voltage and (F) short-circuit current for an optimized FW-TENG made of 20-ZIF-8@spruce(R) and PDMS@spruce(R).

The triboelectric performance of native and functionalized wood samples was systematically evaluated with a Keithley 6514. The sample to be tested was paired with a piece of radial-cut native spruce as reference material to make a TENG with a simple vertical contact-separation design. The surface area was kept constant (2 cm × 3.5 cm), and the force applied was 50 N. As shown in Figure 4A and Figure S15, the electrical output of ZIF-8@spruce(C) gradually increases for increasing 2-MeIm/Zn<sup>2+</sup> ratios, reaching a maximum open-circuit voltage (Voc) of 3.2 V and short-circuit current (Isc) of 0.037 μA for a 2-MeIm/Zn<sup>2+</sup> ratio of 20. This result may be attributed to the tribopositive nature of ZIF-8 and the gradual increase of nanoscale roughness observed, when the size of ZIF-8 nanocrystals grown onto wood is increased by using higher MeIm/Zn<sup>2+</sup> ratios. To demonstrate the superior properties of *in situ* ZIF-8 growth compared to physical deposition, a 20-ZIF-8@spruce(C) sample was prepared by physical coating and its triboelectrical performance was evaluated. The open-circuit voltage was much lower (Voc = 1.1 V) compared to that of a sample prepared by chemical coating (Voc = 3.2 V). We attribute this decreased performance to the less homogeneous distribution of ZIF-8 nanoparticles and their reduced interaction with the wood scaffold (Figure S16). After selecting the most suitable 2-MeIm/Zn<sup>2+</sup> ratio and composite preparation method, we investigated the effects associated with the wood scaffold, including the choice of wood species and cutting direction. Since balsa wood modified with ZIF-8 shrinks considerably, its electrical output has not been measured. Regarding the electrical output of ZIF-8@yew(C) samples, as shown in Figure S17, 20-ZIF-8@yew(C) tends to generate Voc and Isc values similar to those of 20-ZIF-8@spruce(C). However, yew is less available and more expensive compared to spruce, making spruce a better candidate for large-scale applications. For this reason, ZIF-8 was grown on radial- and tangential-cut spruce to investigate the influence of the cutting directions on the electrical performance of ZIF-8@spruce composites. As shown in Figure 4B and Figure S18, 20-ZIF-8@spruce(R) and 20-ZIF-8@spruce(T) generated a higher electrical output than 20-ZIF-8@spruce(C). This result may be attributed to the highly porous structure of cross-cut wood

scaffolds, with big, deep pores (tracheid lumina) that reduce the effective contact surface areas. The highest Voc and Isc values generated by 20-ZIF-8@spruce(R) are 6.0 V and 0.07  $\mu\text{A}$ , respectively. A control experiment, in which two pieces of native radial-cut spruce were assembled into a TENG, was made to evaluate the impact of ZIF-8 modification on the electrical performance of wood. As shown in Figure S19, this native wood-TENG generated ultra-low Voc and Isc under 50 N, respectively 0.3 V and 0.004  $\mu\text{A}$ , resulting from poor polarizability of wood and the weak triboelectrification effect between two identical materials. It is clear from these results that the functionalization with ZIF-8 significantly increases the electron-donating ability of wood, incrementing the electrical output of about 20 times. Conversely, modification of wood with PDMS gave it a strong electron-accepting behavior. The three wood species (spruce, balsa, yew) were cross-cut and coated with PDMS, and assembled in a TENG against radial native spruce as reference material, all other parameters being the same as discussed for the ZIF-8@wood samples. As shown in Figure 4C and Figure S20, PDMS@spruce(C) performs best while PDMS@yew(C) generates the lowest electrical output. These results may be attributed to the effect of surface roughness, as PDMS@yew(C) has a much smoother surface than PDMS@spruce(C). Spruce was then selected to further investigate the effect of cutting direction. Figure 4D and Figure S21 show that radial-cut spruce wood coated with PDMS generates a maximum Voc and Isc values of 18.5 V and 0.25  $\mu\text{A}$ , respectively. These results indicate that coating PDMS on wood greatly increases the electron-accepting ability of wood, with an increment of the electrical output of over 60 times. The modification with ZIF-8 and PDMS enhances the tribopolarity of wood to opposite directions, allowing widening the spectrum of triboelectric behavior (Figure S22). As shown in Figure 4E,F, an optimized FW-TENG made with a pair of 20-ZIF-8@spruce(R) and PDMS@spruce(R) samples (each with dimensions 2 cm  $\times$  3.5 cm) could generate maximum Voc and Isc of 24.3 V and 0.32  $\mu\text{A}$ , respectively, an output which is over 80 times higher than that of a native wood TENG. The transferred charge density of the FW-TENG is shown in Figure S23, with a peak value of 12  $\mu\text{C m}^{-2}$ .

We wanted to improve the triboelectric properties of wood without losing its compelling merits as a building material, such as mechanical robustness and warm colors, even at the price of a relatively lower electrical performance. For this reason, the thickness of wood used in our work is much higher compared to that of more conventional triboelectric materials.<sup>42,43</sup> This weakens the electrostatic induction effect, reducing the electrical output.

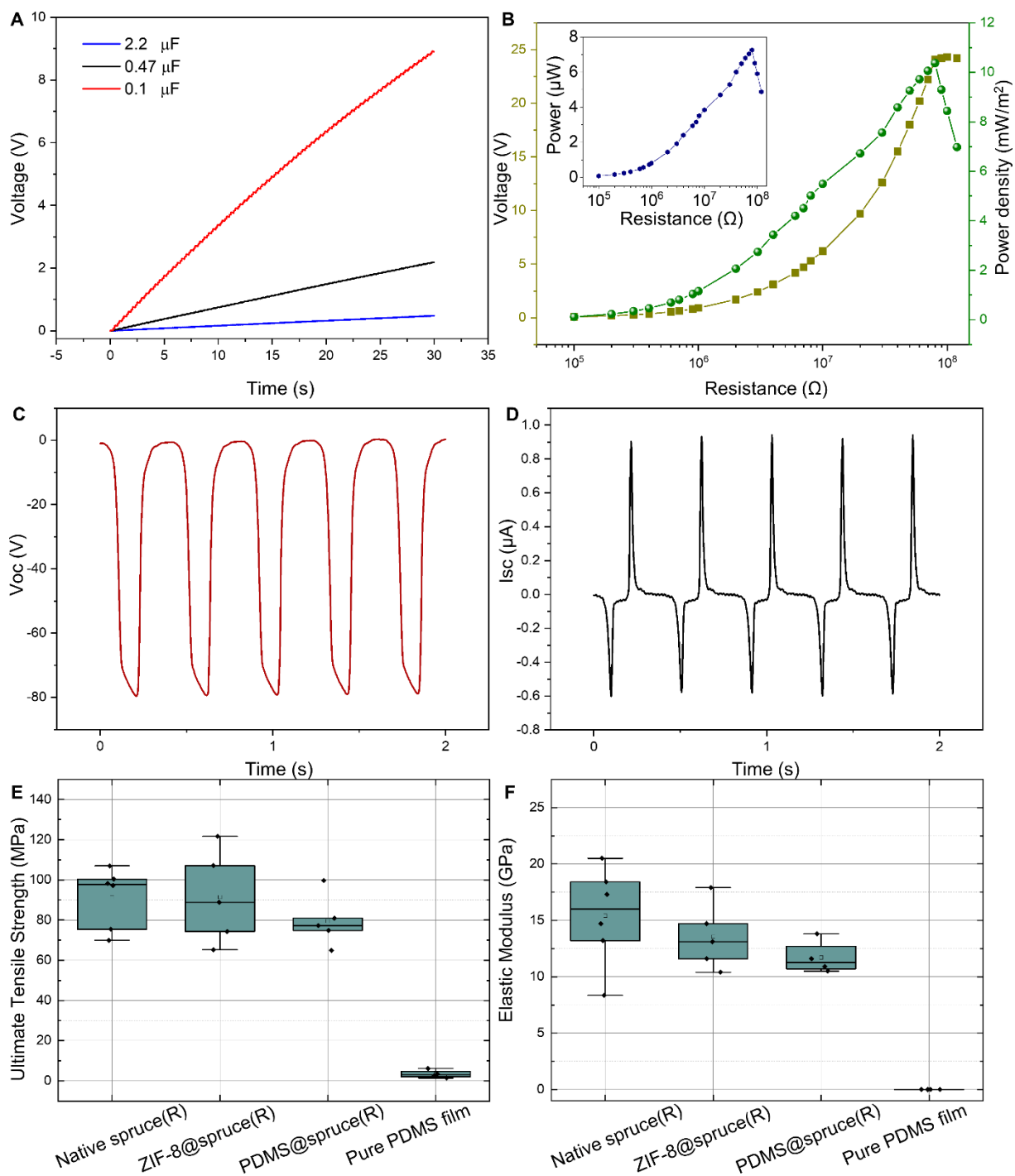


**Figure 5.** Power output and performance of normal- and large-scale FW-TENGs. (A) Voltage profile of capacitors (0.1  $\mu\text{F}$ , 0.47  $\mu\text{F}$ , 2.2  $\mu\text{F}$ ) when charged by the optimized FW-TENG. (B) Electrical output performance of the optimized FW-TENG with an external loading resistance. Inset: power density. (C) Open-circuit voltage and (D) Short-circuit current of the larger-scale optimized FW-TENG (10 cm  $\times$  8 cm) under a force of 50 N. (E) Ultimate tensile strengths and (F) stiffness of native spruce(R) and ZIF-8@spruce(R), PDMS@spruce(R), and pure PDMS film.

Decreasing the thickness is one possible approach to improve the performance of our FW-TENG.<sup>42</sup> Another possibility is to use a different configuration for the PDMS@wood, such as the one shown in Figure S24B, in which the copper foil electrode is placed directly between PDMS and wood. We evaluated the performance of a FW-TENG in this new configuration by pairing the new PDMS@spruce(R) with a 20-ZIF-8@spruce(R), all the other parameters being the same. The output was indeed higher, with a Voc of 80 V and an Isc of 1  $\mu$ A (Figure S24C,D), but this is not the only difference. In this configuration wood acts purely as a mechanical support for the soft PDMS film. The advantages brought by the use of wood as a microstructuring template, enhancing the surface roughness of PDMS at the micro- and nanoscale, could be kept only by using a highly compliant conductive material as the electrode, for example by substituting the copper foil with *e.g.* silver ink. By contrast, in our original configuration (Figure S24A), the microstructure of wood can always be used regardless of the nature of the electrode. Since this new configuration sacrifices some of the merits of wood and, to a certain degree, lacks useful insight for tuning the triboelectric properties of wood itself, in the present study we focused on the original configuration, knowing that more dedicated research will be needed to efficiently solve the trade-off dilemma between mechanical strength of wood and its triboelectrical performance.

A long-term cyclic test was performed to evaluate the mechanical stability of the optimized FW-TENG under a constant force of 50 N. As shown in Figure S25, the output Voc was stable at approximately 24.3 V with minor fluctuations for up to 1500 cycles, indicating good stability. The electricity produced by our FW-TENG could be used to power directly small electronic devices, or could be stored, *e.g.*, in a capacitor, for later use. As shown in Figure 5A, commercial capacitors with three different capacities (0.1  $\mu$ F, 0.47  $\mu$ F, and 2.2  $\mu$ F) were charged using the optimized FW-TENG. In 30 s, the 0.1  $\mu$ F capacitor could reach 8.9 V, the 0.47  $\mu$ F capacitor could reach 2.2 V, while the 2.2  $\mu$ F capacitor could only reach 0.48 V. External resistors varying from 0.1 to 120 M $\Omega$  were connected to the FW-TENG to measure its actual power. As shown in Figure 5B, the voltage gradually increases when the resistance is increased, and eventually reaches a plateau. A maximum instantaneous power of 7.3  $\mu$ W (corresponding to a power density of 10.4 mW m<sup>-2</sup>) was obtained with an optimized load resistance of 80 M $\Omega$ . Scalability is a parameter of great importance to enable applications of TENGs in smart buildings. The scalability of our optimized FW-TENG was then demonstrated by increasing the size of the functionalized wood samples to 10 cm  $\times$  8 cm. These large-scale samples of PDMS@wood and ZIF-8@wood were prepared with the same protocols used for the small samples. As shown in Figure 5C and D, this large-scale FW-TENG can generate a Voc and Isc of 79.6 V and 0.94  $\mu$ A

under a force of 50 N, demonstrating its suitability for application in energy-generating floorings. Recent developments in wood- or cellulose-based TENGs are summarized in Table S5.<sup>44,45</sup> Previous efforts focused on coupling wood or cellulose with highly polarizable materials, such as PTFE, to maximize the electrical output. However, using expensive and non-biodegradable synthetic polymers makes large-scale applications (*e.g.* as building floorings) of such TENGs unsustainable from both the economic and environmental perspective. Our functionalized wood-TENG shows an average electrical output, but has the advantage of reduced materials cost and environmental impact, and it may be of inspiration for future studies on tuning wood tribopolarity.

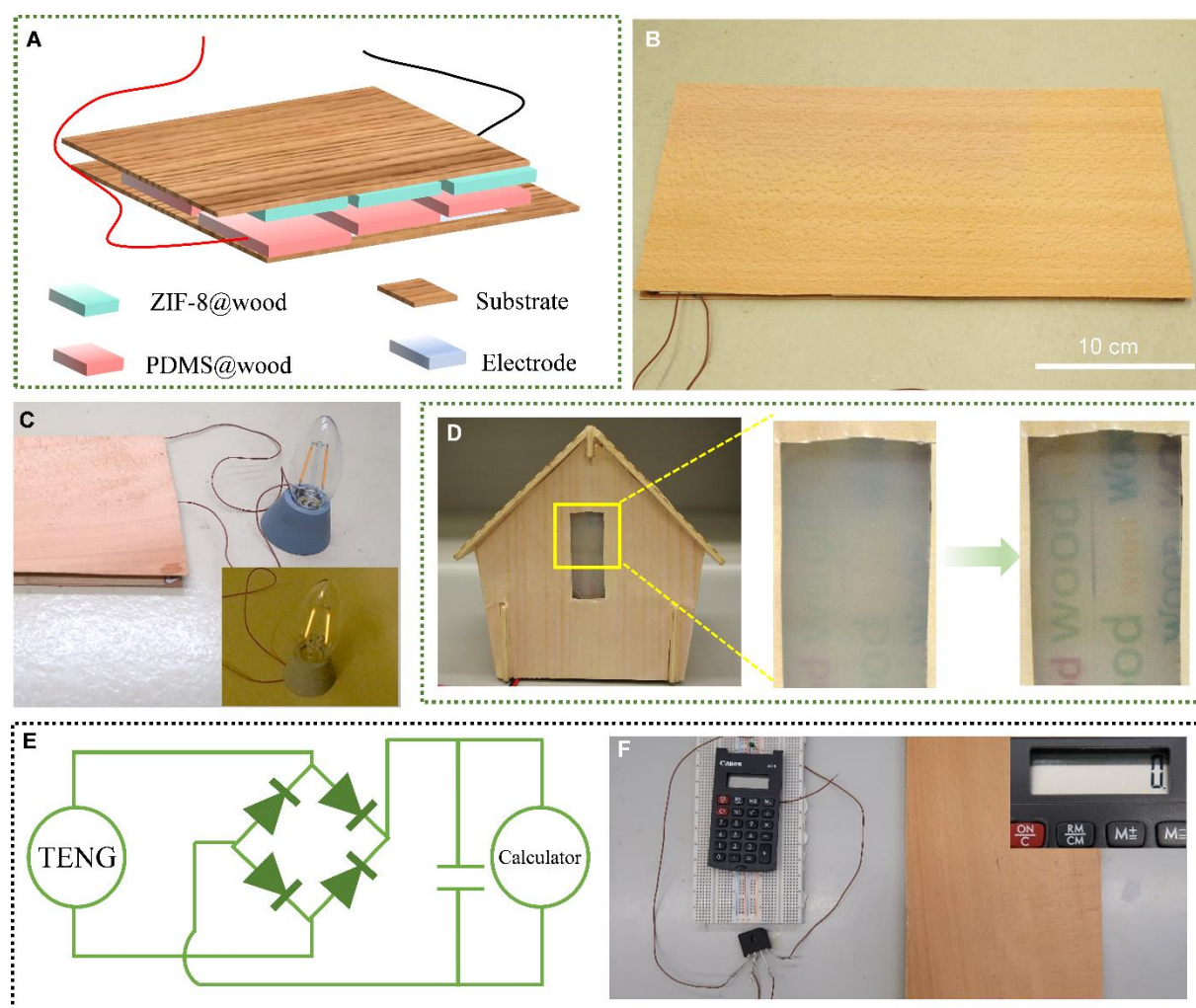


**Figure 6.** Practical smart home applications of our TENG. (A) Schematic representation and (B) photo of a big optimized FW-TENG (45 cm × 20 cm) made of six pairs of opposite tribopolarities functionalized wood, was used to power (C) a household lamp (2W, E14), (D) the smart window of a model wooden house and (E-F) a calculator.

Mechanical strength is another important factor for materials to be used in building applications. Therefore, the optimized composites were characterized also by means of tensile tests (Figure 5E and F). The ultimate tensile strengths of ZIF-8@spruce(R) and PDMS@spruce(R) were  $91.4 \pm 20.7$  MPa and  $79.5 \pm 11.4$  MPa, values comparable to that of native spruce(R) ( $91.4 \pm 13.6$  MPa). For comparison, pure PDMS films with the same shape and thickness were also tested. Their ultimate tensile strength is more than an order of magnitude lower ( $3.4 \pm 1.7$  MPa), making them unsuitable for building applications. Stiffness values (Figure 5F) of ZIF-8@spruce(R) and PDMS@spruce(R), respectively 13.5 GPa and 11.7 GPa, were also high, slightly lower compared to native spruce(R) (15.4 GPa). Without the support of a wood scaffold, the elastic modulus of pure PDMS films is only 2 MPa.

Moreover, the natural wood surface color is preserved both after the *in situ* growth of ZIF-8 and spin-coating of PDMS, as can be seen in Figure S26 and by the small color change ( $\Delta E^*$ ) values listed in Table S6. This is especially important for indoor building applications, in which the warm colors of wood are highly appreciated.<sup>46</sup>

As schematically represented in Figure 6A, many large-scale optimized FW-TENGs can be assembled, connecting more elements in series or in parallel to maximize the electrical output allowing to power more energy-intensive devices. To further demonstrate the up-scaling potential of our FW-TENGs for integration in smart buildings, we fabricated a triboelectric wooden floor demonstrator made of six electrically connected optimized FW-TENGs (10 cm x 8 cm each). As shown in Figure 6B and Figure S27, copper foils with a size of 30 cm × 16 cm were attached to the back of 20-ZIF-8@spruce(R) and PDMS@spruce(R) samples, respectively. Then, the copper foil on each side was covered with a larger native wood veneer (35 cm × 20 cm × 0.1 cm). Conductive wires were led out from the copper foils and directly connected to a household lamp (2 W, E14). As shown in Figure 6C and Video S1, the lamp could be readily switched on when the wood floor prototype was walked upon by a human adult. Figure 6D and Video S2 display the powering of an electrochromic window in a small model house. The window is initially opaque, and becomes transparent when the FW-TENG is pressed by hand. As previously mentioned, the electricity produced could be stored in capacitors. Thus, a circuit connecting the FW-TENG model floor with a commercial full-wave bridge rectifier was designed to power a commercial calculator with the assistance of a 0.1 μF capacitor, as depicted in Figure 6E. In the beginning, the capacitor is empty. The demonstrator was repeatedly pressed for a few seconds, then the calculator could be connected to the capacitor to be powered (see Figure 6F and Video S3). These proof-of-concept applications demonstrate that applicability of large-scaled FW-TENGs in smart buildings.



### 3 Conclusion

We demonstrated that the otherwise negligible triboelectric behavior of native wood could be strongly enhanced by functionalization with ZIF-8 and PDMS, making it possible to fabricate self-powering floors with enhanced wood TENG for smart homes. Compared to native wood, ZIF-8@wood is 20 times more tribopositive, while PDMS@wood is about 60 times more tribonegative. These dramatic changes of tribopolarity are attributed to physical changes (surface morphology and an increase of contact surface area by the treatment) and chemical changes (caused by introducing efficient electron-acceptor and electron-accept species). Two wood samples ( $20 \times 35 \times 1 \text{ mm}^3$ ), one functionalized with ZIF-8 and the other coated with PDMS, could generate a maximum open-circuit voltage of 24.3 V and a short-circuit current of  $0.32 \mu\text{A}$  under a relatively small force of 50 N, which is 80 times higher than that generated by native wood. The output electricity could be increased by assembling six larger-size wood TENG ( $100 \times 80 \times 1 \text{ mm}^3$ ), sufficient to drive both household LED lamps and calculators. Furthermore, our wood TENG could power smart electrochromic windows to modulate sunlight transmittance, reducing the energy consumption for lighting. Both functionalization techniques, *in situ* growth of ZIF-8 and spin-coating of PDMS, preserved to a great extent the compelling properties of wood (*e.g.* mechanical stability and warm colors) making the resulting materials suitable for high-end building applications. The efficient electrical output, the sustainability and scalability of radial-cut wood may contribute to the design of next-generation of sustainable power supplies in smart buildings.

### 4 Experimental Section

#### Materials

Cross-sections of native wood species, including Norway spruce (*Picea abies*), Balsa (*Ochroma pyramidale*), and European yew (*Taxus baccata*) with the dimensions of  $35 \text{ mm} \times 20 \text{ mm} \times 1 \text{ mm}$  (radial  $\times$  tangential  $\times$  longitudinal, R  $\times$  T  $\times$  L) were cut by a laser cutter (Trotec, speedy 300). Radial sections and tangential sections of native wood with the dimensions of  $20 \text{ mm} \times 1 \text{ mm} \times 35 \text{ mm}$  (R  $\times$  T  $\times$  L) and of  $1 \text{ mm} \times 20 \text{ mm} \times 35 \text{ mm}$  (R  $\times$  T  $\times$  L) were cut by saw, respectively. Zinc nitrate hexahydrate ( $\text{Zn}(\text{NO}_3)_2 \cdot 6\text{H}_2\text{O}$ , 98%), methanol ( $\geq 99.9\%$ ) and ethanol ( $\geq 99.8\%$ ) were purchased from Sigma-Aldrich. 2-Methylimidazole (2-MeIm, 97%) and sodium hydroxide (NaOH) were provided by Thermo Fisher GmbH. Poly(dimethylsiloxane) (PDMS, Sylgard 184) prepolymer and curing agent were supplied by Dow Corning Co., Ltd. (Michigan, USA). All chemicals were used as received.

#### Synthesis of ZIF-8@wood

The preparation of ZIF-8@wood samples was adapted from a method reported by Tu et al.<sup>19</sup> Native wood samples were pretreated by immersion in a 15% w/v NaOH aqueous solution for 1 h. The wood samples were first washed with water and then immersed in a NaOH solution (pH = 9) until pH stabilized. These pretreated wood samples were submerged in a mixture of 0.002 mol Zn(NO<sub>3</sub>)<sub>2</sub>, 20 g methanol, and 3 g deionized water for two hours to ensure a sufficient ion exchange between Zn and Na ions. A mixture of 0.04 mol 2-MeIm, 20 g methanol, and 3 g deionized water was subsequently added to the above solution. Stirring at room temperature for 24 h led to the ZIF-8@wood composite. The composite was then rinsed with methanol to remove the unreacted precursors (until the washing solution was transparent), followed by drying in the vacuum-oven at 103°C for 24 h. The 2-MeIm/Zn<sup>2+</sup> molar ratio in the precursor solution ranged from 1, 5, 10 to 20, and the corresponding names of the composites are 1-(MeIm/Zn)@spruce(C), 5-ZIF-8@wood, 10-ZIF-8@wood, and 20-ZIF-8@wood.

### **Fabrication of PDMS@Wood**

The PDMS solution was prepared by mixing the Sylgard 184 elastomer with the curing agent in 10:1 proportion and stirring for 1 min. After that, the PDMS mixture was kept in a vacuum for 20 min to remove air bubbles. The as-prepared mixture of PDMS was coated on the wood by spin coating at 2000 rpm for 30 s, and eventually cured at 60°C for two hours.

### **20-ZIF-8@spruce(C) prepared by physical coating**

Solutions of Zn(NO<sub>3</sub>)<sub>2</sub>·6H<sub>2</sub>O (0.002 mol) and 2-MeIm (0.04 mol) were prepared by dissolving each reactant in a mixture of 20 g methanol and 3 g deionized water. These two solutions were mixed together and stirred at room temperature for 24 h. After washing with methanol (3 × 60 cm<sup>3</sup>), the 20-ZIF-8 particles were dispersed in 50 g methanol to form a 20-ZIF-8 suspension. 20-ZIF-8@spruce(C) samples were obtained by immersing native spruce(C) into the as-prepared 20-ZIF-8 suspension for 1 min, followed by drying at 103°C under vacuum.

### **Device fabrication**

A triboelectric wooden floor demonstrator was made of six pairs of optimized 20-ZIF-8@spruce(R) and PDMS@spruce(R) samples (10 cm × 8 cm each piece). Commercial copper foil (30 cm × 16 cm), were attached to the back of six 20-ZIF-8@spruce(R) (30 cm × 16 cm in total) and six PDMS@spruce(R) (30 cm × 16 cm in total) samples, respectively. Finally, the copper foil on each side was covered with a larger native wood veneer (35 cm × 20 cm × 0.1

cm). Conductive wires were led out from the copper foils and directly connected to the testing instrument or external electronic devices.

### **Characterization techniques**

*Scanning Electron Microscopy (SEM):* Wood samples were cut into small cubes of 5 mm × 5 mm × 1 mm. Then they were put into a vacuum oven at 103°C for 2 hours for drying. Afterward, the wood samples were coated with 10 nm Pt/Pd (80/20) film using a sputter coater (CCU-010, Safematic, Switzerland) to make the surface conductive. The structure of the samples was characterized by field emission scanning electron microscopy (FEI Quanta 200F).

*Atomic Force Microscopy (AFM):* AFM imaging was carried out using a NanoWizard 4 (JPK Instruments AG - Bruker Nano GmbH, Germany) at 20°C and 65% RH climate room. The cross-cut wood samples were glued on a glass slide. Measurements were performed in alternating contact mode (AC mode), using rectangular-shaped silicon cantilevers (NCHR-10, Nano World, Switzerland) with a resonant frequency of 320 kHz and a nominal spring constant of 42 N m<sup>-1</sup>. A scan size of 2.5 μm × 2.5 μm and a resolution of 256 × 256 pixels were used. Imaging was performed at a gain range from 150.0 to 350.0, scanning rates of 0.5 Hz, and setpoint amplitudes of 65 to 75% of the free oscillation amplitude. All images were plotted using the Gwyddion software (v 2.57).

*Optical Profilometry:* 3D images of W-TENG samples were acquired with a Sensofar Plu Neox optical profilometer (Sensofar, Spain). The optical profiling instruments employed a 20× objective with a light beam and scanned under a resolution of 768 × 576 pixels. The scan size was 636.61 × 477.25 μm<sup>2</sup> and the Z scan was between 80 and 150 μm with a threshold of 0.2%. Data were plotted using Gwyddion software (v 2.57), in which a smaller size (300 μm × 200 μm) was selected.

*Fourier transform infrared spectroscopy (FTIR):* Thin wood samples were analyzed with an ATR-FTIR spectrometer (Bruker Tensor 27) equipped with an ATR module over the scan range of 400 to 4000 cm<sup>-1</sup> to see the composition of the chemical change of sample surface upon PDMS and ZIF-8 modification. Before using baseline concave rubberband correction method to do baseline correction, the spectra from five samples were averaged. Data were normalized in the OPUS software and plotted in OriginPro 9.6.

*X-ray powder diffraction (XRD):* The crystal structure of ZIF-8@wood was studied by XRD (Panalytical X'Pert PRO MPD) using Cu Kα radiation (λ = 1.5406 Å). Small cross-cut ZIF-8@spruce samples with a thickness of 1 mm, a length of 2 cm, and a width of 1 cm were used

for the measurements. The diffraction data was conducted with an angular step size of  $0.03^\circ$  and a counting time of 1 s per step and recorded in the  $2\theta$  range  $5-70^\circ$  range.

*Inductively coupled plasma-optical emission spectrometry (ICP-OES):* ICP-OES was conducted using a Horiba Ultra 2 instrument equipped with photomultiplier tube detection. The samples were digested in a MLS turboWave® microwave by heating the material (ca. 10-15 mg) in  $3\text{ cm}^3$  of a 3:1 volumetric mixture of  $\text{HNO}_3$  (Sigma-Aldrich,  $\geq 65\text{ wt.}\%$ ) and  $\text{H}_2\text{O}_2$  (Sigma-Aldrich,  $35\text{ wt.}\%$ ) to 533 K for 50 min with a maximum power of 1200 W and a loading pressure of 70 bar. The obtained clear solutions were filtered and diluted to 25 mL with ultrapure water prior to analysis. The mass percentage of ZIF-8 was calculated from the measured Zn content assuming an ideal stoichiometry for ZIF-8 ( $\text{C}_8\text{H}_{10}\text{N}_4\text{Zn}$ ). The error was estimated as the standard deviation of three independent measurements.

*Measurement of electrical output:* A linear motor (PL01-28x500/420) was used to load the samples with a fixed force. At the same time, a loading cell was mounted on the rigid frame of the motor to monitor the pressure applied to the samples. The electrical output was measured by a Keithley 6514, equipped with a Matlab software.

*Mechanical Tensile Testing:* Tensile tests were conducted on a Zwick/Roell Z010 universal testing machine. The measurements were made with a 10 kN and a 1 kN load cell for the wood-based samples and the PDMS-film (1 mm thickness), respectively. The samples were cut into dog bone shape according to ISO 527-3<sup>47</sup> specimen type 5 parallel to the fibre direction. Additionally, spruce tags were glued to the grip section of the samples as reinforcement. The testing speed was 0.4 mm/min. The E-Modulus was calculated by the slope of a linear regression in the range between 10-40% of the maximal force.

*Measurement of color changes:* Changes in color of wood surface were measured with a Minolta spectrophotometer (CR200, Japan) using the CIE  $L^*a^*b^*$  system based on the ISO 7724 standard test method.<sup>48</sup> The average values of the color parameters were obtained by measuring ten different positions for each sample. In the CIE  $L^*a^*b^*$  system, L represents lightness, a and b represent chromaticity parameter. The overall color change ( $\Delta E^*$ ) was calculated according to the following equation (eq. 2):

$$\Delta E^* = \sqrt{\Delta a^2 + \Delta b^2 + \Delta L^2} \quad (2)$$

where  $\Delta L$ ,  $\Delta a$ , and  $\Delta b$  represent the changes in L, a, and b between the values of native wood and plasma treated wood, respectively. A lower  $\Delta E^*$  value corresponds to a lower color change.

## Acknowledgements

The project was conducted with the support by the SNF project “Hierarchical cellulose scaffolds for structural and functional gradient materials” (200021\_184821/1). The authors thank Thomas Schnider for the wood sample preparation and the technical support. The authors thank Nicolas Bain for access to the spin-coater. K.T. thanks financial support from the China Scholarship Council (CSC) (201703270028).

## Author Contributions

J.S., K.T contributed equally to this work. J.S., K.T., and G.P. conceived the study. J.S., K.T., S.B., S.M.K., Y.D., and S.S. performed experiments and analyzed data. S.M.K., S.N.R., H.G., C.W., K.K., J.P.R., and I.B. verified the experimental design and data analysis, and gave theoretical support. J.S., K.T., and G.P. co-wrote the manuscript. All authors discussed the results and commented on the manuscript.

## Declaration of Interests

The authors declare no conflict of interest.

## References

- 1 Bell, L.E. (2008). Cooling, heating, generating power, and recovering waste heat with thermoelectric systems. *Science* 321, 1457-1461.
- 2 Fan, F.R., Tian, Z.Q., and Wang, Z.L. (2012). Flexible triboelectric generator! *Nano Energy* 1, 328-334.
- 3 He, C., Zhu, W.J., Chen, B.D., Xu, L., Jiang, T., Han, C.B., Gu, G.Q., Li, D.C., and Wang, Z.L. (2017). Smart Floor with Integrated Triboelectric Nanogenerator As Energy Harvester and Motion Sensor. *Acs Appl Mater Inter* 9, 26126-26133.
- 4 Song, Y., Wang, H.B., Cheng, X.L., Li, G.K., Chen, X.X., Chen, H.T., Miao, L.M., Zhang, X.S., and Zhang, H.X. (2019). High-efficiency self-charging smart bracelet for portable electronics. *Nano Energy* 55, 29-36.
- 5 Parida, K., Xiong, J.Q., Zhou, X.R., and Lee, P.S. (2019). Progress on triboelectric nanogenerator with stretchability, self-healability and bio-compatibility. *Nano Energy* 59, 237-257.
- 6 Hao, S.F., Jiao, J.Y., Chen, Y.D., Wang, Z.L., and Cao, X. (2020). Natural wood-based triboelectric nanogenerator as self-powered sensing for smart homes and floors. *Nano Energy* 75.
- 7 Chandrasekhar, A., Vivekananthan, V., Khandelwal, G., Kim, W.J., and Kim, S.J. (2020). Green energy from working surfaces: a contact electrification-enabled data theft protection and monitoring smart table. *Mater Today Energy* 18.
- 8 Kim, I., Jeon, H., Kim, D., You, J., and Kim, D. (2018). All-in-one cellulose based triboelectric nanogenerator for electronic paper using simple filtration process. *Nano Energy* 53, 975-981.
- 9 Zhang, L., Liao, Y., Wang, Y.C., Zhang, S.V., Yang, W.Q., Pan, X.J., and Wang, Z.L. (2020). Cellulose II Aerogel-Based Triboelectric Nanogenerator. *Adv Funct Mater* 30.

- 10 Sun, J.G., Yang, T.N., Kuo, I.S., Wu, J.M., Wang, C.Y., and Chen, L.J. (2017). A leaf-molded transparent triboelectric nanogenerator for smart multifunctional applications. *Nano Energy* 32, 180-186.
- 11 Sun, J.G., Yang, T.N., Wang, C.Y., and Chen, L.J. (2018). A flexible transparent one-structure tribo-piezo-pyroelectric hybrid energy generator based on bio-inspired silver nanowires network for biomechanical energy harvesting and physiological monitoring. *Nano Energy* 48, 383-390.
- 12 Sun, J.G., Guo, H.Y., Ribera, J., Wu, C.S., Tu, K.K., Binelli, M., Panzarasa, G., Schwarze, F.W.M.R., Wang, Z.L., and Burgert, I. (2020). Sustainable and Biodegradable Wood Sponge Piezoelectric Nanogenerator for Sensing and Energy Harvesting Applications. *Acs Nano* 14, 14665-14674.
- 13 Diaz, A.F., and Felix-Navarro, R.M. (2004). A semi-quantitative tribo-electric series for polymeric materials: the influence of chemical structure and properties. *J Electrostat* 62, 277-290.
- 14 Muthu, M., Pandey, R., Wang, X.Z., Chandrasekhar, A., Palani, I.A., and Singh, V. (2020). Enhancement of triboelectric nanogenerator output performance by laser 3D-Surface pattern method for energy harvesting application. *Nano Energy* 78.
- 15 Seung, W., Gupta, M.K., Lee, K.Y., Shin, K.S., Lee, J.H., Kim, T.Y., Kim, S., Lin, J., Kim, J.H., and Kim, S.W. (2015). Nanopatterned Textile-Based Wearable Triboelectric Nanogenerator. *Acs Nano* 9, 3501-3509.
- 16 Yun, B.K., Kim, J.W., Kim, H.S., Jung, K.W., Yi, Y., Jeong, M.S., Ko, J.H., and Jung, J.H. (2015). Base-treated polydimethylsiloxane surfaces as enhanced triboelectric nanogenerators. *Nano Energy* 15, 523-529.
- 17 Luo, J.J., Wang, Z.M., Xu, L., Wang, A.C., Han, K., Jiang, T., Lai, Q.S., Bai, Y., Tang, W., Fan, F.R., and Wang, Z.L. (2019). Flexible and durable wood-based triboelectric nanogenerators for self-powered sensing in athletic big data analytics. *Nat Commun* 10.
- 18 Khandelwal, G., Chandrasekhar, A., Raj, N.P.M.J., and Kim, S.J. (2019). Metal-Organic Framework: A Novel Material for Triboelectric Nanogenerator-Based Self-Powered Sensors and Systems. *Adv Energy Mater* 9.
- 19 Tu, K.K., Puertolas, B., Adobes-Vidal, M., Wang, Y.R., Sun, J.G., Traber, J., Burgert, I., Perez-Ramirez, J., and Keplinger, T. (2020). Green Synthesis of Hierarchical Metal-Organic Framework/Wood Functional Composites with Superior Mechanical Properties. *Adv Sci* 7.
- 20 Khandelwal, G., Raj, N.P.M.J., and Kim, S.J. (2020). Zeolitic Imidazole Framework: Metal-Organic Framework Subfamily Members for Triboelectric Nanogenerator. *Adv Funct Mater* 30.
- 21 Denny, M.S., Moreton, J.C., Benz, L., and Cohen, S.M. (2016). Metal-organic frameworks for membrane-based separations. *Nat Rev Mater* 1.
- 22 Wang, Z.L., Chen, J., and Lin, L. (2015). Progress in triboelectric nanogenerators as a new energy technology and self-powered sensors. *Energ Environ Sci* 8, 2250-2282.
- 23 Li, G.Z., Wang, G.G., Ye, D.M., Zhang, X.W., Lin, Z.Q., Zhou, H.L., Li, F., Wang, B.L., and Han, J.C. (2019). High-Performance Transparent and Flexible Triboelectric Nanogenerators Based on PDMS-PTFE Composite Films. *Adv Electron Mater* 5.
- 24 Tantraviwat, D., Buarin, P., Suntalelat, S., Sripumkhai, W., Pattamang, P., Rujijanagul, G., and Inceesungvorn, B. (2020). Highly dispersed porous polydimethylsiloxane for boosting power-generating performance of triboelectric nanogenerators. *Nano Energy* 67.
- 25 Yang, X.H., Zhu, G., Wang, S.H., Zhang, R., Lin, L., Wu, W.Z., and Wang, Z.L. (2012). A self-powered electrochromic device driven by a nanogenerator. *Energ Environ Sci* 5, 9462-9466.

- 26 Qiu, W.Z., Feng, Y.G., Luo, N., Chen, S.G., and Wang, D.A. (2020). Sandwich-like sound-driven triboelectric nanogenerator for energy harvesting and electrochromic based on Cu foam. *Nano Energy* 70.
- 27 Yeh, M.H., Lin, L., Yang, P.K., and Wang, Z.L. (2015). Motion-Driven Electrochromic Reactions for Self-Powered Smart Window System. *Acs Nano* 9, 4757-4765.
- 28 Yang, Y., Zhang, H.L., Lin, Z.H., Zhou, Y.S., Jing, Q.S., Su, Y.J., Yang, J., Chen, J., Hu, C.G., and Wang, Z.L. (2013). Human Skin Based Triboelectric Nanogenerators for Harvesting Biomechanical Energy and as Self-Powered Active Tactile Sensor System. *Acs Nano* 7, 9213-9222.
- 29 Li, S.Y., Fan, Y., Chen, H.Q., Nie, J.H., Liang, Y.X., Tao, X.L., Zhang, J., Chen, X.Y., Fu, E.G., and Wang, Z.L. (2020). Manipulating the triboelectric surface charge density of polymers by low-energy helium ion irradiation/implantation. *Energ Environ Sci* 13, 896-907.
- 30 Wang, Z.L. (2017). On Maxwell's displacement current for energy and sensors: the origin of nanogenerators. *Mater Today* 20, 74-82.
- 31 Wang, Z.L. (2020). On the first principle theory of nanogenerators from Maxwell's equations. *Nano Energy* 68.
- 32 Zhang, H., Yao, L.J., Quan, L.W., and Zheng, X.L. (2020). Theories for triboelectric nanogenerators: A comprehensive review. *Nanotechnol Rev* 9, 610-625.
- 33 Keunecke, D., Eder, M., Burgert, I., and Niemz, P. (2008). Micromechanical properties of common yew (*Taxus baccata*) and Norway spruce (*Picea abies*) transition wood fibers subjected to longitudinal tension. *J Wood Sci* 54, 420-422.
- 34 Johnson, L.M., Gao, L., Shields, C.W., Smith, M., Efimenko, K., Cushing, K., Genzer, J., and Lopez, G.P. (2013). Elastomeric microparticles for acoustic mediated bioseparations. *J Nanobiotechnol* 11.
- 35 Lee, S., Lee, Y., Kim, D., Yang, Y., Lin, L., Lin, Z.H., Hwang, W., and Wang, Z.L. (2013). Triboelectric nanogenerator for harvesting pendulum oscillation energy. *Nano Energy* 2, 1113-1120.
- 36 Park, S.J., Seol, M.L., Jeon, S.B., Kim, D., Lee, D., and Choi, Y.K. (2015). Surface Engineering of Triboelectric Nanogenerator with an Electrodeposited Gold Nanoflower Structure. *Sci Rep-Uk* 5.
- 37 Persson, B.N.J. (2006). Contact mechanics for randomly rough surfaces. *Surf Sci Rep* 61, 201-227.
- 38 Yang, W.X., Wang, X.L., Li, H.Q., Wu, J., Hu, Y.Q., Li, Z.H., and Liu, H. (2019). Fundamental research on the effective contact area of micro-/nano-textured surface in triboelectric nanogenerator. *Nano Energy* 57, 41-47.
- 39 Dudem, B., Ko, Y.H., Leem, J.W., Lee, S.H., and Yu, J.S. (2015). Highly Transparent and Flexible Triboelectric Nanogenerators with Subwavelength-Architected Polydimethylsiloxane by a Nanoporous Anodic Aluminum Oxide Template. *Acs Appl Mater Inter* 7, 20520-20529.
- 40 Su, Z.M., Han, M.D., Cheng, X.L., Chen, H.T., Chen, X.X., and Zhang, H.X. (2016). Asymmetrical Triboelectric Nanogenerator with Controllable Direct Electrostatic Discharge. *Adv Funct Mater* 26, 5524-5533.
- 41 Zhou, T., Zhang, L.M., Xue, F., Tang, W., Zhang, C., and Wang, Z.L. (2016). Multilayered electret films based triboelectric nanogenerator. *Nano Res* 9, 1442-1451.
- 42 Kang, X.F., Pan, C.X., Chen, Y.H., and Pu, X. (2020). Boosting performances of triboelectric nanogenerators by optimizing dielectric properties and thickness of electrification layer. *Rsc Adv* 10, 17752-17759.
- 43 Fan, F.R., Luo, J.J., Tang, W., Li, C.Y., Zhang, C.P., Tian, Z.Q., and Wang, Z.L. (2014). Highly transparent and flexible triboelectric nanogenerators: performance improvements and fundamental mechanisms. *J Mater Chem A* 2, 13219-13225.

- 44 Zheng, Q.F., Fang, L.M., Guo, H.Q., Yang, K.F., Cai, Z.Y., Meador, M.A.B., and Gong, S.Q. (2018). Highly Porous Polymer Aerogel Film-Based Triboelectric Nanogenerators. *Adv Funct Mater* 28.
- 45 Srither, S.R., Rao, D.S.S., and Prasad, S.K. (2018). Triboelectric Nanogenerator Based on Biocompatible and Easily Available Polymer Films. *Chemistryselect* 3, 5055-5061.
- 46 Rice, J., Kozak, R.A., Meitner, M.J., and Cohen, D.H. (2006). Appearance wood products and psychological well-being. *Wood Fiber Sci* 38, 644-659.
- 47 Breuer, H., Brauer, O., Ebenau, A., Dripke, M., and Post, L. (1997). Determination of the tensile properties of plastics. *Kunstst-Plast Eur* 87, 1012-1014.
- 48 Tu, K.K., Wang, X.Q., Kong, L.Z., Chang, H.J., and Liu, J.L. (2016). Fabrication of robust, damage-tolerant superhydrophobic coatings on naturally micro-grooved wood surfaces. *Rsc Adv* 6, 701-707.



## Supplementary Information

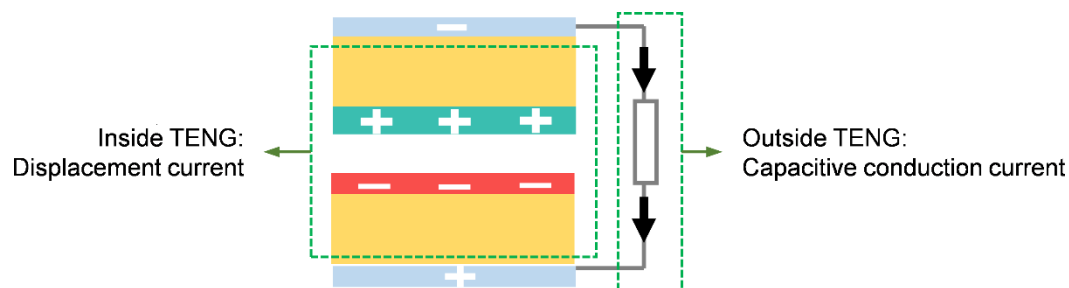


**Figure S1.** Schematic representation of the working mechanism of our functionalized wood TENG.

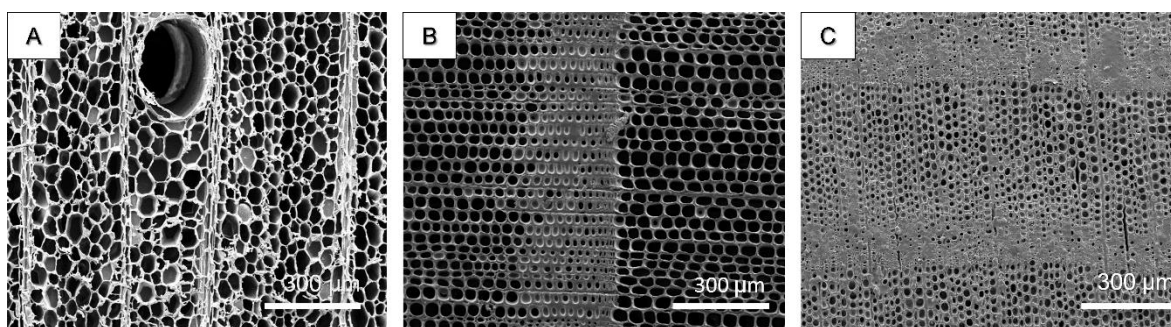


**Figure S2.** SEM images of the cross-section of different native wood species used for porosity analysis. (A) SEM images of native balsa(C). (B) SEM images of native spruce(C). (C) SEM images of native yew(C).

**Table S1.** Pore area and porosity of different wood species (calculated with ImageJ).

	Wood species		
	Balsa	Spruce	Yew
Image size ( $\mu\text{m}^2$ )	1200000	1200000	1200000
Sum area of pores ( $\mu\text{m}^2$ )	763071.164	568799.624	191043.017
Porosity	64%	47%	16%

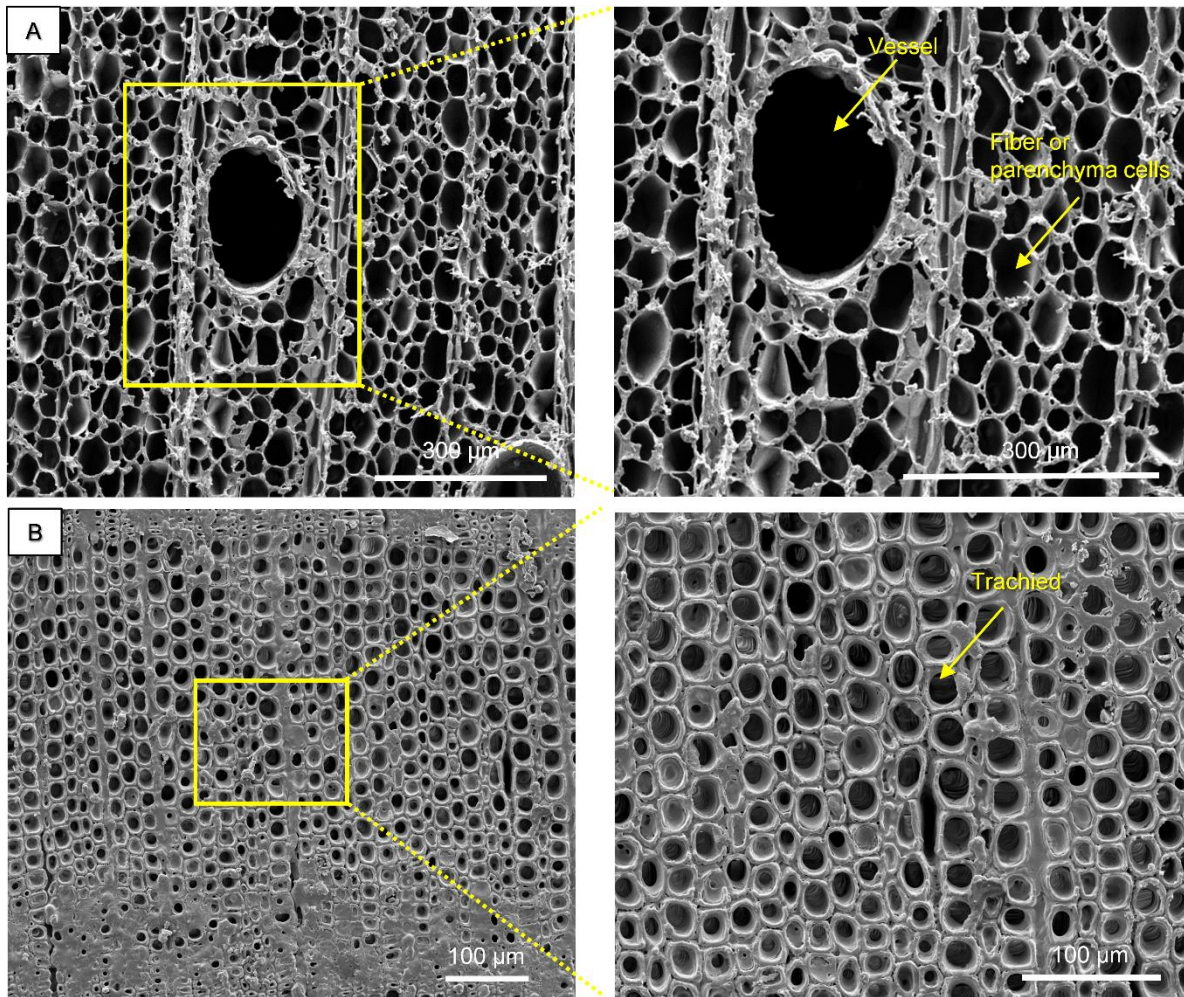


**Figure S3.** Representative SEM images of the cross-section of native wood samples cut by laser ( $L \times R \times T$ : 1 mm  $\times$  35 mm  $\times$  20 mm). (A) SEM images of native balsa(C). (B) SEM images of native yew(C)

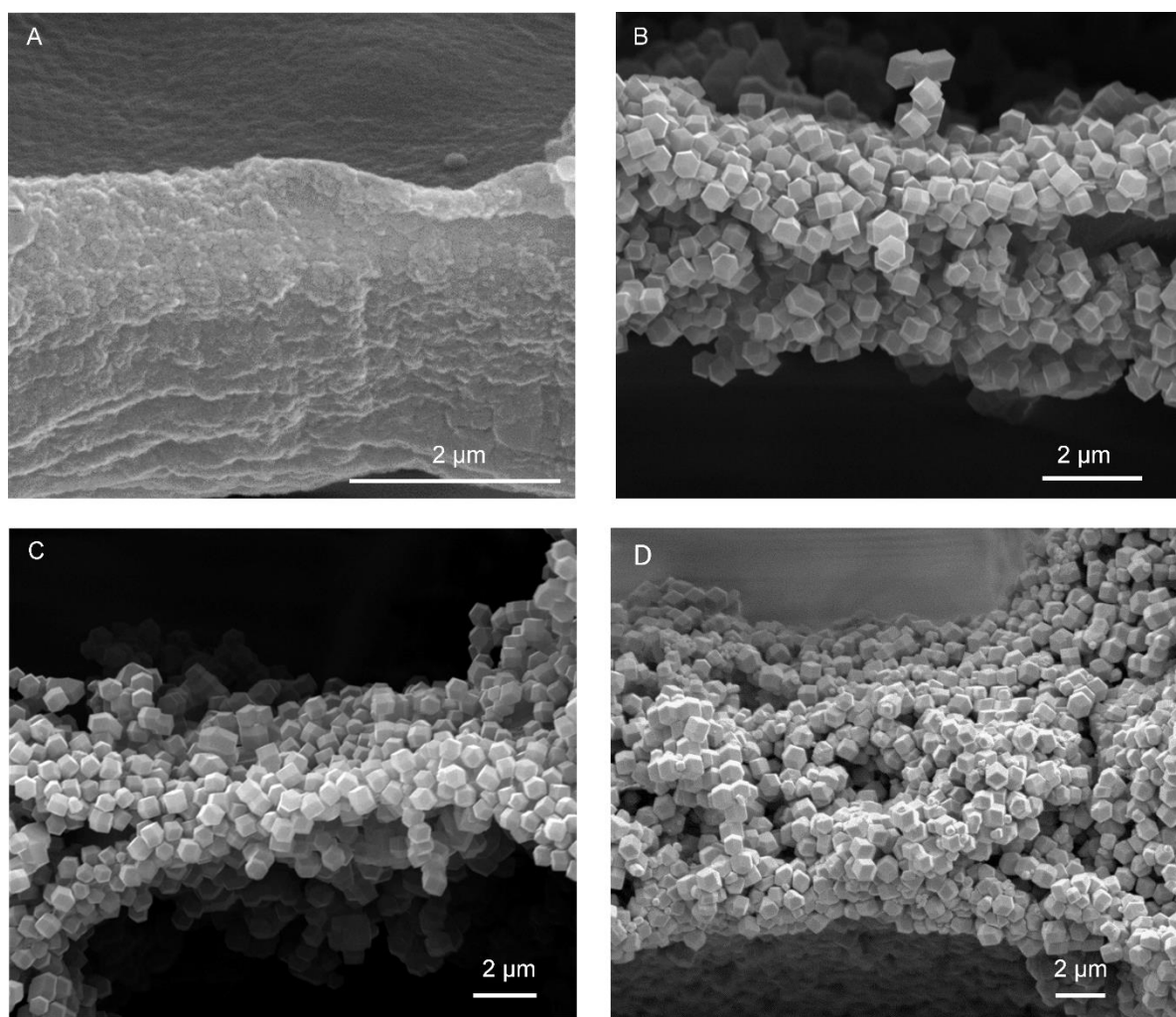


**Figure S4.** SEM images of functionalized wood samples with different 2-MeIm/Zn<sup>2+</sup> molar ratio. (A) SEM images of 1-(MeIm/Zn)@spruce(C). (B) SEM images of 5-ZIF-8@spruce(C). (C) SEM images of 10-ZIF-8@spruce(C). (D) SEM images of 20-ZIF-8@spruce(C).

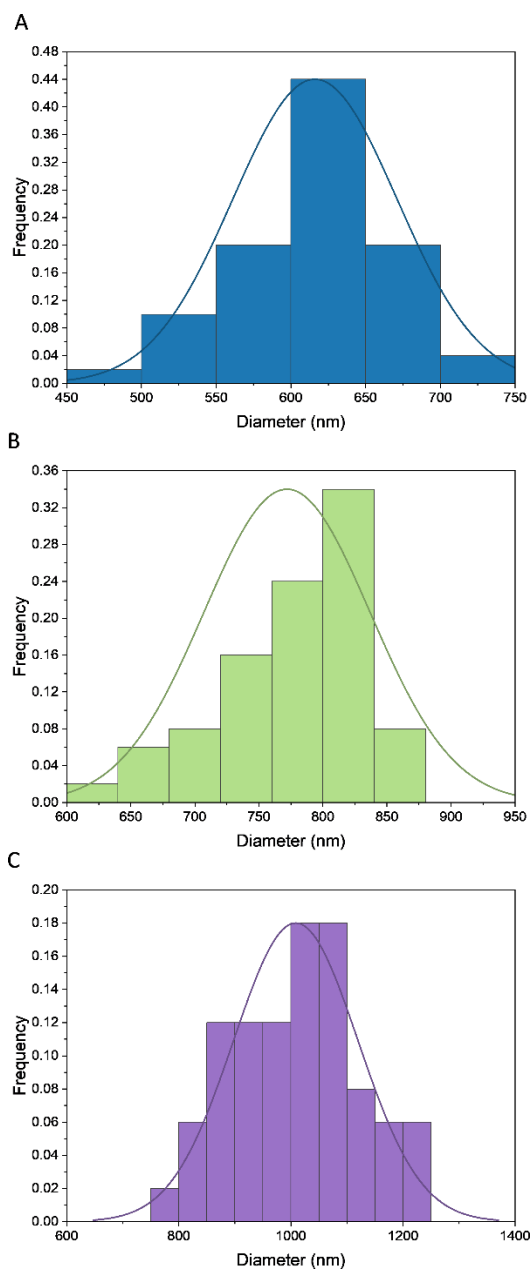


**Figure S5.** Particle size distribution of ZIF-8@spruce(C) with different 2-MeIm/Zn<sup>2+</sup> molar ratio. (A) Particle size distribution of 5-ZIF-8@spruce(C). (B) Particle size distribution of 10-ZIF-8@spruce(C). (C) Particle size distribution of 20-ZIF-8@spruce(C).



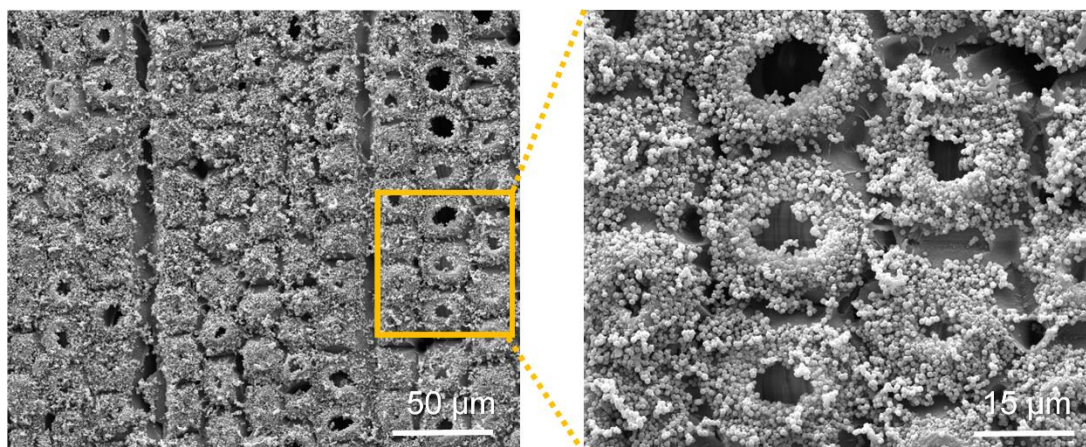


**Figure S6.** Representative SEM images of 20-ZIF-8@yew(C).



**Figure S7.** Photos of cross-cut balsa wood before and after ZIF-8 modification, showing the sample shrinkage.

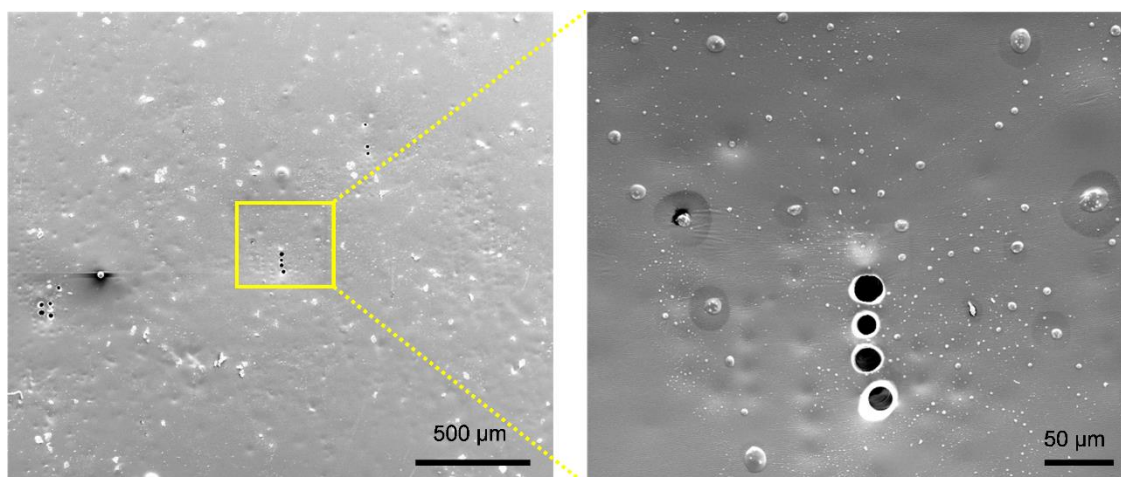


**Figure S8.** Representative SEM images of PDMS@yew(C).

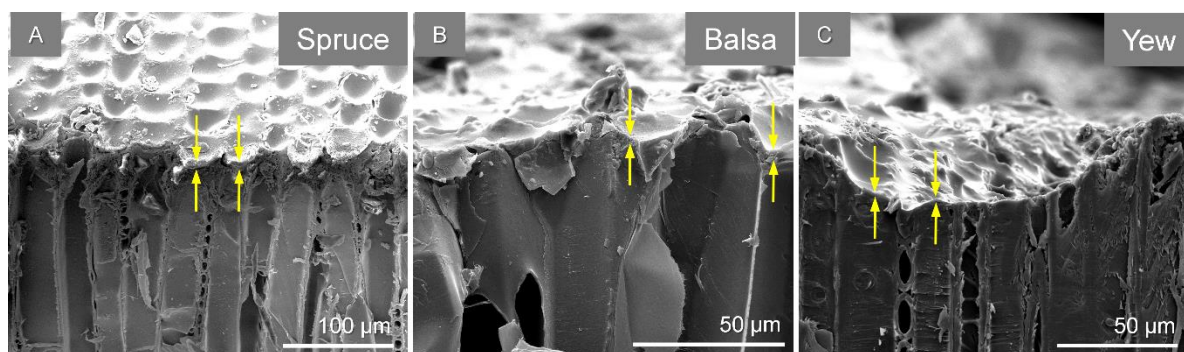


**Figure S9.** Representative SEM images of PDMS@wood(C) samples (tangential sections) showing the distribution of the PDMS film on a cross-section of different wood species. (A) SEM images of PDMS@spruce(C) samples (tangential sections). (B) SEM images of PDMS@balsa(C) samples (tangential sections). (C) SEM images of PDMS@yew(C) samples (tangential sections).

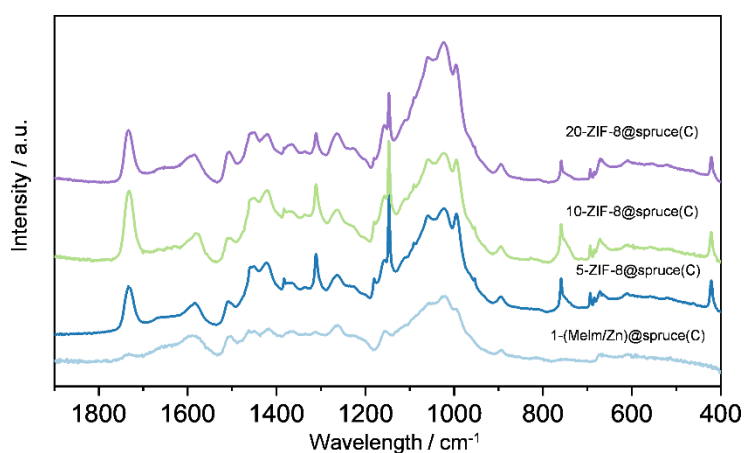


**Figure S10.** FTIR results for 1-(MeIm/Zn)@spruce(C), 5-ZIF-8@spruce(C), 10-ZIF-8@spruce(C), and 20-ZIF-8@spruce(C).

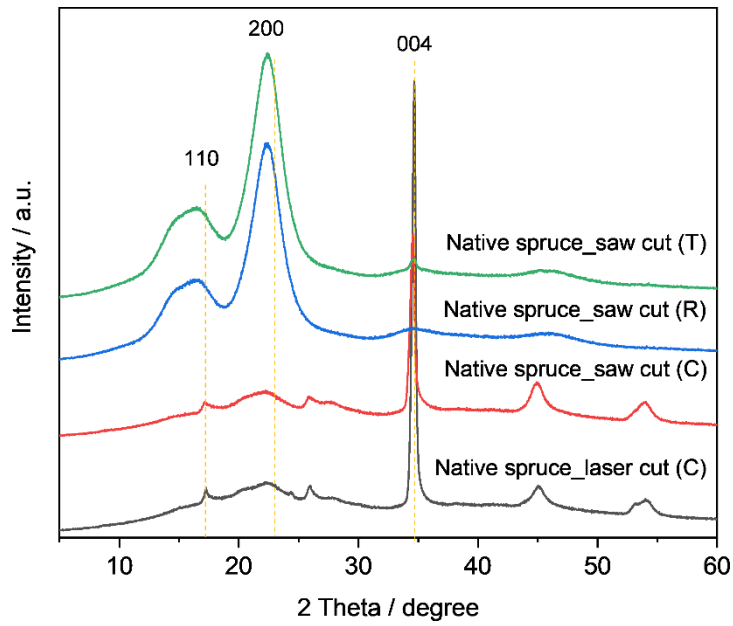


**Figure S11.** XRD results for native spruce cut with different approaches (saw, laser) from different directions, showing the impact of cut direction on the intensity of cellulose peaks.

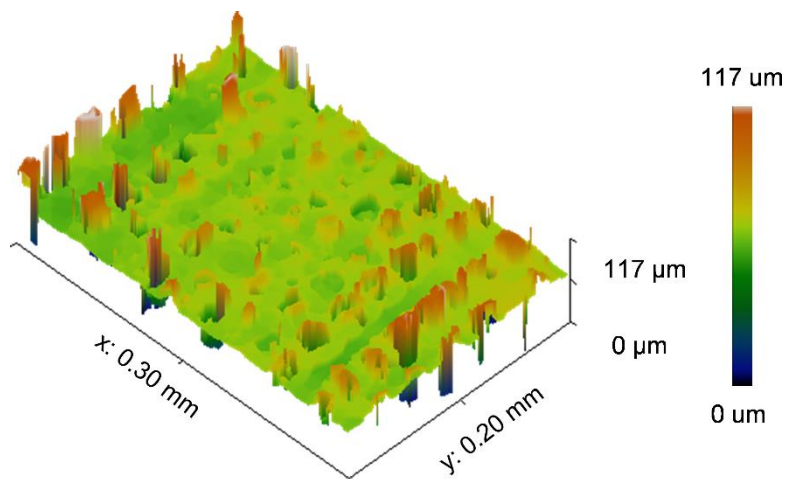


**Figure S12.** 3D surface profile of native yew(C) obtained by optical profilometry.

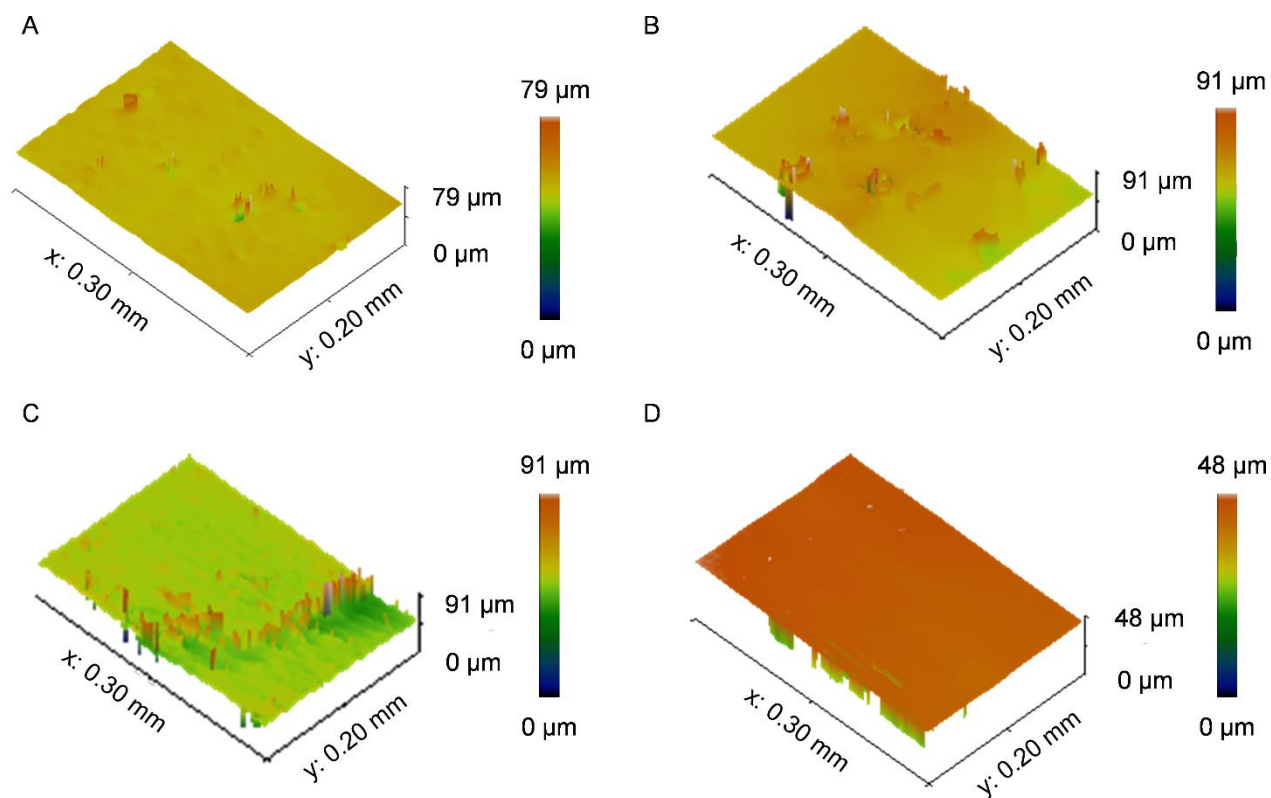


**Figure S13.** 3D surface profiles of PDMS@wood(C) obtained by optical profilometry. (A) 3D surface profiles of PDMS@yew(C). (B) 3D surface profiles of PDMS@balsa(C). (C) 3D surface profiles of PDMS@spruce(R). (D) 3D surface profiles of PDMS@spruce(T).

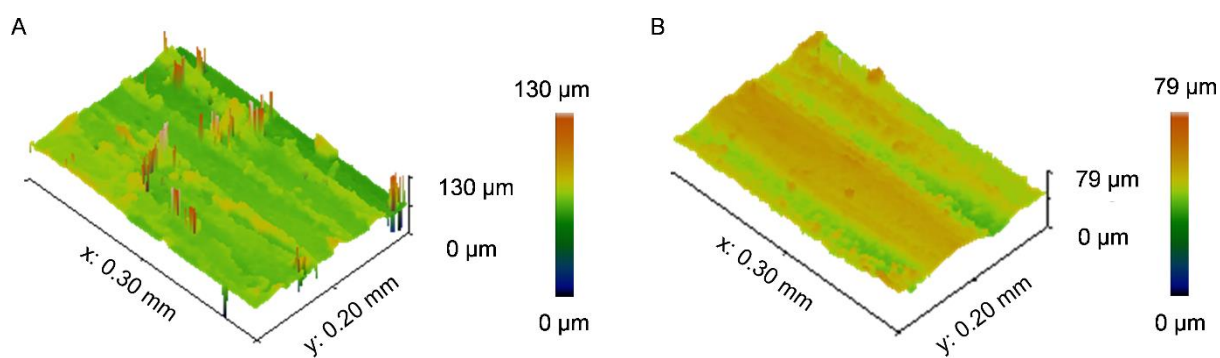


**Figure S14.** 3D surface profiles of 20-ZIF-8@spruce obtained by optical profilometry. (A) 3D surface profiles of 20-ZIF-8@spruce(R). (B) 3D surface profiles of 20-ZIF-8@spruce(T).



**Table S2.** Zn content and MOF loading determined by ICP-OES for ZIF-8@wood samples prepared with different 2-MeIm/Zn<sup>2+</sup> molar ratios.

<b>Sample name</b>	<b>Zn / wt%</b>	<b>Calculated MOF loading / wt.%</b>	<b>Standard deviation / wt.%</b>
<b>native wood</b>	-	-	-
<b>1:1</b>	1.5	*	*
<b>1:5</b>	3.2	11.0	0.4
<b>1:10</b>	2.7	9.3	0.7
<b>1:20</b>	2.5	8.8	0.3

\*According to XRD results, ZIF-8 is not formed in these conditions. Nevertheless, a zinc-based material is formed on the wood substrate as shown also by SEM.

**Table S3.** Surface roughness obtained for different native and modified wood samples, measured by optical profilometry.

<b>Sample names</b>	<b>Ra (μm)</b>
<b>Spruce (C)</b>	11.4
<b>Balsa (C)</b>	11.9
<b>Yew (C)</b>	6.5
<b>Spruce (R)</b>	7.6
<b>Spruce (T)</b>	6.3
<b>20-ZIF-8@spruce (C)</b>	5.5
<b>20-ZIF-8@spruce (R)</b>	4.4
<b>20-ZIF-8@spruce (T)</b>	3.8
<b>PDMS@spruce (C)</b>	4.2
<b>PDMS@spruce (R)</b>	2.5
<b>PDMS@spruce (T)</b>	1.4
<b>PDMS@balsa (C)</b>	4.7
<b>PDMS@yew(C)</b>	0.9

**Table S4.** Roughness of 1-(MeIm/Zn)@spruce(C) and ZIF-8@wood samples measured by AFM.

Sample names	Ra (nm)
1-(MeIm/Zn)@spruce(C)	37.1
5-ZIF-8@spruce(C)	169.1
10-ZIF-8@spruce(C)	233.5
20-ZIF-8@spruce(C)	286.5

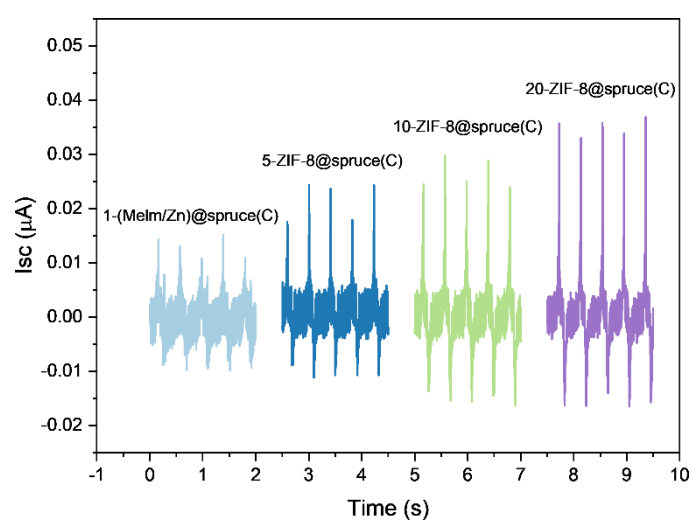


**Figure S15.** Short-circuit current of wood-TENG composed of a piece of native spruce(R) against a piece of ZIF-8@spruce(C) synthesized with different 2-MeIm/Zn<sup>2+</sup> ratios. It is worth mentioning that the 1-(MeIm/Zn)@spruce(C), which does not form ZIF-8 on wood generates the lowest I<sub>sc</sub>.

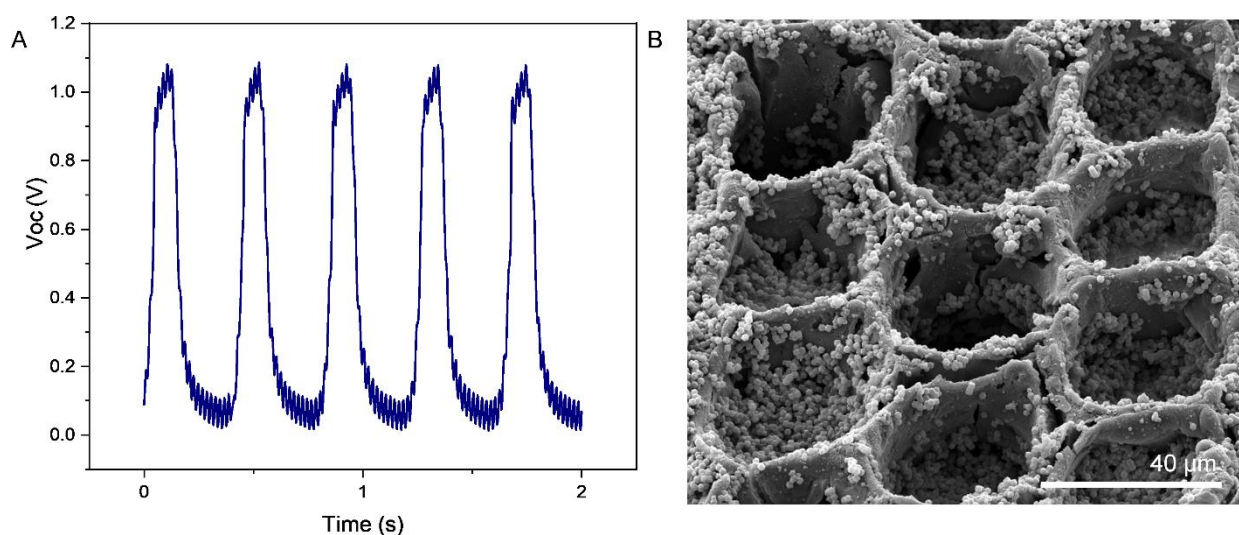


**Figure S16.** Electrical performance and the morphology of ZIF-8@spruce(C) obtained by physical coating. (A) Short-circuit current of wood-TENG made of a piece of native spruce(R) against a piece of ZIF-8@spruce(C) obtained by physical coating. (B) SEM image of ZIF-8@spruce(C) obtained by physical coating.

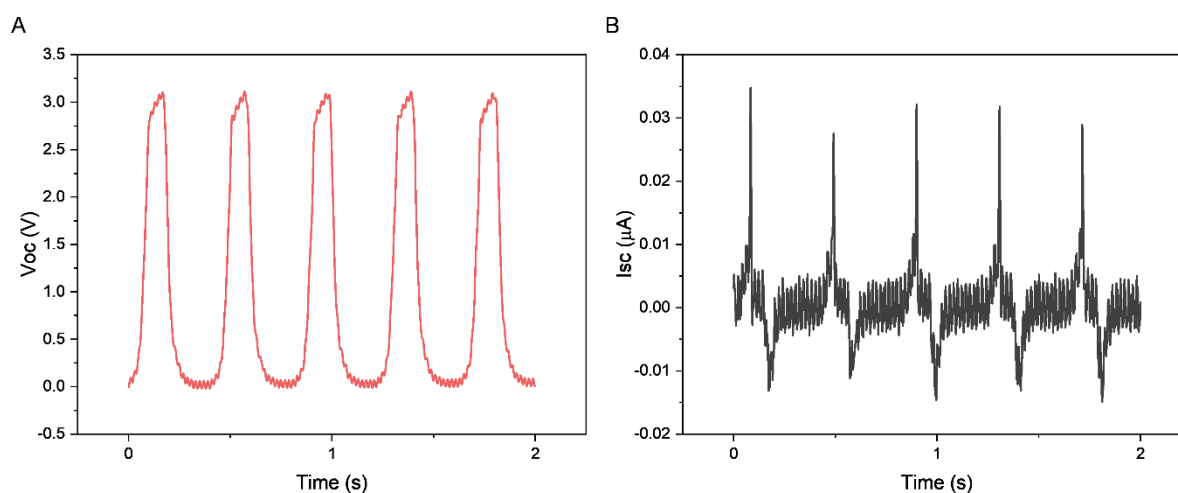


**Figure S17.** Electrical performance of wood-TENG composed of a piece of native spruce(R) against a piece of 20-ZIF-8@yew(C). (A) Open-circuit voltage. (B) Short-circuit current.

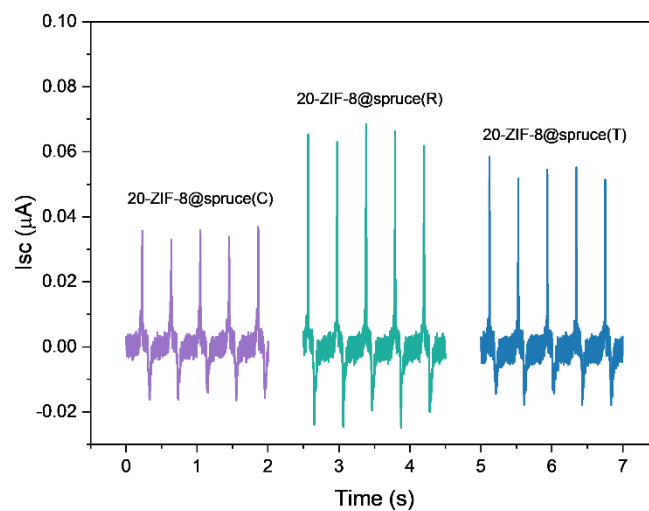


**Figure S18.** Short-circuit current of wood-TENG made of a piece of native spruce(R) against a piece of 20-ZIF-@spruce in different sections.

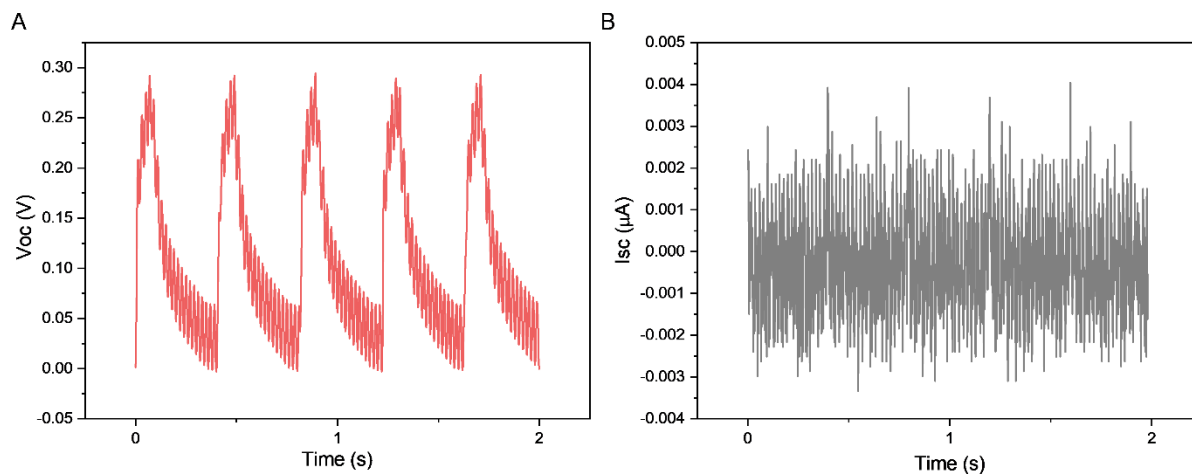


**Figure S19.** Electrical performance of wood-TENG made with two pieces of native spruce (R). (A) Open-circuit voltage. (B) short-circuit current.

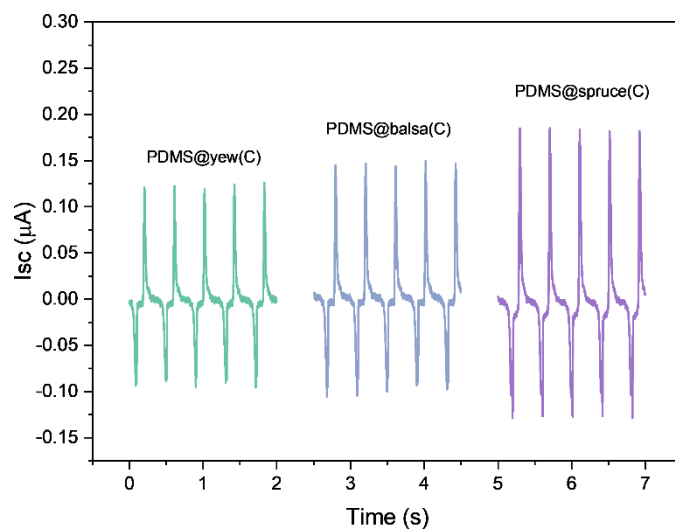


**Figure S20.** Short-circuit current of wood-TENG made with a piece of native spruce(R) paired to a piece of PDMS@yew(C), PDMS@balsa(C), and PDMS@spruce(C), respectively.

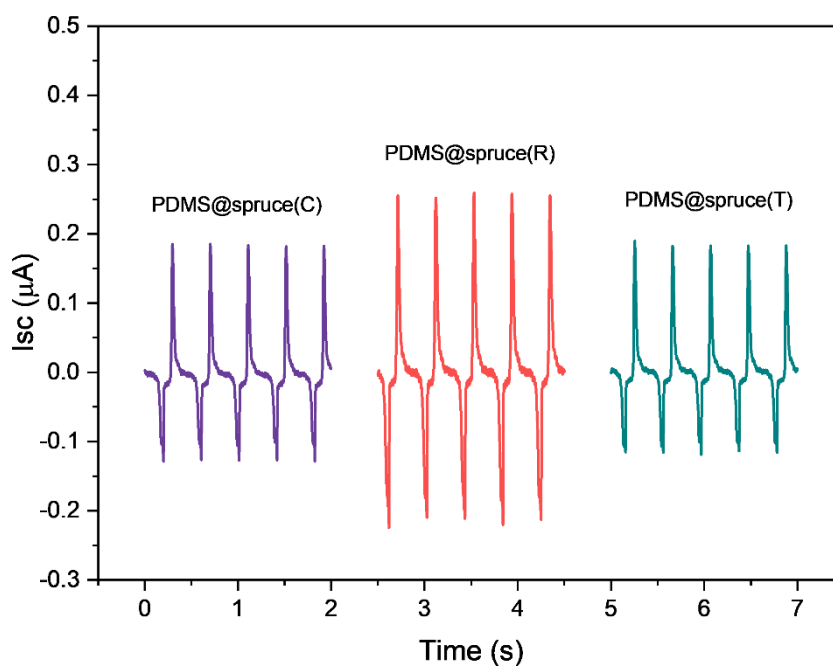


**Figure S21.** Short-circuit current of wood- TENG made with a piece of native spruce(R) paired to a piece of PDMS@spruce cut in different directions.

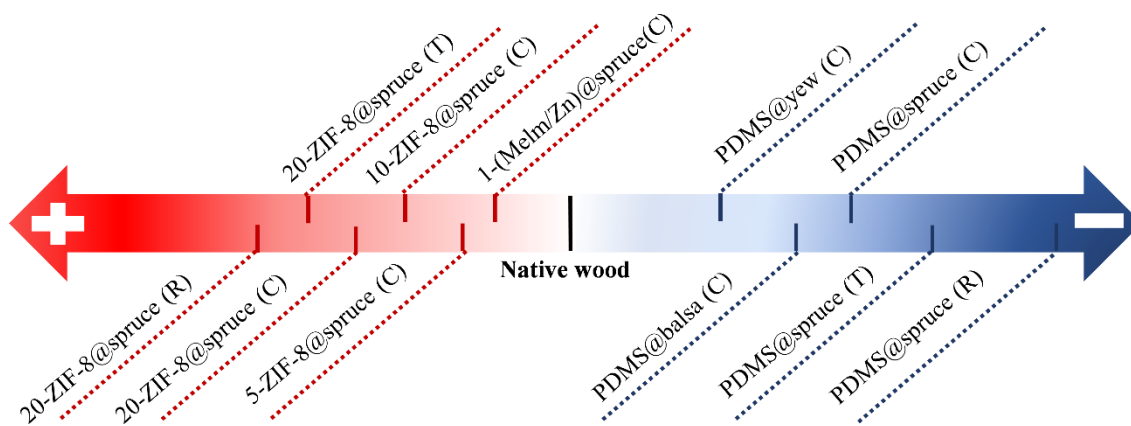


**Figure S22.** Relative position of native, ZIF-8-modified and PDMS-modified wood in the triboelectric series.

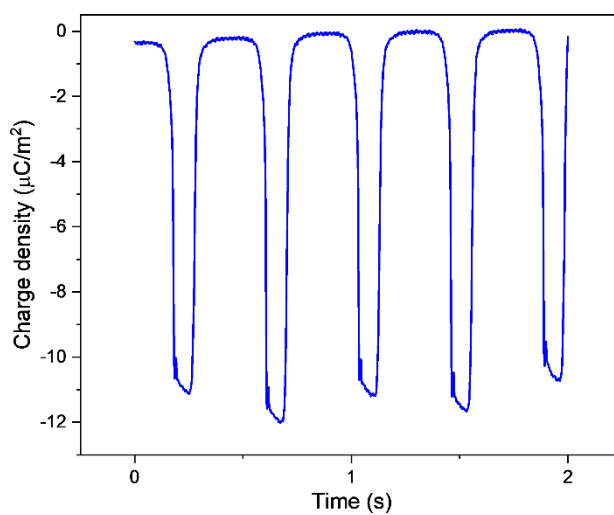


**Figure S23.** Transferred charge density for an optimized FW-TENG made of 20-ZIF-8@spruce(R) and PDMS@spruce(R) couples.

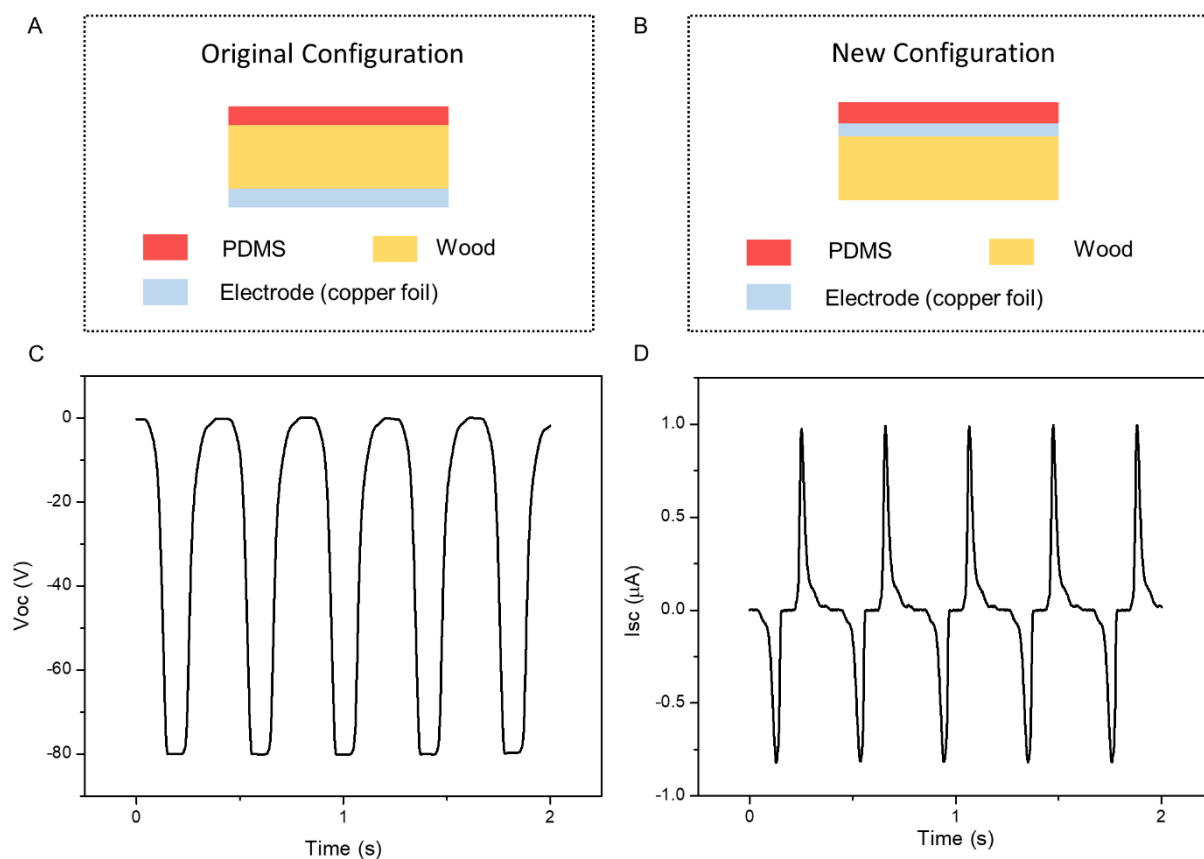


**Figure S24.** Illustration of the PDMS@ spruce(R) with different configurations and electrical performance of the PDMS@ spruce(R) with (“new”) configuration. (A) Illustration of the PDMS@ spruce(R) with the original configuration adopted in the present study. In this case, an electrode (commercial copper foil) is attached to the bottom of the wood, which will not hinder the utilization of the wood's microstructure. (B) Illustration of the PDMS@ spruce(R) with a different (“new”) configuration, where the electrode is placed between PDMS and wood, which may hinder wood's microstructure utilization. (C) Open-circuit voltage of a TENG, made of a piece of 20-ZIF-8@spruce(R) paired with PDMS@spruce(R) using the “new” configuration, all the other parameters being the same. (D) short-circuit current of a TENG, made of a piece of 20-ZIF-8@spruce(R) paired with PDMS@spruce(R) using the “new” configuration, all the other parameters being the same.

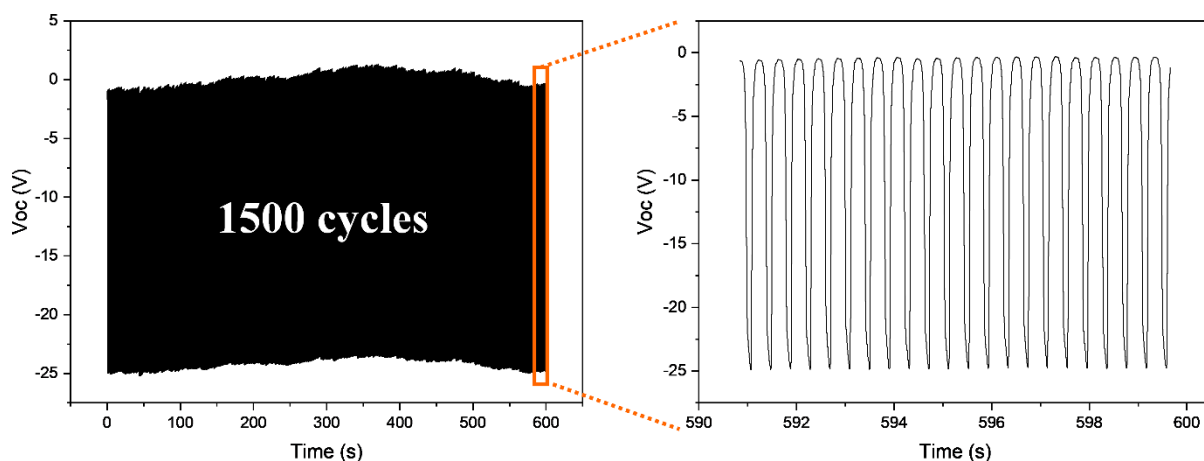


**Figure S25.** Cycling stability of our FW-TENG.

**Table S5.** Wood- and cellulose-based TENGs in previous literature

<b>Triboelectric material 1</b>	<b>Triboelectric material 2</b>	<b>Output performance</b>	<b>Size</b>	<b>Other parameters</b>	<b>Ref.</b>
Natural wood	PTFE	Voc = $220 \pm 20$ V Isc = $5.8 \pm 0.5$ $\mu$ A	64 cm <sup>2</sup>	-, 2 Hz	6
Paper	Kapton film	Voc = 200V Isc = 2.2 $\mu$ A	-	-, -	7
CNF	Silver nanowires	Voc = 21V Isc = 2.5 $\mu$ A	9 cm <sup>2</sup>	16.8 N force, 1 Hz	8
Delignified wood	PTFE	Voc = 81 v Isc = 1.8 $\mu$ A	9 cm <sup>2</sup>	20 N force, 1 Hz	17
CNF aerogel	Porous PDMS	Voc = 22.3 V Isc = 2.2 $\mu$ A	2 cm <sup>2</sup>	6 N force, 10 Hz	42
Cellulose acetate	PTFE	Voc = 4.5 V Isc = 9.1 $\mu$ A	8 cm <sup>2</sup>	0.33 N force, -	43

PTFE: poly(tetrafluoroethylene); CNF: cellulose nanofibrils; PDMS: poly(dimethylsiloxane);

- : not provided.



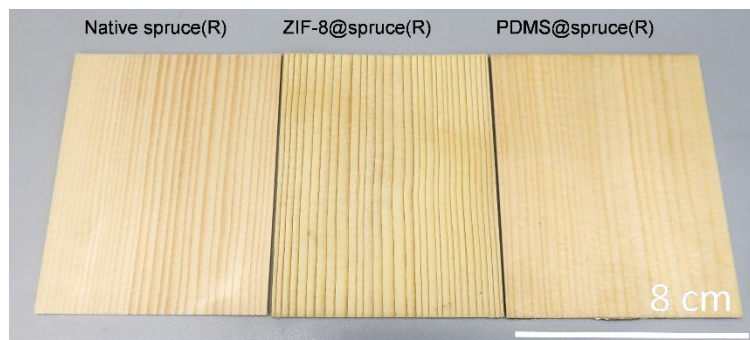


**Figure S26.** Photographs of native wood, ZIF-8@wood, and PDMS@wood, respectively.

**Table S6.** Color changes of wood before and after ZIF-8 and PDMS treatment.

	<b>Native wood</b>	<b>ZIF-8@ wood</b>	<b>PDMS@wood</b>
$\Delta L$	0	$-2.42 \pm 1.63$	$-0.91 \pm 1.35$
$\Delta a$	0	$-3.15 \pm 0.92$	$-0.93 \pm 0.75$
$\Delta b$	0	$5.78 \pm 1.3$	$2.41 \pm 0.85$
$\Delta E^*$	0	$7.01 \pm 2.21$	$2.74 \pm 1.77$



**Figure S27.** Photograph of a large-scale triboelectric wooden floor prototype (45 cm × 20 cm) made with six FW-TENGs electrically connected together.



## 4.4 Natural Wood-based Catalytic Membrane Microreactors for Continuous Hydrogen Generation

*Kunkun Tu<sup>1,2#</sup>, Simon Büchele<sup>3#</sup>, Sharon Mitchell<sup>3</sup>, Laura Stricker<sup>4</sup>, Chun Liu<sup>5</sup>, Christian Goldhahn<sup>1,2</sup>, Julien Allaz<sup>6</sup>, Yong Ding<sup>1,2</sup>, Roman Günther<sup>7,8</sup>, Zhidong Zhang<sup>9</sup>, Jianguo Sun<sup>1,2</sup>, Sandro Stucki<sup>1,2</sup>, Guido Panzarasa<sup>1,2</sup>, Samuel C. Zeeman<sup>5</sup>, Ingo Burgert<sup>1,2</sup>, Javier Pérez-Ramírez<sup>3\*</sup>, Tobias Keplinger<sup>1,2\*</sup>*

<sup>1</sup> Wood Materials Science, Institute for Building Materials, ETH Zürich, 8093 Zürich, Switzerland

<sup>2</sup> WoodTec Group, Cellulose & Wood Materials, EMPA, 8600 Dübendorf, Switzerland

<sup>3</sup> Institute for Chemical and Bioengineering, Department of Chemistry and Applied Biosciences, ETH Zürich, 8093 Zürich, Switzerland

<sup>4</sup> Soft Materials, Department of Materials, ETH Zürich, 8093 Zurich, Switzerland

<sup>5</sup> Institute of Molecular Plant Biology, Department of Biology, ETH Zürich, 8092 Zürich, Switzerland

<sup>6</sup> Institute of Geochemistry and Petrology, ETH Zürich, 8092 Zürich, Switzerland

<sup>7</sup> Laboratory of Adhesives and Polymer Materials, Institute of Materials and Process Engineering, Zürich University of Applied Sciences, 8401 Winterthur, Switzerland

<sup>8</sup> Laboratory for Multifunctional Materials, Department of Materials, ETH Zürich, 8093 Zürich, Switzerland

<sup>9</sup> Durability of Engineering Materials, Institute for Building Materials, ETH Zürich, Stefano-Francini-Platz 3, 8093 Zürich, Switzerland

# These authors contributed equally: Kunkun Tu, Simon Büchele

\* Corresponding authors: E-mail: [jpr@chem.ethz.ch](mailto:jpr@chem.ethz.ch); [tkeplinger@ethz.ch](mailto:tkeplinger@ethz.ch)

## Abstract

The development of controlled processes for continuous hydrogen generation from solid-state storage chemicals such as ammonia borane is central to integrating renewable hydrogen into the clean energy mix. However, to date most reported platforms operate in batch mode, posing a challenge for controllable hydrogen release, catalyst reusability and large-scale operation. To address these issues, we developed flow-through wood-based catalytic microreactors, characterized by inherent natural orientated microchannels. The prepared structured catalysts utilize silver-promoted palladium nanoparticles supported on metal-organic framework (MOF) coated wood microreactors as the active phase. Catalytic tests demonstrate their high controllable hydrogen production in continuous mode and by adjusting the ammonia borane flow and wood species, we reach stable productivities of up to  $10.4 \text{ cm}^3_{\text{H}_2} \text{ min}^{-1} \text{ cm}^{-3}_{\text{cat}}$ . The modular design of the structured catalysts proves readily scalable. Our versatile approach is applicable for other metal and MOF combinations, thus comprising a sustainable and scalable platform for catalytic dehydrogenations and applications in the energy-water nexus.

## Keywords:

structured catalyst, wood, metal-organic framework, hydrogen generation, flow reactor

## 1 Introduction

Green hydrogen ( $\text{H}_2$ ) as a sustainable and clean energy source is an emerging choice to substitute fossil fuels towards a carbon-neutral world.<sup>1,2</sup> Hence, the development of green and renewable hydrogen solutions represents one of the key points in the “European Green Deal”.<sup>3</sup> However, efficient storage, safe transportation, and controllable release of  $\text{H}_2$  remain ongoing challenges.<sup>4,5</sup> In this regard, solid and liquid hydrogen storage chemicals gain interest as promising candidates for onboard hydrogen applications.<sup>6</sup> For example, ammonia borane ( $\text{NH}_3\text{BH}_3$ ) possesses unique properties, such as a gravimetric capacity of 19.6 wt.%  $\text{H}_2$ ,

water-solubility, safe handling and transportation in the dry state, nontoxicity, and chemical stability.<sup>7</sup> In the presence of suitable metal-based catalysts, room-temperature hydrolysis or methanolysis permits hydrogen release.<sup>8-11</sup> Reported systems can be both noble- and base-metal-based,<sup>12,13</sup> and synergistic effects have been evidenced for bimetallic systems including CuRu,<sup>14</sup> PtCu,<sup>15</sup> AgPd,<sup>16,17</sup> as well as NiRu.<sup>18</sup> In particular, AgPd stands out due to its high catalytic activity compared to other monometallic and bimetallic systems.<sup>19-21</sup> In order to avoid metal aggregation during the reaction and hence enhance the catalytic activity, metal-organic frameworks (MOFs) have been proposed as supports for alloy nanoparticles, such as AgPd/UiO-66 and AuCo/MIL-101.<sup>20,22</sup> Their extraordinarily high surface area, well-defined pore structure, and high porosity enable MOFs to stabilize metal nanoparticles while maintaining the accessibility for reagents.<sup>23-25</sup>

Most reported studies utilize catalysts in powder form, which causes multiple drawbacks, such as metal aggregation and metal loss during catalyst recovery, which can significantly reduce their catalytic activity.<sup>26,27</sup> Moreover, the catalysts separation from the reaction mixture is a complex operation, impeding a successful process control, which is essential for safe hydrogen generation in practical applications.<sup>28,29</sup> Alternatively, structured catalysts based on depositing metal catalysts on porous supports were developed to address these limitations.<sup>30-32</sup> However, current catalyst support materials, such as cordierite monoliths, are based on non-renewable resources, often require time- and energy intensive preparative routes. In addition, most of these structured catalyst systems operate in batch mode, unable to control the H<sub>2</sub> production rate. Various bio-based materials, such as rattan and wood, have been used as catalysts carriers.<sup>33,34</sup> In particular, natural wood microreactors possess natural microchannels along its growth direction providing a high-efficiency liquid transportation corridor.<sup>35</sup> In addition they are of low-cost, renewable, and of high mechanical strength.<sup>36</sup> Hence, wood represents an ideal porous scaffold system for flow-through applications, which has been previously demonstrated for contaminant degradation, biocatalysis, and solar steam generation.<sup>37-39</sup> Nevertheless, natural

wood microreactors have yet not been used for hydrogen production. In addition, previously reported flow-through wood reactors mainly utilized low efficient capillary force or gravity rather than pressure.<sup>40,41</sup>

Here, we present a simple and versatile strategy to prepare structured bimetallic silver-palladium catalytic native wood microreactors for continuous hydrogen generation from ammonia borane by a pressure-driven flow-through system. The low surface area of wood materials, which often limits the catalysts loading, is addressed by functionalizing wood scaffolds with the metal-organic-framework (MOF) UiO-66 to support the desired metal species (**Figure 1a**). The structure of UiO-66 is highly stable in water, making it practically applicable in aqueous media.<sup>42</sup> Thanks to the effective coverage of the wood internal surfaces with UiO-66 and the uniform distribution of palladium and silver, the wood-based catalytic microreactor exhibited remarkable H<sub>2</sub> generation performance (**Figure 1b**). In short, the wood-based microreactor is characterized by excellent mechanical properties, high mass transfer efficiency, adjustable H<sub>2</sub> generation rate, easy recovery, scalability, and safety (**Figure 1c**). These desirable features of the microreactor enable its potential applications in catalytic dehydrogenations in the energy-water nexus.

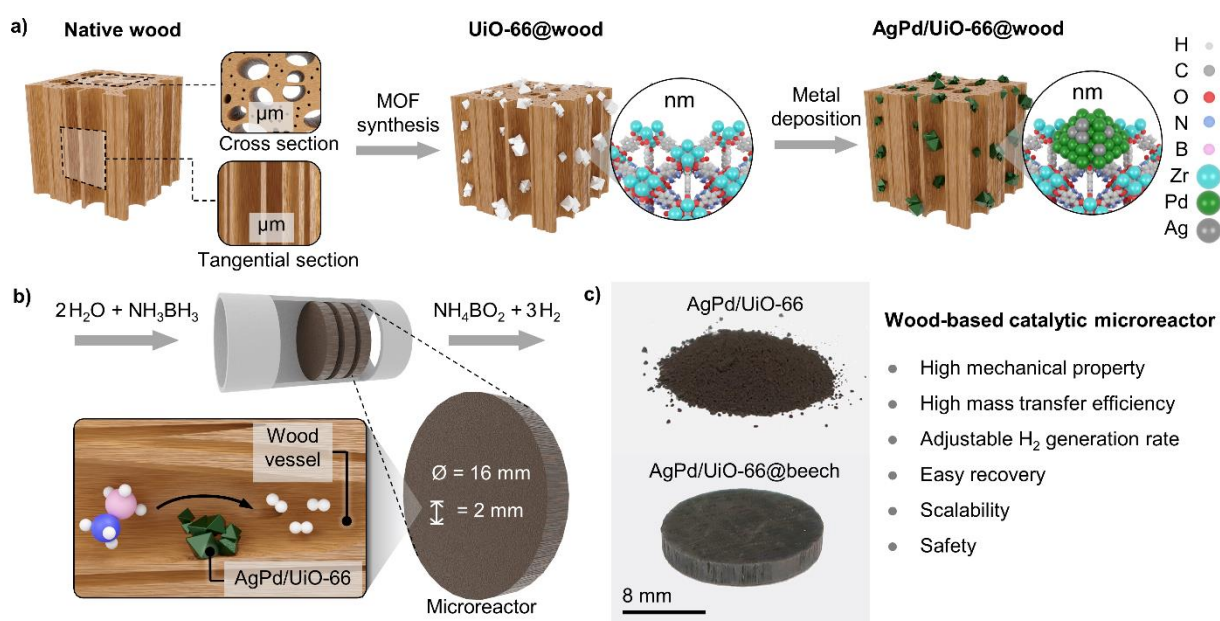


**Figure 1.** Scheme of the synthesis and catalytic application of wood-based structured catalysts. (a) The preparation steps and (b) the modular use of structured catalytic reactors in series for the hydrogen generation from ammonia borane in flow. (c) The utilization of wood-based catalytic microreactor under pressure-driven flow-through system possesses many advantages compared to using powder catalysts in batch mode, including high mechanical property, high mass transfer efficiency, adjustable H<sub>2</sub> generation rate, easy recovery, scalability, and safety.

## 2. Results and Discussion

### 2.1 Functionalizing Wood Microreactors with MOF

Beech, a diffuse-porous hardwood species, was selected to prepare AgPd/UiO-66@wood composites due to its higher elastic modulus (60 MPa) compared to other wood species, such as spruce, basswood, and poplar (**Figure S1**).<sup>43</sup> Beech possesses open and aligned microchannels (5-55  $\mu\text{m}$  diameter), which mainly comprise the cell lumina of vessels and fibers (**Figure 2a**). UiO-66 was grown *in situ* within beech through a hydrothermal treatment with zirconium chloride (ZrCl<sub>2</sub>) and 2-aminoterephthalic acid (NH<sub>2</sub>-BDC) at 393 K. After this *in situ* growth, the microchannels within the wood structure remain intact but the cell wall surface appears slightly rougher compared to native beech evidencing a uniform distribution of UiO-66 particles which are around 200 nm in size (**Figure 2b** and **S2**). The X-ray powder diffraction (XRD) pattern of UiO-66@beech reveals two broad diffraction peaks centered around  $2\theta = 16^\circ$  and  $22^\circ$  associated to cellulose, along with the characteristic diffraction peaks at  $2\theta = 7.4^\circ$  and  $8.5^\circ$ , attributed to the (111) and (200) crystal faces of UiO-66, which confirms the successful MOF incorporation (**Figure S3**).<sup>44,45</sup> Fourier transform infrared (FTIR) spectra also reveal characteristic signatures of UiO-66, including N-H bending ( $1655\text{ cm}^{-1}$ ) and C-H stretching ( $1260\text{ cm}^{-1}$ ) bands, which are absent for native beech (**Figure S4**). The N-H bending band originates from the amino groups of the linker molecule (NH<sub>2</sub>-BDC), which played an essential role in functionalizing the wood with MOF. Uniform distributions of MOFs containing metals other than zirconium could also be obtained using NH<sub>2</sub>-BDC as a linker, including

MOF(Ni)@beech and MOF(FeCo)@beech. In contrast, UiO-66@beech prepared using terephthalic acid (BDC), an organic linker without amino groups, shows little UiO-66 nanoparticles within wood lumina (**Figure S5**). We attribute this to the formation of hydrogen bonds between the amine groups of the NH<sub>2</sub>-BDC linker and the hydroxyl groups of wood macromolecules (cellulose, hemicelluloses, and lignin), which facilitate the MOF crystals nucleation and adhesion within the wood channels.

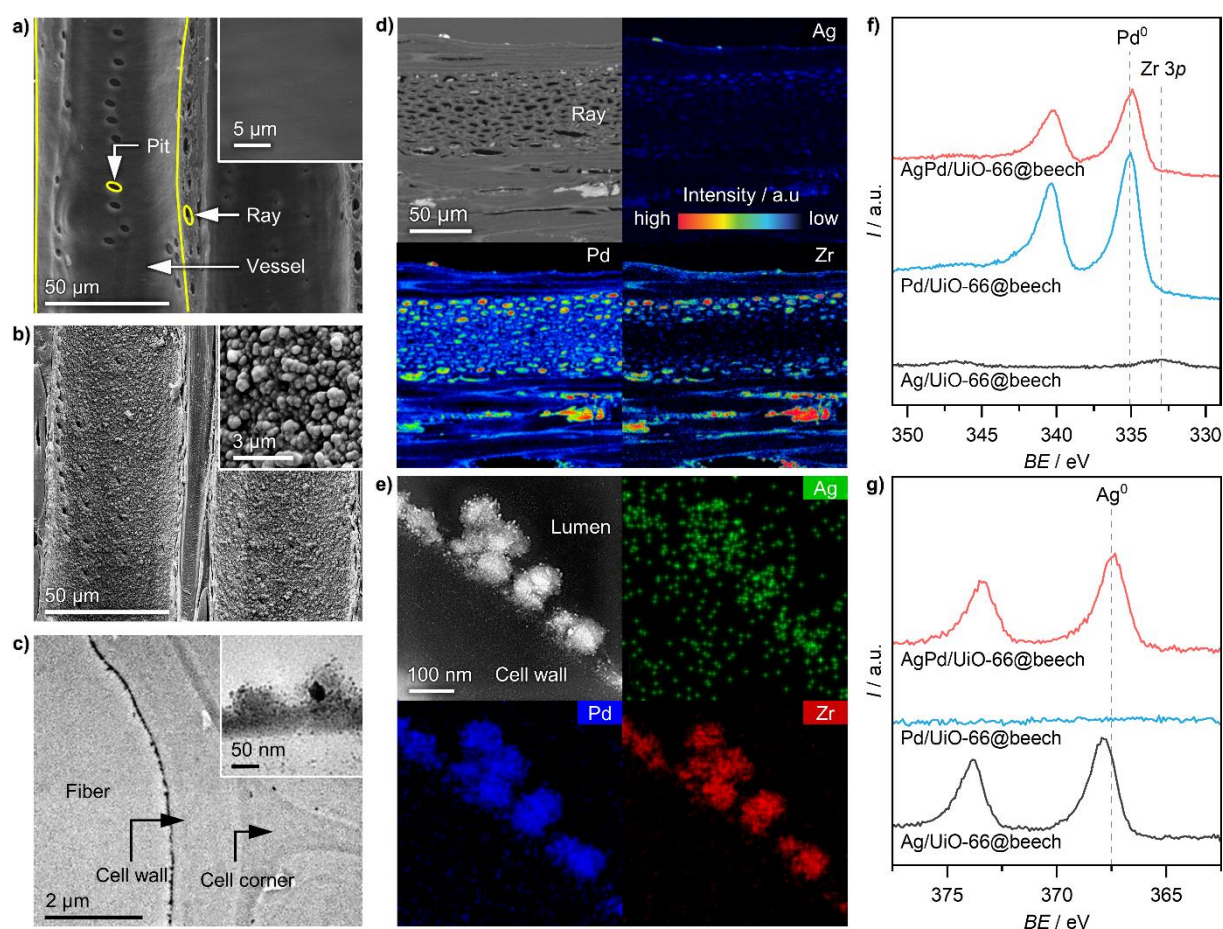


**Figure 2.** Morphology, phase distribution and electronic properties of native wood and structured catalysts. SEM images of (a) native beech and (b) UiO-66@beech tangential sections. The insets correspond to magnified images. (c) TEM image of AgPd/UiO-66@beech cross sections at the cell wall of a fiber. (d) SEM images and corresponding WDS elemental composition maps of AgPd/UiO-66@beech at ray in tangential section. (e) HAADF-STEM images and EDX maps of AgPd/UiO-66@beech. (f) Pd 3d and (g) Ag 3d XPS spectra of AgPd/UiO-66@beech, Ag/UiO-66@beech, and Pd/UiO-66@beech.

## 2.2 Metal Deposition in MOF Functionalized Wood Microreactors

Catalytic palladium and/or silver were formed within the MOF-functionalized wood by a simultaneous wet deposition method followed by reduction with sodium borohydride (NaBH<sub>4</sub>).



The resulting bimetallic structured catalyst, named AgPd/UiO-66@beech, exhibited abundant silver and palladium containing MOF particles of uniform size, distributed on the vessels and fibers lumen surface within beech, as revealed by transmission (TEM) and scanning (SEM) electron microscopy (**Figure 2c** and **S6**). Wavelength-dispersive spectroscopy (WDS) and energy-dispersive X-ray spectroscopy (EDX) elemental maps of AgPd/UiO-66@beech confirm the uniform distribution of palladium at the micro and nano scale (**Figure 2d** and **e**). The hydrothermal synthesis temperature affects the dimensionality of MOFs,<sup>46</sup> which influences the interaction with supported metals and plays an important role for the physical and chemical properties of the metal-MOF systems.<sup>23</sup> Hence, a sample with lower MOF hydrothermal synthesis temperature (353 K), labeled AgPd/UiO-66(353)@beech was investigated too. It shows a similar phase distribution of the MOF and the metals within the wood (**Figure S7**), but significantly lower palladium content, as confirmed by inductively-coupled plasma optical emission spectroscopy (ICP-OES, **Table 1**). In agreement with the chosen synthesis protocol, the palladium content was higher than the silver content (ratio of Pd:Ag = 3.5 for AgPd/UiO-66@beech; ratio in synthesis Pd<sup>2+</sup>:Ag<sup>+</sup>=4). X-ray photoelectron spectroscopy (XPS) shows that for all metal-containing structured catalysts (silver, palladium, and bimetallic samples) both the Pd 3d<sub>5/2</sub> (335.0 eV) and Ag 3d<sub>5/2</sub> (367.3 eV) signal indicate a metallic state with a small shift of 0.4 eV towards lower binding energy in the peak Ag 3d<sub>5/2</sub> position for the bimetallic catalyst, which could be indicative for the formation of alloy particles (**Figure 2f-g** and **S8**).<sup>47,48</sup> No strong contributions indicative of oxidized metal species (Ag<sup>+</sup> or Pd<sup>2+</sup>) occurred at higher binding energies. The XRD reflections at 2θ = 38.3° and 39.8° correspond to Ag(111) and Pd(111), respectively. The characteristic UiO-66 reflection vanishes for AgPd/UiO-66@beech, which implies that the high metal content may alter the MOF crystal structure (**Figure S3**). In addition, argon sorption evidenced a decrease in pore volume, suggesting that the metal nanoparticles are located on the external surface and inside the pores of UiO-66 (**Figure S3**).<sup>49,50</sup> To verify the beneficial role of MOFs for the metal deposition, a

control sample without MOF (AgPd@beech) was prepared, achieving a much lower metal content (0.4 wt.% silver and 0.3 wt.% palladium) and dispersion (**Figure S9** and **Table 1**).

**Table 1.** Metal and MOF content of catalyst powders and structured analogs.

Sample	Ag <sup>a)</sup> / wt.%	Pd <sup>a)</sup> / wt.%	UiO-66 <sup>a,b)</sup> / wt.%
Ag/UiO-66	3.9	-	-
Pd/UiO-66	-	13.5	-
AgPd/UiO-66	2.0	11.7	-
AgPd/UiO-66(353)	1.3	9.0	-
UiO-66@beech	-	-	0.7
AgPd@beech	0.4	0.3	0.0
AgUiO-66@beech	0.8	-	1.5
Pd/UiO-66@beech	-	1.6	1.4
AgPd/UiO-66(353)@beech	0.4	0.6	1.8
AgPd/UiO-66@beech	0.4	1.4	0.6
AgPd/UiO-66@spruce	1.2	2.2	2.2
AgPd/UiO-66@basswood	0.3	2.0	2.5
AgPd/UiO-66@poplar (used <sup>c)</sup> )	0.8 (0.4)	3.3 (2.8)	3.2 (2.9)

a) ICP-OES. b) based on the measurement of the Zr content and assuming a stoichiometric composition of UiO-66. c) after 150 min of reaction,  $F_L = 4 \text{ cm}^3 \text{ min}^{-1}$ ,  $m_{\text{cat}} = 0.14 \text{ g}$ ,  $c_{\text{NH}_3\text{BH}_3,0} = 0.19 \text{ M}$ .

### 2.3 Reference Powder Catalysts

For a better insight into the metal-decorated MOF nanostructures and the interaction between palladium and silver, metal-containing MOF powders were prepared and analyzed in detail. In agreement with the structured catalysts results, the addition of large amounts of metal reduces the crystallinity and pore volume of AgPd/UiO-66 (**Figure S10**). Nevertheless, for AgPd/UiO-66(353), which was prepared at 353 K, the diffraction peaks of UiO-66 can still be detected, and the loss of pore volume is less pronounced (**Figure S11**). This is likely related to the lower metal content compared to AgPd/UiO-66 (10.3 vs. 13.7 wt.% combined silver and palladium), leaving a larger part of the MOF crystal unchanged. The TEM images of the powder samples show that highly dispersed palladium arises even at high metal contents, but Ag tends to agglomerate into large particles located on the external surface of MOF particles (**Figure 3, S12** and **S13**). The role of silver was probed by CO diffuse reflectance infrared Fourier

transform spectroscopy (CO-DRIFTS, **Figure 3c**). A red-shift of the signal for both  $\eta 1$  (end-on) and  $\eta 2$  (bridging) is apparent when comparing AgPd/UiO-66 to Pd/UiO-66, which is most prominent at higher analysis temperatures. Such observations have previously been linked to electronic interactions between metals that affect the CO adsorption properties. This can be related to the formation of an AgPd alloy,<sup>51,52</sup> and is in line with the slight shift towards lower binding energy in the Ag  $3d_{5/2}$  peak observed in XPS and the slight shift of the Pd(111) reflection towards smaller angles observed in XRD (**Figure 3d, S8, and S14**).<sup>47,48</sup> The lattice spacing observed by TEM is close to the one of pure palladium along the (111) lattice (**Figure S15**), while EDX maps show that silver rich regions exist, suggesting that the alloy particles mainly consist of palladium, with a small silver content but enough to modify its surface properties.

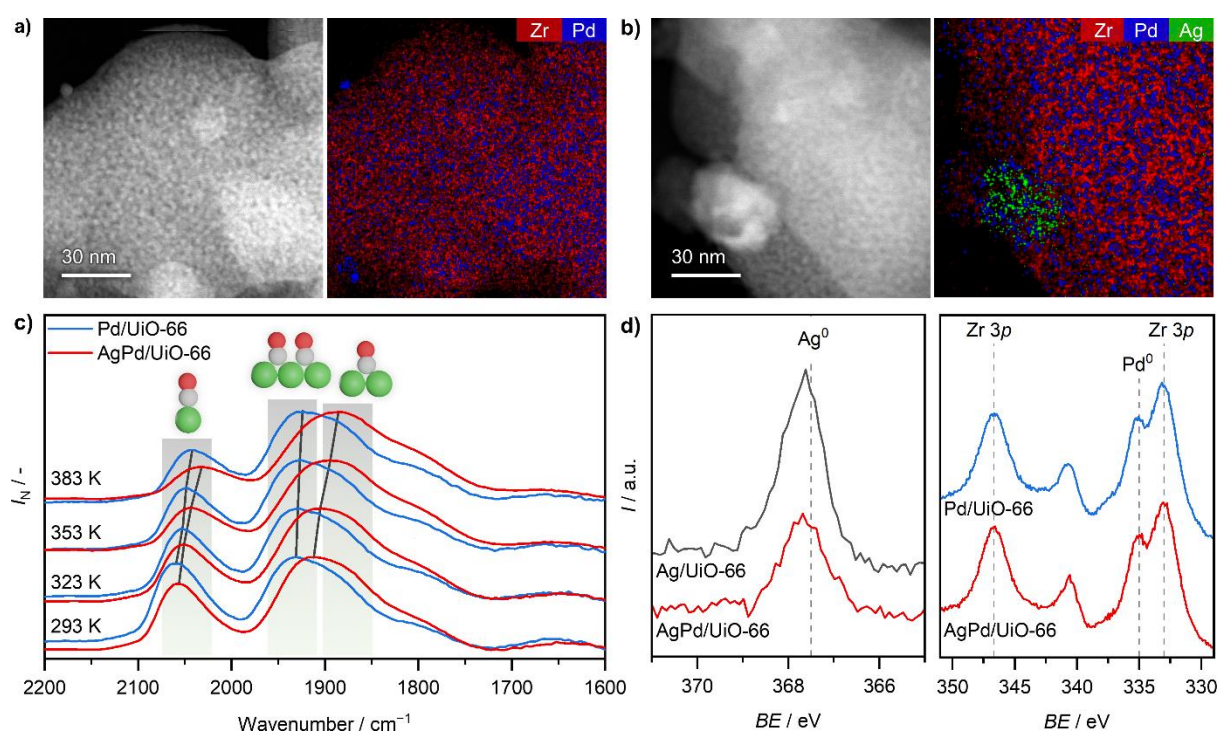


**Figure 3.** Phase distribution and electronic properties of metal-containing MOF powders. HAADF-STEM images and corresponding EDX maps of (a) Pd/UiO-66 and (b) AgPd/UiO-66. (c) CO-DRIFTS at different temperatures for Pd/UiO-66 and AgPd/UiO-66, with schemes identifying different adsorption modes. (d) Ag  $3d$  and Pd  $3d$  XPS spectra of metal-containing UiO-66 samples.

## 2.4 Catalytic Performance in Batch and Continuous Mode

We first evaluated the performance of powder catalysts in the hydrolytic dehydrogenation of ammonia borane in batch tests (**Figure 4a**). The activity of powder catalysts strongly depended on the identity of the active metal phase. The bimetallic AgPd/UiO-66 exhibited higher metal-normalized rate of  $45.4 \text{ mol}_{\text{H}_2} \text{ min}^{-1} \text{ mol}_{\text{metal}}^{-1}$  compared to the monometallic samples Ag/UiO-66 and Pd/UiO-66, which evidence rates of 20.2 and  $16.6 \text{ mol}_{\text{H}_2} \text{ min}^{-1} \text{ mol}_{\text{metal}}^{-1}$ , respectively, supporting the analysis results that silver acts as an electronic promoter of palladium. In the case of powder catalysts termination of the reaction requires the catalysts separation from the reaction mixture with the assistance of centrifugation or filtration, which is unable to switch on/off hydrogen release easily, weakening the safety of hydrogen production in practical application. Structured catalysts performed better than powder catalysts in this aspect (**Figure S16, S17, and Video S1**). Applying the structured catalyst in a flow setup allow to simply switch on/off by controlling the flow rate (**Figure 4b, c, S18 and Video S2**). To assess hydrogen generation performance of the structured catalyst in a flow setup, we used beech-based structured catalysts to enable a fair comparison between different metal species, keeping the wood properties constant. It is apparent that metal is necessary to generate hydrogen, as neither native beech, nor UiO-66@beech, show any catalytic behavior (**Figure 4d**). Consistent with the trend observed for the powder systems, AgPd/UiO-66@beech exhibited the best performance among the evaluated metal combinations. From the results obtained for different beech-based structured catalysts several conclusions can be drawn (**Figure 4d and Table 1**): *i*) Hydrogen generation performance increases with the metal loading. *ii*) Functionalization with UiO-66 enables increased metal loading within the wood, which can be further enhanced by raising the hydrothermal synthesis temperature of the MOF. *iii*) Bimetallic catalysts show higher catalytic activity compared to monometallic systems. In addition, we tested the hydrogen generation performance of MOF(Ni)@beech and MOF(FeCo)@beech to demonstrate that our

approach for preparing microreactors can be readily adapted to other catalysts, thus enabling the development of a sustainable platform for catalytic dehydrogenations (**Figure S19**).

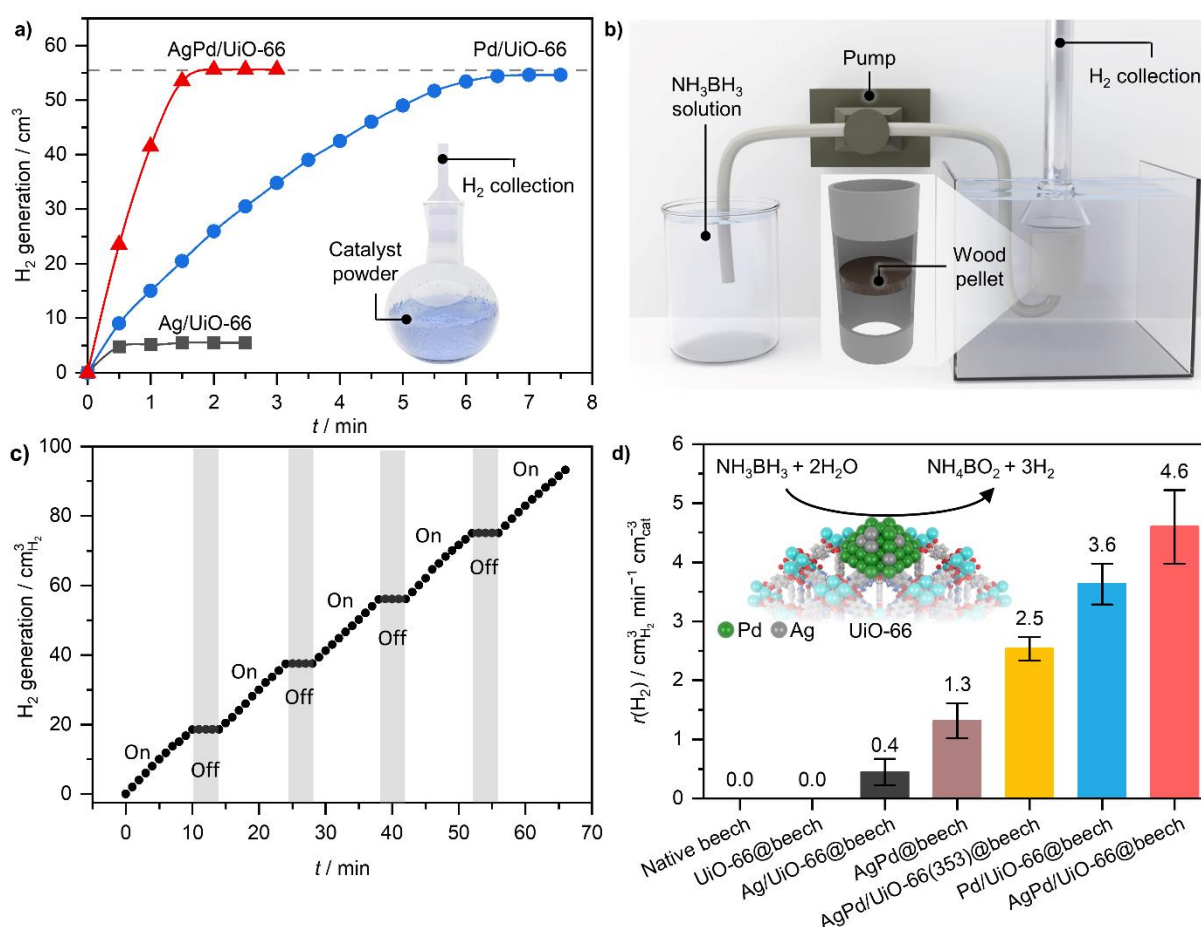


**Figure 4.** The catalytic performance in ammonia borane decomposition. (a) Hydrogen generation performance of metal-containing MOF powders. Inset is the scheme of the hydrogen generation setup for powder samples in batch mode. (b) Scheme of the hydrogen generation setup for structured catalysts in continuous flow. (c) Controllable hydrogen generation from ammonia borane using AgPd/UiO-66@beech under 4 cm<sup>3</sup> min<sup>-1</sup> flow rate (on) or 0 cm<sup>3</sup> min<sup>-1</sup> flow rate (off). (d) Hydrogen generation performance from ammonia borane for different structured catalysts. Reaction conditions: (a)  $V_L = 5 \text{ cm}^3$ ,  $m_{\text{cat}} = 29 \text{ mg}$ ,  $c_{\text{NH}_3\text{BH}_3,0} = 0.19 \text{ M}$ , and (c and d)  $F_L = 4 \text{ cm}^3 \text{ min}^{-1}$ ,  $m_{\text{cat}} = 0.22\text{-}0.27 \text{ g}$ ,  $c_{\text{NH}_3\text{BH}_3,0} = 0.19 \text{ M}$ .

## 2.5 Effect of the Microchannel Structure on Hydrogen Generation

Different wood species have different microstructures. To assess the role of the wood's microstructure in hydrogen generation, bimetallic structured catalysts based on four wood species (labeled AgPd/UiO-66@wood, with wood = spruce, beech, basswood, and poplar) were evaluated. Cross sections reveal different pore sizes, which originate from different cell types.

Spruce is a softwood with mainly one cell type, which varies in size (tracheid); beech, basswood, and poplar are hardwood species mainly consisting of two cell types: vessels (big pores) and fibers (small pores, **Figure 5a**). After functionalization with AgPd/UiO-66 following the same procedure adopted for beech, the lumen surface of each wood sample is uniformly decorated (**Figure S20**). Each wood species displayed different hydrogen generation performance (**Figure 5b** and **S21**). To explain these results, the wood structure can be regarded as an ensemble of aligned microchannels. The applied pressure difference (Poiseuille flow) drives the flow of the ammonia borane solution along a channel. The AgPd/UiO-66 particles on the microchannel wall (cell wall surface) generate hydrogen, which then diffuses inside the liquid towards the center of the channel. A rigorous prediction of the hydrogen concentration field inside the channels is outside the scope of the present work and would require solving the mass and momentum conservation equation (Navier-Stokes) for the flow, as well as two coupled advection-diffusion equations with a source and a sink localized at the channel wall, for the hydrogen and ammonia borane respectively. Moreover, the presence of gaseous hydrogen bubbles further complicates the behavior. However, the trends observed for the total hydrogen generation can be explained with a simplified description of the involved mass transport processes. We observe an increase in the total generated hydrogen (flux  $\dot{m}_{H_2}$ ) with the area of the channels' wall ( $A = \sum_i P_i \cdot L$ , **Figure S21**). Here,  $P_i$  denotes the perimeter of the cross section of the  $i$ -th channel (yellow lines in **Figure 5a** and **b**), extracted from the images of the cross sections according to the procedure described in the experimental section:  $\sum_i P_i$  is the sum of the perimeter of microchannels (vessel and fiber pores in hardwood, tracheid pores in softwood);  $L = 2$  mm is its length, namely the thickness of the wood block, assumed to be constant for all channels. According to the empirical formula for advective mass transport, from a solid surface to an adjacent fluid flow, we expect an increase of the mass flux with the exposed surface area  $A$ , since  $\dot{m}_{H_2} = h_c \cdot \Delta C \cdot A$ .<sup>53</sup> Here,  $h_c$  is the transport coefficient, and  $\Delta C$  is the mass concentration difference between the wall, where hydrogen is generated, and the bulk fluid.

Note that  $\Delta C$  changes along the channel due to the mass transfer process, and  $h_c$  is also a function of the local velocity. Therefore, deviations from a trivial linear trend should be expected. A higher imposed flow results in an overall larger  $\Delta C$ , as advection replenishes the gradients that have been smoothed out by mass transfer. Hence, the hydrogen mass flux is larger for higher driving flows (**Figure 5c**). Following this simplified description and consistent with measurements by mercury porosimetry and SEM in tangential sections (**Figure S22** and **S23**), we found that poplar has the largest channel surface area, and the highest hydrogen generation rate followed by basswood, beech, and spruce. Although AgPd/UiO-66 also grew on the exterior surface of wood, the experimental setup enforced liquid to flow only through the pores of the structured catalyst (**Figure S18**), ensuring that the observed differences are governed by the internal pore structure of distinct wood species. It can also explain the non-linear relationship between metal content and the hydrogen generation rate, as not all metal particles participate in hydrogen generation. By increasing the external flow from  $4 \text{ cm}^3 \text{ min}^{-1}$  to  $12 \text{ cm}^3 \text{ min}^{-1}$ , the hydrogen generation rate increases, though to a different extent for the different species (below 5% for spruce, up to around 50% for beech, **Figure 5c**), due to the anatomical structure differences, such as pits and perforation plates. The highest hydrogen production rate was obtained for the sample AgPd/UiO-66@poplar, showing up to  $10.4 \text{ cm}^3_{\text{H}_2} \text{ min}^{-1} \text{ cm}^{-3}_{\text{cat}}$  at a flow of  $12 \text{ cm}^3 \text{ min}^{-1}$ . The mass transport considerations reveal that employing wood reactors with bigger channel surface area and raising the external flow rate can improve the hydrogen generation performance, mitigating transport limitations. It provides hitherto unexplored information on the structure-performance relationships of wood-based reactors for water-based adsorption and catalytic reactions in flow systems.<sup>37,54-56</sup> However, due to the mass transfer limitation and complex wood structure, it is not straight forward to extract representative kinetic information in flow systems.<sup>57</sup> Detailed kinetic investigations are beyond the scope of this study and will be undertaken in future work.



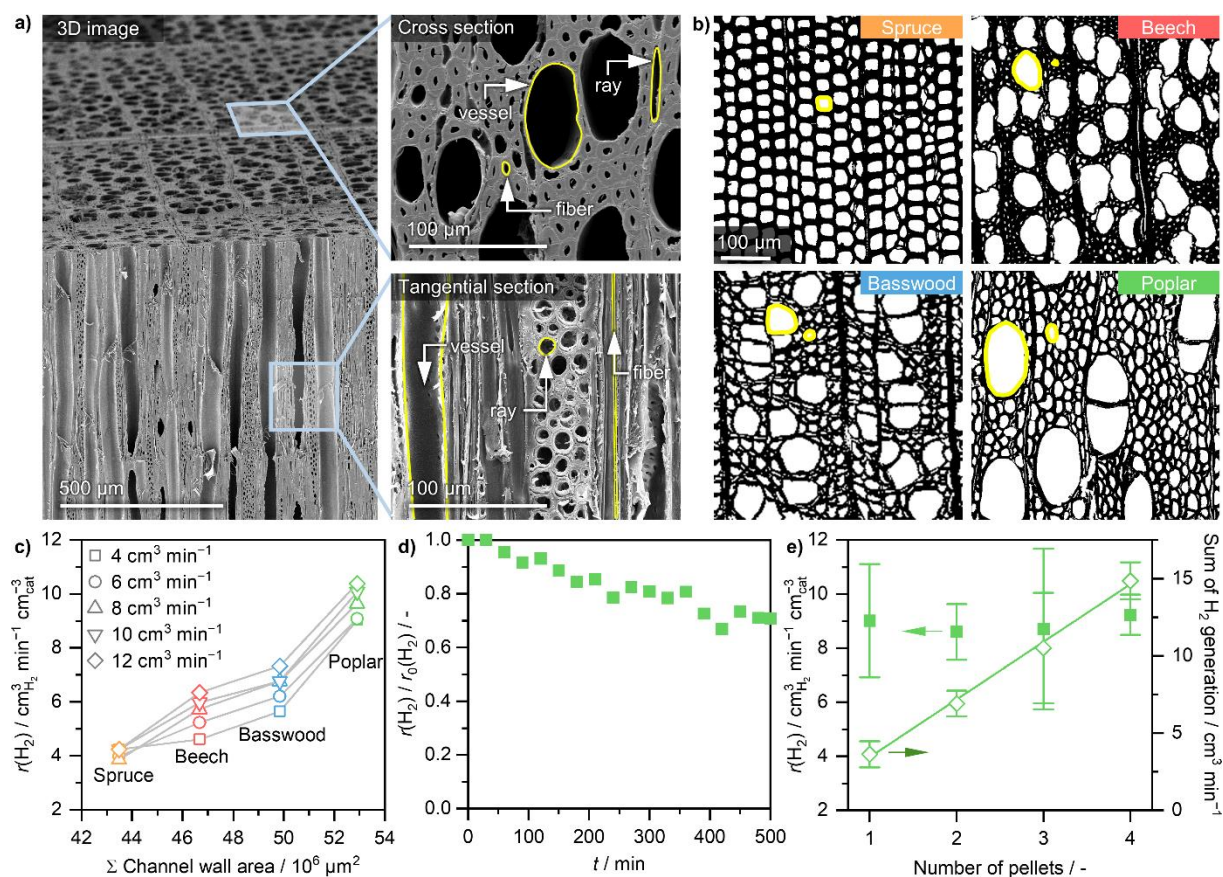


**Figure 5.** Catalytic performance in ammonia borane decomposition for structured catalysts based on different wood species (AgPd/UiO-66@wood) in flow. (a) SEM images of native beech, where micrometer-sized pores from vessels and fibers indicated in the cross and tangential sections comprise the longitudinal channels of the resulting microreactor. (b) Cross-section morphology obtained by SEM of different native wood species. The scale bar applies for all images. (c) Hydrogen generation rate of AgPd/UiO-66@wood for different wood species as a function of the ammonia borane solution flow rate and the sum of the channel wall area, extracted from SEM. (d) Normalized hydrogen generation rate for AgPd/UiO-66@poplar as function of time during stability test. (e) Hydrogen generation rate and total hydrogen generation of AgPd/UiO-66@poplar as a function of the number of pellets. Reaction conditions:  $F_L = 4\text{-}12 \text{ cm}^3 \text{ min}^{-1}$ ,  $m_{\text{cat}} = 0.14\text{-}0.55 \text{ g}$ ,  $c_{\text{NH}_3\text{BH}_3,0} = 0.19 \text{ M}$ .

## 2.6 Reusability and scalability of the catalysts

In general, the reusability of catalysts is crucial for practical applications. For catalyst powders, the recovery requires separation by centrifugation or filtration, which can cause metal aggregation and significant material losses, leading to the activity decrease. For example, AgPd/UiO-66 and Pd<sup>0</sup>/CeO<sub>2</sub> have been reported to lose around 50 % of activity after only five



cycles of reaction, which corresponds to a total reaction time of only 21 min (AgPd/UiO-66) and 108 min (Pd<sup>0</sup>/CeO<sub>2</sub>), respectively.<sup>20,58</sup> In contrast, the presented microreactors are applied in flow enabling continuous operation, preserving over 70% of its initial activity after 500 min on stream (**Figure 5d**). Only little metal loss is evidenced after reaction, while the electronic state of the metal and the morphology of the MOF remain unchanged (**Figure S24** and **Table 1**). We successfully assessed the scalability of our hydrogen generation system by displaying the hydrogen generation rate as a function of the total volume of the wood, which can be adjusted by changing the number of pellets applied in the continuous-flow setup (**Figure 5e**). The overall hydrogen generation increases linearly with the number of the AgPd/UiO-66@poplar pellets, while the volume-normalized rate stays constant, confirming its linear scalability and synthetic reproducibility. As little as four pieces of AgPd/UiO-66@poplar generate 14.85 cm<sup>3</sup> min<sup>-1</sup> of hydrogen, showing potential for large-scale applications.

### 3. Conclusion

Structured catalytic native wood microreactors for the continuous generation of H<sub>2</sub> from ammonia borane were successfully prepared using MOF-functionalized natural wood supports to stabilize metallic palladium and silver. Wood inherent interconnected microchannels, enable its direct application as a catalyst carrier. The use of an amine-containing linker proved essential to ensure a high coverage of MOF on the wood, which endows the incorporation of highly dispersed metal species. In-depth characterization confirmed the uniform distribution of the MOF and supported metals over the wood microchannel surfaces. Comparison with analogous powder samples proofed similar nanostructures and electronic properties of the supported metal species. The structured catalysts had good reusability and permitted fine control over the hydrolysis reaction by separating from the ammonia borane solution or by changing the flow rate. Quantification of the microchannel surface area demonstrated the strong influence of the wood microstructure on the performance, with structured reactors based on poplar reaching maximal rates up to 10.4 cm<sup>3</sup>H<sub>2</sub> min<sup>-1</sup> cm<sup>-3</sup><sub>cat</sub>. Over 70% of the initial activity is preserved after

500 min of reaction, representing significantly increased stability compared to previously reported systems. The modular design of the applied reactor displays a linear dependence between the hydrogen generation performance and the total wood volume, demonstrating strong potential as a scalable platform for catalytic applications in energy- and environmental-related fields.

#### 4. Experimental section

*Materials and Chemicals:* Native European beech (*Fagus sylvatica*), Norway spruce (*Picea abies*), American basswood (*Tilia americana*), and Poplar (*Populus spp.*) were cut into cylindrical wood sheets (2 mm thickness along the longitudinal direction) using a circular saw. From these wood sheets, circular samples (16 mm diameter) were obtained using a laser cutter (Trotec. Speedy 300). Zirconium chloride ( $\text{ZrCl}_4$ ,  $\geq 99.5\%$  trace metals basis), 2-aminoterephthalic acid ( $\text{NH}_2\text{-BDC}$ , 99%), silver nitrate ( $\text{AgNO}_3$ , puriss. p.a.,  $\geq 99.5\%$  AT), palladium chloride ( $\text{PdCl}_2$ , ReagentPlus®, 99%), and ammonia borane ( $\text{NH}_3\text{BH}_3$ , 97%) were obtained from Sigma-Aldrich. Sodium borohydride ( $\text{NaBH}_4$ ) and hydrochloric acid ( $\text{HCl}$ , 37%) were purchased from VWR (Germany). N,N-dimethyl formamide (DMF) and ethanol were of analytical grade. All chemicals were used as received without any purification.

*Preparation of Structured Catalysts:* For the functionalization of wood with MOF,  $\text{ZrCl}_4$  (625 mg) was dissolved in a DMF:HCl mixture (30  $\text{cm}^3$ , 5:1, V:V) and in a separate vessel  $\text{NH}_2\text{-BDC}$  (670 mg) was dissolved in DMF (50  $\text{cm}^3$ ). The  $\text{ZrCl}_4$  and  $\text{NH}_2\text{-BDC}$  solutions were mixed under sonication for 20 min. The native wood samples, together with the prepared mixture solution were sealed in a Teflon-lined stainless-steel autoclave (100  $\text{cm}^3$ ) and heated to 393 K for 24 h. After cooling to room temperature, the resulting samples were washed with DMF three times until the yellowish washing solution color became transparent. Then the samples were rinsed with ethanol (3 $\times$ 30  $\text{cm}^3$ ) to obtain UiO-66@wood. Depending on the temperature of hydrothermal synthesis, 353 or 393 K, respectively, the resulting samples were denoted UiO-66(353)@wood or UiO-66@wood (wood = beech, spruce, basswood, or poplar). To deposit

metals (palladium and/or silver) on the structured catalysts, 20 pieces of UiO-66@wood were immersed in AgNO<sub>3</sub> solution (170 cm<sup>3</sup>, 5.9 mM) and stirred at room temperature overnight. Then PdCl<sub>2</sub> solution (355 cm<sup>3</sup>, 11.3 mM) was added and stirred for 24 h. Subsequently, NaBH<sub>4</sub> solution (100 cm<sup>3</sup>, 0.5 M) was added to reduce the deposited metal species. The samples were removed from the solution after no more gas was generated, washed with water (3×100 cm<sup>3</sup>) and ethanol (3×100 cm<sup>3</sup>). The obtained AgPd/UiO-66@wood was dried at 353 K under reduced pressure. AgPd/UiO-66(353)@wood was obtained using UiO-66(353)@wood as the starting material applying the same procedure. Ag/UiO-66@wood was prepared to omit the step of immersing in PdCl<sub>2</sub> solution, and Pd/UiO-66@wood was prepared to omit the step of immersing in AgNO<sub>3</sub> solution.

*Characterization:* Longitudinal compression tests on different wood species with a size of 60 × 20 × 20 mm (L × R × T) were performed using a universal testing equipment (Zwick Roell) equipped with a 100 kN load cell. For scanning electron microscopy (SEM), wood samples were polished using a microtome and then coated with a 10 nm Au film to avoid sample charging. Images were acquired using a field emission scanning electron microscope (FEI Quanta 200F) at an acceleration voltage of 20 kV. Wavelength-dispersive spectroscopy (WDS): To prepare suitable block sections, AgPd/UiO-66@beech was embedded in epoxy resin. After curing at 333 K, the embedded sample was ground and polished to expose the tangential section of the wood sample. Finally, the samples were coated with 20 nm carbon. Measurements were conducted using a focused beam with a voltage of 7 keV, a counting time of 80 ms per pixel, and a scan size of 600 × 360 μm. X-ray powder diffraction (XRD, Panalytical X'Pert PRO MPD) was performed using Cu Kα radiation ( $\lambda = 1.5406 \text{ \AA}$ ). The diffractometer was operating at 40 kV and 45 mA with an angular step size of 0.03° and a counting time of 1 s per step. Fourier transform infrared spectroscopy (FTIR, Bruker Tensor 27): Thin wood samples were analyzed in attenuated total reflection (ATR) mode over the scan range of 400 to 4000 cm<sup>-1</sup>. Each sample was tested five times to get an average spectrum for comparison. Diffuse

reflectance infrared Fourier transform spectroscopy of CO (CO-DRIFTS) on powder samples was measured on a Bruker Optics Vertex 70 spectrometer equipped with an in situ cell and a liquid-N<sub>2</sub>-cooled mercury cadmium telluride detector. The sample was dried under argon flow (20 cm<sup>3</sup> min<sup>-1</sup>) at 473 K for 1 h, reduced in hydrogen (20 cm<sup>3</sup> min<sup>-1</sup>) for 30 min at the same temperature, and cooled to room temperature in argon (20 cm<sup>3</sup> min<sup>-1</sup>). Then background spectra were acquired and the sample was subsequently exposed to diluted CO (5 vol.% in He, 30 cm<sup>3</sup> min<sup>-1</sup>) for 15 min. Spectra were acquired in the range of 4000-400 cm<sup>-1</sup> (2 cm<sup>-1</sup> resolution) after flushing with Ar (20 cm<sup>3</sup> min<sup>-1</sup>) until no gas-phase CO was detected. Tests were conducted at 293, 323, 353, and 383 K, with an equilibration time of 5 min at each temperature. Transmission electron microscopy (TEM): sections of structured catalysts were prepared according to a reported procedure.<sup>59</sup> Ultra-thin sections (90 nm) were microtome cut with a diamond knife and placed on formvar carbon-coated copper grids. The samples were stained sequentially with uranyl acetate and Reynolds' lead citrate before investigating using a Jeol JEM-1400 Plus TEM. High-angle annular dark field-scanning transmission electron microscopy (HAADF-STEM) and energy-dispersive X-ray spectroscopy (EDX) were conducted in a Talos F200X instrument with a FEI SuperX detector at 200 kV acceleration potential. Powder catalysts were dusted on standard copper mesh holey carbon films (EMresolutions). X-ray photoelectron spectroscopy (XPS) was performed using a Physical Electronics Quantera SXM spectrometer using monochromatic Al K $\alpha$  radiation generated from an electron beam operated at 15 kV and 49.3 W. The spectra were collected under ultra-high vacuum conditions (residual pressure  $\approx 1 \times 10^{-6}$  Pa) at a pass energy of 55.0 eV. Structured catalysts were directly mounted on the sample holder, while powder samples were first pressed onto indium foil. To compensate for electrical charging during analysis, electron- and ion-neutralizers were operated during the analysis and all spectra were referenced to the Zr 3d<sub>5/2</sub> peak of UiO-66 at 182.3 eV. Inductively coupled plasma-optical emission spectrometry (ICP-OES) was conducted using a Horiba Ultra 2 instrument equipped with photomultiplier tube

detection. The samples were digested in a MLS turboWave® microwave by heating the material (ca. 10-15 mg) in 3 cm<sup>3</sup> of a 3:1 volumetric mixture of HNO<sub>3</sub> (Sigma-Aldrich, ≥65 wt.%) and H<sub>2</sub>O<sub>2</sub> (Sigma-Aldrich, 35 wt.%) to 533 K for 50 min with a maximum power of 1200 W and a loading pressure of 70 bar. The obtained clear solutions were filtered and diluted prior to analysis. The loading of UiO-66 was determined from the concentration of Zr assuming a MOF stoichiometry of C<sub>24</sub>H<sub>17</sub>N<sub>3</sub>O<sub>16</sub>Zr<sub>3</sub>. Argon sorption was measured at 77 K using a Micromeritics 3Flex instrument. Before the measurement, the samples were degassed under vacuum at 363 K for 48 h. Mercury porosimetry at 293 K was measured in a Micromeritics AutoPore 9520 porosimeter operated from vacuum to 418 MPa. Samples were degassed in situ prior to measurement. A contact angle of 140° for mercury and a pressure equilibration of 10 s were applied. The pores perimeter of native wood samples were obtained with ImageJ from 500 μm × 500 μm crops of SEM images of the cross section of the different wood species using the Analyze Particles plugin after adjustment of brightness, contrast and thresholding<sup>60</sup>. To extract the sum of channel wall area, the average sum of perimeters obtained from four different 500 μm × 500 μm areas were multiplied by the thickness of the wood pieces (2 mm).

#### *Catalytic Evaluation*

Batch operation: The performance of powder and structured catalysts was compared at room temperature in a batch setup. Firstly, 29.5 mg of powder catalyst was put in a 25 cm<sup>3</sup> round-bottomed flask. In the case of AgPd/UiO-66@beech 246.7 mg were used to apply a similar overall metal content as for the powder systems Then aqueous ammonia borane solution (5 cm<sup>3</sup>, C<sub>NH<sub>3</sub>BH<sub>3</sub>,0</sub>= 0.19 M) was injected into the flask using a syringe. A gas burette filled with water was connected to the reaction flask to measure the released gas volume. The volume of the evolved gas was monitored by recording the displacement of water in the gas burette. The reaction rates were calculated from the amount of hydrogen produced after one minute of reaction, divided by the total moles of metal that were present in the catalysts.

Continuous operation: The performance of structured catalysts for continuous hydrogen generation from ammonia borane was evaluated in a customized setup (**Figure 4b**, **S18** and Video S1). The substrate solution was pumped by a Masterflex L/S 7523 pump (Cole-Parmer, Vernon Hills, IL) from a reservoir ( $C_{\text{NH}_3\text{BH}_3\text{O}} = 0.19 \text{ M.}$ ) into a chamber with a constant flow between  $4$  and  $12 \text{ cm}^3 \text{ min}^{-1}$ . The structured catalysts, with a size of  $16 \text{ mm}$  in diameter and  $2 \text{ mm}$  in thickness along the longitudinal direction, were fixed and sealed within the chamber to ensure flow exclusively along the longitudinal direction of the microreactors. The chamber outlet was connected to a gas burette filled with water, and the generated hydrogen volume was monitored by recording the displacement of water in the gas burette. The reaction rates were calculated from the amount of hydrogen recorded in intervals of one minute during continuous reaction. Five samples were evaluated for each test to obtain the average and the standard deviations of the hydrogen production rate. To facilitate a comparison between different wood species, the hydrogen production rate was normalized by the volume of the structured catalysts.

### **Author Contributions**

#Kunkun Tu and Simon Büchele contributed equally to this work.

\*Javier Pérez-Ramírez and Tobias Keplinger are corresponding authors.

K.T., S.B., S.M., J.P.R., and T.K. conceived the study. K.T., S.B., S.M., L.S., C.L., C.G., J.A., Y.D., R.G., Z.Z., J.S., and S.S. performed experiments and analyzed data. S.M., C.G., Z.Z., G.P., S.C.Z., I.B., J.P.R. and T.K. verified the experimental design and data analysis, and gave theoretical support. K.T., S.B., S.M., J.P.R., and T.K. co-wrote the manuscript. All authors discussed the results and commented on the manuscript.

### **Competing Financial Interests**

The authors declare no competing financial interests.

### **Acknowledgements**

The project was conducted with the support of the SNF project “Hierarchical cellulose scaffolds for structural and functional gradient materials” (200021\_184821/1). We thank the Scientific Center for Optical and Electron Microscopy at ETH Zurich and the Swiss Federal Laboratories for Material Science and Technology for providing access to their facilities and Thomas Schnider for the wood sample preparation. K.T. thanks financial support from the China Scholarship Council (CSC) (201703270028). L. S. acknowledges financial support from the Swiss National Science Foundation SNSF (project 200020\_192336).

## References

- 1 Xu, Q., Liu, Y., Jiang, H., Hu, Y., Liu, H., and Li, C. (2019). Unsaturated sulfur edge engineering of strongly coupled MoS<sub>2</sub> nanosheet–carbon macroporous hybrid catalyst for enhanced hydrogen generation. *Adv. Energy Mater.* *9*, 1802553.
- 2 Lubitz, W., and Tumas, W. (2007). Hydrogen: an overview. *Chem. Rev.* *107*, 3900-3903.
- 3 Commission, E. (2019). The european green deal. In E. Commission, ed. final, 11. December [https://ec.europa.eu/info/sites/default/files/european-green-deal-communication\\_en.pdf](https://ec.europa.eu/info/sites/default/files/european-green-deal-communication_en.pdf) accessed: July 2021 ed. European Commission.
- 4 van Renssen, S. (2020). The hydrogen solution? *Nat. Clim. Change* *10*, 799-801.
- 5 Abdalla, A.M., Hossain, S., Nisfindy, O.B., Azad, A.T., Dawood, M., and Azad, A.K. (2018). Hydrogen production, storage, transportation and key challenges with applications: A review. *Energy Convers. Manage.* *165*, 602-627.
- 6 Faverio, C., Boselli, M.F., Medici, F., and Benaglia, M. (2020). Ammonia borane as a reducing agent in organic synthesis. *Organic & Biomolecular Chemistry* *18*, 7789-7813.
- 7 Lin, Y., Mao, W.L., and Mao, H.-k. (2009). Storage of molecular hydrogen in an ammonia borane compound at high pressure. *Proc. Natl. Acad. Sci. U. S. A.* *106*, 8113-8116.
- 8 Sun, D.H., Mazumder, V., Metin, O., and Sun, S.H. (2011). Catalytic hydrolysis of ammonia borane via cobalt palladium nanoparticles. *ACS Nano* *5*, 6458-6464.
- 9 Yüksel Alpaydın, C., Gülbay, S.K., and Ozgur Colpan, C. (2020). A review on the catalysts used for hydrogen production from ammonia borane. *Int. J. Hydrogen Energy* *45*, 3414-3434.
- 10 Rossin, A., and Peruzzini, M. (2016). Ammonia–borane and amine–borane dehydrogenation mediated by complex metal hydrides. *Chem. Rev.* *116*, 8848-8872.
- 11 Wang, C., and Astruc, D. (2021). Recent developments of nanocatalyzed liquid-phase hydrogen generation. *Chem. Soc. Rev.* *50*, 3437-3484.
- 12 Manna, J., Akbayrak, S., and Özkar, S. (2017). Palladium(0) nanoparticles supported on polydopamine coated CoFe<sub>2</sub>O<sub>4</sub> as highly active, magnetically isolable and reusable catalyst for hydrogen generation from the hydrolysis of ammonia borane. *Appl. Catal. B* *208*, 104-115.
- 13 Wang, C., Zhao, J., Du, X., Sun, S., Yu, X., Zhang, X., Lu, Z., Li, L., and Yang, X. (2021). Hydrogen production from ammonia borane hydrolysis catalyzed by non-noble metal-based materials: a review. *J. Mater. Sci.* *56*, 2856-2878.
- 14 Huang, X., Liu, Y., Wen, H., Shen, R., Mehdi, S., Wu, X., Liang, E., Guo, X., and Li, B. (2021). Ensemble-boosting effect of Ru-Cu alloy on catalytic activity towards hydrogen evolution in ammonia borane hydrolysis. *Appl. Catal., B* *287*, 119960.
- 15 Gao, M., Yang, W., and Yu, Y. (2018). Monodisperse PtCu alloy nanoparticles as highly efficient catalysts for the hydrolytic dehydrogenation of ammonia borane. *Int. J. Hydrogen Energy* *43*, 14293-14300.
- 16 Sun, D., Li, P., Yang, B., Xu, Y., Huang, J., and Li, Q. (2016). Monodisperse AgPd alloy nanoparticles as a highly active catalyst towards the methanolysis of ammonia borane for hydrogen generation. *RSC Adv.* *6*, 105940-105947.
- 17 Kahri, H., Sevim, M., and Metin, Ö. (2017). Enhanced catalytic activity of monodispersed AgPd alloy nanoparticles assembled on mesoporous graphitic carbon nitride for the hydrolytic dehydrogenation of ammonia borane under sunlight. *Nano Res.* *10*, 1627-1640.
- 18 Chen, G., Desinan, S., Rosei, R., Rosei, F., and Ma, D. (2012). Synthesis of Ni–Ru alloy nanoparticles and their high catalytic activity in dehydrogenation of ammonia borane. *Chem. - Eur. J.* *18*, 7925-7930.

- 19 Özkar, S. (2020). Transition metal nanoparticle catalysts in releasing hydrogen from the methanolysis of ammonia borane. *Int. J. Hydrogen Energy* 45, 7881-7891.
- 20 Shang, N.-Z., Feng, C., Gao, S.-T., and Wang, C. (2016). Ag/Pd nanoparticles supported on amine-functionalized metal-organic framework for catalytic hydrolysis of ammonia borane. *Int. J. Hydrogen Energy* 41, 944-950.
- 21 Liu, Y., Guan, H., Zhang, J., Zhao, Y., Yang, J.-H., and Zhang, B. (2018). Polydopamine-coated halloysite nanotubes supported AgPd nanoalloy: An efficient catalyst for hydrolysis of ammonia borane. *Int. J. Hydrogen Energy* 43, 2754-2762.
- 22 Li, J., Zhu, Q.-L., and Xu, Q. (2014). Highly active AuCo alloy nanoparticles encapsulated in the pores of metal-organic frameworks for hydrolytic dehydrogenation of ammonia borane. *Chem. Commun.* 50, 5899-5901.
- 23 Meilikhov, M., Yussenko, K., Esken, D., Turner, S., Van Tendeloo, G., and Fischer, R.A. (2010). Metals@MOFs – Loading MOFs with metal nanoparticles for hybrid functions. *Eur. J. Inorg. Chem.* 2010, 3701-3714.
- 24 Rossin, A., Tuci, G., Luconi, L., and Giambastiani, G. (2017). Metal-organic frameworks as heterogeneous catalysts in hydrogen production from lightweight inorganic hydrides. *ACS Catalysis* 7, 5035-5045.
- 25 Luconi, L., Tuci, G., Giambastiani, G., Rossin, A., and Peruzzini, M. (2019). H<sub>2</sub> production from lightweight inorganic hydrides catalyzed by 3d transition metals. *Int. J. Hydrogen Energy* 44, 25746-25776.
- 26 Li, M., Hu, J., and Lu, H. (2016). A stable and efficient 3D cobalt-graphene composite catalyst for the hydrolysis of ammonia borane. *Catalysis Science & Technology* 6, 7186-7192.
- 27 Liu, Q., Zhang, S., Liao, J., Feng, K., Zheng, Y., Pollet, B.G., and Li, H. (2017). CuCo<sub>2</sub>O<sub>4</sub> nanoplate film as a low-cost, highly active and durable catalyst towards the hydrolytic dehydrogenation of ammonia borane for hydrogen production. *J. Power Sources* 355, 191-198.
- 28 Özkar, S. (2021). Magnetically separable transition metal nanoparticles as catalysts in hydrogen generation from the hydrolysis of ammonia borane. *Int. J. Hydrogen Energy* 46, 21383-21400.
- 29 Mboyi, C.D., Poinso, D., Roger, J., Fajerweg, K., Kahn, M.L., and Hierso, J.C. (2021). The Hydrogen - Storage Challenge: Nanoparticles for Metal - Catalyzed Ammonia Borane Dehydrogenation. *Small*, 2102759.
- 30 Cui, L., Xu, Y.H., Niu, L., Yang, W.R., and Liu, J.Q. (2017). Monolithically integrated CoP nanowire array: An on/off switch for effective on-demand hydrogen generation via hydrolysis of NaBH<sub>4</sub> and NH<sub>3</sub>BH<sub>3</sub>. *Nano Res.* 10, 595-604.
- 31 Wang, Y., Zou, K., Zhang, D., Li, G., Meng, W., Wang, D., Cao, Z., Zhang, K., and Wu, S. (2020). Co-Mo-B nanoparticles supported on carbon cloth as effective catalysts for the hydrolysis of ammonia borane. *Int. J. Hydrogen Energy* 45, 14418-14427.
- 32 Tang, C., Xie, L.S., Wang, K.Y., Du, G., Asiri, A.M., Luo, Y.L., and Sun, X.P. (2016). A Ni<sub>2</sub>P nanosheet array integrated on 3D Ni foam: an efficient, robust and reusable monolithic catalyst for the hydrolytic dehydrogenation of ammonia borane toward on-demand hydrogen generation. *J. Mater. Chem. A* 4, 12407-12410.
- 33 Hui, B., Li, J., Lu, Y., Zhang, K., Chen, H., Yang, D., Cai, L., and Huang, Z. (2021). Boosting electrocatalytic hydrogen generation by a renewable porous wood membrane decorated with Fe-doped NiP alloys. *Journal of Energy Chemistry* 56, 23-33.
- 34 Li, J., Ma, R., Lu, Y., Wu, Z., Su, M., Jin, K., Qin, D., Zhang, R., Bai, R., and He, S. (2020). A gravity-driven high-flux catalytic filter prepared using a naturally three-dimensional porous rattan biotemplate decorated with Ag nanoparticles. *Green Chemistry* 22, 6846-6854.



- 35 Guo, R., Cai, X., Liu, H., Yang, Z., Meng, Y., Chen, F., Li, Y., and Wang, B. (2019). In situ growth of metal–organic frameworks in three-dimensional aligned lumen arrays of wood for rapid and highly efficient organic pollutant removal. *Environ. Sci. Technol.* *53*, 2705-2712.
- 36 Chen, C., Kuang, Y., Zhu, S., Burgert, I., Keplinger, T., Gong, A., Li, T., Berglund, L., Eichhorn, S.J., and Hu, L. (2020). Structure–property–function relationships of natural and engineered wood. *Nature Reviews Materials*.
- 37 Chen, F., Gong, A.S., Zhu, M., Chen, G., Lacey, S.D., Jiang, F., Li, Y., Wang, Y., Dai, J., Yao, Y., et al. (2017). Mesoporous, three-dimensional wood membrane decorated with nanoparticles for highly efficient water treatment. *ACS Nano* *11*, 4275-4282.
- 38 Goldhahn, C., Taut, J.A., Schubert, M., Burgert, I., and Chanana, M. (2020). Enzyme immobilization inside the porous wood structure: a natural scaffold for continuous-flow biocatalysis. *RSC Adv.* *10*, 20608-20619.
- 39 Liu, K.-K., Jiang, Q., Tadepalli, S., Raliya, R., Biswas, P., Naik, R.R., and Singamaneni, S. (2017). Wood–graphene oxide composite for highly efficient solar steam generation and desalination. *ACS applied materials & interfaces* *9*, 7675-7681.
- 40 Zhu, X., Hu, J., Liu, G., Xu, D., Wei, Y., Li, D., Chang, S., Li, X., and Liu, Y. (2021). Unique 3D interpenetrating capillary network of wood veneer for highly efficient cross flow filtration. *J. Mater. Sci.* *56*, 3155-3167.
- 41 Che, W., Xiao, Z., Wang, Z., Li, J., Wang, H., Wang, Y., and Xie, Y. (2019). Wood-based mesoporous filter decorated with silver nanoparticles for water purification. *ACS Sustain. Chem. Eng.* *7*, 5134-5141.
- 42 Liu, X., Demir, N.K., Wu, Z., and Li, K. (2015). Highly water-stable zirconium metal–organic framework UiO-66 membranes supported on alumina hollow fibers for desalination. *J. Am. Chem. Soc.* *137*, 6999-7002.
- 43 Goldhahn, C., Schubert, M., Lüthi, T., Keplinger, T., Burgert, I., and Chanana, M. (2020). Wood–gelatin bio-composite membranes with tunable flux. *ACS Sustainable Chem. Eng.* *8*, 7205-7213.
- 44 Tu, K., Puértolas, B., Adobes-Vidal, M., Wang, Y., Sun, J., Traber, J., Burgert, I., Pérez-Ramírez, J., and Keplinger, T. (2020). Green synthesis of hierarchical metal–organic framework/wood functional composites with superior mechanical properties. *Adv. Sci.* *7*, 1902897.
- 45 Aghajanzadeh, M., Zamani, M., Molavi, H., Khieri Manjili, H., Danafar, H., and Shojaei, A. (2018). Preparation of Metal–Organic Frameworks UiO-66 for Adsorptive Removal of Methotrexate from Aqueous Solution. *J. Inorg. Organomet. Polym. Mater.* *28*, 177-186.
- 46 Khoshhal, S., Ghoreyshi, A.A., Jahanshahi, M., and Mohammadi, M. (2015). Study of the temperature and solvent content effects on the structure of Cu–BTC metal organic framework for hydrogen storage. *RSC Adv.* *5*, 24758-24768.
- 47 Ma, Y., Bansmann, J., Diemant, T., and Behm, R. (2009). Formation, stability and CO adsorption properties of PdAg/Pd (1 1 1) surface alloys. *Surf. Sci.* *603*, 1046-1054.
- 48 Zeledón, J.A.Z., Stevens, M.B., Gunasooriya, G.K.K., Gallo, A., Landers, A.T., Kreider, M.E., Hahn, C., Nørskov, J.K., and Jaramillo, T.F. (2021). Tuning the electronic structure of Ag-Pd alloys to enhance performance for alkaline oxygen reduction. *Nat. Commun.* *12*, 1-9.
- 49 Kruk, M., and Jaroniec, M. (2003). Argon adsorption at 77 K as a useful tool for the elucidation of pore connectivity in ordered materials with large cage-like mesopores. *Chem. Mater.* *15*, 2942-2949.
- 50 Silvestre-Albero, J., Silvestre-Albero, A., Rodríguez-Reinoso, F., and Thommes, M. (2012). Physical characterization of activated carbons with narrow microporosity by

- nitrogen (77.4 K), carbon dioxide (273 K) and argon (87.3 K) adsorption in combination with immersion calorimetry. *Carbon* 50, 3128-3133.
- 51 Ström, L., Ström, H., Carlsson, P.-A., Skoglundh, M., and Härelind, H. (2018). Catalytically active Pd–Ag alloy nanoparticles synthesized in microemulsion template. *Langmuir* 34, 9754-9761.
- 52 Li, M., and Shen, J. (2001). Microcalorimetric and infrared spectroscopic studies of CO and C<sub>2</sub>H<sub>4</sub> adsorption on Pd/SiO<sub>2</sub> and Pd–Ag/SiO<sub>2</sub> catalysts. *Mater. Chem. Phys.* 68, 204-209.
- 53 Bejan, A. (2013). Mass Transfer. In *Convection Heat Transfer*, pp. 489-536. <https://doi.org/10.1002/9781118671627.ch11>.
- 54 Xie, Z.-T., Asoh, T.-A., and Uyama, H. (2020). Facile Fabrication of a Flow Reactor from Natural Wood. *Chem. Lett.* 49, 1232-1235.
- 55 Zhang, X.-F., Wang, Z., Song, L., and Yao, J. (2021). In situ growth of ZIF-8 within wood channels for water pollutants removal. *Sep. Purif. Technol.* 266, 118527.
- 56 Guo, R., Cai, X., Liu, H., Yang, Z., Meng, Y., Chen, F., Li, Y., and Wang, B. (2019). In Situ Growth of Metal-Organic Frameworks in Three-Dimensional Aligned Lumen Arrays of Wood for Rapid and Highly Efficient Organic Pollutant Removal. *Environ. Sci. Technol.* 53, 2705-2712.
- 57 Murathan, H.B., Özkan, G., Akkuş, M.S., Özgür, D.Ö., and Özkan, G. (2018). Hydrogen production from the methanolysis of ammonia borane by Pd-Co/Al<sub>2</sub>O<sub>3</sub> coated monolithic catalyst. *Int. J. Hydrogen Energy* 43, 10728-10733.
- 58 Tonbul, Y., Akbayrak, S., and Özkar, S. (2016). Palladium(0) nanoparticles supported on ceria: Highly active and reusable catalyst in hydrogen generation from the hydrolysis of ammonia borane. *Int. J. Hydrogen Energy* 41, 11154-11162.
- 59 Pfister, B., Lu, K.-J., Eicke, S., Feil, R., Lunn, J.E., Streb, S., and Zeeman, S.C. (2014). Genetic Evidence That Chain Length and Branch Point Distributions Are Linked Determinants of Starch Granule Formation in Arabidopsis. *Plant Physiol.* 165, 1457-1474.
- 60 Schindelin, J., Arganda-Carreras, I., Frise, E., Kaynig, V., Longair, M., Pietzsch, T., Preibisch, S., Rueden, C., Saalfeld, S., Schmid, B., et al. (2012). Fiji: an open-source platform for biological-image analysis. *Nat. Methods* 9, 676-682.

## Supplementary Information

### 1. Experimental Section

#### 1.1. Preparation of Powder Catalyst

UiO-66 was prepared according to a reported procedure.<sup>1</sup> Briefly, ZrCl<sub>4</sub> (625 mg) was dissolved in a mixture of dimethylformamide (DMF, 30 cm<sup>3</sup>) and hydrochloric acid (HCl, DMF:HCl = 5:1, V:V) and in a separate vessel 2-aminoterephthalic acid (NH<sub>2</sub>-BDC, 670 mg) was dissolved in DMF (50 cm<sup>3</sup>). The ZrCl<sub>4</sub> and NH<sub>2</sub>-BDC solutions were mixed under sonication for 20 min, sealed in a Teflon-lined stainless autoclave (100 cm<sup>3</sup>), and hydrothermally treated at 393 K for 24 h. After cooling to room temperature, the resulting solids were collected by centrifugation at 8000 rpm for 10 min, washed with DMF (3 × 30 cm<sup>3</sup>) and ethanol (3 × 30 cm<sup>3</sup>), and subsequently dried at 353 K under vacuum. For comparative purposes, **UiO-66** was also prepared by hydrothermal synthesis at 353 K following the same procedure, resulting in the sample denoted **UiO-66(353)**. To introduce the desired metals, the MOF powder (50 mg) was added to a solution of AgNO<sub>3</sub> (1.7 mg in 1.7 cm<sup>3</sup> H<sub>2</sub>O) and stirred at room temperature for 1 h before adding a solution of PdCl<sub>2</sub> (7.1 mg in 3.55 cm<sup>3</sup> H<sub>2</sub>O) and stirring for additional 4 h. Then, NaBH<sub>4</sub> solution (1 cm<sup>3</sup>, 0.5 M) was added under stirring, and allowed to react for 1 h to reduce the metal species. After filtration, the resulting solid was washed with water (3 × 30 cm<sup>3</sup>) and ethanol (3 × 30 cm<sup>3</sup>) consecutively. The obtained samples were dried at 353 K under reduced pressure and labeled **AgPd/UiO-66** and **AgPd/UiO-66(353)**. For the synthesis of **Ag/UiO-66**, the addition of PdCl<sub>2</sub> was omitted, while to obtain **Pd/UiO-66**, the MOF powder was added directly to the PdCl<sub>2</sub> solution.

#### 1.2. Functionalization of Wood Microreactors with Different MOFs

**MOF(Ni)@beech** was synthesized using a solvothermal route adapted from a previously reported procedure for MOF(Ni) (molecular formula, Ni<sub>4</sub>O(H<sub>2</sub>N-BDC)<sub>3</sub>) powder.<sup>2</sup> Briefly, a mixture of nickel(II) nitrate hexahydrate (Ni(NO<sub>3</sub>)<sub>2</sub>·6H<sub>2</sub>O, Sigma-Aldrich, 99%, 1.05 g), NH<sub>2</sub>-BDC (0.33 g) and triethylamine (TEA, Sigma-Aldrich, ≥99.5%, 0.36 cm<sup>3</sup>) were added to DMF

(30 cm<sup>3</sup>) and mixed under ultrasonication. After that, the homogeneous solution was transferred to an autoclave with 5 pieces of beech samples and hydrothermally treated at 378 K for 24 h. After cooling to room temperature, the resulting materials were washed with DMF (3 × 30 cm<sup>3</sup>) and ethanol (3 × 30 cm<sup>3</sup>). Finally, the product was dried overnight at 378 K under vacuum. **MOF(FeCo)@beech** was synthesized using a solvothermal route adapted from a previously reported procedure for MOF(FeCo) (molecular formula, Fe<sub>2</sub>CoO(NH<sub>2</sub>-BDC)<sub>3</sub>) powder.<sup>3</sup> Briefly, equimolar amount of iron(III) chloride hexahydrate (FeCl<sub>3</sub>·6H<sub>2</sub>O, Sigma-Aldrich, 97%, 0.54 g) and cobalt(II) chloride (CoCl<sub>2</sub>, Sigma-Aldrich, 97%, 0.26 g) were added to DMF (15 cm<sup>3</sup>). NH<sub>2</sub>-BDC (0.363 g) was separately dissolved in DMF (15 cm<sup>3</sup>). Both solutions were then mixed by stirring for 15 min, transferred to an autoclave containing 5 pieces of beech samples, and then hydrothermally treated, washed, and dried according to the same procedure as MOF(Ni)@beech.

## 2. Results Section

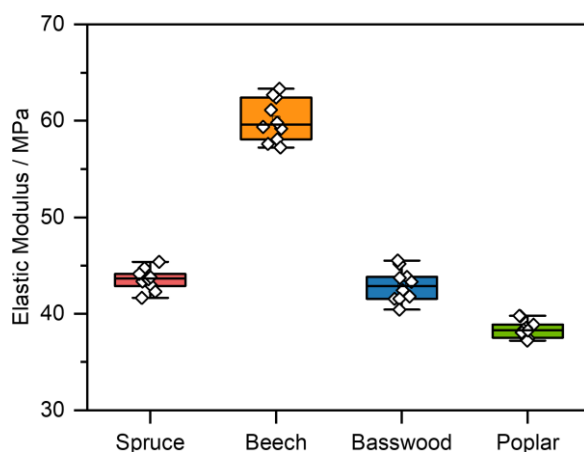


**Figure S1.** The elastic moduli of different wood species.

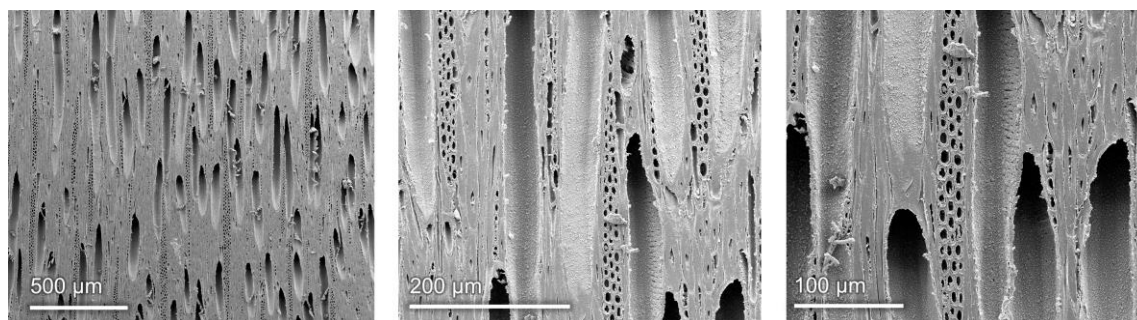


**Figure S2.** SEM images of a tangential section of UiO-66@beech at different magnifications.

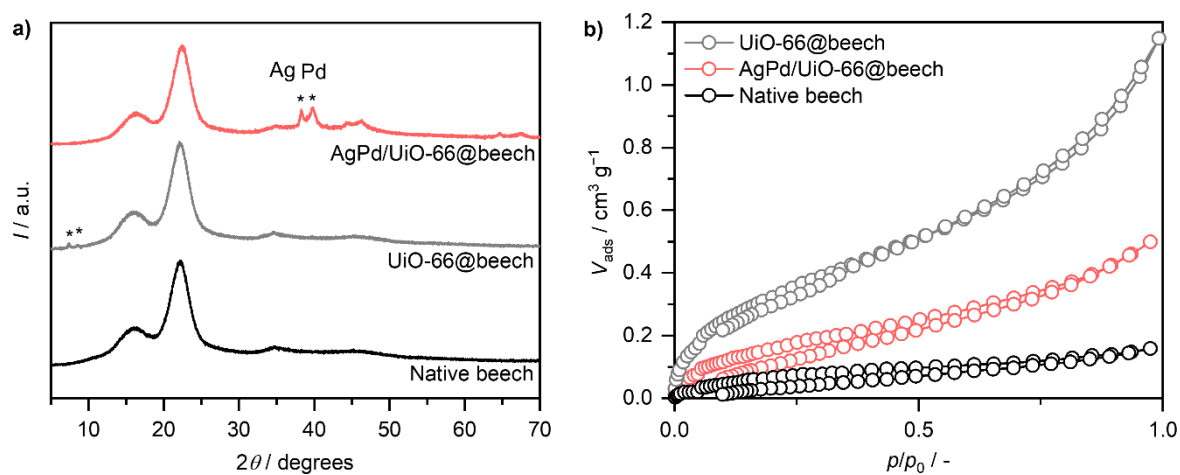


**Figure S3.** (a) XRD patterns and (b) argon isotherms at 77 K of beech before and after functionalization with UiO-66 and of the corresponding bimetallic structured catalyst.

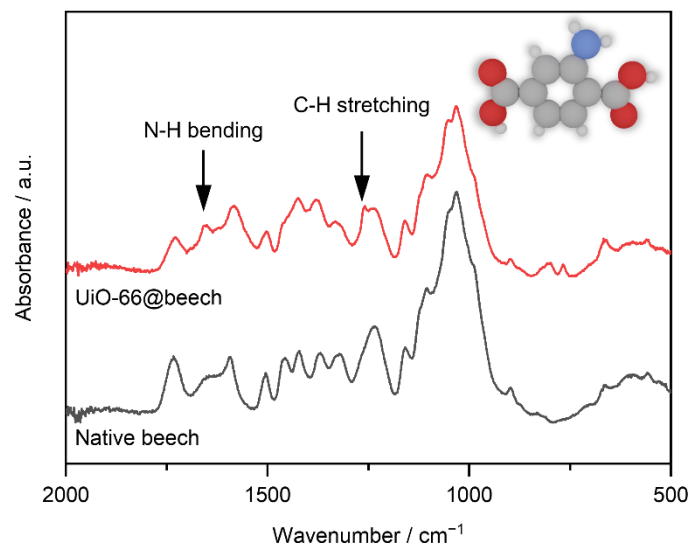


**Figure S4.** FTIR spectra of beech before and after functionalization with UiO-66. The appearance of characteristic N-H bending and C-H stretching modes confirms the incorporation of the NH<sub>2</sub>-BDC linker in UiO-66@beech.

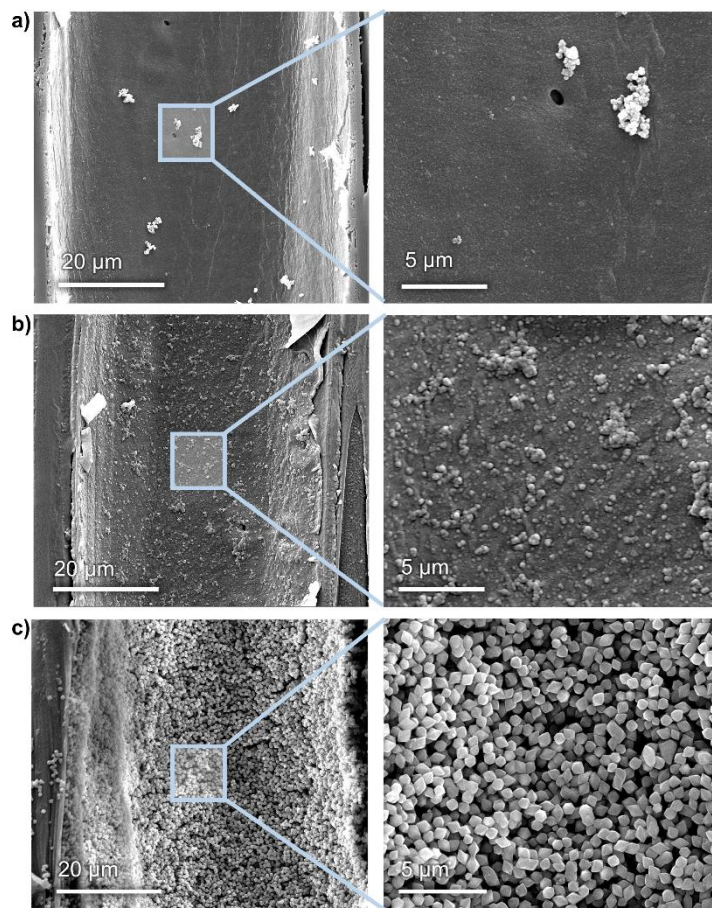


**Figure S5.** SEM images of tangential sections of beech functionalized with different MOFs: (a) UiO-66@beech prepared using BDC as the organic linker and (b) MOF(Ni)@beech and (c) MOF(FeCo)@beech (both prepared using NH<sub>2</sub>-BDC as the organic linker). The NH<sub>2</sub>-BDC linker enables the formation of different wood-MOF composites with a homogeneous MOF coverage.

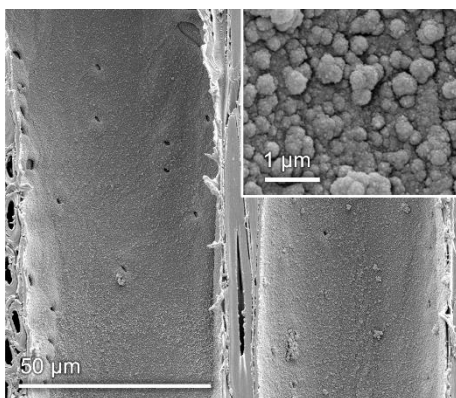


**Figure S6.** SEM images of a tangential section of the bimetallic structured catalyst, AgPd/Uio-66@beech.

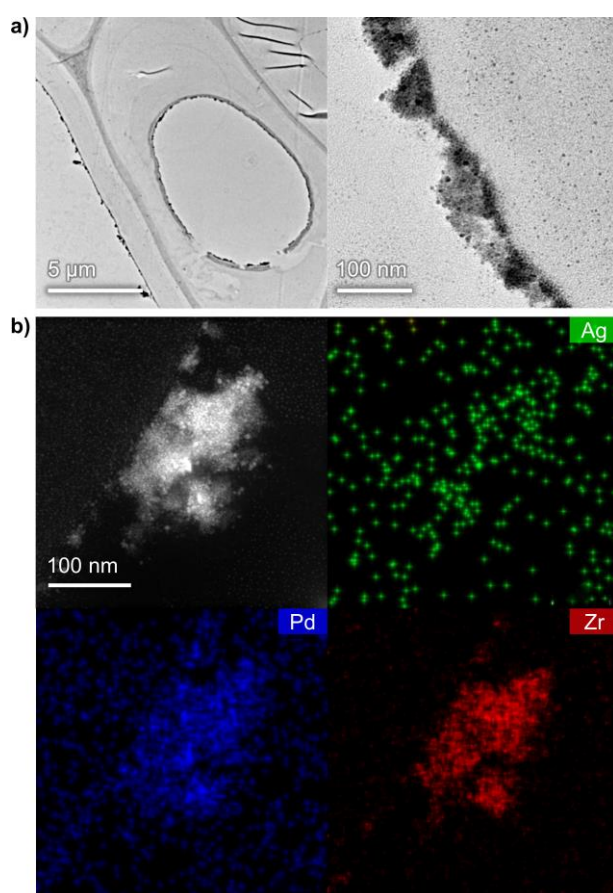


**Figure S7.** (a) TEM and (b) HAADF-STEM images and corresponding elemental maps of the bimetallic structured catalyst, AgPd/Uio-66(353)@beech.



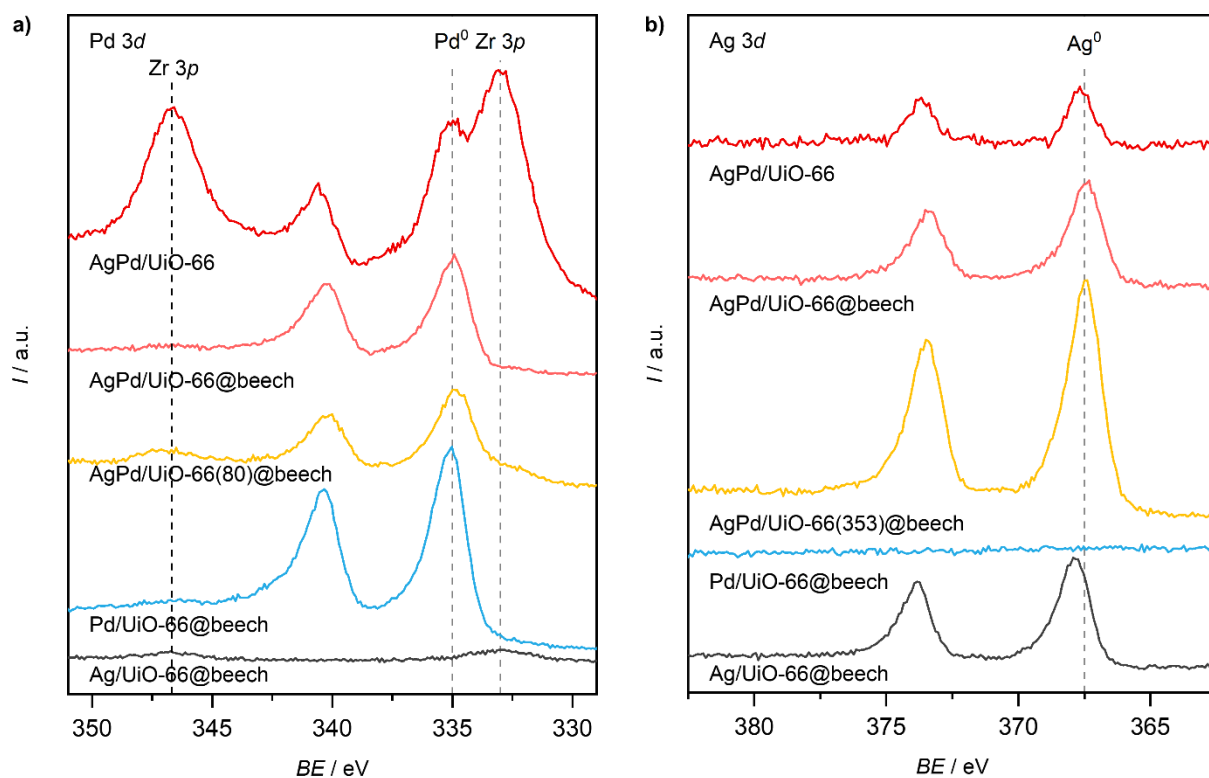


**Figure S8.** (a) Pd 3d and (b) Ag 3d XPS spectra of metal-containing MOF powders and structured catalysts.

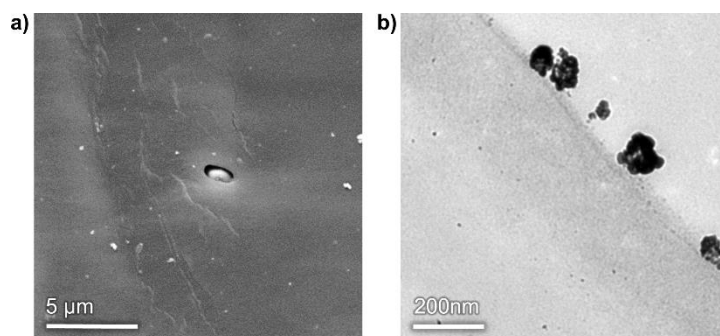


**Figure S9.** (a) SEM image of a tangential section and (b) TEM image of a cross section of a bimetallic structured catalyst without MOF functionalization, AgPd@beech. These images provide evidence for the formation of large metal nanoparticles in absence of UiO-66.



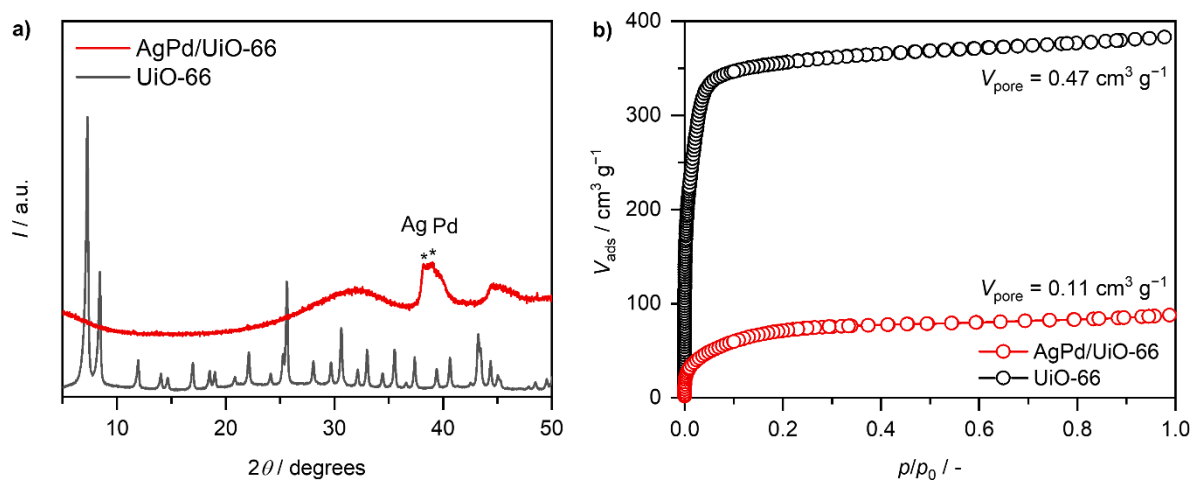


**Figure S10.** (a) XRD patterns and (b) argon isotherms at 77 K of bimetallic and metal-free MOF powders. The high metal content leads to a reduced crystalline order and pore volume.

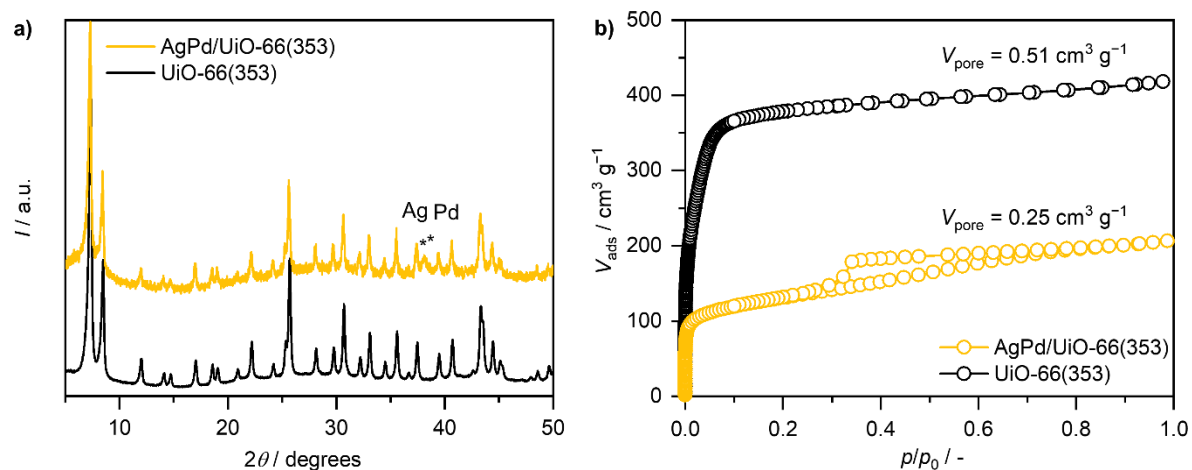


**Figure S11.** (a) XRD patterns and (b) argon isotherms at 77 K of bimetallic and metal-free MOF powders, hydrothermally synthesized at 353 K. The high metal content leads to a reduction in pore volume while affecting the crystalline order to a lesser extent.

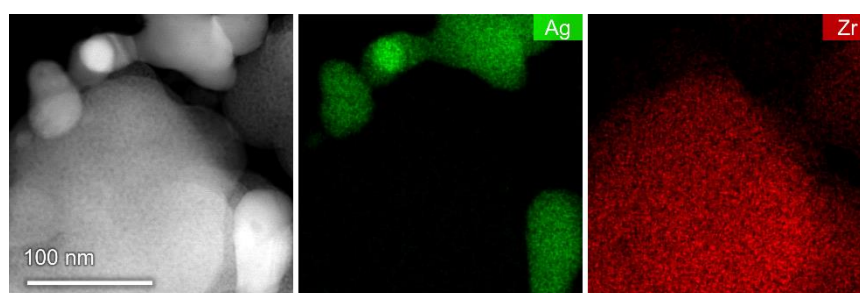


**Figure S12.** HAADF-STEM image and corresponding EDX maps of silver-containing MOF powder, Ag/UiO-66.

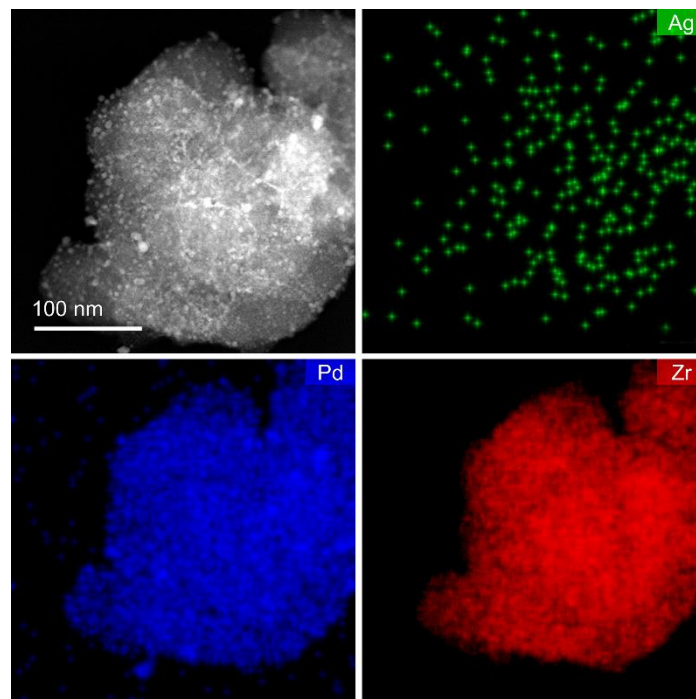


**Figure S13.** HAADF-STEM image and corresponding EDX maps of bimetallic MOF powder, hydrothermally synthesized at 353 K, AgPd/UiO-66(353).

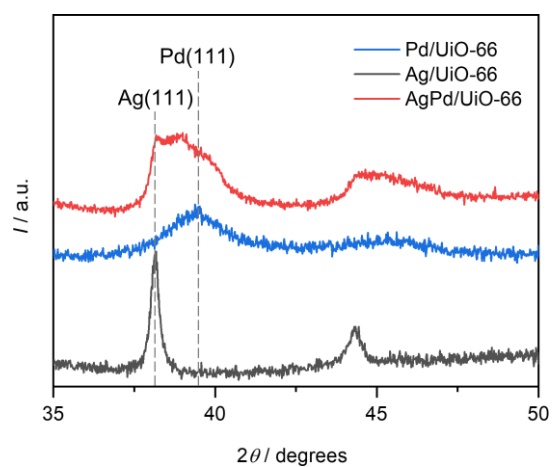


**Figure S14.** XRD patterns of metal-containing MOF powders.

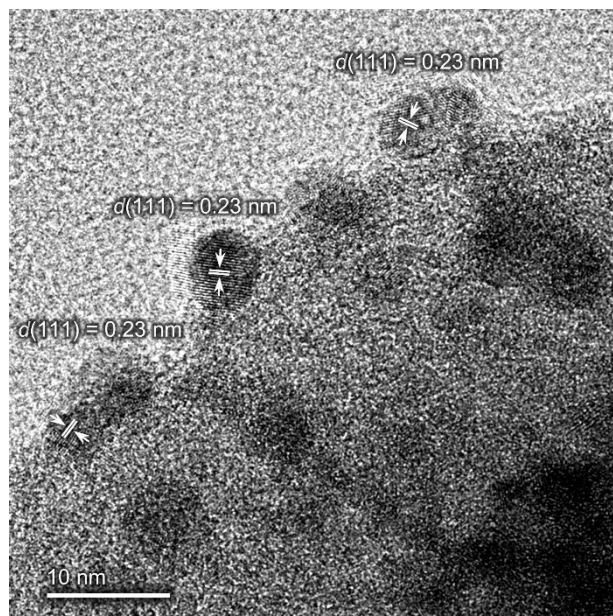


**Figure S15** TEM image of bimetallic MOF powder, hydrothermally synthesized at 353 K, AgPd/UiO-66(353). The measured lattice spacing is indicated.

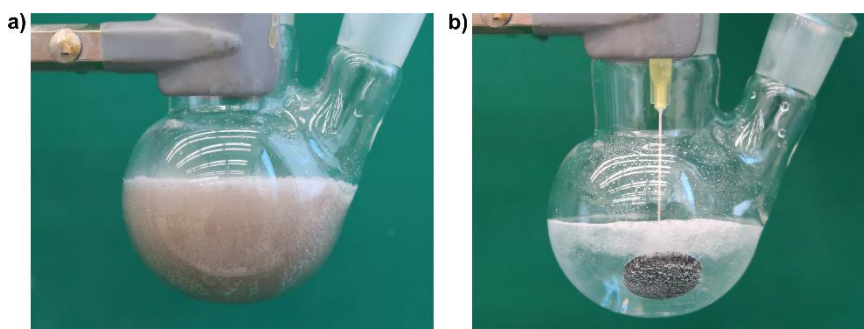


**Figure S16.** Photographs of (a) MOF powder (AgPd/UiO-66) and (b) bimetallic structured catalyst (AgPd/UiO-66@beech) in ammonia borane solution during batch hydrogen generation tests. See also **Video S1**.

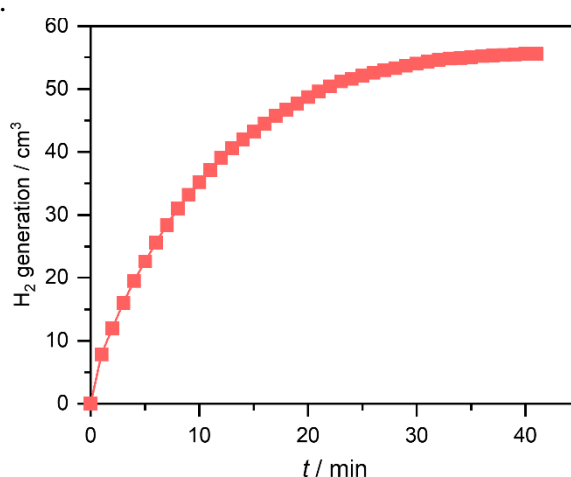


**Figure S17.** Hydrogen generation from ammonia borane over bimetallic structured catalyst, AgPd/UiO-66@beech, in batch tests. Conditions:  $V_L = 5 \text{ cm}^3$ ,  $m_{\text{cat}} = 246.7 \text{ mg}$ ,  $\text{CNH}_3\text{BH}_3\cdot\text{O} = 0.19 \text{ M}$ .

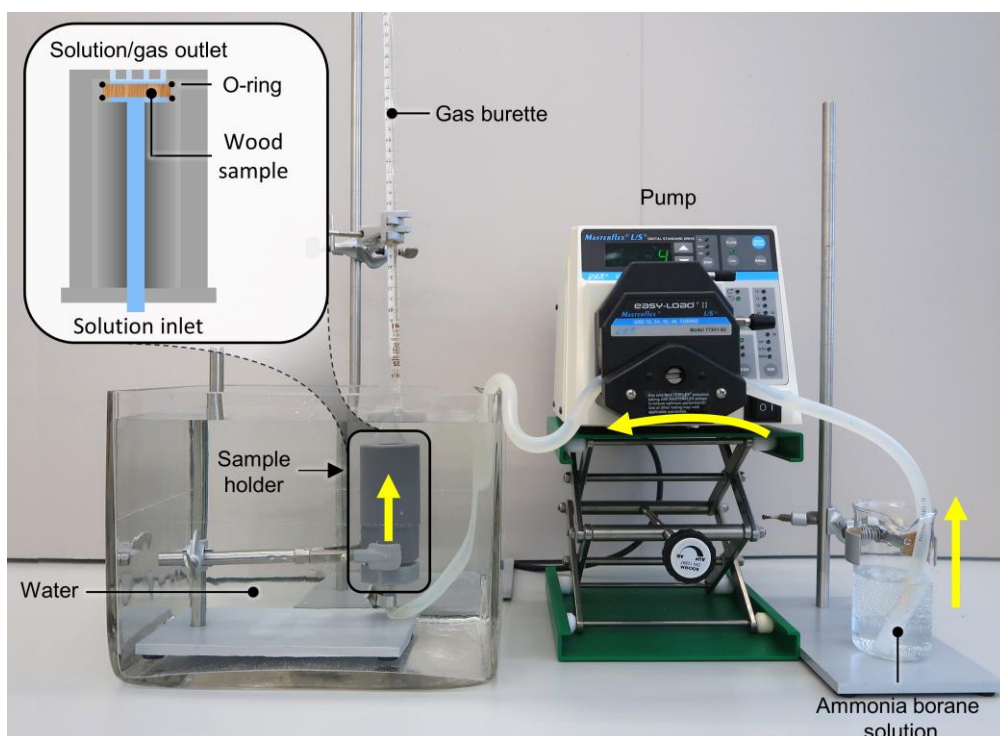


**Figure S18.** The setup for hydrogen generation from ammonia borane in flow. A scheme of the structured catalyst, mounted in the sample holder, is inset.

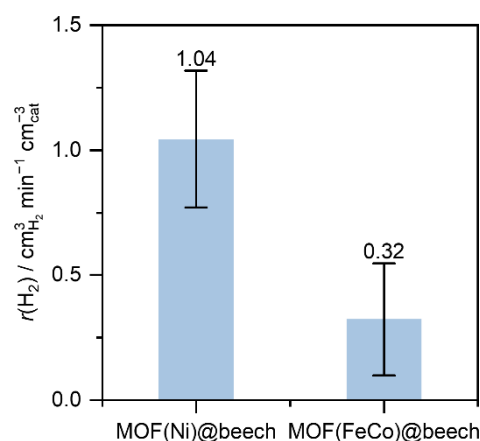


**Figure S19.** Hydrogen generation rate from ammonia borane of structured catalysts, comprising beech functionalized with different MOFs, MOF(Ni)@beech and MOF(FeCo)@beech, in flow. Conditions:  $F_L = 4 \text{ cm}^3 \text{ min}^{-1}$ ,  $c_{\text{NH}_3\text{BH}_3,0} = 0.19 \text{ M}$ .



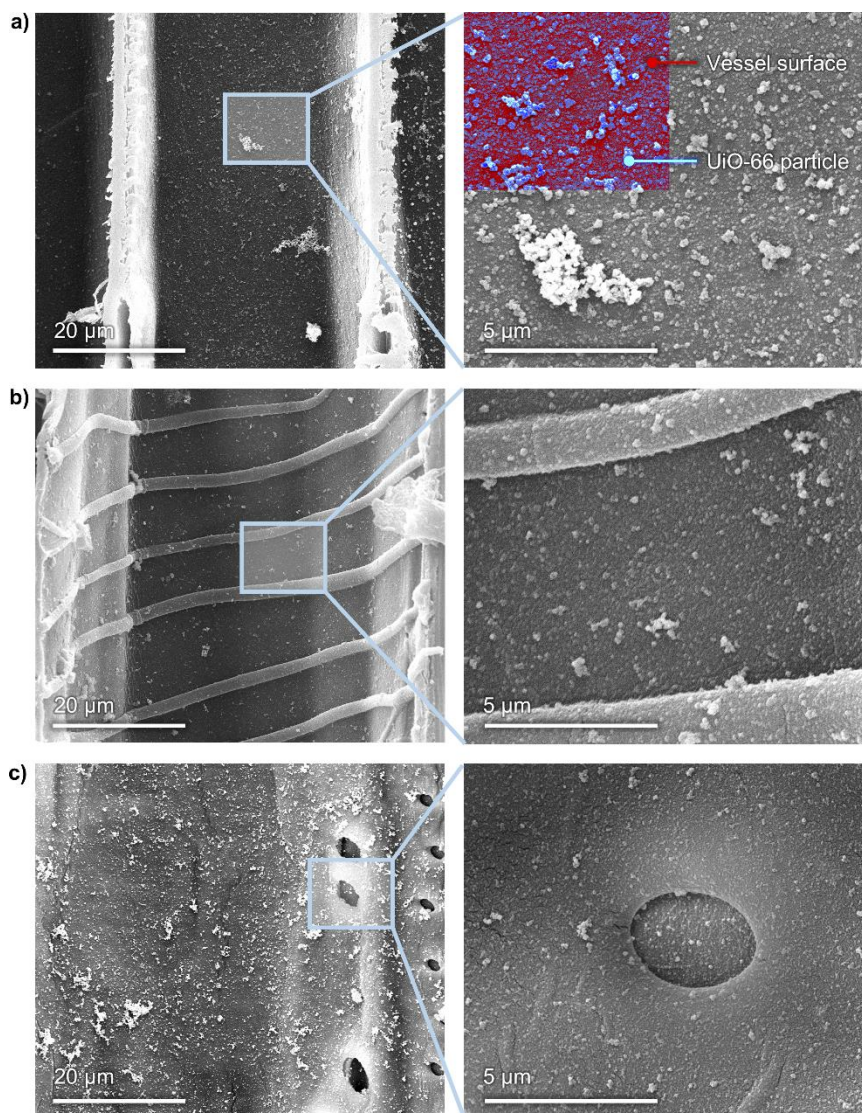


**Figure S20.** SEM images of tangential sections of bimetallic structured catalysts obtained with different wood species: (a) AgPd/UiO-66@spruce, (b) AgPd/UiO-66@basswood, and (c) AgPd/UiO-66@poplar, evidencing the distribution of metal-impregnated UiO-66 on the surface of microchannels. The MOF phase and wood surface are marked with color in the top left quarter of part (a).

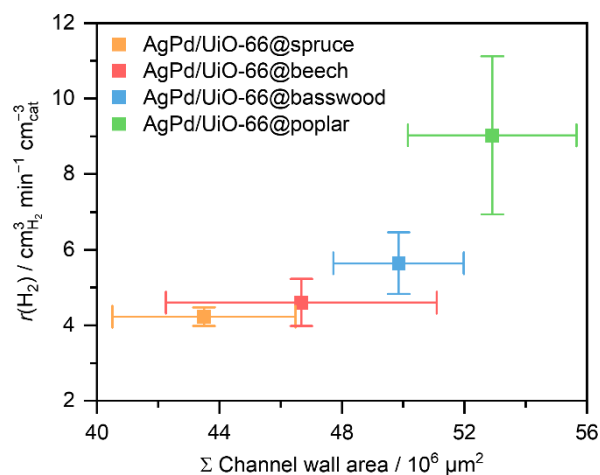


**Figure S21.** Hydrogen generation rate of bimetallic structured catalysts based on different wood species as a function of the sum of the channel wall area. The error bars on the  $x$ -axis indicate the standard deviation obtained for measuring the channel wall area in four different regions of native wood microreactors. The error bar on the  $y$ -axis represents the standard deviation for three independent catalytic runs. Conditions:  $F_L = 4 \text{ cm}^3 \text{ min}^{-1}$ ,  $m_{\text{cat}} = 0.14\text{-}0.55 \text{ g}$ ,  $c_{\text{NH}_3\text{BH}_3,0} = 0.19 \text{ M}$

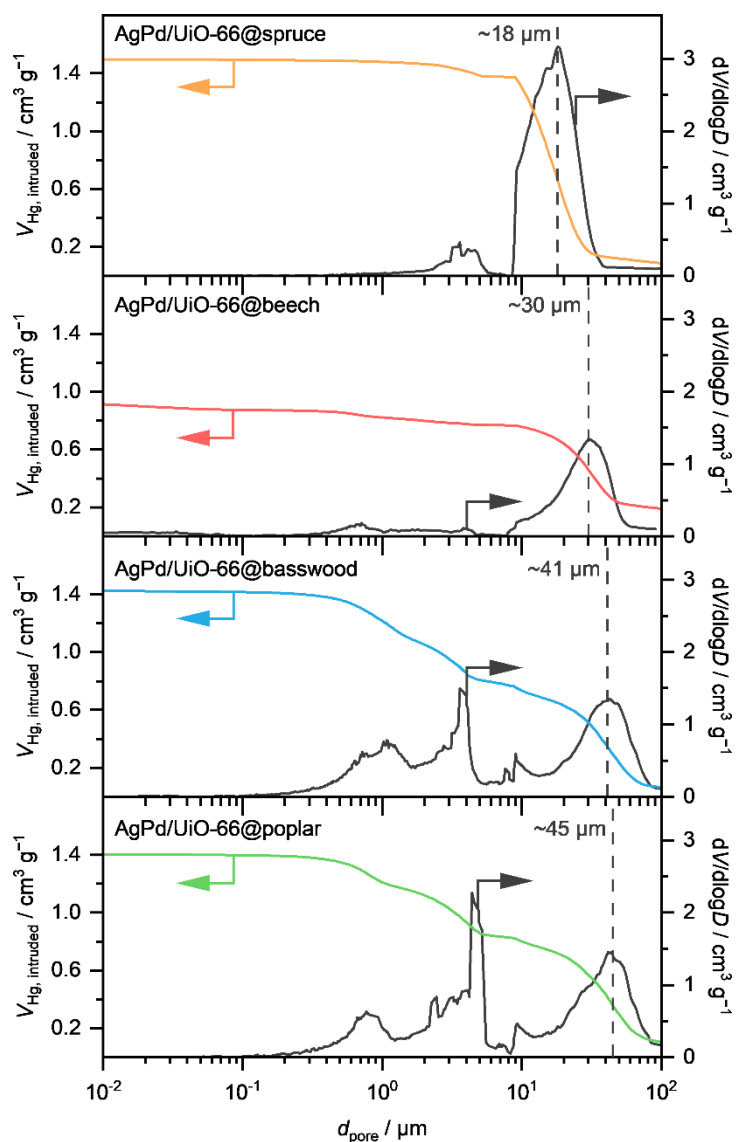


**Figure S22.** Mercury porosimetry and corresponding pore size distributions of bimetallic structured catalysts based on different wood species. The maximum in pore size distribution corresponding to vessels is indicated and increases in the order of spruce < beech < basswood ≤ poplar. Pore size distributions were estimated using the Washburn equation.

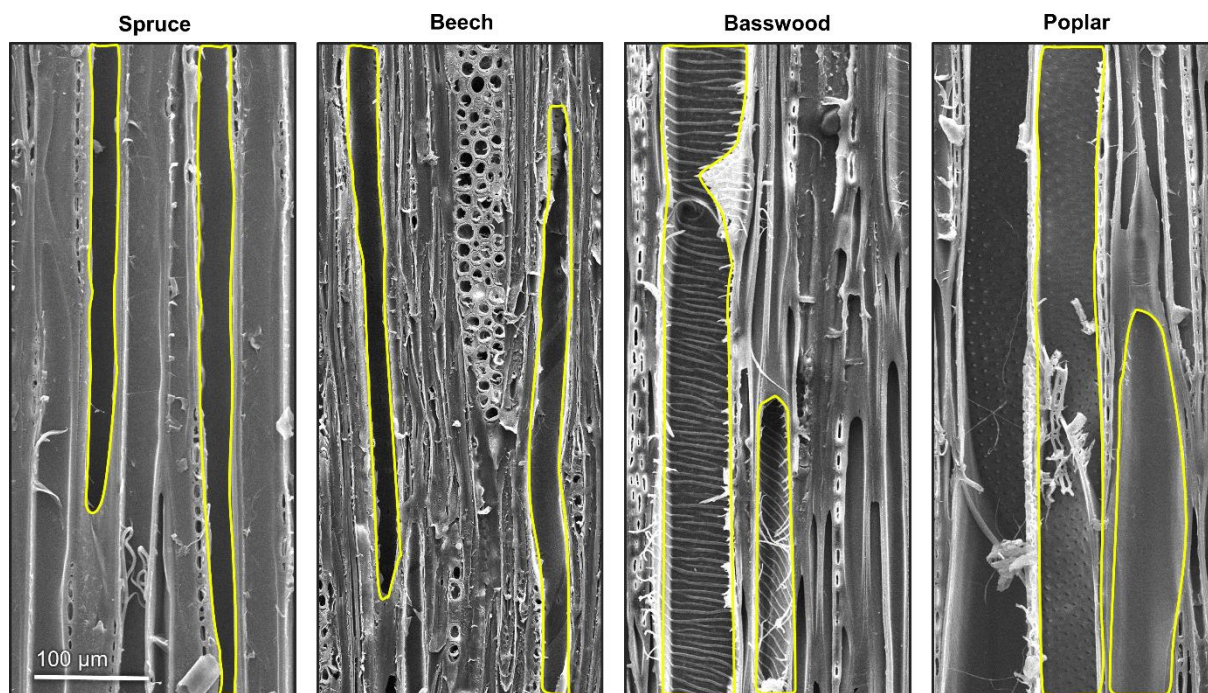


**Figure S23.** SEM images of tangential sections of different native wood species used for the preparation of microreactors. Open vessels (tracheids, in case of spruce) are indicated in yellow showing an increase size from left to right. The scale bar applies for all images.



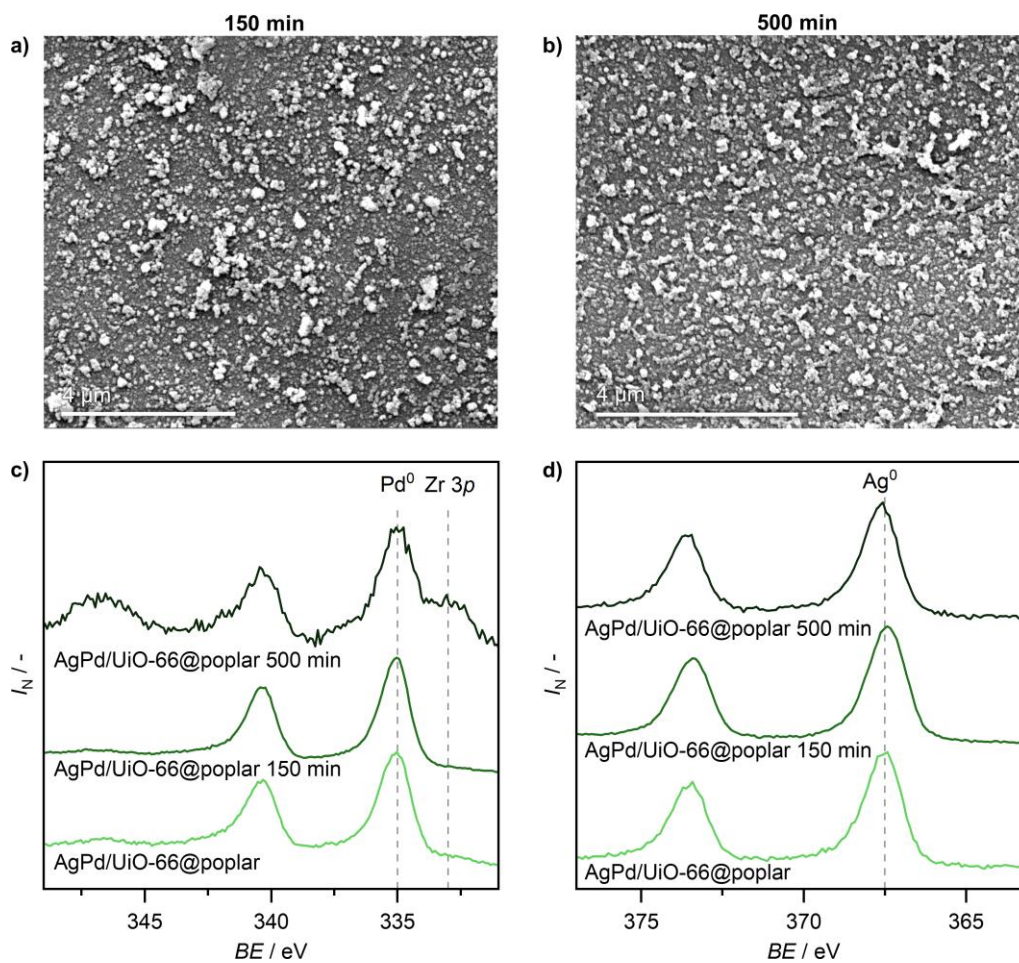


**Figure S24.** SEM images of tangential sections of AgPd/UiO-66@poplar after (a) 150 min and (b) 500 min of reaction. Normalized (c) Pd 3d and (d) Ag 3d XPS spectra of fresh and used AgPd/UiO-66@polar. Reaction conditions:  $F_L = 4 \text{ cm}^3 \text{ min}^{-1}$ ,  $m_{\text{cat}} = 0.14 \text{ g}$ ,  $c_{\text{NH}_3\text{BH}_3,0} = 0.19 \text{ M}$ .

## Supplementary References

- 1 Shang, N.-Z., Feng, C., Gao, S.-T., and Wang, C. (2016). Ag/Pd nanoparticles supported on amine-functionalized metal–organic framework for catalytic hydrolysis of ammonia borane. *Int. J. Hydrogen Energy* *41*, 944-950.
- 2 Wang, Z., Dong, P., Sun, Z., Sun, C., Bu, H., Han, J., Chen, S., and Xie, G. (2018). NH<sub>2</sub>-Ni-MOF electrocatalysts with tunable size/morphology for ultrasensitive C-reactive protein detection via an aptamer binding induced DNA walker–antibody sandwich assay. *J. Mater. Chem. B* *6*, 2426-2431.
- 3 Iqbal, B., Saleem, M., Arshad, S.N., Rashid, J., Hussain, N., and Zaheer, M. (2019). One-pot synthesis of heterobimetallic metal–organic frameworks (MOFs) for multifunctional catalysis. *Chem. - Eur. J.* *25*, 10490-10498.

## 5 General Discussion and Outlook

The main goal of this thesis was to functionalize wood materials by MOFs to develop MOF/wood hybrid materials and explore their applications in gas adsorption and separation, mechanical energy harvesting, and hydrogen generation. In this regard, we successfully introduced versatile green synthesis methods for the *in situ* growth of MOFs within wood substrates and applied them in diverse applications, as presented in chapters 4.2 to 4.4. This chapter will further discuss the results of these publications presented in these chapters.

### 5.1 Wood structure-fabrication-function relationships

#### 5.1.1 The effect of wood hierarchical structure

Wood is a hierarchically structured material made up of well-connected hollow fibrous structures that comprises various length scales. This unique hierarchical and open porous structure, which combines exceptional mechanical properties with lightweight, makes it an ideal scaffold for the production of high-performance composite materials.<sup>94</sup> The chemical constituents of wood are similar, which are mainly cellulose, hemicelluloses, and lignin. The composition only has a slight difference in the hemicelluloses and lignin within softwood and hardwood. These differences do not have a substantial on the preparation of MOF/wood composites. Hence, different wood species can be considered for this kind of nano- and micro-functionalization, utilizing the large number of wood inherent hydroxyl groups and partially carboxyl groups. To enhance the affinity of MOFs and wood, these functional groups within wood can work as active sites for chemical modifications or supplying anchoring points for the nucleation and growth of MOF, which is further discussed in chapter 5.2.

As shown in chapter 4.2, through the assessment of the CO<sub>2</sub> adsorption capacity, adsorption efficiency of the ZIF-8 loaded within wood (*ca.* 48 cm<sup>3</sup> g<sup>-1</sup><sub>ZIF-8</sub> at  $p/p_0=1$ ) is similar to that of pure ZIF-8 (*ca.* 44 cm<sup>3</sup> g<sup>-1</sup><sub>ZIF-8</sub> at  $p/p_0=1$ ). Furthermore, the crystal size of ZIF-8 within wood (420±113 nm) is also in line with that of pure ZIF-8 (460±57 nm). These investigations and results confirm that the embedding process and the utilization of wood as a substrate did not alter the adsorption capacity of the MOF.

However, the difference at the tissue level among wood species leads to differences in morphology and porosity, allowing for the selection of wood species according to the specific application. Especially when the application is based on the surface or on the bulk wood, the principle of selection might be different. In this thesis, we illustrate the selection principle by two applications: surface modification for triboelectric nanogenerator and bulk wood

modification for CO<sub>2</sub> adsorption and hydrogen generation, which are further discussed in 5.1.2 and 5.1.3, respectively.

### **5.1.2 The effect of wood surface morphology**

The surface morphology of wood materials is critical for applications based on the wood surface. In chapter 4.3, we evaluated the effect of wood surface morphology on the triboelectric output of TENGs.

The surface morphology varies for different wood species, cutting planes, as well as cutting techniques and other parameters, leading to a different wood surface roughness. Although there are several studies on the impact of wood surface roughness on finishing costs and the perceived quality of wood products,<sup>95</sup> there is a lack of studies on how the surface roughness of wood affects the triboelectricity of wood. The surface roughness measurements of wood are often performed with a contact stylus profilometer,<sup>96</sup> but in the thesis (chapter 4.3) we used optical profilometry as an optical method, which is generally faster.

As shown in chapter 4.3, even though cut in the same direction (cross-cut), spruce, yew, and balsa show different surface roughness due to their differences in porosity. Cross-cut native balsa has the highest average roughness (Ra) value of 11.9 μm, while cross-cut native yew has the lowest (6.5 μm). The higher Ra value of cross-cut wood samples may result from a higher porosity. In addition, the surface roughness varies depending on the cutting direction for the same wood species. The Ra value of the cross-section is higher than the tangential- and the radial-sections. This originates from the axial alignment of fibers, vessels and tracheids.

Surface roughness has been confirmed to have a great impact on the electrical output (voltage and current) of TENGs.<sup>97,98</sup> Generally, to enhance the electrical output, several methods can be applied to the tribo-material surface to produce roughness, e.g., photolithography templates, sandpaper treatment, cold compression, nanoimprint, and physical/chemical etching, which are all complicated and energy-consuming processes.<sup>99-105</sup> In contrast, the wood surface morphology of different species, anatomical planes, and cutting parameters inherently supply the basic surface roughness that is needed for a tribo-material. Higher surface roughness usually results in an increased effective surface area, thus improving the electrical performance of a TENG.<sup>97,98</sup> However, an extremely rough surface, on the other hand, can cause tip-to-tip contacts between the triboelectric materials, resulting only in partial contact and, as a result, a reduction in electrical output.<sup>106</sup> Hence, the surface roughness should be controlled to achieve high-performance TENGs. After comparing the electrical output of PDMS spinning coated cross-cut spruce, yew, and balsa, radial- and tangential- cut spruce, we found that radial-cut

spruce can supply the most suitable surface roughness. Here, PDMS is used for making the triboelectrical properties of native wood more tribonegative.

In addition to electrical output, the wood morphology has been confirmed to affect also performance in other fields of application. For example, Wang et al. found that wood cutting methods (circular saw cut and microtome cut) strongly affect wood surface morphology, and that they are critical for both the contact angle hysteresis and the wood templating applications.<sup>107,108</sup>

In the future, we need to conduct further wood surface analysis to explore the effect of cutting techniques and parameters on surface roughness as well as triboelectricity. In addition, it is worthy to study the impact of wood morphology on the wood modification and functionalization.

### **2.3.1 The effect of wood porous structure**

Conventional porous membranes are usually synthesized in bottom-up assembly methods from polymeric or inorganic building blocks.<sup>109,110</sup> These approaches involve energy-intensive processes, often unsustainable building blocks, and solvent-based chemistry, which may lead to a substantial negative environmental impact. In contrast, bulk wood materials are already suited as a membrane or microreactor due to their natural porosity. Different wood species show a large variability of cell structures resulting in various porosity. The porous wood structures and aligned lumina arrays make bulk wood materials suitable for a variety of applications, including wastewater treatment, oil-water separation, catalysis, electrocatalytic water splitting, and energy-efficient desalination.<sup>92,111 24,112-118</sup> Even though wood reactors have been utilized for water-based adsorption and catalysis in flow systems, structure-performance relations remain widely unexplored. Researches related to capillary force-driven flow systems, including the effects of porosity, and wood membrane thickness have been studied,<sup>119</sup> but there were only a few studies related to pressure-driven flow systems, at the beginning of the thesis.<sup>93</sup> In chapter 4.4, we evaluated the effects of the diverse porous structure of distinct functionalized wood microreactor on its H<sub>2</sub> generation performance from ammonia borane in pressure-driven flow system.

#### **(a) Capillary force-driven flow systems**

Wood porosity depends on the wood species and is a critical property for energy-water related applications in capillary force-driven flow systems. Previous studies have shown that wood with higher porosity enables more rapid water transport.<sup>119</sup>

Studies also evaluated the relationship between the thickness of the wood membrane and water transport. The decrease of the wood membrane thickness can increase the effective capillarity-driven pressure gradient, which in turn can be employed to increase the water transport rate in wood samples.<sup>119</sup> In addition, thinner membranes increase the probability to have fully cut open fibers. These open cell structure offers unhindered flow through the samples.<sup>93</sup> For spruce, the probability to have continuous, open fibers through the entire sample thickness are 66%, 33%, and 0%, when the membranes are 1 mm, 2 mm, or 3 mm thick respectively.<sup>120</sup>

### **(b) Pressure-driven flow system**

Goldhahn et al. (2020) found that in the pressure-driven flow system, the flux of unmodified beech does not change in the thickness range investigated (between 3 mm and 7 mm).<sup>93</sup> However, due to differences in wood cell wall surface area induced by differing pore architectures, the performance of modified wood products based on different wood species may differ.

To understand the wood cell wall surface area' effects on the water-based catalysis efficiency in pressure-driven flow systems, we made a detailed survey in chapter 4.4. In this manuscript, we decorated AgPd/UiO-66 particles on the wood cell wall surface as the catalysis microreactor. The ammonia borane solution goes through the microreactor in a constant trans-membrane pressure. The hydrogen can be generated at the cell wall surface and then diffuses in the liquid towards the center of the lumen. Under a certain flow speed ( $4 \text{ cm}^3 \text{ min}^{-1}$ ), when using the wood membranes made from different wood species (spruce, beech, basswood, and poplar) with the same thickness (2 mm), we observed an increase in the total generated hydrogen as a function of the area of the channels' wall. A simplified description of the involved mass transport processes can explain the observed trends in total hydrogen generation, which is  $\dot{m}_{\text{H}_2} = h_c \cdot \Delta C \cdot A$ .<sup>121</sup> Here,  $h_c$  is the transport coefficient, and  $\Delta C$  is the mass concentration difference between the wall, where hydrogen is generated, and the bulk fluid.

However, by increasing the external flow from  $4 \text{ cm}^3 \text{ min}^{-1}$  to  $12 \text{ cm}^3 \text{ min}^{-1}$ , the hydrogen generation rate increases, though to a different extent for the different species (below 5% for spruce, up to around 50% for beech). The reason behind this may be because of the different number of open channels within the membranes. Further investigations are needed on the impact of the pits and the related relevance of wood membrane thickness on the pressure-driven flow systems.

## 5.2 Enhancing the affinity between wood and MOFs

In recent years, several wood-based MOF composites have been explored and reported, such as UiO-66/wood for organic pollutants removal,<sup>66</sup> such as rhodamine 6G, propranolol, and bisphenol A, ZIF-8/wood for removal of Cu<sup>2+</sup> ion and methylene blue, as well as iodine capture,<sup>122,123</sup> and MOF-199/wood for antibacterial application.<sup>124</sup>

In addition, delignified wood was also investigated as the substrate support for MOFs, such as Cu-BTC/delignified wood for CO<sub>2</sub> capture,<sup>125</sup> Fe<sub>3</sub>O<sub>4</sub>/ZIF-67@delignified wood for microwave adsorption,<sup>126</sup> and ZIF-67@delignified wood for the removal of tetracycline from water.<sup>127</sup> The MOF/wood composites have great potential in water-based applications, which need high affinity between MOFs and wood materials to avoid the leakage of MOFs from the surface of the wood channels.

As summarized in chapter 4.1, to enhance the affinity between cellulose materials and MOFs, three main chemical pre-treatment methods, which are adjusting charges, increasing the accessibility of the hydroxyl groups, and adding functional groups, can be applied before depositing MOFs on cellulose. The most widely used pre-treatment method is adjusting charges, including TEMPO oxidation and carboxymethylation. They are often performed in the presence of sodium hypochlorite (NaClO) and sodium chloroacetate (ClCH<sub>2</sub>COONa), which are toxic and non-environmental friendly.<sup>18,48,128</sup>

In the manuscript shown in chapters 4.2 and 4.3, we developed a universal green pre-treatment method for the *in situ* growth of MOF nanocrystals on wood substrates. In our approach, native wood is simply pretreated with sodium hydroxide. This step fulfills simultaneously two main functions. Firstly, it ensures the ion exchange of the proton in the wood's inherent carboxyl groups by sodium cations, thereby providing nucleation sites for the subsequent growth of the MOF crystals. Secondly, it provides a rough fibrillary structure that aids the MOFs' anchoring to the wooden substrate. Based on this pre-treatment, MOF crystals can be deposited onto the wood lumen surface uniformly and firmly *via* H-bonding and electrostatic interactions. Experiments in chapter 4.2 also show the fewer MOFs formed within the wood structures without pre-treatment. Different MOFs such as ZIF-8 and MOF-199 can be grown on various wood substrates including beech, spruce, and basswood by using this pre-treatment approach.

In the manuscript presented in chapter 4.4, we further improved the procedure for the growth of MOF crystals within the wood substrate. The organic linker used for UiO-66 synthesis is 2-aminoterephthalic acid (NH<sub>2</sub>-BDC). The amino groups within this linker molecule is able to form hydrogen bonds with the hydroxyl groups of wood macromolecules (cellulose,

hemicelluloses, and lignin). It can facilitate the nucleation and adhesion of UiO-66 crystals within the wood channels. This method is “green” and easy to conduct without using the pre-treatment steps mentioned above, and can be widely used for various MOF formations within wood structures, such as MOF(Ni) and MOF(FeCo).

### **5.3 Critical role of controlling MOF loading and crystal structure**

Due to the extremely high surface area and pore volumes, MOFs have been used in a variety of applications like gas storage and separation,<sup>72</sup> catalysis,<sup>129</sup> and energy storage.<sup>130</sup> The functionality of MOFs is the main reason for the application of the MOF/wood composites. However, it is difficult to control the MOF loading and crystal structure within the composites.

#### **5.3.1 MOF loading**

Increasing the MOF loading within the wood materials can significantly improve the performance of the composites. As the pore structure of wood is limited by its intrinsic structure, the area for MOFs to anchor is also restricted. In the manuscript shown in chapter 4.2, we use layer-by-layer methods to increase the MOF loading. The surface area of the ZIF-8/beechn composites increased from 26 m<sup>2</sup> g<sup>-1</sup> to 84 m<sup>2</sup> g<sup>-1</sup> after two cycles of layer-by-layer deposition. In the manuscript shown in chapter 4.4, we simply used wood species with higher porosity to enhance the MOF loading. The UiO-66 loadings within wood structure range from 0.6 to 3.2 wt.%, due to the wood substrate selection, in the order of beech, spruce, basswood to poplar. The modification methods mentioned above are based on the wood membranes with relative high thickness (above 5 mm). In chapter 4.3, ZIF-8/wood composites prepared based on cross-cut spruce with 1 mm thickness, showed higher ZIF-8 loading (around 9 wt.%). This is much higher than ZIF-8 loading of ZIF-8/wood composites prepared from 5 mm thick wood membranes (around 1.8 wt.%) and can be explained by the lower permeability of thicker wood specimens, limiting their modification.

#### **5.3.2 The crystal size and structure of MOFs**

As shown in chapter 4.2, the MOF crystal structure and properties within MOF/wood composites are not affected by the embedding process. Hence, we can easily control the MOF size and crystal structure, when fabricating the MOF/wood composites. As discussed in chapter 4.3 and 4.4, the MOF crystal structure can be controlled by the ratio of metal ions and organic linker as well as synthesis temperature. The crystal size of the MOF deposited on the wood surface strongly affects the surface roughness at the nanoscale, leading to the variation of the triboelectric output (chapter 4.3). In addition, studies in chapter 4.4 have confirmed that the



hydrothermal synthesis temperature of MOFs influenced the interaction with supported metals, leading to the difference in the catalysis activity of the composites.

## **5.4 Outlook**

In summary, the studies presented in this thesis show a potential alternative to the processing and handling issues of MOF powders. The introduction of MOFs to wood widely expands the utilization of wood materials in various fields, including gas adsorption and separation, energy harvesting, and hydrogen generation. The mechanical properties of the resulting MOF/wood composites clearly surpass those obtained for conventional polymer substrates as shown in chapter 4.2. However, there are still a few research topics that need to be explored in the future.

### **(a) Improve the understanding of composites**

It is essential to have a deeper understanding of MOF/wood composites in terms of functionalization and applications. Techniques like X-ray tomography might be useful as one can visualize wood pore arrangements as well as MOF crystals distribution within the wood by 3D reconstructions with the aid of advanced image software. Detailed investigations with high resolution are possible with the help of synchrotron radiation facilities. In combination with simulation, the liquid and gas transport pathways within the composites can be predicted prior to applying it to real applications.

### **(b) Increase the MOF loading**

As mentioned above, the performance of composites can be considerably improved by increasing the MOF loading within the wood materials. The principle of the methods we used in this thesis is based on keeping the original structure of wood. Delignification is reported as a possible method to increase the MOF loading, due to the removal of lignin leading to more space for MOFs to anchor.<sup>125</sup> However, it will inevitably sacrifice some mechanical properties of the composites. Hence, it is essential to find a way to increase the MOF loading within wood composites, but retain the mechanical properties of wood. We also need to find ways to establish pathways in case of closed lumina in wood during the deposition process of MOFs within wood materials. On the other hand, increasing the MOF loading will also lead to problems such as low permeability for gas and liquid and weak interaction between MOF nanoparticles and wood substrates. We need to pay attention to these possible issues during the fabrication and application process.

### **(c) Enhance interaction between the MOFs and wood**

In this thesis, hydrogen bonding and electrostatic interactions were used to maintain the MOF structure stable on the wood surface, but they are relatively weak when compared with covalent bonds. Enhancing the interaction between MOFs and wood is critical for the long-term stability of the composite. It may be possible to have post-modifications using cross-linkers after preparation of MOF/wood composites to further enhance the interaction of MOFs with wood substrates.

#### **(d) Large-scale**

The fabrication and application of MOF/wood hybrid materials has been conducted at the laboratory scale in this thesis. To expand the usage of MOF/wood composites to an industrial scale, we need to further adjust and optimize the fabrication process, the application setup, and the disposal of the waste in the future.

Firstly, to accommodate industrial demand, greener, cheaper, and more facile synthesis protocols should be explored when fabricating MOF/wood composites. Various promising novel synthetic routes, i.e. electrochemical, mechanochemical, microwave, spray drying, and flow chemistry synthesis can be employed on MOF synthesis and MOF/wood composites preparation.<sup>131</sup> These synthesis processes should be able to control the MOF crystal size precisely and make it uniformly distributed within the wood scaffold in large-scale fabrication. Meanwhile, during the synthesis of the MOFs powders or MOF/wood composites, sometimes it is unavoidable to use non-environmental friendly organic solvents or expensive organic linkers, which will increase the cost and reduce the safety for preparing the composites.

Secondly, MOF/wood composites with better performance should be designed for the various applications. We also need to optimize the devices and setups in which we apply the composites to make them more suitable for industrial-level applications. For instance, it may be possible to improve the triboelectric performance of MOF/wood composites by changing the pairing triboelectric materials or using a different configuration.

Finally, because of environmental concerns, after-use disposal of the composites must be considered. Normally, the wood products can be recovered and utilized or used for energy production after service life. However, the disposal/waste management of MOF within the wood should be further investigated.

## Literature of Chapter 1, 3, and 5

- 1 Li, X., Damartzis, T., Stadler, Z., Moret, S., Meier, B., Friedl, M., and Marechal, F. (2020). Decarbonization in complex energy systems: a study on the feasibility of carbon neutrality for Switzerland in 2050. *Frontiers in Energy Research* 8, 274.
- 2 Li, S., and Huo, F. (2015). Metal-organic framework composites: from fundamentals to applications. *Nanoscale* 7, 7482-7501.
- 3 Ren, J., Langmi, H.W., North, B.C., and Mathe, M. (2015). Review on processing of metal-organic framework (MOF) materials towards system integration for hydrogen storage. *International Journal of Energy Research* 39, 607-620.
- 4 Kang, Z., Fan, L., and Sun, D. (2017). Recent advances and challenges of metal-organic framework membranes for gas separation. *J. Mater. Chem. A* 5, 10073-10091.
- 5 Park, J., and Oh, M. (2017). Construction of flexible metal-organic framework (MOF) papers through MOF growth on filter paper and their selective dye capture. *Nanoscale* 9, 12850-12854.
- 6 Kreno, L.E., Leong, K., Farha, O.K., Allendorf, M., Van Duyne, R.P., and Hupp, J.T. (2012). Metal-organic framework materials as chemical sensors. *Chem Rev* 112, 1105-1125.
- 7 Nguyen, V.D., Nguyen, C.K., Tran, K.N., Tu, T.N., Nguyen, T.T., Dang, H.V., Truong, T., and Phan, N.T.S. (2018). Zeolite imidazolate frameworks in catalysis: Synthesis of benzimidazoles via cascade redox condensation using Co-ZIF-67 as an efficient heterogeneous catalyst. *Applied Catalysis A: General* 555, 20-26.
- 8 Chen, Y.-Z., Zhang, R., Jiao, L., and Jiang, H.-L. (2018). Metal-organic framework-derived porous materials for catalysis. *Coord. Chem. Rev.* 362, 1-23.
- 9 Khandelwal, G., Maria Joseph Raj, N.P., and Kim, S.-J. (2020). ZIF-62: a mixed linker metal-organic framework for triboelectric nanogenerators. *J. Mater. Chem. A* 8, 17817-17825.
- 10 Gomes Silva, C., Luz, I., Llabres i Xamena, F.X., Corma, A., and Garcia, H. (2010). Water stable Zr-benzenedicarboxylate metal-organic frameworks as photocatalysts for hydrogen generation. *Chemistry* 16, 11133-11138.
- 11 Ashour, R.M., Abdel-Magied, A.F., Wu, Q., Olsson, R.T., and Forsberg, K. (2020). Green Synthesis of Metal-Organic Framework Bacterial Cellulose Nanocomposites for Separation Applications. *Polymers-Basel* 12, 1104.
- 12 Peterson, G.W., Lee, D.T., Barton, H.F., Epps, T.H., and Parsons, G.N. (2021). Fibre-based composites from the integration of metal-organic frameworks and polymers. *Nat. Rev. Mater.* 6, 605-621.
- 13 Zhang, Y., Feng, X., Yuan, S., Zhou, J., and Wang, B. (2016). Challenges and recent advances in MOF-polymer composite membranes for gas separation. *Inorg. Chem. Front.* 3, 896-909.
- 14 El Hankari, S., Bousmina, M., and El Kadib, A. (2019). Biopolymer@ Metal-Organic Framework Hybrid Materials: A Critical Survey. *Prog. Mater Sci.*, 100579.
- 15 Hou, X., Zhou, H., Zhang, J., Cai, Y., Huang, F., and Wei, Q. (2018). High Adsorption Pearl-Necklace-Like Composite Membrane Based on Metal-Organic Framework for Heavy Metal Ion Removal. *Particle & Particle Systems Characterization* 35.
- 16 Yang, K., Dai, Y., Zheng, W., Ruan, X., Li, H., and He, G. (2018). ZIFs-modified GO plates for enhanced CO<sub>2</sub> separation performance of ethyl cellulose based mixed matrix membranes. *Sep. Purif. Technol.*
- 17 Sultan, S., Abdelhamid, H.N., Zou, X.D., and Mathew, A.P. (2019). CelloMOF: Nanocellulose Enabled 3D Printing of Metal-Organic Frameworks. *Adv. Funct. Mater.* 29.

- 18 Matsumoto, M., and Kitaoka, T. (2016). Ultraselective Gas Separation by Nanoporous Metal-Organic Frameworks Embedded in Gas-Barrier Nanocellulose Films. *Adv. Mater.* *28*, 1765-1769.
- 19 Zhu, L., Zong, L., Wu, X., Li, M., Wang, H., You, J., and Li, C. (2018). Shapeable Fibrous Aerogels of Metal-Organic-Frameworks Templated with Nanocellulose for Rapid and Large-Capacity Adsorption. *ACS Nano* *12*, 4462-4468.
- 20 Mahltig, B., Swaboda, C., Roessler, A., and Böttcher, H. (2008). Functionalising wood by nanosol application. *J. Mater. Chem.* *18*, 3180-3192.
- 21 Jiang, F., Li, T., Li, Y., Zhang, Y., Gong, A., Dai, J., Hitz, E., Luo, W., and Hu, L. (2018). Wood-Based Nanotechnologies toward Sustainability. *Adv. Mater.* *30*.
- 22 Berglund, L.A., and Burgert, I. (2018). Bioinspired Wood Nanotechnology for Functional Materials. *Adv Mater.*
- 23 Guan, H., Cheng, Z., and Wang, X. (2018). Highly Compressible Wood Sponges with a Spring-like Lamellar Structure as Effective and Reusable Oil Absorbents. *ACS Nano* *12*, 10365-10373.
- 24 Chen, X., Zhu, X., He, S., Hu, L., and Ren, Z.J. (2020). Advanced nanowood materials for the water-energy nexus. *Adv. Mater.*, 2001240.
- 25 Chen, C.J., and Hu, L.B. Nanoscale Ion Regulation in Wood-Based Structures and Their Device Applications. *Adv. Mater.*, 2002890.
- 26 Chen, C., Kuang, Y., Zhu, S., Burgert, I., Keplinger, T., Gong, A., Li, T., Berglund, L., Eichhorn, S.J., and Hu, L. (2020). Structure-property-function relationships of natural and engineered wood. *Nat. Rev. Mater.*
- 27 Pu, Y., Kosa, M., Kalluri, U.C., Tuskan, G.A., and Ragauskas, A.J. (2011). Challenges of the utilization of wood polymers: how can they be overcome? *Appl. Microbiol. Biotechnol.* *91*, 1525-1536.
- 28 Brandt, A., Gräsvik, J., Hallett, J.P., and Welton, T. (2013). Deconstruction of lignocellulosic biomass with ionic liquids. *Green chemistry* *15*, 550-583.
- 29 Wang, Y., Wang, X., Xie, Y., and Zhang, K. (2018). Functional nanomaterials through esterification of cellulose: a review of chemistry and application. *Cellulose* *25*, 3703-3731.
- 30 Karaaslan, M.A., Tshabalala, M.A., and Buschle-Diller, G. (2010). Wood hemicellulose/chitosan-based semi-interpenetrating network hydrogels: Mechanical, swelling and controlled drug release properties. *BioResources* *5*, 1036-1054.
- 31 Kong, L., Tu, K., Guan, H., and Wang, X. (2017). Growth of high-density ZnO nanorods on wood with enhanced photostability, flame retardancy and water repellency. *Appl. Surf. Sci.* *407*, 479-484.
- 32 Hill, C.A. (2007). *Wood modification: chemical, thermal and other processes* (John Wiley & Sons).
- 33 Merk, V., Chanana, M., Gaan, S., and Burgert, I. (2016). Mineralization of wood by calcium carbonate insertion for improved flame retardancy. *Holzforschung* *70*, 867-876.
- 34 Wan, J., Song, J., Yang, Z., Kirsch, D., Jia, C., Xu, R., Dai, J., Zhu, M., Xu, L., Chen, C., et al. (2017). Highly Anisotropic Conductors. *Adv. Mater.* *29*.
- 35 Merk, V., Chanana, M., Gierlinger, N., Hirt, A.M., and Burgert, I. (2014). Hybrid wood materials with magnetic anisotropy dictated by the hierarchical cell structure. *ACS Appl. Mater. Interfaces* *6*, 9760-9767.
- 36 Merk, V., Chanana, M., Keplinger, T., Gaan, S., and Burgert, I. (2015). Hybrid wood materials with improved fire retardance by bio-inspired mineralisation on the nano- and submicron level. *Green Chemistry* *17*, 1423-1428.
- 37 Keplinger, T., Cabane, E., Berg, J.K., Segmehl, J.S., Bock, P., and Burgert, I. (2016). Smart Hierarchical Bio-Based Materials by Formation of Stimuli-Responsive Hydrogels inside the Microporous Structure of Wood. *Adv. Mater. Interfaces* *3*, 1600233.

- 38 Yu, Z.-L., Yang, N., Zhou, L.-C., Ma, Z.-Y., Zhu, Y.-B., Lu, Y.-Y., Qin, B., Xing, W.-Y., Ma, T., and Li, S.-C. (2018). Bioinspired polymeric woods. *Science advances* 4, eaat7223.
- 39 Pan, Z.Z., Nishihara, H., Iwamura, S., Sekiguchi, T., Sato, A., Isogai, A., Kang, F., Kyotani, T., and Yang, Q.H. (2016). Cellulose Nanofiber as a Distinct Structure-Directing Agent for Xylem-like Microhoneycomb Monoliths by Unidirectional Freeze-Drying. *ACS Nano* 10, 10689-10697.
- 40 Wang, Q., and Astruc, D. (2019). State of the art and prospects in metal–organic framework (MOF)-based and MOF-derived nanocatalysis. *Chem. Rev.* 120, 1438-1511.
- 41 Kirchon, A., Feng, L., Drake, H.F., Joseph, E.A., and Zhou, H.-C. (2018). From fundamentals to applications: a toolbox for robust and multifunctional MOF materials. *Chem. Soc. Rev.* 47, 8611-8638.
- 42 Falcaro, P., Ricco, R., Doherty, C.M., Liang, K., Hill, A.J., and Styles, M.J. (2014). MOF positioning technology and device fabrication. *Chem. Soc. Rev.* 43, 5513-5560.
- 43 Liu, J., Thallapally, P.K., McGrail, B.P., Brown, D.R., and Liu, J. (2012). Progress in adsorption-based CO<sub>2</sub> capture by metal-organic frameworks. *Chem. Soc. Rev.* 41, 2308-2322.
- 44 Khandelwal, G., Chandrasekhar, A., Raj, N., and Kim, S.J. (2019). Metal-Organic Framework: A Novel Material for Triboelectric Nanogenerator-Based Self-Powered Sensors and Systems. *Adv. Energy Mater.* 9, 1803581.
- 45 Zhu, B., Zou, R., and Xu, Q. (2018). Metal–Organic Framework Based Catalysts for Hydrogen Evolution. *Adv. Energy Mater.* 8.
- 46 Zhang, X., Chen, A., Zhong, M., Zhang, Z., Zhang, X., Zhou, Z., and Bu, X.-H. (2019). Metal–organic frameworks (MOFs) and MOF-derived materials for energy storage and conversion. *Electrochemical Energy Reviews* 2, 29-104.
- 47 Peplow, M. (2015). Materials science: the hole story. *Nature News* 520, 148.
- 48 Kim, M.L., Otal, E.H., and Hinestroza, J.P. (2019). Cellulose meets reticular chemistry: interactions between cellulosic substrates and metal–organic frameworks. *Cellulose* 26, 123-137.
- 49 da Silva Pinto, M., Sierra-Avila, C.A., and Hinestroza, J.P. (2012). In situ synthesis of a Cu-BTC metal–organic framework (MOF 199) onto cellulosic fibrous substrates: cotton. *Cellulose* 19, 1771-1779.
- 50 Wang, C., Qian, X., and An, X. (2015). In situ green preparation and antibacterial activity of copper-based metal–organic frameworks/cellulose fibers (HKUST-1/CF) composite. *Cellulose* 22, 3789-3797.
- 51 Au-Duong, A.-N., and Lee, C.-K. (2017). Flexible Metal–Organic Framework-Bacterial Cellulose Nanocomposite for Iodine Capture. *Crystal Growth & Design* 18, 356-363.
- 52 Ren, W., Gao, J., Lei, C., Xie, Y., Cai, Y., Ni, Q., and Yao, J. (2018). Recyclable metal-organic framework/cellulose aerogels for activating peroxydisulfate to degrade organic pollutants. *Chem. Eng. J.* 349, 766-774.
- 53 Wang, R., Cao, J., Cai, S., Yan, X., Li, J., Yourey, W.M., Tong, W., and Tang, H. (2018). MOF@Cellulose Derived Co–N–C Nanowire Network as an Advanced Reversible Oxygen Electrocatalyst for Rechargeable Zinc–Air Batteries. *ACS Applied Energy Materials* 1, 1060-1068.
- 54 Mubashir, M., Fong, Y.Y., Leng, C.T., Keong, L.K., and Jusoh, N. (2020). Study on the effect of process parameters on CO<sub>2</sub>/CH<sub>4</sub> binary gas separation performance over NH<sub>2</sub>-MIL-53(Al)/cellulose acetate hollow fiber mixed. *Polym. Test.* 81, 106223.
- 55 He, S., Chen, C., Chen, G., Chen, F., Dai, J., Song, J., Jiang, F., Jia, C., Xie, H., Yao, Y., et al. (2020). A High-Performance, Scalable Wood-based Filtration Device with a Reversed-Tree Design. *Chem. Mater.*

- 56 Qiu, J.L., Fan, P., Yue, C.L., Liu, F.Q., and Li, A.M. (2019). Multi-networked nanofibrous aerogel supported by heterojunction photocatalysts with excellent dispersion and stability for photocatalysis. *J. Mater. Chem. A* 7, 7053-7064.
- 57 Wang, Z., Song, L., Wang, Y., Zhang, X.-F., Hao, D., Feng, Y., and Yao, J. (2019). Lightweight UiO-66/cellulose aerogels constructed through self-crosslinking strategy for adsorption applications. *Chem. Eng. J.* 371, 138-144.
- 58 Chen, B., Yang, Z., Zhu, Y., and Xia, Y. (2014). Zeolitic imidazolate framework materials: recent progress in synthesis and applications. *J. Mater. Chem. A* 2, 16811-16831.
- 59 Feng, S., Zhang, X., Shi, D., and Wang, Z. (2021). Zeolitic imidazolate framework-8 (ZIF-8) for drug delivery: a critical review. *Frontiers of Chemical Science and Engineering* 15, 221-237.
- 60 Pan, Y., Liu, Y., Zeng, G., Zhao, L., and Lai, Z. (2011). Rapid synthesis of zeolitic imidazolate framework-8 (ZIF-8) nanocrystals in an aqueous system. *Chem Commun (Camb)* 47, 2071-2073.
- 61 Yu, J., Xie, L.H., Li, J.R., Ma, Y., Seminario, J.M., and Balbuena, P.B. (2017). CO<sub>2</sub> Capture and Separations Using MOFs: Computational and Experimental Studies. *Chem Rev* 117, 9674-9754.
- 62 Chui, S.S.-Y., Lo, S.M.-F., Charmant, J.P., Orpen, A.G., and Williams, I.D. (1999). A chemically functionalizable nanoporous material [Cu<sub>3</sub> (TMA)<sub>2</sub> (H<sub>2</sub>O)<sub>3</sub>]<sub>n</sub>. *Science* 283, 1148-1150.
- 63 Shoaee, M., Anderson, M.W., and Attfield, M.P. (2008). Crystal Growth of the Nanoporous Metal–Organic Framework HKUST - 1 Revealed by In Situ Atomic Force Microscopy. *Angew. Chem. Int. Ed.* 47, 8525-8528.
- 64 Britt, D., Tranchemontagne, D., and Yaghi, O.M. (2008). Metal-organic frameworks with high capacity and selectivity for harmful gases. *Proceedings of the National Academy of Sciences* 105, 11623-11627.
- 65 Liu, X., Demir, N.K., Wu, Z., and Li, K. (2015). Highly water-stable zirconium metal–organic framework UiO-66 membranes supported on alumina hollow fibers for desalination. *Journal of the American Chemical Society* 137, 6999-7002.
- 66 Guo, R., Cai, X., Liu, H., Yang, Z., Meng, Y., Chen, F., Li, Y., and Wang, B. (2019). In Situ Growth of Metal–Organic Frameworks in Three-Dimensional Aligned Lumen Arrays of Wood for Rapid and Highly Efficient Organic Pollutant Removal. *Environ. Sci. Technol.* 53, 2705-2712.
- 67 Meilikhov, M., Yusenko, K., Esken, D., Turner, S., Van Tendeloo, G., and Fischer, R.A. (2010). Metals@MOFs – Loading MOFs with metal nanoparticles for hybrid functions. *Eur. J. Inorg. Chem.* 2010, 3701-3714.
- 68 Shang, N.-Z., Feng, C., Gao, S.-T., and Wang, C. (2016). Ag/Pd nanoparticles supported on amine-functionalized metal–organic framework for catalytic hydrolysis of ammonia borane. *Int. J. Hydrogen Energy* 41, 944-950.
- 69 Gao, S.-T., Liu, W., Feng, C., Shang, N.-Z., and Wang, C. (2016). A Ag–Pd alloy supported on an amine-functionalized UiO-66 as an efficient synergetic catalyst for the dehydrogenation of formic acid at room temperature. *Catalysis Science & Technology* 6, 869-874.
- 70 Ten, S., Torbina, V.V., Zaikovskii, V.I., Kulinich, S.A., and O, V.V. (2020). Bimetallic AgPd/UiO-66 Hybrid Catalysts for Propylene Glycol Oxidation into Lactic Acid. *Materials (Basel)* 13.
- 71 Cai, W., Wang, J., Chu, C., Chen, W., Wu, C., and Liu, G. (2019). Metal–Organic Framework-Based Stimuli-Responsive Systems for Drug Delivery. *Adv Sci (Weinh)* 6, 1801526.

- 72 Lin, R.-B., Xiang, S., Zhou, W., and Chen, B. (2020). Microporous metal-organic framework materials for gas separation. *Chem-Us* 6, 337-363.
- 73 Ghazvini, M.F., Vahedi, M., Nobar, S.N., and Sabouri, F. (2020). Investigation of the MOF adsorbents and the gas adsorptive separation mechanisms. *Journal of Environmental Chemical Engineering*, 104790.
- 74 Tsai, C.-W., Niemantsverdriet, J., and Langner, E.H. (2018). Enhanced CO<sub>2</sub> adsorption in nano-ZIF-8 modified by solvent assisted ligand exchange. *Microporous Mesoporous Mater.* 262, 98-105.
- 75 Bera, B. (2016). Literature review on triboelectric nanogenerator. *Imperial Journal of Interdisciplinary Research (IJIR)* 2, 1263-1271.
- 76 Fan, F.-R., Tian, Z.-Q., and Wang, Z.L. (2012). Flexible triboelectric generator. *Nano energy* 1, 328-334.
- 77 Khandelwal, G., Raj, N., and Kim, S.J. (2020). Zeolitic Imidazole Framework: Metal-Organic Framework Subfamily Members for Triboelectric Nanogenerator. *Adv. Funct. Mater.* 30, 1910162.
- 78 Wen, R., Guo, J., Yu, A., Zhai, J., and Wang, Z.l. (2019). Humidity - Resistive Triboelectric Nanogenerator Fabricated Using Metal Organic Framework Composite. *Adv. Funct. Mater.* 29.
- 79 Khandelwal, G., Raj, N.P.M.J., Vivekananthan, V., and Kim, S.-J. (2021). Biodegradable metal-organic framework MIL-88A for triboelectric nanogenerator. *Iscience* 24, 102064.
- 80 Zaman, N., Noor, T., and Iqbal, N. (2021). Recent advances in the metal-organic framework-based electrocatalysts for the hydrogen evolution reaction in water splitting: a review. *RSC Adv.* 11, 21904-21925.
- 81 Lin, Y., Mao, W.L., and Mao, H.-k. (2009). Storage of molecular hydrogen in an ammonia borane compound at high pressure. *Proceedings of the National Academy of Sciences* 106, 8113-8116.
- 82 Li, J., Zhu, Q.L., and Xu, Q. (2015). Non-noble bimetallic CuCo nanoparticles encapsulated in the pores of metal-organic frameworks: synergetic catalysis in the hydrolysis of ammonia borane for hydrogen generation. *Catalysis Science & Technology* 5, 525-530.
- 83 Li, J., Zhu, Q.L., and Xu, Q. (2014). Highly active AuCo alloy nanoparticles encapsulated in the pores of metal-organic frameworks for hydrolytic dehydrogenation of ammonia borane. *Chem Commun (Camb)* 50, 5899-5901.
- 84 Chen, Y., Huang, X., Zhang, S., Li, S., Cao, S., Pei, X., Zhou, J., Feng, X., and Wang, B. (2016). Shaping of Metal-Organic Frameworks: From Fluid to Shaped Bodies and Robust Foams. *Journal of the American Chemical Society* 138, 10810-10813.
- 85 Campbell, J., Davies, R., Braddock, D.C., and Livingston, A. (2015). Improving the permeance of hybrid polymer/metal-organic framework (MOF) membranes for organic solvent nanofiltration (OSN)—development of MOF thin films via interfacial synthesis. *J. Mater. Chem. A* 3, 9668-9674.
- 86 Rangnekar, N., Mittal, N., Elyassi, B., Caro, J., and Tsapatsis, M. (2015). Zeolite membranes—a review and comparison with MOFs. *Chem. Soc. Rev.* 44, 7128-7154.
- 87 Qian, D., Lei, C., Hao, G.P., Li, W.C., and Lu, A.H. (2012). Synthesis of hierarchical porous carbon monoliths with incorporated metal-organic frameworks for enhancing volumetric based CO<sub>2</sub> capture capability. *ACS Appl Mater Interfaces* 4, 6125-6132.
- 88 Toumpanaki, E., Shah, D.U., and Eichhorn, S.J. (2020). Beyond What Meets the Eye: Imaging and Imagining Wood Mechanical-Structural Properties. *Adv. Mater.*, e2001613.
- 89 James, E., and Browning, N. (1999). Practical aspects of atomic resolution imaging and analysis in STEM. *Ultramicroscopy* 78, 125-139.

- 90 Schlumberger, C., and Thommes, M. (2021). Characterization of Hierarchically Ordered Porous Materials by Physisorption and Mercury Porosimetry—A Tutorial Review. *Adv. Mater. Interfaces* 8, 2002181.
- 91 Sun, J., Guo, H., Schädli, G.N., Tu, K., Schär, S., Schwarze, F.W., Panzarasa, G., Ribera, J., and Burgert, I. (2021). Enhanced mechanical energy conversion with selectively decayed wood. *Science Advances* 7, eabd9138.
- 92 Goldhahn, C., Taut, J.A., Schubert, M., Burgert, I., and Chanana, M. (2020). Enzyme immobilization inside the porous wood structure: a natural scaffold for continuous-flow biocatalysis. *RSC Adv.* 10, 20608-20619.
- 93 Goldhahn, C., Schubert, M., Lüthi, T., Keplinger, T., Burgert, I., and Chanana, M. (2020). Wood–Gelatin Bio-Composite Membranes with Tunable Flux. *ACS Sustainable Chemistry & Engineering* 8, 7205-7213.
- 94 Burgert, I., Cabane, E., Zollfrank, C., and Berglund, L. (2015). Bio-inspired functional wood-based materials–hybrids and replicates. *60*, 431-450.
- 95 Gurau, L., and Irle, M. (2017). Surface roughness evaluation methods for wood products: A review. *Current forestry reports* 3, 119-131.
- 96 Thoma, H., Peri, L., and Lato, E. (2015). Evaluation of wood surface roughness depending on species characteristics. *Maderas. Ciencia y tecnología* 17, 285-292.
- 97 Lee, S., Lee, Y., Kim, D., Yang, Y., Lin, L., Lin, Z.H., Hwang, W., and Wang, Z.L. (2013). Triboelectric nanogenerator for harvesting pendulum oscillation energy. *Nano Energy* 2, 1113-1120.
- 98 Sun, J.G., Yang, T.N., Kuo, I.S., Wu, J.M., Wang, C.Y., and Chen, L.J. (2017). A leaf-molded transparent triboelectric nanogenerator for smart multifunctional applications. *Nano Energy* 32, 180-186.
- 99 Wang, Z.L., Chen, J., and Lin, L. (2015). Progress in triboelectric nanogenerators as a new energy technology and self-powered sensors. *Energ Environ Sci* 8, 2250-2282.
- 100 Li, G.Z., Wang, G.G., Ye, D.M., Zhang, X.W., Lin, Z.Q., Zhou, H.L., Li, F., Wang, B.L., and Han, J.C. (2019). High-Performance Transparent and Flexible Triboelectric Nanogenerators Based on PDMS-PTFE Composite Films. *Adv Electron Mater* 5.
- 101 Tantraviwat, D., Buarin, P., Suntalelat, S., Sripumkhai, W., Pattamang, P., Rujijanagul, G., and Inceesungvorn, B. (2020). Highly dispersed porous polydimethylsiloxane for boosting power-generating performance of triboelectric nanogenerators. *Nano Energy* 67.
- 102 Sriphan, S., and Vittayakorn, N. (2018). Facile roughness fabrications and their roughness effects on electrical outputs of the triboelectric nanogenerator. *Smart Mater. Struct.* 27, 105026.
- 103 Dudem, B., Ko, Y.H., Leem, J.W., Lee, S.H., and Yu, J.S. (2015). Highly Transparent and Flexible Triboelectric Nanogenerators with Subwavelength-Architected Polydimethylsiloxane by a Nanoporous Anodic Aluminum Oxide Template. *Acs Appl Mater Inter* 7, 20520-20529.
- 104 Su, Z.M., Han, M.D., Cheng, X.L., Chen, H.T., Chen, X.X., and Zhang, H.X. (2016). Asymmetrical Triboelectric Nanogenerator with Controllable Direct Electrostatic Discharge. *Adv Funct Mater* 26, 5524-5533.
- 105 Zhou, T., Zhang, L.M., Xue, F., Tang, W., Zhang, C., and Wang, Z.L. (2016). Multilayered electret films based triboelectric nanogenerator. *Nano Res* 9, 1442-1451.
- 106 Park, S.J., Seol, M.L., Jeon, S.B., Kim, D., Lee, D., and Choi, Y.K. (2015). Surface Engineering of Triboelectric Nanogenerator with an Electrodeposited Gold Nanoflower Structure. *Sci Rep-Uk* 5.
- 107 Wang, Y., Tian, T., and Cabane, E. (2017). Wood composites with wettability patterns prepared by controlled and selective chemical modification of a three-dimensional wood scaffold. *ACS Sustainable Chemistry & Engineering* 5, 11686-11694.



- 108 Wang, Y., Vitas, S., Burgert, I., and Cabane, E. (2019). Beech wood cross sections as natural templates to fabricate superhydrophobic surfaces. *Wood science and technology* 53, 985-999.
- 109 Hosono, N., Guo, W., Omoto, K., Yamada, H., and Kitagawa, S. (2019). Bottom-up Synthesis of Defect-free Mixed-matrix Membranes by Using Polymer-grafted Metal–Organic Polyhedra. *Chem. Lett.* 48, 597-600.
- 110 Horovitz, I., Avisar, D., Baker, M.A., Grilli, R., Lozzi, L., Di Camillo, D., and Mamane, H. (2016). Carbamazepine degradation using a N-doped TiO<sub>2</sub> coated photocatalytic membrane reactor: Influence of physical parameters. *J. Hazard. Mater.* 310, 98-107.
- 111 Vidiella del Blanco, M., Fischer, E.J., and Cabane, E. (2017). Underwater Superoleophobic Wood Cross Sections for Efficient Oil/Water Separation. *Adv. Mater. Interfaces* 4, 1700584.
- 112 Sheng, X., Li, Y., Yang, T., Timmer, B.J.J., Willhammar, T., Cheung, O., Li, L., Brett, C.J., Roth, S.V., Zhang, B., et al. (2020). Hierarchical micro-reactor as electrodes for water splitting by metal rod tipped carbon nanocapsule self-assembly in carbonized wood. *Appl. Catal. B* 264, 118536.
- 113 Chen, H., Zou, Y., Li, J., Zhang, K., Xia, Y., Hui, B., and Yang, D. (2021). Wood aerogel-derived sandwich-like layered nanoelectrodes for alkaline overall seawater electrosplitting. *Appl. Catal., B* 293, 120215.
- 114 Chen, F., Gong, A.S., Zhu, M., Chen, G., Lacey, S.D., Jiang, F., Li, Y., Wang, Y., Dai, J., Yao, Y., et al. (2017). Mesoporous, three-dimensional wood membrane decorated with nanoparticles for highly efficient water treatment. *ACS Nano* 11, 4275-4282.
- 115 Che, W., Xiao, Z., Wang, Z., Li, J., Wang, H., Wang, Y., and Xie, Y. (2019). Wood-based mesoporous filter decorated with silver nanoparticles for water purification. *ACS Sustainable Chem. Eng.* 7, 5134-5141.
- 116 Cheng, Z., Guan, H., Meng, J., and Wang, X. (2020). Dual-functional porous wood filter for simultaneous oil/water separation and organic pollutant removal. *ACS Omega* 5, 14096-14103.
- 117 Chen, Y., Zhang, L., Yang, Y., Pang, B., Xu, W., Duan, G., Jiang, S., and Zhang, K. (2021). Recent progress on nanocellulose aerogels: preparation, modification, composite fabrication, applications. *Adv. Mater.* 33, 2005569.
- 118 Wang, Z., Guo, P., Heng, L., and Jiang, L. (2021). Nano/submicrometer-emulsion oily wastewater treatment inspired by plant transpiration. *Matter* 4, 1274-1286.
- 119 Jia, C., Li, Y., Yang, Z., Chen, G., Yao, Y., Jiang, F., Kuang, Y., Pastel, G., Xie, H., Yang, B., et al. (2017). Rich Mesostructures Derived from Natural Woods for Solar Steam Generation. *Joule* 1, 588-599.
- 120 Ding, Y., Tu, K., Burgert, I., and Keplinger, T. (2020). Janus wood membranes for autonomous water transport and fog collection. *J. Mater. Chem. A* 8, 22001-22008.
- 121 Bejan, A. (2013). Mass Transfer. In *Convection Heat Transfer*, pp. 489-536. <https://doi.org/10.1002/9781118671627.ch11>.
- 122 Zhang, X.-F., Wang, Z., Song, L., and Yao, J. (2021). In situ growth of ZIF-8 within wood channels for water pollutants removal. *Sep. Purif. Technol.* 266, 118527.
- 123 Wang, Z., He, Y., Zhu, L., Zhang, L., Liu, B., Zhang, Y.K., and Duan, T. (2021). Natural porous wood decorated with ZIF-8 for high efficient iodine capture. *Mater. Chem. Phys.* 258, 123964.
- 124 Su, M., Zhang, R., Li, H., Jin, X., Li, J., Yue, X., and Qin, D. (2019). In situ deposition of MOF199 onto hierarchical structures of bamboo and wood and their antibacterial properties. *RSC Adv.* 9, 40277-40285.
- 125 Wang, S.N., Wang, C., and Zhou, Q. (2021). Strong Foam-like Composites from Highly Mesoporous Wood and Metal-Organic Frameworks for Efficient CO<sub>2</sub> Capture. *ACS Appl. Mater. Interfaces* 13, 29949-29959.

- 126 Xu, L., Xiong, Y., Dang, B., Ye, Z., Jin, C., Sun, Q., and Yu, X. (2019). In-situ anchoring of Fe<sub>3</sub>O<sub>4</sub>/ZIF-67 dodecahedrons in highly compressible wood aerogel with excellent microwave absorption properties. *Materials & Design* 182.
- 127 Chen, G., He, S., Shi, G., Ma, Y., Ruan, C., Jin, X., Chen, Q., Liu, X., Dai, H., and Chen, X. (2021). In-situ immobilization of ZIF-67 on wood aerogel for effective removal of tetracycline from water. *Chem. Eng. J.* 423, 130184.
- 128 Zhou, S., Kong, X., Zheng, B., Huo, F., Stromme, M., and Xu, C. (2019). Cellulose Nanofiber @ Conductive Metal-Organic Frameworks for High-Performance Flexible Supercapacitors. *ACS Nano* 13, 9578-9586.
- 129 Lee, J., Farha, O.K., Roberts, J., Scheidt, K.A., Nguyen, S.T., and Hupp, J. (2009). Metal-organic framework materials as catalysts. *Chem. Soc. Rev.* 38, 1450-1459.
- 130 Baumann, A.E., Burns, D.A., Liu, B., and Thoi, V.S. (2019). Metal-organic framework functionalization and design strategies for advanced electrochemical energy storage devices. *Communications Chemistry* 2, 1-14.
- 131 Rubio-Martinez, M., Avci-Camur, C., Thornton, A.W., Imaz, I., Maspoch, D., and Hill, M.R. (2017). New synthetic routes towards MOF production at scale. *Chem. Soc. Rev.* 46, 3453-3480.

# Curriculum Vitae

## Kunkun Tu

Date of Birth: August 27<sup>th</sup>, 1990

Place of Birth: Jiangsu Province, China

Nationality: Chinese

Email: tuk@ethz.ch

Address: Institute for Building Materials – Wood Materials Science  
Laura-Hezner-Weg 7,  
8093 Zürich, Switzerland



## EDUCATIONAL BACKGROUND

---

- 2017-now      Ph.D. Candidate in Civil Engineering  
  
Wood Materials Science, Institute for Building Materials, ETH Zürich  
  
Doctoral Thesis: Functionalization of Wood Materials by Metal-organic Frameworks  
  
Advisor: Prof. Dr. Ingo Burgert
- 2014 –2017      Master of Engineering in Wood Science and Technology,  
  
Research Institute of Wood Industry, Chinese Academy of Forestry  
  
Mater Thesis: Controllable Fabrication and Characterization of Robust  
Superhydrophobic Coatings on Wood Surface  
  
Advisor: Prof. Dr. Xiaoqing Wang
- 2010 – 2014      Bachelor of Engineering in Wood Science and Engineering,  
  
College of Material Science and Engineering, Nanjing Forestry University  
  
Bachelor Thesis: Research of the Red Discoloration of Hainan Rubber Wood  
  
Advisor: Prof. Dr. Ping Miao

## PUBLICATIONS

---

- **Tu, K.**,<sup>#</sup> Büchele, S.,<sup>#</sup> Mitchell, S., Stricker, L., Liu, C., Goldhahn, C., Allaz, J., Ding, Y., Günther, R., Zhang, Z., Sun, J., Panzarasa, G., Zeeman, S.C., Burgert, I., Pérez-Ramírez, J., Keplinger, T. Structured Wood-based Catalytic Microreactors for Continuous Hydrogen Generation from Ammonia Borane. *ACS Applied Materials & Interfaces*, 2022 (14)
- Sun, J.,<sup>#</sup> **Tu, K.**,<sup>#</sup> Büchele, S., Koch, S-M, Ding, Y., Ramakrishna, S-N, Stucki, S., Guo, H. Wu, C., Keplinger, T., Pérez-Ramírez, J., Burgert, I., Panzarasa, G. Functionalized Wood with Tunable Tribo-Polarity for Efficient Triboelectric Nanogenerators. *Matter*, 2021 (4) (Featured article)
- **Tu, K.**,<sup>#</sup> Puértolas, B.,<sup>#</sup> Adobes-Vidal, M., Wang, Y., Sun, J., Traber, J., Burgert, I., Pérez-Ramírez, J., Keplinger, T. Green Synthesis of Hierarchical Metal-Organic Framework/Wood Functional Composites with Superior Mechanical Properties. *Advanced Science*, 2020 (7). (Back Cover)
- Fu, Q., **Tu, K.**, Goldhahn, C., Keplinger, T., Adobes-Vidal, M., Sorieul, M., Burgert, I. Luminescent and Hydrophobic Wood Films as Optical Lighting Materials. *ACS Nano*, 2020 (14).
- Ding, Y., **Tu, K.**, Burgert, I., Keplinger, T. Janus Wood Membranes for Autonomous Water Transport and Fog Collection. *Journal of Materials Chemistry A*, 2020 (8).
- Sun, J., Guo, H., Schädli, G-N., **Tu, K.**, Schär, S., Schwarze, F.WMR., Panzarasa, G., Ribera, J., Burgert, I. Enhanced Mechanical Energy Conversion with Selectively Decayed Wood. *Science Advances*, 2021 (7).
- Sun, J., Guo, H., Ribera, J., Wu, C., **Tu, K.**, Binelli, M., Panzarasa, G., Schwarze, F.WMR., Wang, Z-L., Burgert, I. Sustainable and Biodegradable Wood Sponge Piezoelectric Nanogenerator for Sensing and Energy Harvesting Applications. *ACS Nano*, 2020 (14).
- Frey, M., Biffi, G., Adobes-Vidal, M., Zirkelbach, M., Wang, Y., **Tu, K.**, Hirt, A.M., Masania, K., Burgert, I., Keplinger, T; Tunable Wood by Reversible Interlocking and Bioinspired Mechanical Gradients. *Advanced Science*, 2019 (6).
- **Tu, K.**, Wang, X., Kong, L., Guan, H. Facile Preparation of Mechanically Durable, Self-healing and Multifunctional Superhydrophobic Surfaces on Solid Wood. *Materials & Design*, 2018 (140). (ESI 1%High Citation in 2018)
- Kong, L., **Tu, K.**, Guan, H., Wang, X. Growth of High-density ZnO Nanorods on Wood with Enhanced Photostability, Flame Retardancy and Water Repellency. *Applied Surface*

Science, 2017 (407).

- **Tu, K.**, Wang, X., Kong, L., Chang, H., Liu J. Fabrication of Robust, Damage-tolerant Superhydrophobic Coatings on Naturally Micro-grooved Wood Surfaces. RSC Advances, 2016 (6).
- **Tu, K.**, Kong, L., Wang, X., Liu J. Semitransparent, Durable Superhydrophobic Polydimethylsiloxane/SiO<sub>2</sub> Nanocomposite Coatings on Varnished Wood. Holzforschung, 2016 (70).
- Chang, H., **Tu, K.**, Wang, X., Liu J. Fabrication of Mechanically Durable Superhydrophobic Wood Surfaces Using Polydimethylsiloxane and Silica Nanoparticles. RSC Advances, 2015 (5).
- Chang, H., **Tu, K.**, Wang, X., Liu J. Facile Preparation of Stable Superhydrophobic Coatings on Wood Surfaces using Silica-polymer Nanocomposites. BioResources, 2015 (10).

## PATENTS

---

- Wang, X., **Tu, K.**, Liu J., Chai, Y., Kong, L. (2015) “A method to improve the durability of superhydrophobic films on wood surface” Patent 201510949397.3
- Wang, X., Chang, H., **Tu, K.**, Liu J., Chai, Y. (2015) “A method to fabricate superhydrophobic wood surface by a sol—gel process” Patent 201510949411.X
- Wang, X., **Tu, K.**, Liu J., Chai, Y., Kong, L. Guan, H. (2018) “A multifunctional repairable superhydrophobic wood preparation method” Patent CN107629684A

## CONFERENCE CONTRIBUTIONS

---

- Poster Tu, K., Puértolas, B., Sun, J., Adobes-Vidal, M., Panzarasa, G., Burgert, I., Pérez-Ramírez, J., Keplinger, T. Hierarchical Metal-Organic Framework/Wood Composites with Superior Mechanical Properties for Multi-functional applications, MOFs for energy and the environment Faraday Discussion, online, 2021
- Talk Tu, K. Green Synthesis of Hierarchical Metal-Organic Framework/Wood Functional Composites with Superior Mechanical Properties, Meet & Share, ETH Zürich, 2020
- Talk Tu, K. Green Synthesis of Hierarchical Metal-Organic Framework/Wood Functional Composites, Wood Science & Technology Colloquium, Dübendorf, Switzerland, 2019
- Talk Tu, K., Wang, Y., Keplinger, T., Burgert, I. Formation of MOFs within Porous Wood Supports for CO<sub>2</sub> Capture, Wood Nanotechnology Conference, Ascona, Switzerland, 2018



# Declaration

I, Kunkun Tu, declare that this thesis is my own work and has not been submitted in any form for another degree or diploma at any university or other institute.

Information derived from the published and unpublished work of others has been acknowledged in the text and a list of references is given in the bibliography.

*Kunkun Tu*

Zürich, 12.11.2021